

Control of intermetallics in the interface in directed energy deposition of titanium on stainless steel 316L

Présentée le 24 mai 2023

Faculté des sciences et techniques de l'ingénieur
Laboratoire des matériaux photoniques et caractérisation
Programme doctoral en science et génie des matériaux

pour l'obtention du grade de Docteur ès Sciences

par

Di CUI

Acceptée sur proposition du jury

Prof. V. Subramanian, président du jury
Prof. P. Hoffmann, Dr M. Leparoux, directeurs de thèse
Prof. M. Rauch, rapporteur
Dr A. Popescu, rapporteur
Prof. R. Logé, rapporteur

Acknowledgements

I would like to thank my PhD director Prof. Dr. Patrik Hoffmann. He introduced me to additive manufacturing of metals when I started my internship at Empa and that experience ignited my enthusiasm in this dynamic and fast growing field. With his guidance through my PhD program, I have learned a lot and I am excited to have made my own contribution to this field. I would like to thank my co-director Dr. Marc Leparoux for his constant support. I appreciate all the discussions, experiments, trips and beers together that helped me through difficult times.

I would like to thank Prof. Dr. Vivek Subramanian from EPFL, Prof. Dr. Roland Logé from EPFL, Prof. Dr. Matthieu Rauch from ECN (Nantes, France) and Dr. Andrei Popescu from INFLPR (Magurele, Romania) for kindly accepting to be jury members of my PhD defense. Discussions with you all during my oral exam are very much appreciated.

I would like to thank Dr. Briac Lanfant, Dr. Marie Le Dantec, Dr. Keith Thomas, Dr. Agnieszka Priebe, Dr. Antaryami Mohanta and Dr. Xiao Jia for the scientific and personal discussions, the hiking and the sports together.

I would like to thank Dr. Xavier Maeder, Dr. Vigneashwara Pandiyan, Dr. Maicol Fabbri, Dr. Akash Aggarwal, Dr. Giandomenico Lupo, Dr. Quang Tri Le, Dr. Thu-Hoai Le, Dr. Xiaoshuang Li, Dr. Ariyan Arabi-Hashemi, Dr. Kai Zweiacker, Dr. Viktor Lindström, Dr. Christian Leinenbach, Dr. Kilian Wasmer, Dr. Sébastien Vaucher and Prof. emer. Wilfried Kurz for their help with the experiments and fruitful scientific discussions.

I would like to thank Bernhard von Gunten, Peter Ramseier, Gerhard Bürki, Christian Affolter, Hans-Rudolf Sieber, Jérémie Bérard, Hans Rudolf Elsener, Erwin Pieper and Mikael Debray for their technical support, without which the scientific works could not have been pushed forward.

Thank you to Katrin Gurtner, Eveline Straubhaar and Sandra Beer who always take great care of the administrative affairs for me at Empa.

Thank you to all the members of Abteilung 204 "Laboratory for Advanced Materials Processing" and Abteilung 206 "Laboratory for Mechanics of Materials & Nanostructures" for their support, their help, and the scientific discussions. It has been a great time pursuing my PhD studies in this open, friendly and international environment.

Last but most importantly, I am grateful to my family and friends who always support me to follow my heart and explore life as I decide to. Special thanks to my love Lijin for your warm company and faith in me. Your confidence in me encouraged me through the most difficult times and brought me to the dawn. Knowing you are there for me, even though mostly far across the continents and oceans, has always filled me with love and given me the strength to carry on.

Di Cui, 15.05.2023

Acknowledgements

Abstract

Application of a single metal or alloy is often restricted by its properties from optimal combination of performance and cost. Therefore, there is a vast need of joining dissimilar metals for various applications in biomedical, aerospace, automobile and many other fields. However, for many dissimilar metals, brittle intermetallic compounds (IMCs) are formed at the joint. Plus due to the often mismatching coefficients of thermal expansion (CTE), material failure easily happens at the joint. This problem has long existed for conventional joining techniques. Titanium(-alloys) and stainless steel (SS) 316L is a representative material pair that suffers from this problem. Brittle IMCs such as Fe_2Ti and FeTi are formed in the joint upon mixing of the base materials. Many joining techniques like diffusion bonding, explosive welding, laser welding, friction welding, etc. have been investigated to produce a sound joint between Ti(-alloys) and 316L. Either the joint exhibits poor mechanical strength, or the form of the base materials is largely limited. To the best of the author's knowledge, a convenient and reliable solution to the joining of Ti(-alloys) and SS 316L remains to be developed.

Additive manufacturing (AM) is a solid freeform manufacturing technology that builds three-dimensional (3D) parts by progressively adding thin layers of materials in pre-determined geometry. Directed energy deposition (DED) is an AM technology with unique advantages in building up dissimilar metals directly within a single work piece. Thus, gradient materials or steep transitions between two base metals can be realized.

The present research is focused on joining Ti and 316L by DED with a 500 W maximum power continuous wave (CW) 1068 nm laser beam. Several results have been achieved in this PhD work.

With the DED of Ti single tracks in the conventional process window, the deposition geometry, microstructures, chemical composition transition and phases have been studied. From the 316L side to the Ti side, four possible interfacial regions have been observed in the deposition with decreasing Fe concentration. Three types of composition transitions were found. Low melt depth and dilution ratio are found to lead to complete transition from 316L to pure Ti, with the IMCs constrained within two thin interfacial bands at the bottom of the solidified melt pool. The transition distance, namely the total thickness of the interfacial bands, is found in a range of 20~70 μm .

DED with high powder feedrate, high nozzle velocity and high laser power is found to be beneficial for reducing the total thickness of the IMC-containing interfacial bands while forming acute contact angles on the lateral sides of the single track. Powder feedrate of 21 g/min, nozzle velocity of 13000 mm/min and laser power of 500 W is a representative parameter set. A

Abstract

transition layer thickness down to around 11 μm has been achieved. With Ti cuboids deposited on top of layers printed of such parameter sets, the ultimate shear strength (USS) of the interface is measured in a range of 45~153 MPa.

Thermal management further improved the USS of the interface. Preheating to 520°C, holding the temperature for an hour after deposition finished and cooling down at 25°C/5min increased the USS to a range of 173~381 MPa. The highest USS achieved is 381 ± 24 MPa, exceeding the weaker base material pure Ti (371 MPa) and below the stronger base material 316L (517 MPa).

This work could be continued by optimizing the DED parameters and thermal management parameters. Phases and residual stress in the interfacial thin bands can be more precisely investigated with localized techniques like transmission electron microscopy (TEM) and modeling techniques. The strategy for the Ti-316L system can be adopted for other dissimilar material pairs that also form brittle IMCs to open up opportunities to more applications.

Keywords

Additive manufacturing, directed energy deposition, dissimilar joining, titanium, stainless steel, powders, laser, intermetallic compounds, chemical composition, preheat

Résumé

L'application d'un seul métal ou alliage est souvent limitée par ses propriétés pour obtenir une combinaison optimale de performance et de coût. Par conséquent, il y a un besoin considérable de joindre ensemble différents métaux pour répondre aux besoins dans diverses applications pour le biomédical, l'aérospatial, l'automobile et de nombreux autres domaines. Cependant, pour de nombreux cas, des composés intermétalliques fragiles (IMC) se forment au niveau de la jointure. De plus, en raison des coefficients d'expansion thermique (CTE) souvent très différents, une fissure se produit facilement au niveau de la jointure. Ce problème rencontré aussi avec les techniques conventionnelles de soudure est connu depuis longtemps. Le titane ainsi que ses alliages et l'acier inoxydable (SS) 316L sont une paire de matériaux représentative de ce problème. Des IMC cassants tels que Fe_2Ti et FeTi se forment au niveau de la jonction lors du mélange de ces deux métaux. De nombreuses techniques d'assemblage telles que le brasage par diffusion, la soudure explosive, la soudure laser, la soudure par friction, etc. ont été étudiées pour produire un joint solide entre le Ti (-alliages) et le 316L. Soit ce joint présente une faible résistance mécanique, soit la forme des matériaux de base est largement limitée. À la connaissance de l'auteur, une solution pratique et fiable pour la jonction de Ti (-alliages) et de SS 316L reste à être développée.

La fabrication additive (AM) est une technologie de fabrication solide sans forme qui construit des pièces tridimensionnelles (3D) en ajoutant progressivement des couches minces de matériaux dans une géométrie prédéterminée. Le dépôt sous énergie dirigée (DED) est une technologie AM avec des avantages uniques pour la construction directement en une seule pièce de métaux différents. Ainsi, des matériaux à gradient ou des transitions abruptes entre deux métaux de base peuvent être réalisés.

La présente recherche est axée sur la jonction de Ti et de 316L par DED avec un faisceau laser à onde continue (CW) de 1068 nm et une puissance maximale de 500 W. Plusieurs résultats ont été obtenus dans ce travail de doctorat.

Tout d'abord des lignes uniques de Ti ont été déposées sur un substrat en acier inoxydable en utilisant des paramètres classiques de cette technologie additive. La géométrie de dépôt, les microstructures, la transition de la composition chimique et les phases ont été étudiées. Du substrat en 316L jusqu'aux extrémités supérieures du dépôt de titane, quatre régions interfaciales possibles ont été observées avec la diminution de la concentration en Fe. Trois types de transitions de composition ont été trouvés. Une faible profondeur de fusion et un faible taux de dilution conduisent à une transition complète du 316L au Ti pur, les phases intermétalliques étant limitées dans deux bandes minces au fond du bain de fusion solidifié. La

Résumé

distance de transition, à savoir l'épaisseur totale des bandes interfaciales, se situe dans une plage de 20 à 70 μm .

Une nouvelle stratégie basée sur un taux d'alimentation en poudre élevé, une vitesse de buse élevée et une puissance laser élevée s'avère bénéfique pour réduire l'épaisseur totale des bandes interfaciales contenant des IMC tout en formant des angles de contact aigus sur les côtés latéraux du dépôt. Par exemple, un taux d'alimentation en poudre de 21 g/min, une vitesse de buse de 13000 mm/min et une puissance laser de 500 W ont conduit à de bons résultats. Une épaisseur de couche de transition d'environ 11 μm a été alors obtenue. Pour toutefois évaluer le dépôt d'une structure en 3D avec des dimensions respectables, des cuboïdes de Ti ont été déposés sur des pré-couches de Ti imprimées avec de tels paramètres. La résistance ultime au cisaillement (USS) de l'interface est mesurée dans une plage de 45 à 153 MPa. Une gestion thermique a encore amélioré l'USS de l'interface. Le préchauffage à 520°C, le maintien de la température pendant une heure après la fin du dépôt et le refroidissement à 25°C/5min ont permis d'augmenter l'USS dans une plage de 173 à 381 MPa. La plus haute résistance au cisaillement atteinte est de 381 ± 24 MPa, dépassant la résistance du matériau de base plus faible, soit Ti pur (371 MPa) même si cette résistance reste en dessous de celle de l'acier 316L (517 MPa). Ce travail pourrait être poursuivi en continuant d'optimiser les paramètres DED et de gestion thermique. Les phases et les contraintes résiduelles dans les bandes minces interfaciales peuvent être étudiées plus précisément avec des techniques localisées telles que la microscopie électronique en transmission (TEM) ainsi que par une modélisation. La stratégie proposée pour le système Ti-316L peut être sans doute transférée à d'autres paires de matériaux dissimilaires qui forment également des IMC fragiles et ainsi ouvrir des opportunités à davantage d'applications.

Mots-Clefs

Fabrication additive, dépôt sous énergie dirigée, jointure dissemblable, titane, acier inoxydable, poudres, laser, composés intermétalliques, composition chimique, préchauffage

Table of Contents

Acknowledgements	i
Abstract	iii
Keywords.....	iv
Résumé	v
Mots-Clefs.....	vi
Table of Contents	vii
List of figures.....	xi
List of tables.....	xvii
Nomenclature	xix
Chapter 1. Introduction.....	1
Chapter 2. State of the art.....	5
2.1. Direct Joining of Ti(-alloys) and steels.....	5
2.1.1. Laser welding.....	5
2.1.2. Diffusion bonding.....	6
2.1.3. Friction stir welding.....	7
2.1.4. Explosive welding.....	8
2.1.5. Roll cladding.....	9
2.1.6. Directed energy deposition	11
2.2. Joining of Ti and steels with filler materials.....	12
Chapter 3. Materials and methods.....	13
3.1. Materials.....	13
3.1.1. Substrate	13
3.1.2. Powder	13
3.2. Directed Energy Deposition System	14
3.2.1. Configuration.....	14
3.2.2. Chamber and purifier	16
3.2.3. Laser and beam properties	16
3.2.4. Nozzle.....	16
3.2.5. Hot plate	17
3.2.6. Powder feeding system	19
3.2.7. Model, toolpath and code.....	21
3.2.8. Structures to print and process parameters to control.....	22

Table of Contents

3.3. Interface characterization	23
3.3.1. Sample cutting and embedding.....	23
3.3.2. Cross-section grinding and polishing	23
3.3.3. Optical microscope (OM) observations.....	24
3.3.4. Scanning electron microscope (SEM) observations.....	24
3.3.5. Energy dispersive X-ray spectroscopy (EDS)	24
3.3.6. Electron back scatter diffraction (EBSD).....	24
3.3.7. Microhardness measurement: Vickers hardness test.....	25
3.3.8. Interface strength measurement: Shear test	25
3.3.9. Fracture surface characterization.....	26
Chapter 4. Single track and single wall trials.....	27
4.1. Single track trials.....	28
4.1.1. Results	28
4.1.2. Discussion	41
4.1.3. Conclusion	50
4.2. Single wall trials	51
4.2.1. Results	51
4.2.2. Discussion	55
4.2.3. Conclusion	58
4.3. Summary	58
Chapter 5. Overflowing upper layer	61
5.1. Results.....	62
5.2. Discussion.....	65
5.3. Conclusion	67
Chapter 6. High powder feedrate DED.....	69
6.1. Entering the high powder feedrate regime	69
6.1.1. Results.....	69
6.1.2. Discussion.....	70
6.1.3. Conclusion	71
6.2. High powder feedrate single tracks.....	71
6.2.1. Results.....	72
6.2.2. Discussion.....	77
6.3. High powder feedrate single layer with cuboids on top	78
6.3.1. Results.....	79

6.3.2. Discussion.....	95
6.3.3. Conclusion.....	102
Chapter 7. Conclusions and outlooks.....	105
7.1. Conclusions.....	105
7.2. Outlooks.....	108
Appendix A - Single track trials.....	111
Appendix B - High powder feedrate DED.....	113
Appendix C - EDM cutting plan.....	115
References.....	117
Appendix D - Interface Control in Additive Manufacturing of Dissimilar Metals Forming Intermetallic Compounds—Fe-Ti as a Model System.....	129
Appendix E - Additive Manufacturing of Ti-Nb Dissimilar Metals by Laser Metal Deposition	145
Curriculum Vitae.....	161

Table of Contents

List of figures

Fig. 1-1. Fe-Ti binary phase diagram. ^[12]	1
Fig. 1-2. Illustration of crack and buckle of material B at the surface of material A under different stress conditions.....	2
Fig. 2-1. (a) The appearance of the laser welded seam between stainless steel and titanium alloy and (b) scanning electron microscope (SEM) image of its cross-section.....	5
Fig. 2-2. (a) The weld zone between TC4 and SS showing the reaction layer. (b) The reaction layer. The joint fractured at zone B and zone C during tensile tests.....	6
Fig. 2-3. Diffusion bonding setup arrangement in Gleeble showing SS321/Ti-5Al-2.5Sn ELL sample under heating.	7
Fig. 2-4. Schematic illustration of the setup and arrangement of specimens for FSW (in mm).....	7
Fig. 2-5. Interfacial microstructures take by electron back scatter diffraction (EBSD) phase maps and the tensile test results of the joint between Ti-6Al-4V and 30CrMnSiNi2A medium carbon steel produced by friction stir welding.....	8
Fig. 2-6. a) Schematic of explosive welding configuration. b) Typical interface formed in explosive welding.....	9
Fig. 2-7. Schematic diagram of the assembling form (a) and hot rolling process (b) in roll cladding of Ti-alloy and X65 steel.....	9
Fig. 2-8. The backscattered electron images of the clad interface at different rolling temperatures. (a) 850°C, (b) 900°C, (c) 950°C, (d) 1000°C, e~f are enlarged shapes in a~d, respectively. Red arrows mark the TiC precipitates.....	10
Fig. 2-9. Schematic representation of (a) cold spraying of Ti on a steel plate and (b) hot-rolling process.	10
Fig. 2-10. Fracture morphology of as-rolled and annealed (450°C, 550°C and 650°C for 3 h) Ti/steel clad plates after tensile test.....	11
Fig. 2-11. Direct deposition of SS316 on Ti6Al4V substrate with a laser beam diameter of 2 mm. (a) SS316 layer fell off from Ti6Al4V substrate; (b) Fracture morphology. ^[6]	11
Fig. 3-1. A photo of the stainless steel 316L substrate.....	13
Fig. 3-2. PSD of the Cp-Ti grade 1 45-106 µm powder measured with laser diffraction is plotted as black continuous curve ^[84]	14
Fig. 3-3. SEM images of the 45-106 µm powder particles and their cross-sections, respectively ^[84]	14
Fig. 3-4. Processing chamber of the DED machine BeAM Mobile 1.0.....	15
Fig. 3-5. Schematic of the cross-sectional view of the nozzle.....	17
Fig. 3-6. a) The hot plate fixed on the platform. The aluminum clamps are for fixing the 316L substrate on the top of the hot plate. b) The thermometer used to calibrate the temperature at the top surface of the 316L substrate.....	18

List of figures

Fig. 3-7. The evolution of the temperature at the center and close to the edge of the 316L substrate over time. The hotplate was set to 540°C (HT) at 0 min and set to room temperature (RT) at 32 min.....	19
Fig. 3-8. a) The volumetric powder feeders and b) the rotating plate carrying the powder.....	20
Fig. 3-9. Ti powder feedrate calibration measurements with rotating velocity of the plate.....	21
Fig. 3-10. The interface of the Siemens NX software. The models of five cuboids on the substrate are on the far edge. The toolpaths for three single layer samples are shown in colored curves.....	22
Fig. 3-11. a) The sample holder of the shear tester with a Ti cuboid sample on the fixed 316L substrate. The red arrow indicates the direction of the shear force. b) A cuboid sample after being sheared. The delaminated interface is marked with the white box.....	25
Fig. 4-1. SEM image of the cross-section of single track PF2_1.....	29
Fig. 4-2. Schematic of a single track cross-section. The penetration depth D, added height H and width W are marked.....	29
Fig. 4-3. The dimensions D, H and W measured from PF1_2 single tracks produced on different days.....	30
Fig. 4-4. D, H, W, DL and AR measured from the samples in the PF groups.....	31
Fig. 4-5. The D, H, W, DL and AR measured from the samples in the LP groups.....	32
Fig. 4-6. The D, H, W, DL and AR measured from the samples in the NV groups.....	33
Fig. 4-7. SEM image of the cross-section of track PF2_1.....	34
Fig. 4-8. The four reaction regions between the 316L substrate and the Ti particles in Track PF_2_1. Their microstructural features are marked with white arrows.....	35
Fig. 4-9. The range of Fe atomic percentage in the features in the reaction regions I, II, III and IV marked on the Fe-Ti binary phase diagram.....	36
Fig. 4-10. EDS line scan on track PF3_3. The scan was done along the green arrowed line. The horizontal axis is atomic percentage and the vertical axis is distance. The orange and cyan curves correspond to Fe and Ti respectively. The severe cracks with voids are marked with a white arrow.....	37
Fig. 4-11. EDS line scan on track PF2_1. A crack between two Ti particles is marked with a white arrow.....	38
Fig. 4-12. SEM image of the cross-section of Track PF1_2. The cracks are marked with white arrows.....	39
Fig. 4-13. EDS line scan on track NV1_1. The two bands between the substrate and the deposition are marked with white arrows.....	40
Fig. 4-14. Vickers microhardness $HV_{0.01}$ measured in 316L, Regions I~IV and Ti.....	41
Fig. 4-15. The analytical area is controlled by both the beam diameter and the scatter within the sample. At a higher accelerating voltage, scattering within the sample generates a larger analytical area; at a lower accelerating voltage the expanding beam diameter makes for a larger analytical area. Beam diameters were measured on JEOL JXA-8530F field emission electron microprobe. Size of X-ray generation volume calculated from the Castaing equation ^[89] . 30 kV was used in this study for the EDS analyses, indicating an analytical area with a diameter much larger than 1.4 μm	42
Fig. 4-16. The influence of contact angle and AR on deposition quality. Inter-track porosity is marked in case of obtuse contact angle and $AR > 50\%$	46

Fig. 4-17. OM images of the cross-section of single tracks with transition type 3 - reaching Ti. θ_1 in LP1_3 indicates an obtuse contact angle and θ_2 in NV1_1 indicates an acute contact angle. The red lines and arrows indicate measurement of the dimensions.....	47
Fig. 4-18. Contour plots of D, DL and AR against PF and NV from LP groups.....	48
Fig. 4-19. a) Attenuation of laser beam due to powder particle shadowing ^[103] . b) Image of the interaction zone obtained with a thermal camera for two powders with different sizes. The red and blue colors indicate higher and lower radiated energy, respectively ^[105]	49
Fig. 4-20. Contour plots of D, DL and AR against LP and PF from NV groups.....	50
Fig. 4-21. Cross-sections of Wall PF2_3 and PF3_3. The cracks are marked with white arrows.....	52
Fig. 4-22. a) SEM image of the cross-section of Wall PF2_1. The positions of b), c) and d) are marked with white boxes. EDS mapping of the interfacial regions in b) is shown on the top of b).....	53
Fig. 4-23. Cross-sections of Wall PF1_2, PF1_3 and PF2_1. The widths of their corresponding single tracks are indicated with diamond-arrowed white lines. The ratio of the single wall width to the single track width is marked in each image.....	54
Fig. 4-24. The cross-section of Wall NV1_1. The delamination is marked with a red arrow and the cracks are marked with white arrows.....	55
Fig. 4-25. Schematic of the overflowing method for extending the thin interface.....	57
Fig. 5-1. OM image of the cross-section of the 1 st layer deposited with LP = 175 W, NV = 1000 mm/min and PF = 3.0 g/min. The partially melted Ti particles and reticular Region I are marked.....	62
Fig. 5-2. OM images of the cross-sections of 2-layer single wall samples in groups S1~S4. In each group, NV is constant and LP increases from 175 W to 350 W. NV increases from 500 mm/min in S1 to 1200 mm/min in S4. PF is 3.0 g/min for all samples. Magnification is constant for all images.....	63
Fig. 5-3. Contour plot of deposition area against LP and NV with a constant PF=3.0 g/min.....	64
Fig. 5-4. Contour plot of WRR against LP and NV with a constant PF=3.0 g/min.....	65
Fig. 5-5. a) Schematic of the overhanging problem after depositing multiple tracks. b) Top view of three single layers printed with the overflowing strategy. c) Cross-section of part of a single layer showing the overhanging problem.....	66
Fig. 6-1. The OM images of the cross-section of the M group single tracks. The acute contact angle in M4 is marked as θ_3	70
Fig. 6-2. Photos of the as-printed high PF single tracks in groups Fc and Pc.....	72
Fig. 6-3. OM images of the cross-sections of samples in groups Fa~Fe. In each group, PF is constant and NV increases from 4000 mm/min to 30000 mm/min. PF increases from 6 g/min in Fa to 32 g/min in Fe. LP is at the maximum value 500 W for all samples.....	74
Fig. 6-4. OM images of the cross-sections of samples in groups Pa~Pe. In each group, LP is constant and NV increases from 4000 mm/min to 30000 mm/min. LP increases from 300 W in Pa to 500 W in Pe. PF is at the maximum value 32 g/min for all samples.....	75
Fig. 6-5. OM image of Track Fa_1.....	76

List of figures

Fig. 6-6. OM image of the interface between track Fd_1 and the 316L substrate. In some parts of the lower band closer to 316L, reticular Region I is observed.....	76
Fig. 6-7. OM image of track Fd_4. Two smooth bands can be observed.....	77
Fig. 6-8. Two Ti cuboids deposited on different Ti single layers on the 316L substrate.....	80
Fig. 6-9. OM images of the Ti-316L interface in a) single layer RT_Fd_4, b) cuboid RT_Fd_4, c) single layer HT_Fd_4 and d) cuboid HT_Fd_4.....	81
Fig. 6-10. SEM image of the Ti-316L interface in single layer HT_Fd_4. The chemical composition profile along the green line is shown on the right. The red boxes mark the area and range of Fe ₂₂ ~100.....	82
Fig. 6-11. The transition distance in the single layer and cuboid samples fabricated with RT and HT conditions.....	83
Fig. 6-12. SEM image of the Ti-316L interface in cuboid HT_Fc_5. The Fe ₂₂ border is marked with red broken curves. b) is the area marked with the white box in a).....	84
Fig. 6-13. Specimens after shear test: a) RT_Pe_4, b) RT_Fd_4, c) HT_Pe_4 and d) HT_Fd_4.....	85
Fig. 6-14. Shear force - displacement response of four specimens RT_Pe_4, RT_Fd_4, HT_Pe_4 and HT_Fd_4.....	86
Fig. 6-15. The maximum shear force and ultimate shear strength measured from the cuboid samples.	87
Fig. 6-16. Cuboid samples with their failure features marked. a) HT_Pe_5 with features ij and USS=332 MPa, b) RT_Pd_3 with feature j and USS=61 MPa, c) RT_Fd_3 with features jk and USS=45 MPa.....	88
Fig. 6-17. A Cuboid HT_Fd_3 specimen with its failure feature i and the interfacial thin bands. USS=338 MPa.....	89
Fig. 6-18. a) Top view of a shear fractured HT_Pe_4 specimen. b) high magnification image of feature i , the shear between the cuboid and the first layer, c) high magnification image of feature j , the detachment of the first layer from the substrate. d), e) high magnification images of the areas marked in b) and c) respectively.....	90
Fig. 6-19. a) and b) are the EDS line scan results from the green lines in Fig. 6-18b and Fig. 6-18c in HT_Pe_4, respectively. The periodic fracture features are marked with grey overlay.....	91
Fig. 6-20. Results of EDS line scans on the 316L side of the fracture surface in cuboid samples Pe_4, Fd_3 and Fd_4 produced at both RT and HT. The periodic fracture features are marked in grey and not considered.	92
Fig. 6-21. EDS mapping results from samples RT/HT_Pe_4 and RT/HT_Fd_4. For each samples, the four images from top to bottom are the SEM image, the overlapped distribution of Ti and Fe, the distribution of Ti, and the distribution of Fe. The concentration in the insets are in at.%.	93
Fig. 6-22. The atomic ratio Fe : Fe+Ti and USS from samples RT/HT_Pe_4 and RT/HT_Fd_4. The USS of Ti and 316L from literature are also plotted.	94
Fig. 6-23. a) SEM image of the substrate side from a shear fractured HT_Fd_4 specimen. b) EDS line scan result from the green line in a).....	95

Fig. 6-24. The ultimate shear strength measured from the cuboid samples grouped by failure feature combination.....	97
Fig. 6-25. Flutes in the fracture on the Ti side of a) HT_Pe_4 in this study and b) a hot-roll diffusion bonded Ti/carbon steel joint with nickel interlayer in literature ^[62]	99
Fig. 6-26. Cleavage fractures in the interface in a) RT_Pe_4 in this study and b) a laser welded joint between Ti6Al4V and SS 201 in literature ^[28]	99
Fig. 6-27. Dimples on the fracture surface of a) the interface of HT_Fd_4 in this study, b) 316L prepared by SLM ^[135] and c) 316L prepared by DED ^[136]	100
Fig. 6-28. Temperature dependence of hardness and yield stress of FeTi ^[140]	101
Fig. A-1. Microscopic images of the cross-sections of the single track samples described in 4.1.1. LP groups have a constant LP of 250 W. NV groups have a constant NV of 1000 mm/min. PF groups have a constant PF of 2.5 g/min.....	112
Fig. C-1. The schematic of the top view of a single layer sample with five cuboids on top of it. The red boxes are the cutting path for extracting the shear test samples with EDM.....	115

List of tables

Table 3-1. Chemical composition of the 316L substrate. 13

Table 3-2. Chemical composition of the 45-106 μm Cp-Ti grade 1 powder. 13

Table 4-1. Parameters for the single tracks DED trials. 28

Table 4-2. Compositions and phases in the reaction regions. 43

Table 4-3. Types of composition transitions and defects observed. 43

Table 4-4. The parameters, geometric dimensions and transition types of the single track samples. ... 45

Table 4-5. The geometric dimensions of track and wall samples printed with PF1_2, PF1_3 and PF2_1 parameter sets. Ratios are the wall dimension to the track dimension. 55

Table 5-1. Parameters for the 2nd layers in the DED experiments with overflowing upper layer. 61

Table 6-1. Parameters for single tracks showing the effect of entering the high PF regime. 69

Table 6-2. Parameters for the Ti single layers. Reference parameters for the Ti cuboids on top are in the last row. 79

Table 6-3. The USS and combinations of failure features in the cuboid samples after shear tests. 89

Table B-1. Parameters for the high PF single tracks in the F series. 113

Table B-2. Parameters for the high PF single tracks in the P series. 114

Nomenclature

3D	Three-dimensional
A	Area of the delaminated interface
AM	Additive manufacturing
AR	Aspect ratio, the ratio of H/W
CAD	Computer aided design
CNC	Computer numerical control
CSAM	Cold spray additive manufacturing
CTE	Coefficients of thermal expansion (K^{-1})
CV	Coefficient of variation
CW	Continuous wave
D	Penetration depth, the depth of the solidified melt pool below the surface of the substrate (μm)
DED	Directed energy deposition
Diff	Diffusion coefficient of Fe in β -Ti ($\text{m}^2 \text{s}^{-1}$)
Diff ₀	Diffusion constant of Fe in β -Ti ($\text{m}^2 \text{s}^{-1}$)
DL	Dilution, the ratio of D/(D+H)
EBSD	Electron back scatter diffraction
EDM	Electrical discharge machining
EDS	Energy dispersive X-ray spectroscopy
F _{max}	Maximum shear force recorded during a shear test (N)
FSW	Friction stir welding
H	Added height, the height of the deposited material above the surface of the substrate (μm)
HAZ	Heat-affected zone
HS	Hatch spacing, the distance between the centerlines of two single tracks (mm)
HT	High temperature
HV	Vickers microhardness
i	Shear between the cuboid and the top of the first layer
IMC	Intermetallic compound
j	Detachment of the bottom of the first layer (with the cuboid on top) from the substrate
k	Detachment of the single layer part (without the cuboid on top) from the substrate
LP	Laser power (W)
NV	Nozzle velocity (mm/min)
OM	Optical microscope
OPS	Oxide polishing suspension
PF	Powder feedrate (g/min)
PSD	Particle size distributions
Q	Activation energy of diffusion for Fe in β -Ti (J mol^{-1})
R	Gas constant ($\text{J K}^{-1} \text{mol}^{-1}$)
RT	Room temperature
SE	Secondary electron
SEM	Scanning electron microscopy
SLM	Selective laser melting
SS	Stainless steel
t	Diffusion time (s)
T	Diffusion temperature (K)
TEM	Transmission electron microscopy
USS	Ultimate shear strength (MPa)
UTS	Ultimate tensile strength (MPa)
VRC	Vacuum roll cladding
W	Melt pool width, the width of the melt pool at the level of the surface of the substrate (μm)

Nomenclature

WRR	Wall to Reticular region Ratio, the ratio of the width of the single wall to the width of the reticular region
X	Thickness of the diffusion reaction layer (μm)
ΔZ	Z increment, the increment of the height of nozzle after each layer is finished (mm)

Chapter 1. Introduction

Titanium and its alloys are considered key engineering materials thanks to their outstanding combination of high strength-to-weight ratio, superior heat and corrosion resistance and biocompatibility [1] [2] [3] [4] [5]. Therefore, Ti(-alloys) have been considered excellent engineering materials in biomedical, aerospace, automobile, nuclear and many other industries [6] [7] [8]. However, the high cost and difficult machining of Ti(-alloys) limits their application. To combine the excellent properties of Ti(-alloys) and good formability, economic prices and other advantages of other alloys, the need of joining Ti(-alloys) with dissimilar metals for wider applications have arisen [9] [10] [11]. Stainless steels (SS) are more economic engineering materials with excellent corrosion resistance and mechanical properties. By manipulating the part design, dissimilar joining of Ti(-alloys) and SS can provide combined advantages for novel applications in various industries.

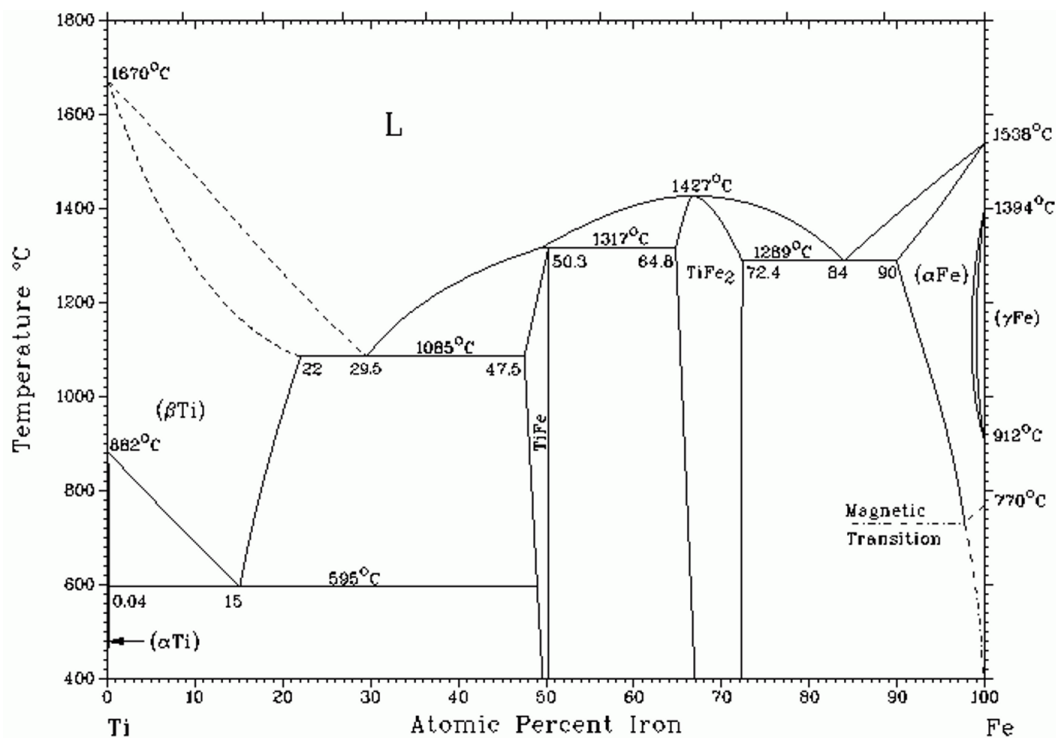


Fig. 1-1. Fe-Ti binary phase diagram. [12]

Joining of Ti(-alloys) and SS has been attempted with many techniques. The Fe-Ti binary phase diagram is shown in **Fig. 1-1**. In direct joining of these dissimilar materials, brittle intermetallic compounds (IMCs) like Fe₂Ti and FeTi form in the interfacial region [13]. A preliminary work by the author on the Fe-Ti system is included in Appendix D [14]. Another work by the author on successful deposition of Ti-Nb dissimilar metals is included in Appendix E to demonstrate metal pairs that do not form IMCs face less harsh challenges [15]. As most joining techniques involve

heating and cooling, the mismatch between the coefficients of thermal expansion (CTE) of the base materials drastically increases the thermal stress and residual stress at the joint ^{[16] [17] [18]}. When cooled down from an elevated temperature, the CTE mismatch between two materials can induce tensile or compressive stress at the interface. **Fig. 1-2** illustrates that crack and buckle can happen under these stress conditions, respectively. As a result of the mechanical and metallurgical factors, cracks are easily formed in the IMCs in the interfacial region, and quickly lead to failure of the joint. To avoid the mixing of Ti(-alloys) and SS, interlayer of a third metal/alloy has been applied between the base materials. Such techniques either produce an interface with poor strength or involves toxic filler material like V and Cr ^{[19] [20] [21]}.

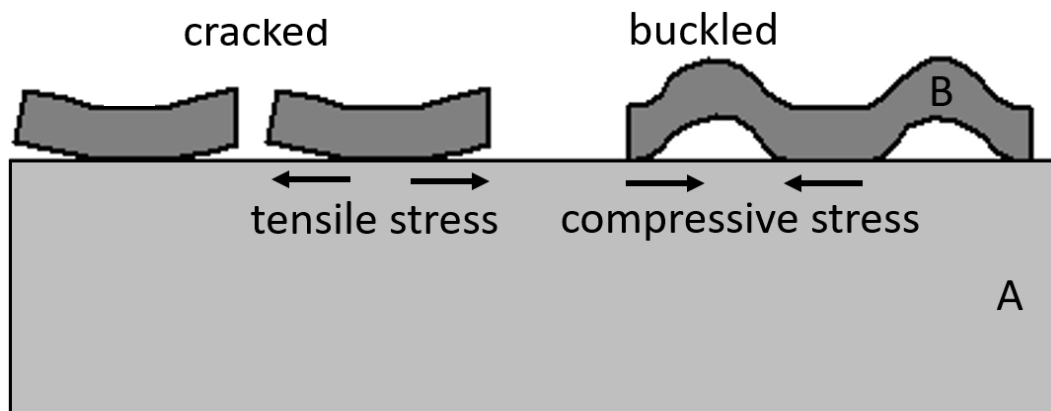


Fig. 1-2. Illustration of crack and buckle of material B at the surface of material A under different stress conditions.

Laser welding has features of small beam size, precise position control and high energy density. These features narrow down the extension of heat-affected zone (HAZ) and therefore reduce residual stresses and distortions ^{[22] [23]}. With the rapid development of computer technology, computer aided design (CAD) emerged and laser could then be used for creating 3D metal parts with similar principles as welding. This new way of manufacturing is laser additive manufacturing (AM). As a solid freeform manufacturing technology, laser AM enables direct fabrication of detailed work pieces by accurately depositing desired material at set positions within a pre-determined domain ^{[13] [24]}.

Directed energy deposition (DED) is a powder-feeding AM technology capable of directly producing dense metal parts with complex geometry and especially varying composition. In a DED process, a laser beam is focused on a metal substrate to create a melt pool, where a co-axially or laterally fed powder jet is also focused on. The metal powder is heated by the laser and normally melts in the melt pool and solidifies rapidly. Movement of the laser head and substrate can be controlled by a computer numerical control (CNC) system. The laser head and substrate move according to pre-defined route pattern to deposit the 3D work piece. DED has

unique advantages in depositing dissimilar materials within a single work piece. The melting of the substrate material and powder material can be controlled to achieve metallurgical bonding with proper dilution of the Fe element in the deposition. Therefore, DED has been selected in this thesis to tackle the cracking problem when joining Ti(-alloys) and SS.

Chapter 2. State of the art

This chapter reviews the techniques that have been practiced to join Ti(-alloys) with steels. Section 2.1 is focused on direct joining of Ti(-alloys) and steels. Section 2.2 is focused on joining of Ti(-alloys) and steels with intermediate filler materials.

2.1. Direct Joining of Ti(-alloys) and steels

2.1.1. Laser welding

Laser welding is a fusion welding technique featuring fast process time and small heat affected zone. During the process, a laser beam runs along the contact line of two metal parts and melts them together. The mixed melt solidifies to create metallurgical bonding between the parts. It has been applied to weld various alloy pairs like Ti-6Al-4V/Inconel 718, Ti/SS 316L, Ti-6Al-4V/AZ31B, etc. [1] [9] [25] [26] [27] Chen et. al used a continuous wave CO₂ laser to weld Ti-6Al-4V and SS 201 plates at 2000 W and a speed of 2 m/min [28]. When the laser beam was centered on the Ti-Fe interface, continuous distribution of large amount of Ti-Fe IMCs occurred in the weld seam, causing a large brittleness. The ultimate tensile strength (UTS) of the joint was only 65 MPa. When the laser beam was offset by 0.6 mm toward the SS, the IMCs had uniform thickness of around 30 μm along the interface (shown in **Fig. 2-1**), and the UTS was improved to 150 MPa.

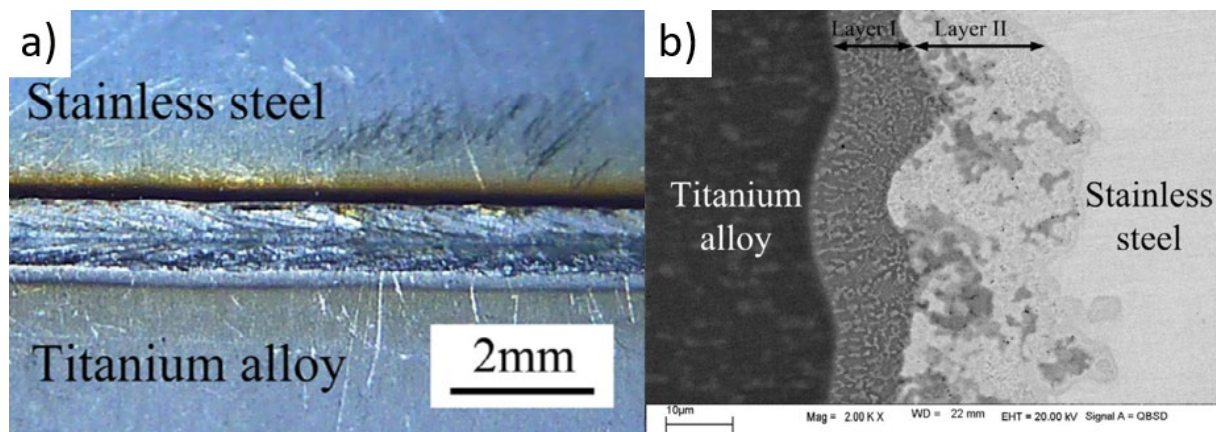


Fig. 2-1. (a) The appearance of the laser welded seam between stainless steel and titanium alloy and (b) scanning electron microscope (SEM) image of its cross-section.

Zhang et al. used a Nd:YAG pulsed laser to weld TC4 (Ti-6Al-4V) and SS 301L [29]. The laser was offset toward the Ti alloy by 0.45 mm. A reaction layer with an average width of 40 μm was observed. The joint fractured in zone B and zone C of the reaction layer during tensile tests. The maximum UTS of the joint was about 336 MPa. The high cooling rate of pulse laser welding was believed to lead to a narrower eutectic reaction zone without mixing the base materials in

the liquid state. The dendritic structures also had finer structures. As a result, higher mechanical strength was obtained.

The drawback of laser welding is that the different temperatures at different depths could cause non-uniform extent of eutectic reaction. In deeper positions, the reaction tends to be insufficient and can lead to insufficient closure of porosities. In shallower positions, the reaction tends to form an IMC layer that could be too thick.

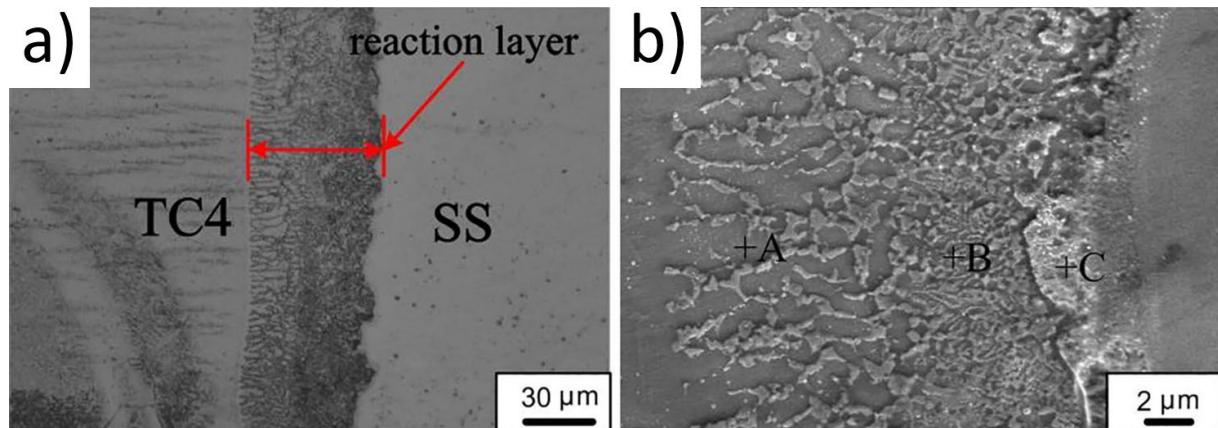


Fig. 2-2. (a) The weld zone between TC4 and SS showing the reaction layer. (b) The reaction layer. The joint fractured at zone B and zone C during tensile tests.

2.1.2. Diffusion bonding

In order to reduce the mixing of the base materials in the liquid state, solid-state welding techniques have been investigated.

Diffusion bonding is a near net shape joining process in which the contact surfaces achieve porosity closure via creep and atom diffusion under certain temperature and pressure ^{[30] [31]}. As a typical solid-state welding technique, it has been studied extensively to join Ti(-alloys) with SS ^{[32] [33] [34] [35] [36] [37] [38] [39] [40] [41] [42]}. Kumar et al. used vacuum diffusion bonding to join Ti5Al2.5Sn-ELI to SS 321 for aerospace applications ^[43]. The set up of vacuum diffusion bonding is shown in **Fig. 2-3**. Different temperatures of 750, 850, 900 and 950°C were used to bond the base materials with a pressure of 10 MPa and processing time of 30min.

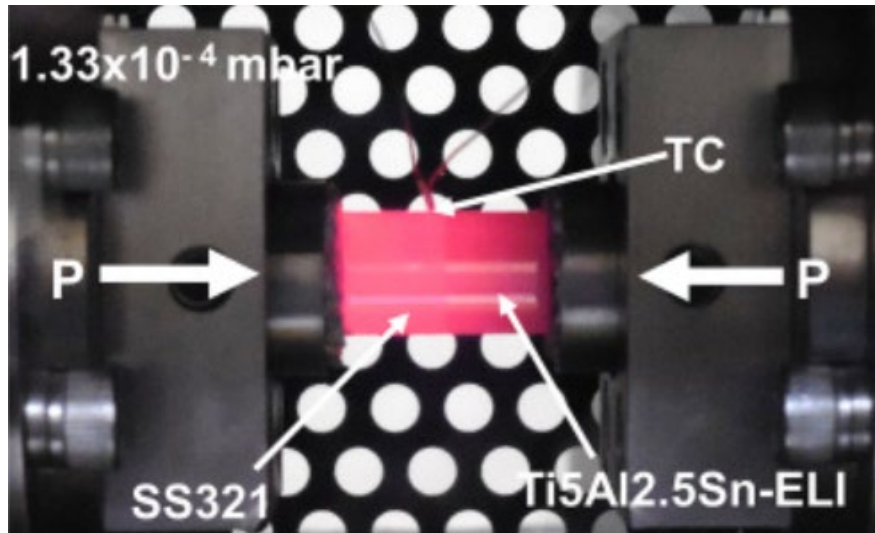


Fig. 2-3. Diffusion bonding setup arrangement in Gleeble showing SS321/Ti-5Al-2.5Sn ELI sample under heating.

The highest ultimate shear strength (USS) achieved was 348 MPa with a bonding temperature of 850°C, around 65% of the USS of SS 321. Compared with lower temperature, the complete collapse of surface asperities made intimate contact at the joint surface. Compared with higher temperatures, interface layers with the optimal width had minimum embrittlement effect. Thus 850°C resulted in the best mechanical strength.

The main drawback of diffusion bonding is that the surfaces to be bonded must be flat or fitting completely.

2.1.3. Friction stir welding

Friction stir welding (FSW) is a dynamic solid-state welding process that produces a weld under the compressive force contact of one rotating and one stationary work pieces ^{[44] [45]}. **Fig. 2-4** illustrates the setup of specimens for FSW ^[46].

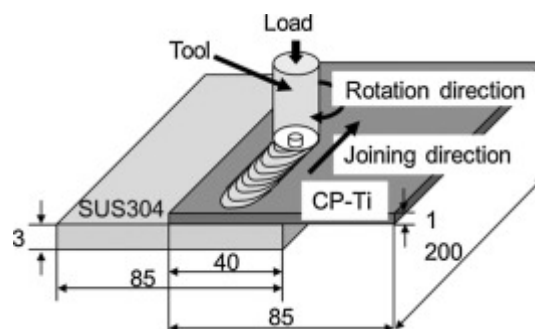


Fig. 2-4. Schematic illustration of the setup and arrangement of specimens for FSW (in mm).

Li et al. fabricated defect-free butt welds of Ti alloy/steel via friction stir welding for the first time^[47]. Joints of Ti-6Al-4V and 30CrMnSiNi2A medium carbon steel were produced with varied rotation speed at 600 and 950 rpm with a constant travel speed of 47.5 mm/min. **Fig. 2-5** shows that both samples fractured at the steel side during tensile testing. The excellent mechanical strength of the interface was explained due to two reasons. On one hand, the less brittle IMC FeTi (600HV) instead of Fe₂Ti (1000HV)^[28] was the main IMC phase formed at the interface. On the other hand, the FeTi layer had an average thickness of only 5 μm and did not embrittle the weld^[48]. The formation of the thin FeTi layer was believed as a result of tremendously high cooling rate and short diffusion time.

The plate form of the base material, the size (diameter and height) of the stirring tool head and the wearing of the tool limit the application of FSW.

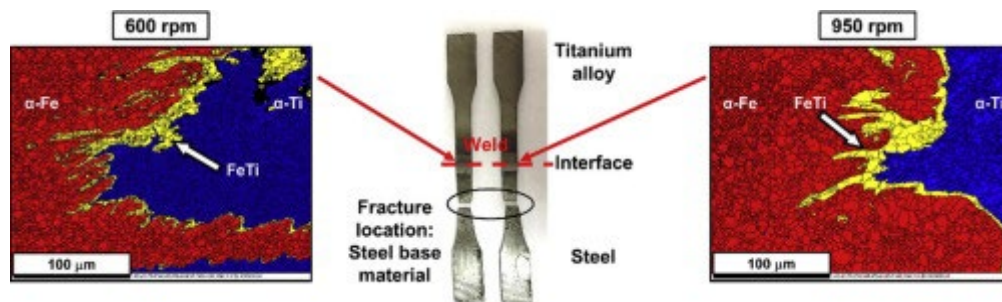


Fig. 2-5. Interfacial microstructures take by electron back scatter diffraction (EBSD) phase maps and the tensile test results of the joint between Ti-6Al-4V and 30CrMnSiNi2A medium carbon steel produced by friction stir welding.

2.1.4. Explosive welding

Explosive welding is also suitable for base metals in the form of plates^{[10] [49] [50] [51]}. **Fig. 2-6a** shows the schematic of explosive welding^[52]. The energy of the explosive is used to press the titanium plate against the steel plate and bond them metallurgically. **Fig. 2-6b** shows the typical wavy interface formed in explosive welding. Chen et al.^[52] found that the welding surface showing small vortex led to shear fracture in Ti with an USS of 354~431 MPa. Larger vortex led to fracture in the interface with an USS of 352~401 MPa.

The nature of explosive welding requires high enough impact resistance and ductility of the processed metals and alloys. Only simple shape parts may be bonded. Safety aspects of storage and using explosives also limit its application.

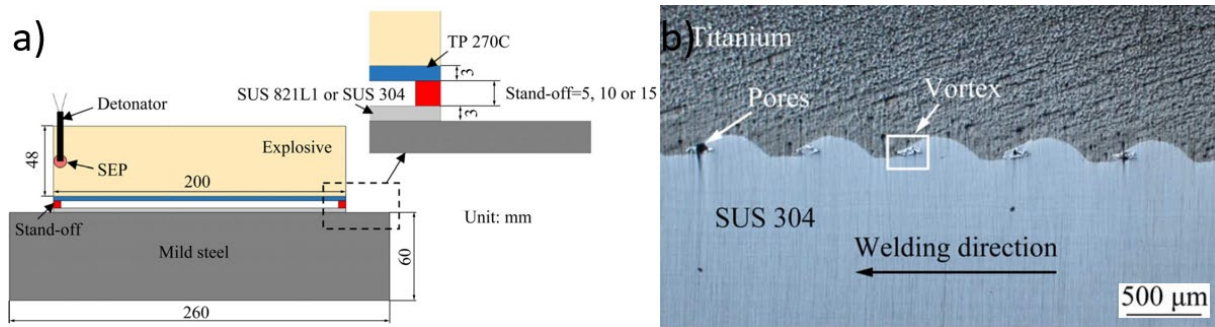


Fig. 2-6. a) Schematic of explosive welding configuration. b) Typical interface formed in explosive welding.

2.1.5. Roll cladding

Vacuum roll cladding (VRC) is suitable for bonding base metals in the form of large plates^[53]^[54]. **Fig. 2-7** shows the schematic diagram of the assembling form and hot rolling process^[55]. Wang et al. used VRC to bond TC4 (Ti-6Al-4V) and X65 steel at 850~1000°C and the clad interfaces are shown in **Fig. 2-8**. The joint exhibited USS of 172~320 MPa with the highest value obtained at 900°C with a diffusion distance of 3.5 μm (Fe in TC4). At a lower temperature of 850°C the thinnest reaction layer formed, but the non-uniform interface of TiC aggregations generated stress concentrations that resulted in lower shear strength. At high temperatures of 950°C and 1000°C, shear strength declined sharply to the worst performance with the coexistence of mixture compounds like TiC, FeTi, and Fe₂Ti.

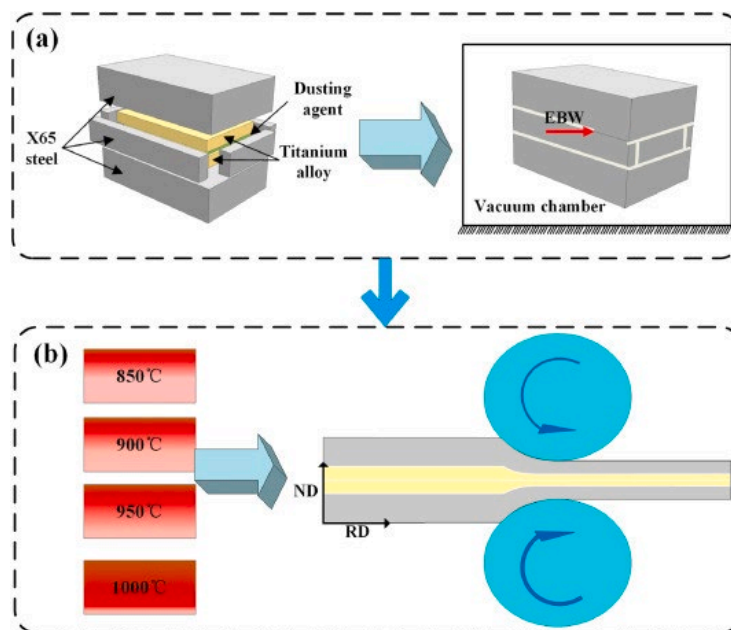


Fig. 2-7. Schematic diagram of the assembling form (a) and hot rolling process (b) in roll cladding of Ti-alloy and X65 steel.

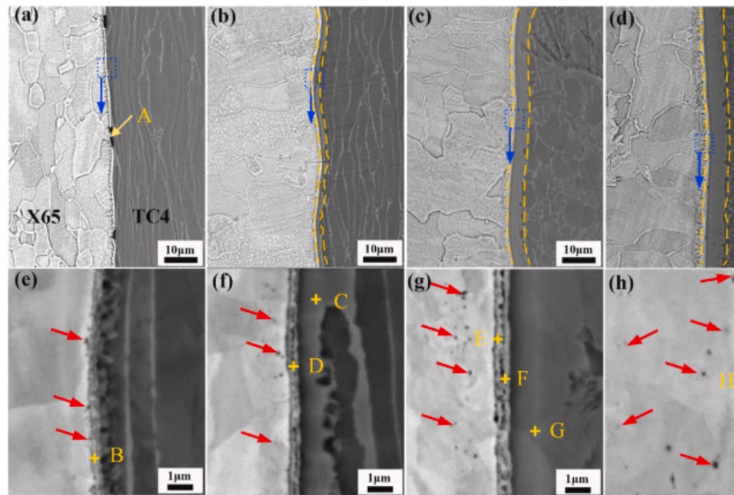


Fig. 2-8. The backscattered electron images of the clad interface at different rolling temperatures. (a) 850°C, (b) 900°C, (c) 950°C, (d) 1000°C, e~f are enlarged shapes in a~d, respectively. Red arrows mark the TiC precipitates.

Zhao et al. combined additive manufacturing and hot-rolling to fabricate Ti/steel clad plates^[3]. Three steps were taken to create Ti coating on mild steel sheets: cold spray additive manufacturing (CSAM), hot-rolling and annealing. The schematic of the first two steps are shown in **Fig. 2-9**. Annealing at 550°C resulted in completely ductile fracture at the interface with a UTS of 564 MPa with excellent elongation of 18% and a USS of 280 MPa. The fracture surfaces of the as-rolled and annealed joints after tensile test are shown in **Fig. 2-10**. The dimples indicating ductile fracture are marked in **Fig. 2-10b, d** and **f**. The radial patterns associated with brittle rapid tearing are marked in **Fig. 2-10h**. The best result from 550°C annealing was estimated due to recovery and recrystallization promoted plasticity without overgrowth of undesired TiC phase.

Roll cladding requires the base materials to be in the form of plates and not brittle.

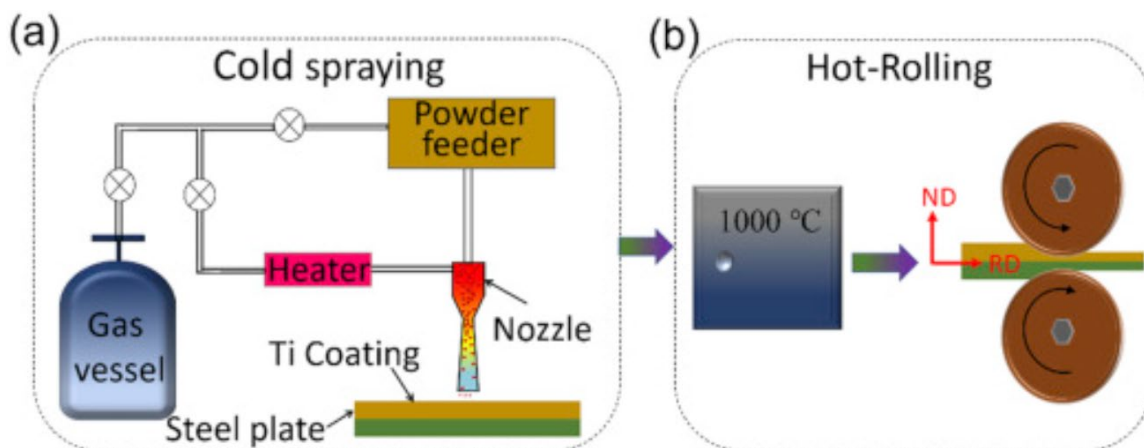


Fig. 2-9. Schematic representation of (a) cold spraying of Ti on a steel plate and (b) hot-rolling process.

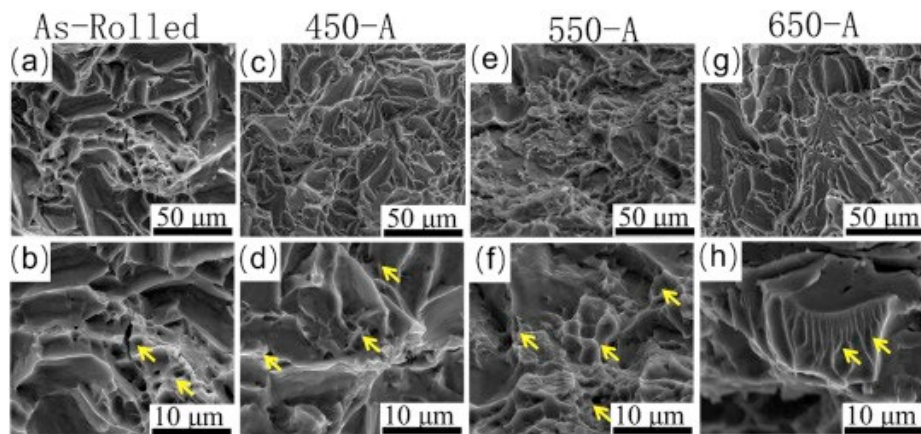


Fig. 2-10. Fracture morphology of as-rolled and annealed (450°C, 550°C and 650°C for 3 h) Ti/steel clad plates after tensile test.

2.1.6. Directed energy deposition

DED of Ti(-alloys) and steels was first explored by Sahasrabudhe et al. [56] Direct deposition of Ti64 (Ti-6Al-4) on SS 410 and compositionally graded SS 316 to Ti64 both failed due to extensive cracking. On one hand, large amounts of IMCs like Cr_2Ti , FeTi and Fe_2Ti were found in the interface. On the other hand, the thermal stress developed in SS 316 was calculated to be approximately 4 times as much as that in Ti64 without assuming any other phase formation. Li et al. also reported that the deposited SS 316 layer directly fell off from the Ti-6Al-4V substrate with clear cracking sound during DED [6]. **Fig. 2-11** shows the fractured deposition and the fracture surface with classic cleavage fracture mechanism. Rashkovets et al. [57] tried the same process with different parameters and obtained less disastrous results, but still observed cracks at the interface. Cracking was estimated due to the thermal stress and high temperature gradient during the cooling phase.

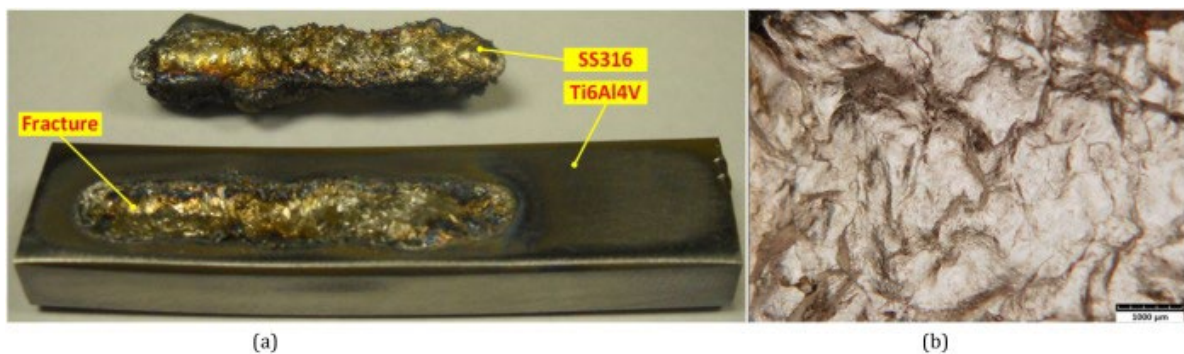


Fig. 2-11. Direct deposition of SS316 on Ti6Al4V substrate with a laser beam diameter of 2 mm. (a) SS316 layer fell off from Ti6Al4V substrate; (b) Fracture morphology. [6]

2.2. Joining of Ti and steels with filler materials

Various filler materials have been investigated in various welding techniques to bypass the IMC and CTE mismatch problems in direct joining of Ti(-alloys) and steels. The most popular filler materials are Ni^{[58] [59] [60] [61] [62] [63]}, Cu^{[64] [65] [66]}, Ag^[67], Al^{[68] [69]}. Complex alloys or multiple layers of filler materials like Ni/Cr^{[70] [71]}, V-Cr-Ni^[72], Nb/Cu/Ni^{[73] [74] [75] [76]} and Zr-Ti-Ni-Cu-Be^[77] have also been experimented.

Interlayer method has also been adopted in DED of Ti and steels to avoid formation of the Fe-Ti IMCs. Li et al.^[78] proceeded with a transition composition route with three filler materials (Ti6Al4V-V-Cr-Fe-SS316). HV gradients from Ti6Al4V through interlayers to SS316 were slight instead of steep, indicating a relatively smooth transition. Bobbio et al.^[79] used a combination of equilibrium calculations and Scheil-Gulliver simulations to design a compositional pathway of SS316-NiCr-Cr-V-Ti6Al4V. Detrimental phases were also avoided along the gradient path. Similar researches^{[80] [81]} provided a solution for crack-free joining under certain circumstances. However, introducing of pure form of non-biocompatible elements V and Cr^{[20] [82]} limited its application in the medical industry.

To conclude, the abovementioned fusion welding and solid-state welding techniques have both shown possibilities of obtaining a joint of Ti(-alloys) and steels with certain interface strength while brittle Ti-Fe IMCs were present. However, either the form of the base materials or the toxicity of the filler materials limits the application of the joint in certain cases. This thesis is therefore dedicated to direct joining of Ti and SS with a strong interface and flexible geometry design via DED.

Chapter 3. Materials and methods

3.1. Materials

3.1.1. Substrate

150 × 150 mm² stainless steel 316L plates with a thickness of 4 mm (HABA AG, Cham, Switzerland) were used as substrate for depositing Ti. A photo of such a substrate is shown in **Fig. 3-1**.

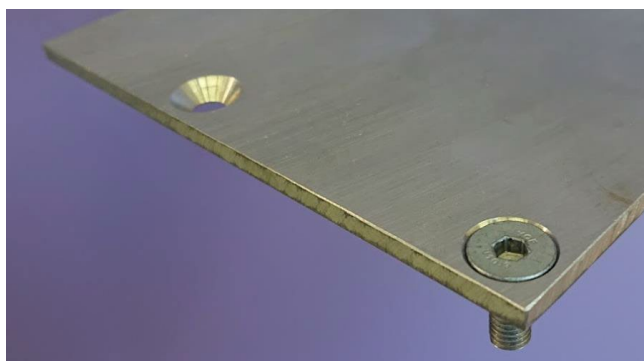


Fig. 3-1. A photo of the stainless steel 316L substrate.

The chemical composition according to the supplier is shown in Table 3-1.

Table 3-1. Chemical composition of the 316L substrate.

Element	C	N	Si	Mn	P	S	Ni	Cr	Mo	Fe
wt. %	≤0.03	≤0.11	≤1.00	≤2.00	≤0.045	≤0.015	10.0-13.0	16.5-18.5	2.00-2.50	Balance

3.1.2. Powder

Commercially pure Cp-Ti grade 1 powder (AP&C Advanced Powders & Coatings Inc., Quebec, Canada) with a particle size distribution of 45-106 μm was used in this study as the deposition material. According to the supplier, the chemical compositions of the powder conform with the ASTM B348 standard ^[83]. The composition of the powder is shown in Table 3-2 for reference.

Table 3-2. Chemical composition of the 45-106 μm Cp-Ti grade 1 powder.

Element	C	O	N	H	Fe	Other each	Other total	Ti
wt. %	≤0.02	≤0.08	≤0.02	≤0.002	≤0.03	≤0.1	≤0.4	Balance

The particle size distributions (PSD) of the powder measured with laser diffraction as per ASTM B822 by the supplier is shown in **Fig. 3-2**. Scanning electron microscopy (SEM) images of the

powder particles and their cross-sections are shown in **Fig. 3-3** ^[84]. The powder particles are highly spherical and have very few satellites or voids.

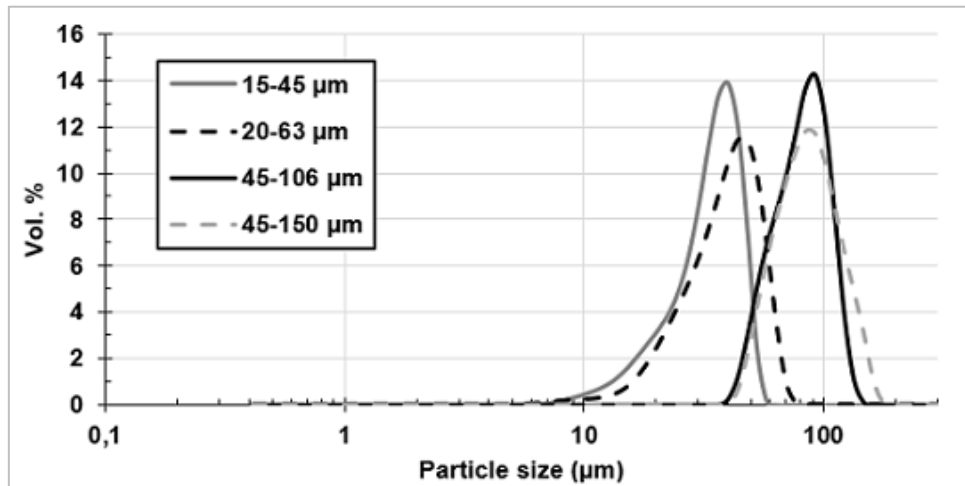


Fig. 3-2. PSD of the Cp-Ti grade 1 45-106 μm powder measured with laser diffraction is plotted as black continuous curve ^[84].

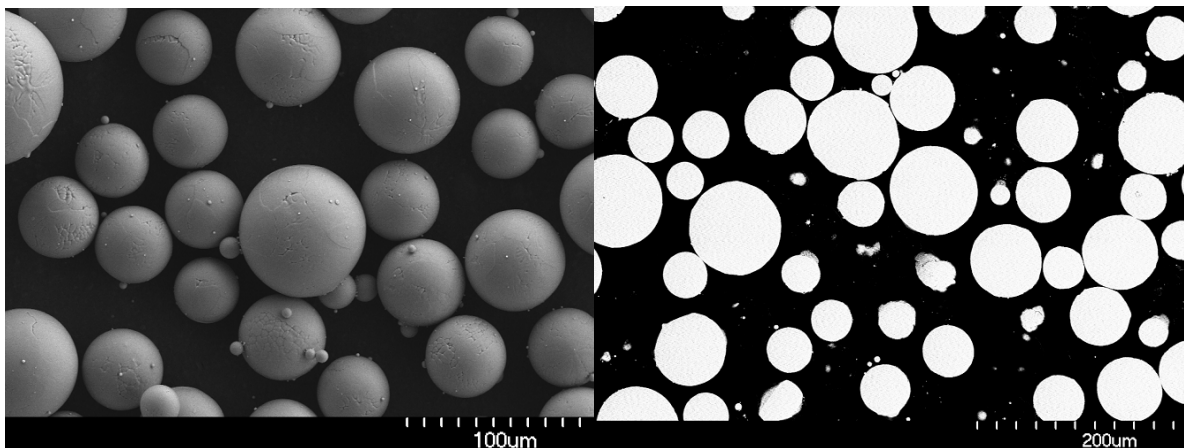


Fig. 3-3. SEM images of the 45-106 μm powder particles and their cross-sections, respectively ^[84].

3.2. Directed Energy Deposition System

3.2.1. Configuration

Directed energy deposition is an advanced powder-injective laser additive manufacturing technology. In this process, the metal powder is injected to the melt pool through a nozzle. The nozzle usually has a ring-shaped channel for focusing the powder jet at a certain distance below its exit, where the laser is also focused. This common focal point is then aligned to the surface of the substrate. During the process, the nozzle moves above the substrate following a

toolpath to deposit the powder material layer by layer, and eventually forming a predesigned 3D structure.

A commercial DED machine BeAM Mobile 1.0 (BeAM Machines, Strasbourg, France) was used in this study. The machine has a 3-axis arm that supports the nozzle and a 2-rotative-axis platform for fixing the substrate. The maximum nozzle velocity in automatic mode is 30000 mm/min. The processing chamber is shown in **Fig. 3-4** with the movement axes marked.

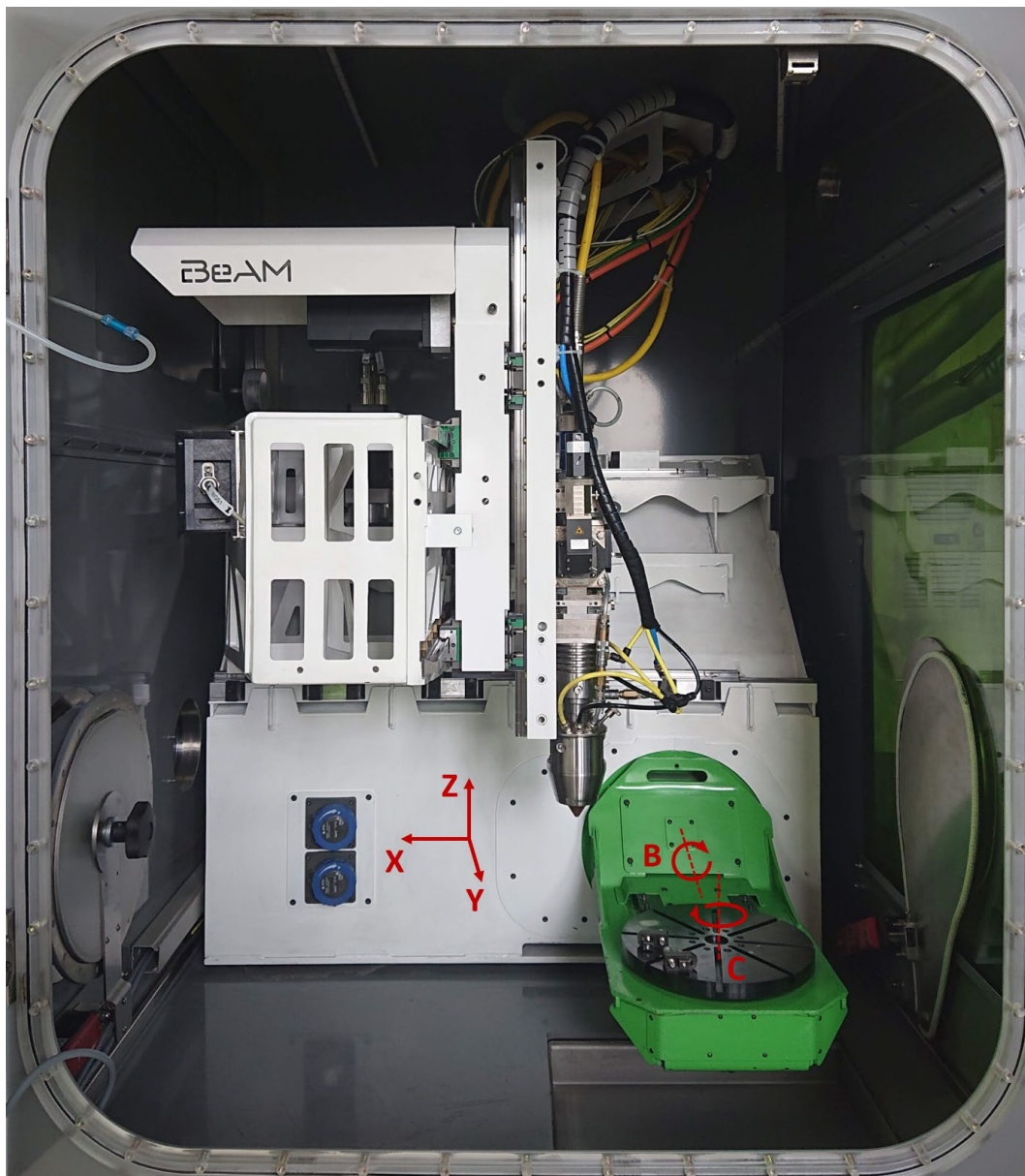


Fig. 3-4. Processing chamber of the DED machine BeAM Mobile 1.0.

3.2.2. Chamber and purifier

The airtight process chamber of the DED system allows to work under a controlled atmosphere. It is equipped with a gas purifier (GS MEGA E-Line, GS GLOVEBOX Systemtechnik GmbH, Malsch, Germany) that can eventually reduce the concentration of O₂ to below 1 ppm and H₂O to below 50 ppm.

In this study, all structures were fabricated under argon. The inertizing process consists of two steps. In the first step, rapid purge, argon is fed into the chamber from argon bottles, pushing out and diluting the air in the chamber. When O₂ concentration is below 0.1%, rapid purge is stopped manually. In the second step, purification, the gas in the chamber runs through the purifier and returns to the process chamber. The purifier further reduces O₂ and H₂O concentrations and keep them at low levels until the process is finished. Typically, the DED processes were conducted when O₂ and H₂O concentrations are in the ranges of 1.0-10.0 ppm and 50.0-300.0 ppm, respectively.

3.2.3. Laser and beam properties

The DED system uses a continuous wave (CW) Ytterbium fiber laser (YLR-Series, IPG Photonics, Oxford, Massachusetts, USA) as the energy source. The laser has a wavelength of 1068 nm and a maximum power of 500 W. According to the machine manufacturer, the transverse profile of the laser is Gaussian, the diameter of the focal spot is about 800 μm and the Rayleigh length is 18 mm.

3.2.4. Nozzle

The nozzle is made of copper. The high thermal conductivity of copper helps to dissipate the heat at the tip of the nozzle which is close to the hot melt pool during the DED process. A schematic of the cross-section of the nozzle is shown in **Fig. 3-5**. The nozzle consists of three coaxial cones, which form one circular channel and two ring-shaped channels. The circular channel in the center allows the laser beam and the primary gas (3 L/min) to pass through and prevents metal vapor from entering the optics, which could coat the lenses and affect the transmission of laser or damage the optic elements. The intermediate ring-shaped channel allows the shaping gas (6 L/min) to pass through. The outer ring-shaped channel allows the powder carried by the shield gas to pass through. The three gases work together to focus the powder jet 3.5 mm below the exit of the nozzle to a circular area with a diameter of around 1 mm.

During the DED process, the nozzle has a standoff distance of 3.5 mm above the substrate. The focal points of the laser and of the powder jet are thus aligned together on the surface of the substrate.

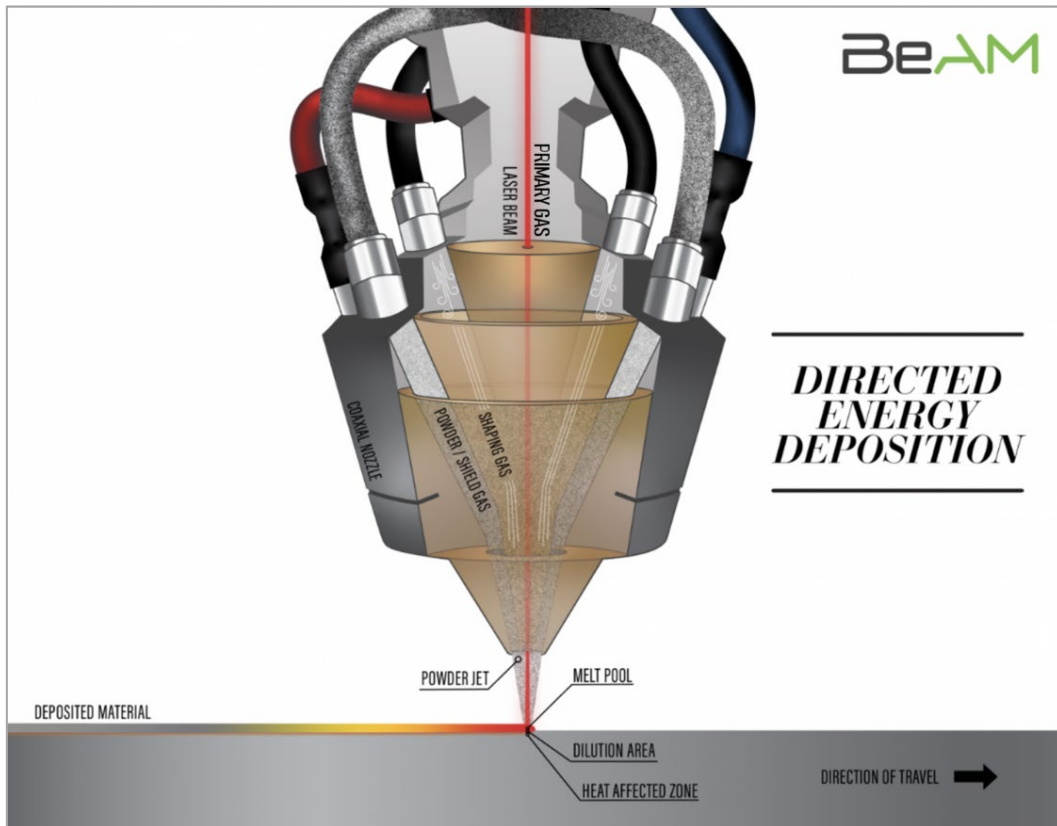


Fig. 3-5. Schematic of the cross-sectional view of the nozzle.

3.2.5. Hot plate

A ceramic top hot plate (Fisherbrand Isotemp, Fisher Scientific AG, Reinach, Switzerland) was used in this study for preheating the 316L substrate. The hot plate is able to heat up to 540°C and maintain at the set temperature. The temperature at the top surface of the preheated 316L substrate can reach around 520°C (measured below).

The hot plate can be fixed on the platform by screws. 316L substrates are fixed on the hot plate with aluminum clamps shown in **Fig. 3-6a**.

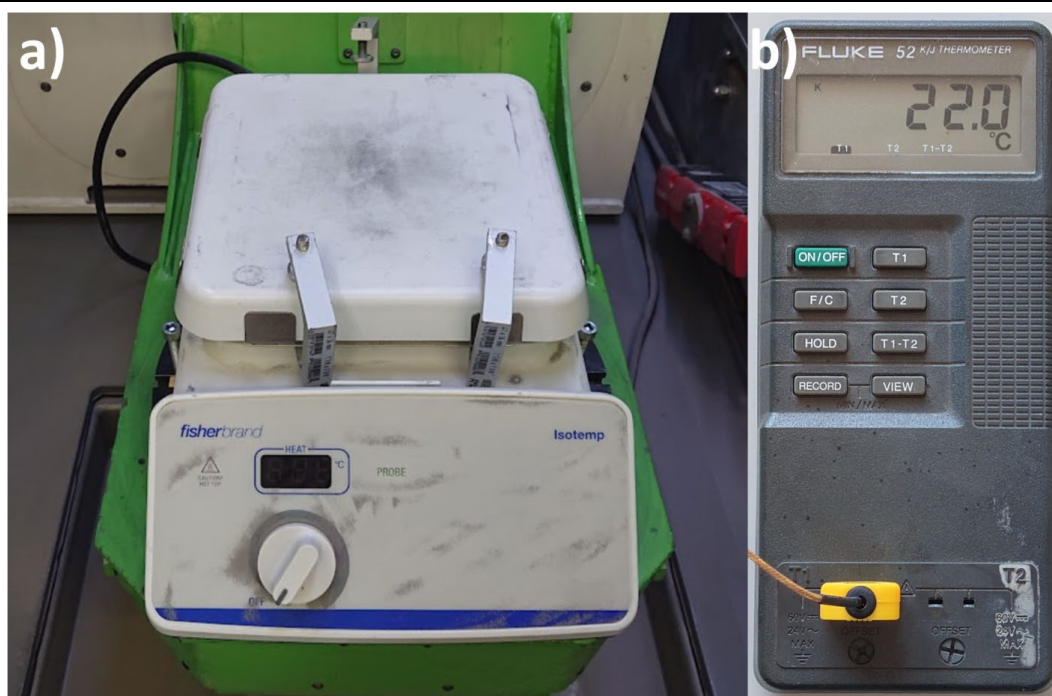


Fig. 3-6. a) The hot plate fixed on the platform. The aluminum clamps are for fixing the 316L substrate on the top of the hot plate. b) The thermometer used to calibrate the temperature at the top surface of the 316L substrate.

The temperature at the center and close to the edge of the 316L substrate were measured with a K-type thermocouple on a thermometer (FLUKE 52, Fluke Corporation, Everett, Washington, USA) shown in **Fig. 3-6b**. **Fig. 3-7** shows the temperature evolution over time during the calibration. At room temperature (RT), the hotplate was set for 540°C (HT) at 0 min. In around 10 min, the temperature at the center of the substrate reached around 520°C and stabilized. At 32 min, the hotplate was switched off, and it took the substrate around 30 min to cool down to around 120°C. The temperature close to the edge of the substrate was approximately 20°C lower than at the center.

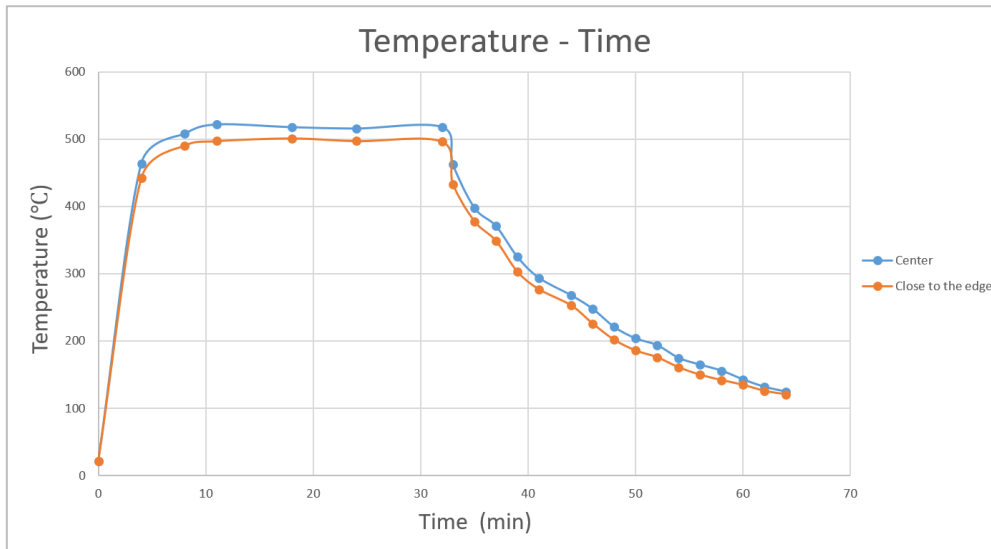


Fig. 3-7. The evolution of the temperature at the center and close to the edge of the 316L substrate over time. The hotplate was set to 540°C (HT) at 0 min and set to room temperature (RT) at 32 min.

3.2.6. Powder feeding system

The DED system is equipped with two volumetric powder feeders (Medicoat AG, Wohlen, Switzerland) shown in **Fig. 3-8**. The powder is stored in the cylindrical reservoirs. When the powder feeder is activated, the agitator in the reservoir stirs the powder at a given velocity to let the powder flow through a small opening at the bottom of the reservoir. The powder falls in a groove of the plate that rotates at a controlled velocity. A static plastic baffle on the rotating plate then blocks the powder and guides it centrifugally. The powder falls off the edge of the rotating plate and is transported by the argon shield gas into the tube connecting to the deposition nozzle. It requires a good flowability of the powder.

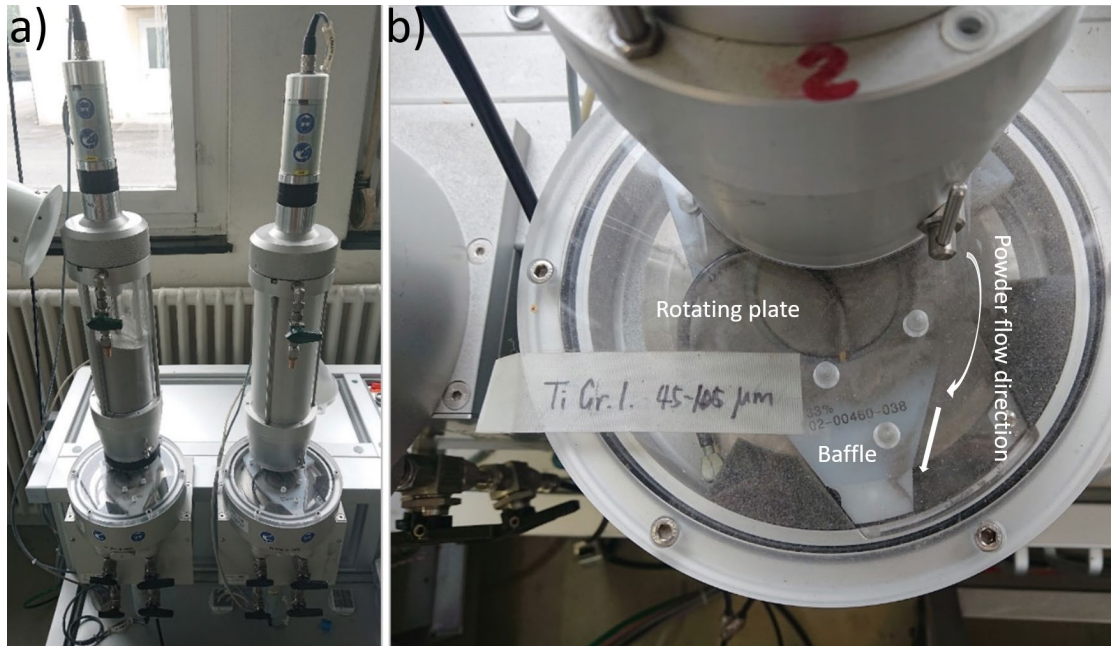


Fig. 3-8. a) The volumetric powder feeders and b) the rotating plate carrying the powder.

In this study, the rotating velocity of the agitator is fixed at 2 rpm and the flowrate of the powder-carrying argon shield gas is fixed at 3 L/min. Only the rotating velocity of the plate is adjusted to obtain different powder feedrates. The rotating velocity has a maximum value of 10 rpm, and it can be adjusted to integer percents. The powder feedrate is measured before and after deposition experiments by weighing the powder collected at the exit of the nozzle in one minute for three times. As calibration, the correlation between the feedrate of Cp-Ti grade 1 Ti powder (45-106 μm) and the rotating velocity of plate is plotted in **Fig. 3-9**. When the rotating velocity of the plate is above 7.5 rpm (75% of 10 rpm), occasional powder bursts at the exit of the nozzle have been observed. This is due to the collapse of accumulated powder in the nozzle. In order to avoid the disturbance of such powder bursts to the DED process, the maximum powder feedrate has been set at 32 g/min by top limiting the plate rotating velocity to 7.5 rpm.

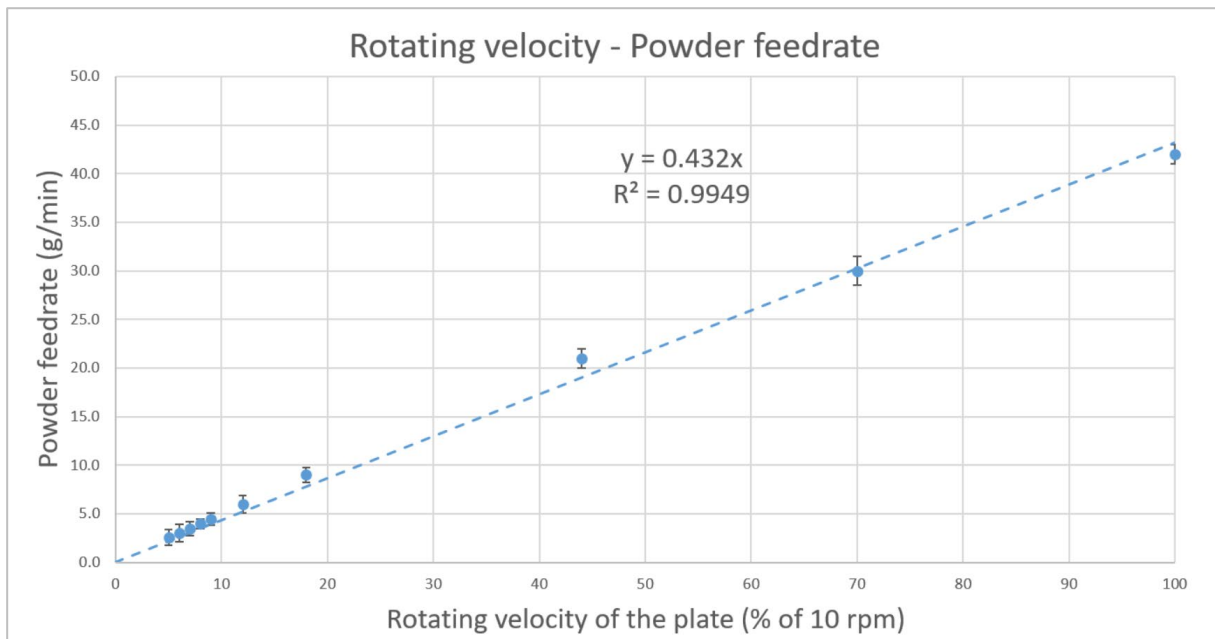


Fig. 3-9. Ti powder feedrate calibration measurements with rotating velocity of the plate.

3.2.7. Model, toolpath and code

The printed structures are first drawn in Siemens NX software (Siemens Digital Industries Software, Plano, Texas, USA) as 3D models. Toolpaths for the deposition nozzle are then generated with customized parameters such as nozzle velocity, hatch spacing, Z increment, etc. **Fig. 3-10** shows the models of five cuboids on the substrate and the toolpaths for three single layer samples (each consisting of multiple parallel single tracks) for example. For easier recognition, the toolpaths for the five cuboids and the models of the three single layer samples are hidden to avoid overlapping. For the three single layer samples, the material is to be deposited on the purple sections, and the sections with other colors are for connecting the depositing movements of the nozzle. Yellow, pink and blue colors are for engage, retract and approach movements. In this study, the engage and retract movements are given the same nozzle velocity as the depositing movement. The approach movement has a nozzle velocity of 4000 mm/min. Different nozzle velocities can be designated to different sections. With the UserTools package (Janus Engineering France, Issy Les Moulineaux, France), options such as powder feeder and laser parameters and actions can be added to desired positions in the toolpaths. The toolpaths with DED functions are converted to G-code programs with a dedicated postprocessor. These G-code programs can then be run on the BeAM DED system to produce the designed parts.

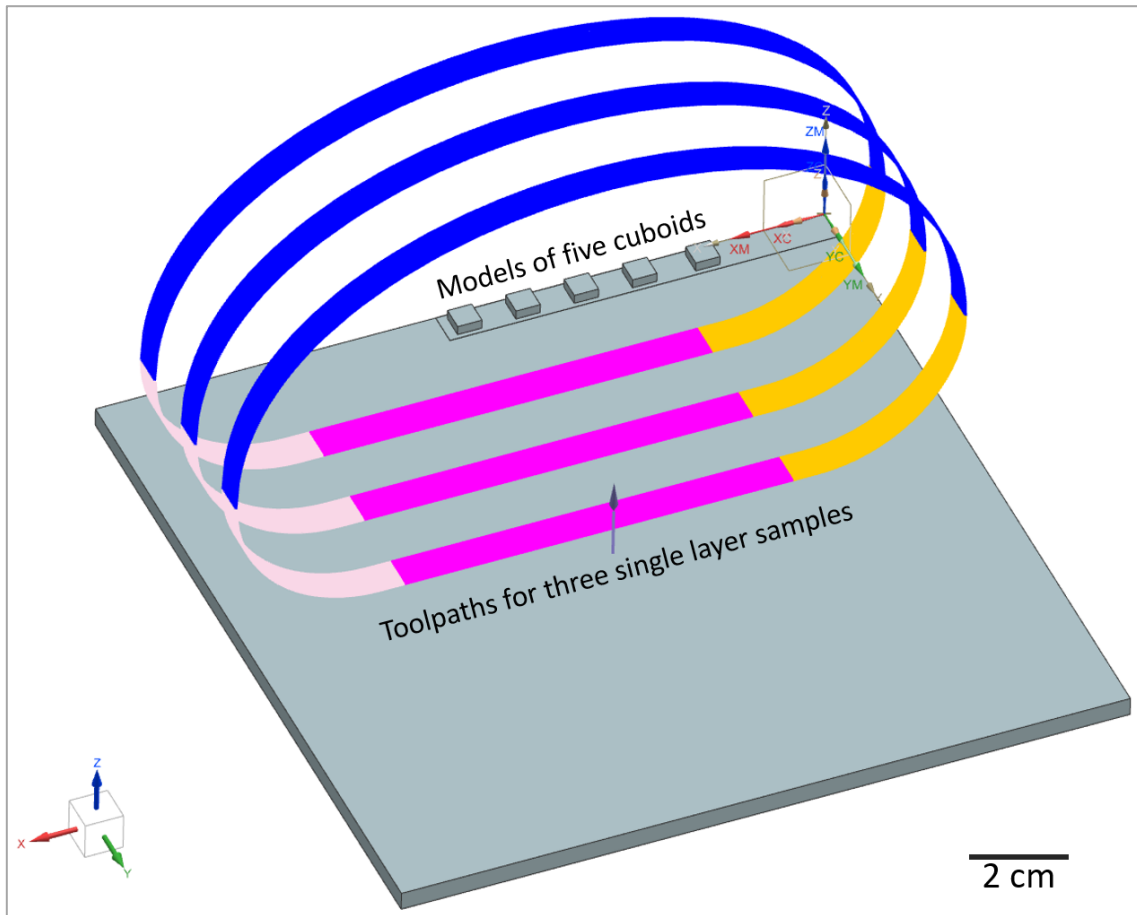


Fig. 3-10. The interface of the Siemens NX software. The models of five cuboids on the substrate are on the far edge. The toolpaths for three single layer samples are shown in colored curves.

3.2.8. Structures to print and process parameters to control

3D structures have to be deposited for application. But to understand the DED process, simpler geometries had to be studied first. Therefore, the deposition of different structures have been studied progressively in this study. The printed structures are defined as below.

A single track is printed when the nozzle deposits along a straight line. A single wall is printed when single tracks are stacked up vertically. A single layer is printed when multiple single tracks are deposited on the substrate parallel with a certain ratio of overlap between every two adjacent tracks. In order to avoid heat concentration at the ends of the tracks, the single tracks in single walls and single layers are deposited in the same direction, instead of with a meander strategy. A cuboid is printed when single layers are stacked up vertically. In this study, the printing direction is rotated by 90° after finishing every layer in a cuboid.

For printing single tracks, only three parameters need to be determined: Laser power LP (W), nozzle velocity NV (mm/min) and powder feedrate PF (g/min).

LP, NV and PF determine the features of the basic single tracks, and they need to be controlled when printing any structure.

Z increment ΔZ (mm), as the increment of the height of nozzle after each layer is finished, needs to be controlled when printing single walls and cuboids.

Hatch spacing HS (mm), as the distance between the centerlines of two single tracks, needs to be controlled when printing single layers and cuboids.

For all structures printed beyond a single track, the time lapse between individual further laser actions needs to be considered (in the second range) due to heat accumulation from the earlier exposures. In most of the irradiations, the heat evacuation should be fast enough to avoid unwanted heat accumulation.

3.3. Interface characterization

Interface quality is the focus of this study. The interfaces in the samples formed in the DED process were investigated with various characterization methods.

3.3.1. Sample cutting and embedding

A manual and an automatic cutting machine (Discotom-2 and Accutom-5, Struers GmbH, Birmensdorf, Switzerland) were used with Alu-Oxide cut-off wheels to cut the samples for cross-sections.

A three-component resin Technovit® 4000 (Kulzer GmbH, Wehrheim, Germany) was used to embed samples for further grinding and polishing.

3.3.2. Cross-section grinding and polishing

The embedded samples were first ground with 600, 1200 and 2500 grit SiC grinding papers. They were then polished with 6 and 3 μm diamond pastes, and finally with an oxide polishing suspension (OPS) solution (0.04 μm SiO_2 with 10% H_2O_2). The polished samples were cleaned with water and ethanol and dried using compressed air following by a hot fan. It is important to eliminate or reduce the surface roughness and stress for subsequent investigation of the

crystallographic and chemical features using SEM, energy dispersive X-ray spectroscopy (EDS) and EBSD analyses.

3.3.3. Optical microscope (OM) observations

Cross-sections that are only needed for dimensions of the printed structures or basic crystallographic morphology were observed with an optical microscope (ZEISS Axioplan, Munich, Germany).

3.3.4. Scanning electron microscope (SEM) observations

All SEM observations were carried out on a high resolution SEM (Mira Tescan 3, Brno, Czech Republic). The areas around the interesting parts of the sample cross-sections were painted with silver paste that connects to the metallic sample holder to avoid charging of the samples.

SEM observations of the sample microstructure in cross-section were carried out with an acceleration voltage of 30 kV and beam current of around 1000 pA. The observations were done in secondary electron (SE) mode.

3.3.5. Energy dispersive X-ray spectroscopy (EDS)

The EDS analyses were performed with an EDS detector (EDAX, Mahwah, NJ, USA) mounted in the Mira Tescan 3 SEM chamber. The measurements were carried out with an acceleration voltage of 30 kV and a beam current of around 2000 pA.

Although 316L contains not only Fe but also Cr, Ni and other alloying elements, the EDS analysis in this study considers only the ratio of Fe and Ti for simplification. For example, an EDS result showing 51 at.% of Fe and 19 at.% of Ti would be considered as $\text{Fe}_{73}\text{Ti}_{27}$ for analyzing the phases.

3.3.6. Electron back scatter diffraction (EBSD)

EBSD analyses were performed with an EBSD camera (EBSD—Ametek, Mahwah, NJ, USA) mounted in the Mira Tescan 3 SEM chamber to investigate the crystalline structure.

3.3.7. Microhardness measurement: Vickers hardness test

The Vickers hardness was measured with a load of 10 g and a dwell time of 10 s (ESI Prüftechnik GmbH, LMA-302-VLX, Wendlingen, Germany).

3.3.8. Interface strength measurement: Shear test

The mechanical strength of the joint was characterized with ultimate shear strength.

In order to avoid introducing crack tips to the interface, electrical discharge machining (EDM) instead of wheel cutting was selected to cut the samples. Cuboid samples were cut vertically to expose their cross-sections.

The shear tests were performed on a shear tester (Electronic Digimes 1000, Walter + Bai AG, Löhningen, Switzerland). The sample holder of the shear tester with a mounted sample is shown in **Fig. 3-11a**. A pressure head with a flat front surface applies a force up to 20 kN normal to the cross-section of the sample above the substrate at a strain rate of 2.4 mm/min. The pressure head was set just above the interfacial region.

The stress-force curve is automatically recorded until shortly after the maximum shear force F_{\max} occurs. The pressure head is stopped when the stress-force curve is complete. **Fig. 3-11b** shows a cuboid sample that has been sheared. The area of the delaminated interface A is then measured, and the ultimate shear strength USS is calculated as $USS = F_{\max}/A$.

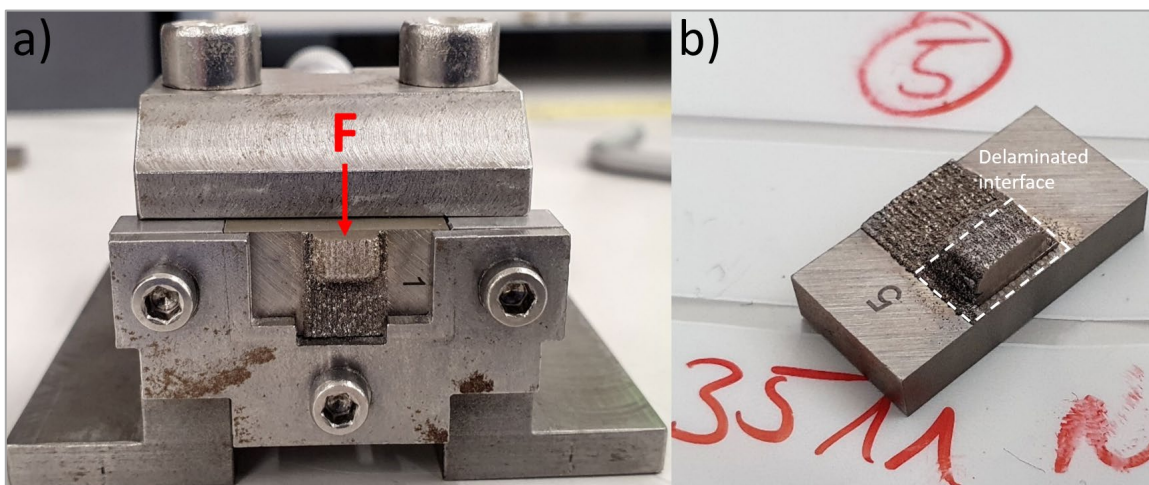


Fig. 3-11. a) The sample holder of the shear tester with a Ti cuboid sample on the fixed 316L substrate. The red arrow indicates the direction of the shear force. b) A cuboid sample after being sheared. The delaminated interface is marked with the white box.

3.3.9. Fracture surface characterization

The fracture surface of the samples after shear tests described in 3.4.8 were observed with SEM. EDS point analyses and line scans were performed on the surfaces to obtain chemical composition.

Chapter 4. Single track and single wall trials

Spherical Cp-Ti grade 1 powder with a particle size distribution of 45-106 μm was deposited on 316L substrate with the BeAM DED system.

The parameter set for depositing 316L powder on a 316L substrate is laser power $LP = 250\text{ W}$, nozzle velocity $NV = 1000\text{ mm/min}$ and powder feedrate $PF = 5.0\text{ g/min}$ according to the DED machine manufacturer. This parameter set was for depositing dense 316L parts. Due to the significant difference in the density of 316L (8.0 g/cm^3) and of Ti (4.5 g/cm^3), for achieving a similar volume of deposition, PF was adjusted to 2.5 g/min when setting the reference parameter set for the deposition of Ti on 316L.

Ti single tracks were deposited on 316L substrates with different LP, NV and PF basing on the reference parameters. The influence of the parameters PF, LP and NV on the tracks were studied with the following groups.

The parameters for printing the single tracks are divided into the following groups:

1. PF groups for constant powder feedrate.
2. LP groups for constant laser power.
3. NV groups for constant nozzle velocity.

Within each group, two of the three investigated parameters were varied. Table 4-1 summarizes the different groups.

When subsequent tracks are deposited on the first single track, despite the selected printing strategy with a delay in the second range for the following track, it has to be verified if heat dissipation through the previous deposited tracks could have an influence on the interface with the 316L substrate. Therefore, the single track parameters were also used to print 5-layer single walls to check the influence of the additional layers on the interface between the deposited material and the substrate. The measured height H of each single track sample was used as the Z increment ΔZ for printing its corresponding single wall sample.

The single track and single wall samples were cut perpendicular to the nozzle scan direction. The cross-sections were polished and observed with OM and SEM. EDS analyses were done on interesting zones to identify the phases. Vickers hardness tests were done on regions with different microstructures to obtain the microhardness of the various phases.

Table 4-1. Parameters for the single tracks DED trials.

Group	Sample No.	LP (W)	NV (mm/min)	PF (g/min)	
PF	PF1	1	175	700	2.5
		2	250	700	2.5
		3	350	700	2.5
	PF2	1	175	1000	2.5
		2	250	1000	2.5
		3	350	1000	2.5
	PF3	1	175	1400	2.5
		2	250	1400	2.5
		3	350	1400	2.5
LP	LP1	1	250	700	2.5
		2	250	700	3.5
		3	250	700	5.0
	LP2	1	250	1000	2.5
		2	250	1000	3.5
		3	250	1000	5.0
	LP3	1	250	1400	2.5
		2	250	1400	3.5
		3	250	1400	5.0
NV	NV1	1	175	1000	2.5
		2	250	1000	2.5
		3	350	1000	2.5
	NV2	1	175	1000	3.5
		2	250	1000	3.5
		3	350	1000	3.5
	NV3	1	175	1000	5.0
		2	250	1000	5.0
		3	350	1000	5.0

4.1. Single track trials

4.1.1. Results

Fig. 4-1 shows the SEM image of the cross-section of track PF2_1 for example. The top surface of the deposited track seems to have cracked. A few large spherical (diameter around 100 μm) and smaller non-spherical inclusions are observed in the track. Cracks run through the track but not penetrating into the spherical inclusions. A border can be clearly seen between the track and the substrate material.

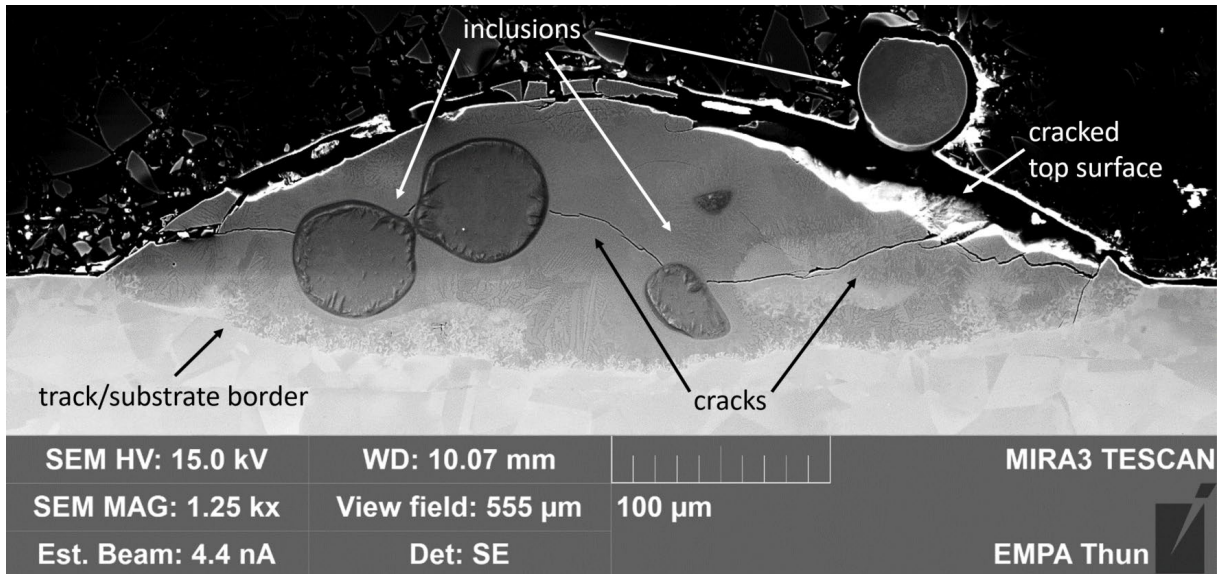


Fig. 4-1. SEM image of the cross-section of single track PF2_1.

The other single tracks show similar features to track PF2_1, but with different geometric dimensions. Their cross-sections are presented in **Fig. A-1** in Appendix A.

4.1.1.1. Cross-section geometry

Several dimensions are considered when analyzing the geometry of the single track cross-sections. Penetration depth D is the depth of the solidified melt pool below the surface of the substrate. Added height H is the height of the deposited material above the surface of the substrate. Melt pool width W is the width of the melt pool at the level of the surface of the substrate. These features are marked on schematic of a single track cross-section in **Fig. 4-2**. The ratio $D/(D+H)$ is denoted as dilution DL . The ratio H/W is denoted as aspect ratio AR .

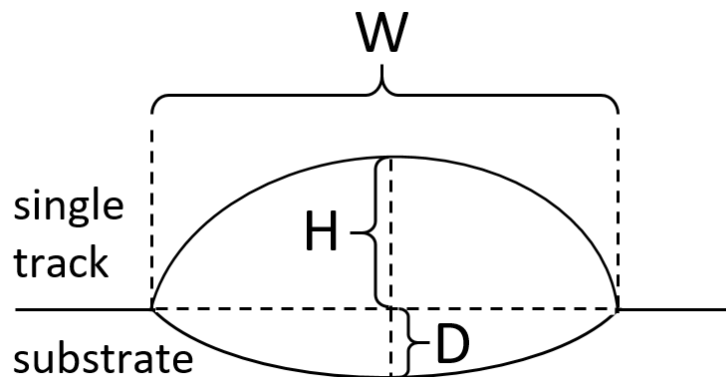


Fig. 4-2. Schematic of a single track cross-section. The penetration depth D , added height H and width W are marked.

Geometry Reproducibility

The PF1_2 parameter set was used to print single tracks on different days to estimate the reproducibility of the process. Three cross-sections were taken on each day for measuring the geometric dimensions. The average and standard deviation of the penetration depth D, the added height H and width W are plotted in **Fig. 4-3**.

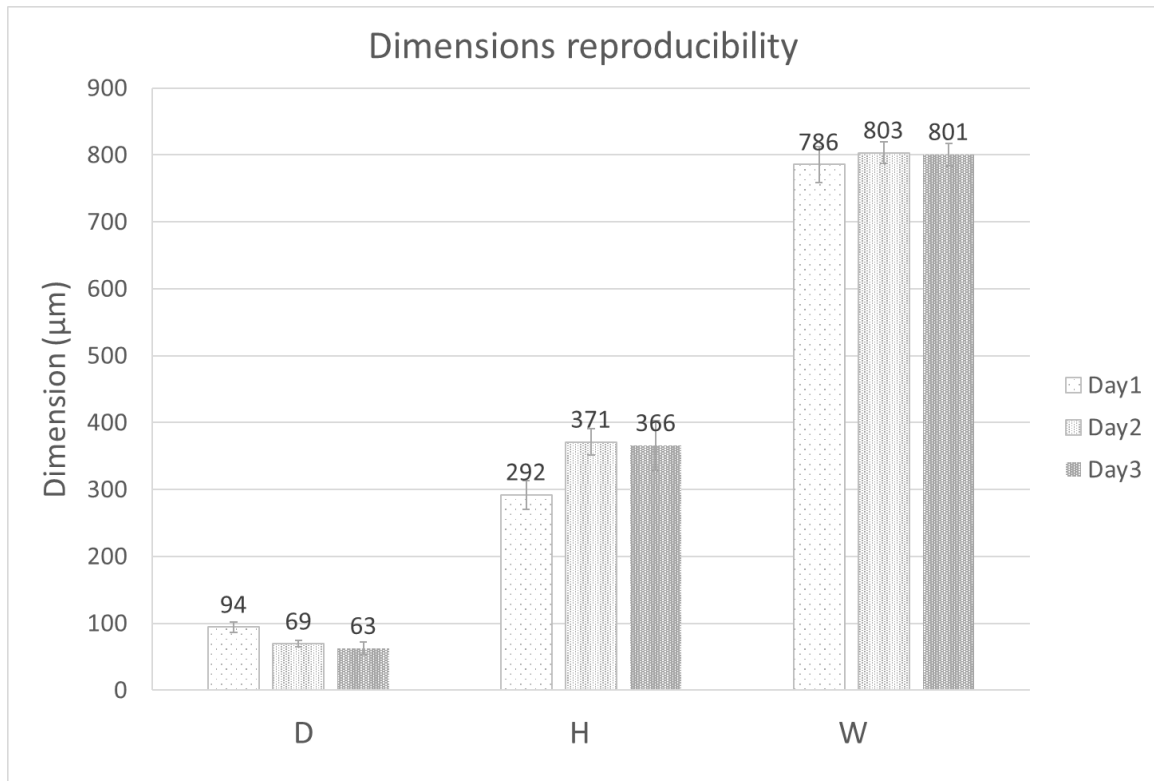


Fig. 4-3. The dimensions D, H and W measured from PF1_2 single tracks produced on different days.

For the PF1_2 single tracks printed on different days, D has an average of 75 μm and a coefficient of variation (CV) of 22%. H has an average of 343 μm and a CV of 13%. W has an average of 797 μm and a CV of 1%.

Geometric dimensions

a) PF groups - Constant powder feedrate PF

A constant PF of 2.5 g/min was used for printing all the samples in the PF groups. The geometric dimensions D, H, W and ratios DL and AR of the PF groups are summarized in **Fig. 4-4**.

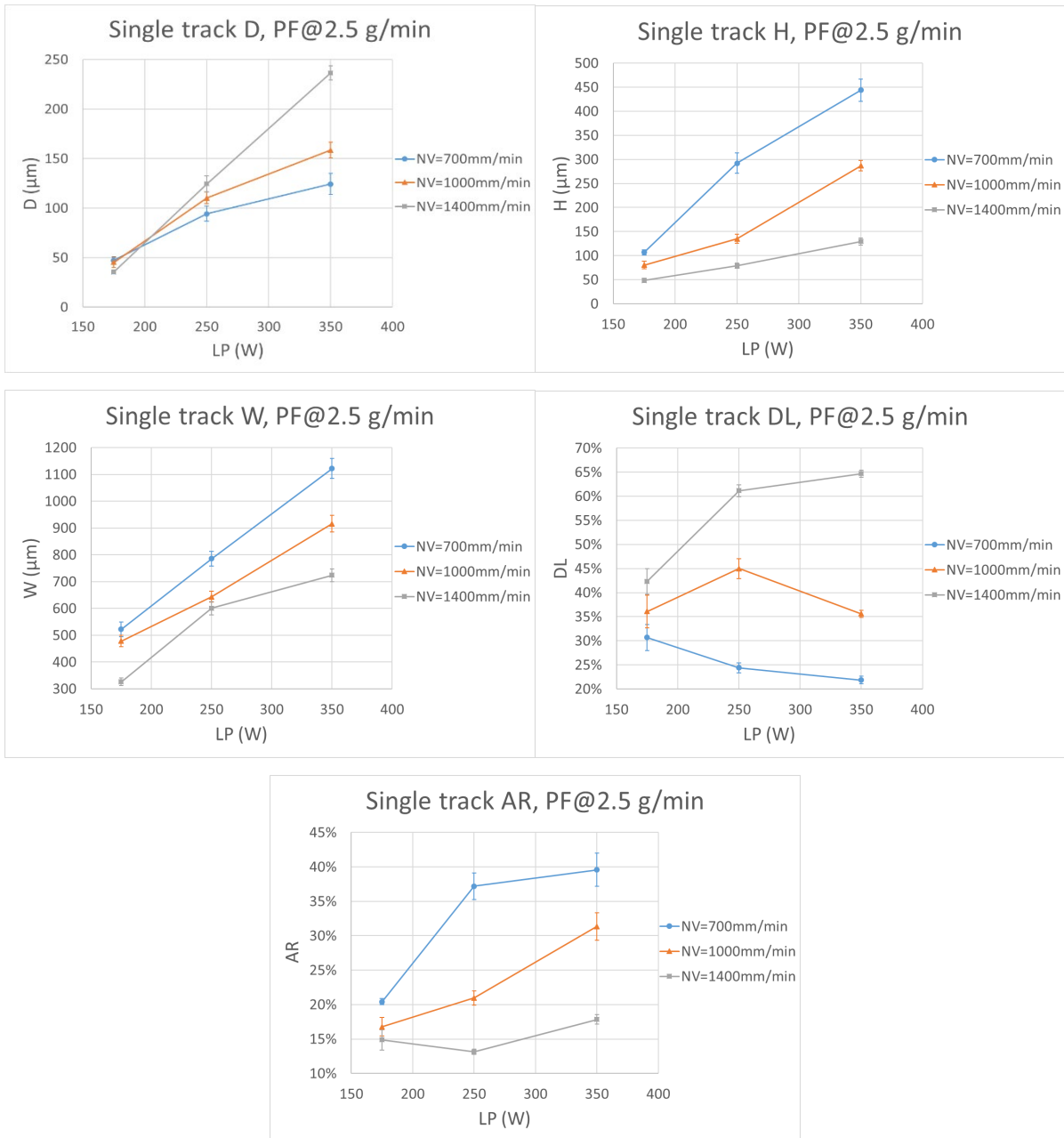


Fig. 4-4. D, H, W, DL and AR measured from the samples in the PF groups.

Within the studied ranges of laser power LP and nozzle velocity NV: D, H and W increased with increasing LP for a fixed NV. H and W decreased with increasing NV for a fixed LP. DL does not show a common trend with LP for the studied NVs. DL increased with increasing NV for a fixed LP. AR increased with increasing LP for a fixed NV of at least 1000 mm/min. AR decreased with increasing NV for a fixed LP.

b) LP groups - Constant laser power LP

A constant LP of 250 W was used for printing all the samples in the LP groups. The geometric dimensions D, H, W and ratios DL and AR of the LP groups are summarized in **Fig. 4-5**.

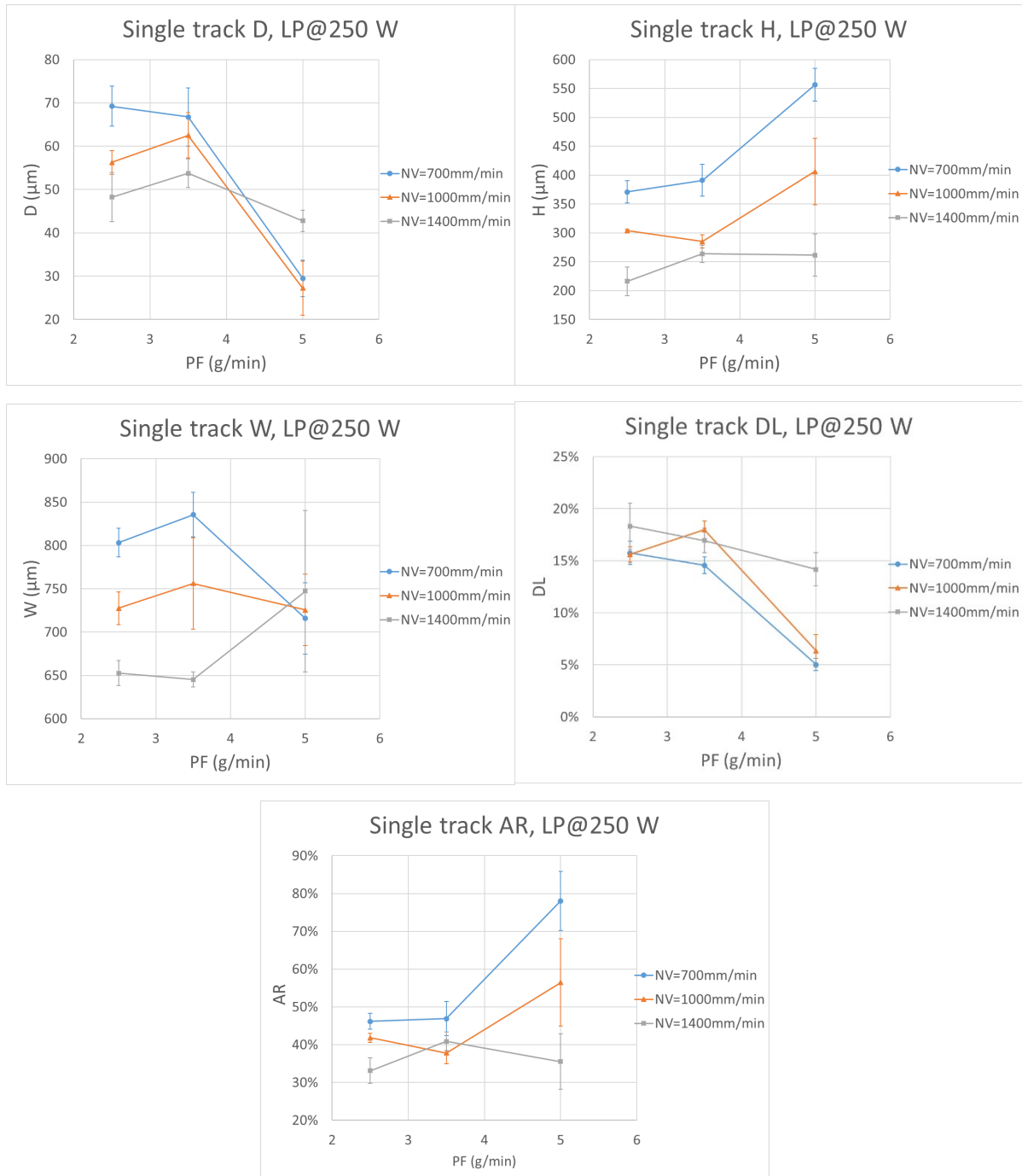


Fig. 4-5. The D, H, W, DL and AR measured from the samples in the LP groups.

Within the studied ranges of PF and NV: D decreased with increasing PF above 3.5 g/min for a fixed NV. D does not show a common trend with NV for the studied PFs. H does not show a common trend with PF for the studied NVs. H decreased with increasing NV for a fixed PF. W does not show a common trend with PF for the studied NVs. W decreased with increasing NV for a fixed PF of at most 3.5 g/min. DL generally decreased with increasing PF for a fixed NV. DL does not show a common trend with NV for the studied PFs. AR does not show a general trend with PF or NV.

c) NV groups - Constant nozzle velocity NV

A constant NV of 1000 mm/min was used for printing all the samples in the NV groups. The geometric dimensions D, H, W and ratios DL and AR of the NV groups are summarized in **Fig. 4-6**.

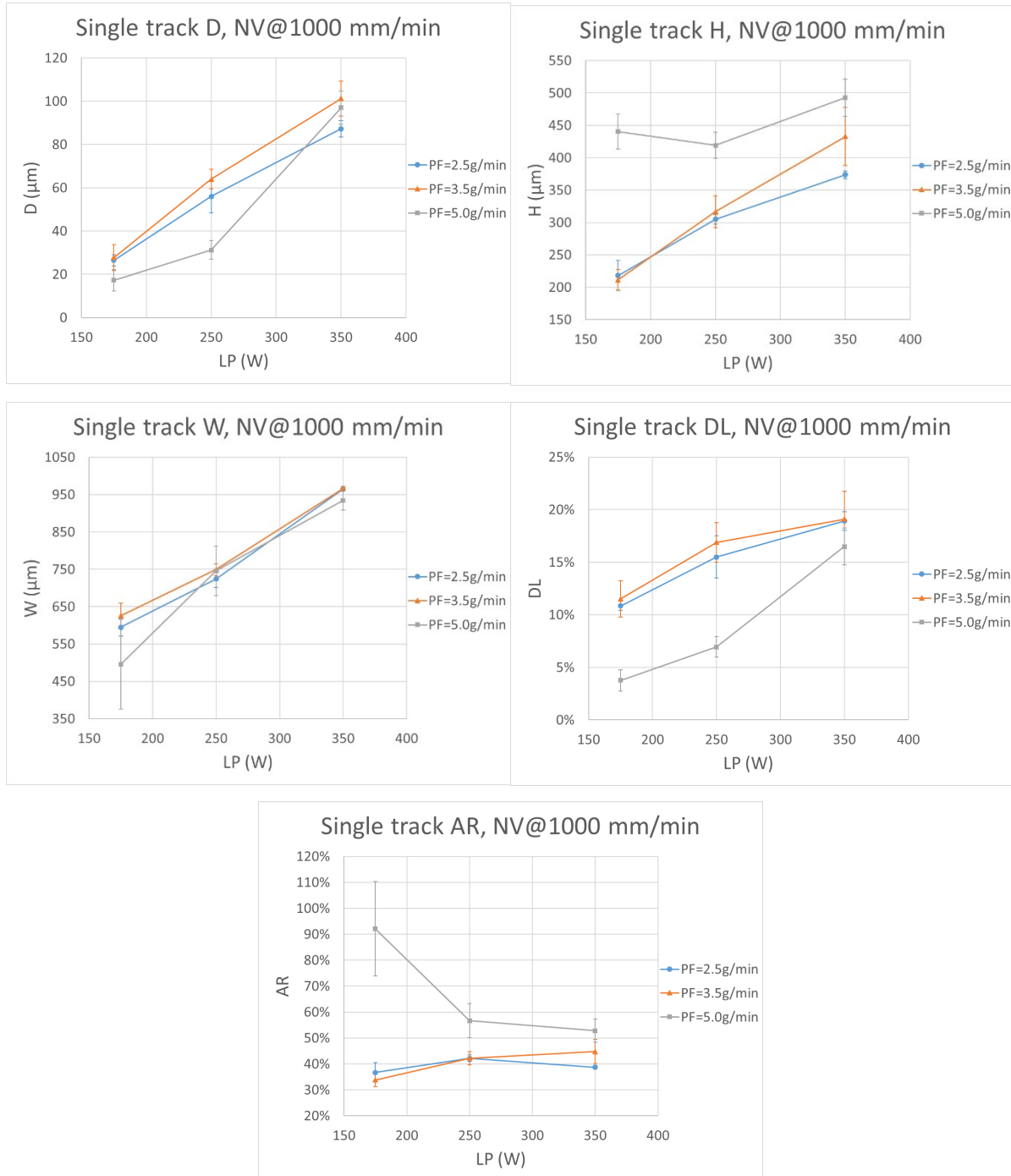


Fig. 4-6. The D, H, W, DL and AR measured from the samples in the NV groups.

Within the studied ranges of LP and PF: D, W and DL increased with increasing LP for a fixed PF. D, W and DL do not show a common trend with PF for the studied LPs. H does not show a general trend with LP or PF. AR does not show a general trend with LP or PF.

4.1.1.2. Microstructures and phases

Fig. 4-7 shows the complex microstructures in the middle part of track PF2_1. To identify phase compositions in the different regions, EDS point analyses were performed on all the microstructures and the results are marked in Fig. 4-7. The microstructures that are present in other tracks are all observed in track PF2_1.

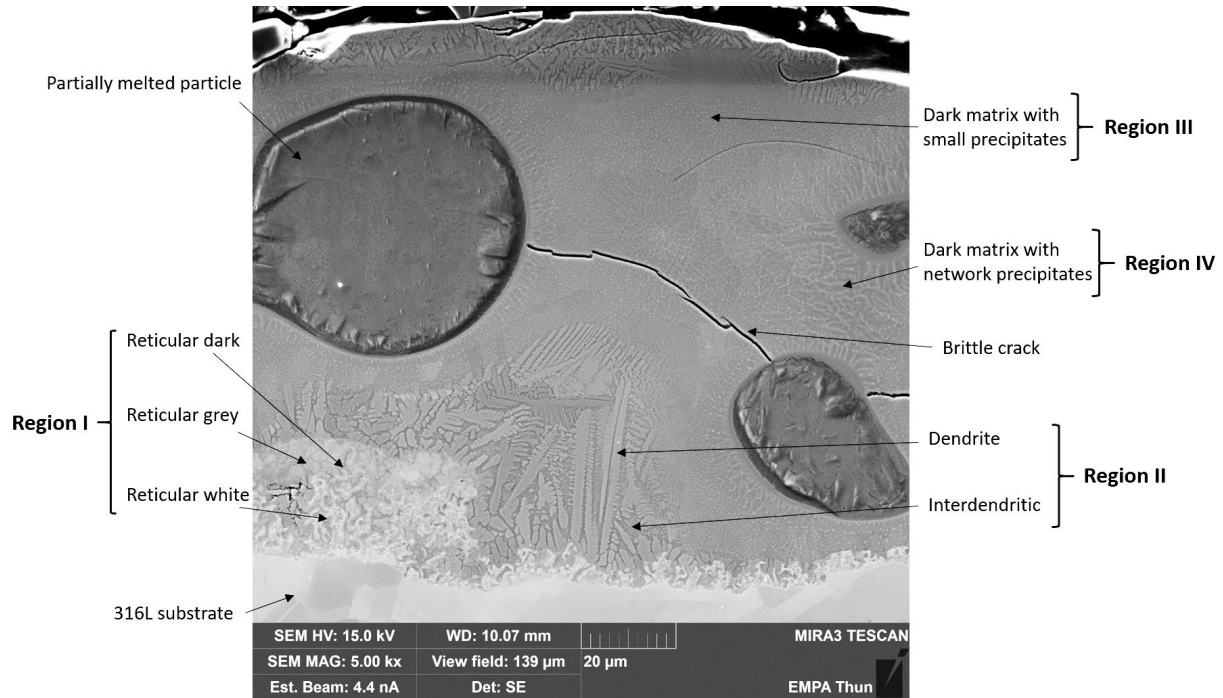


Fig. 4-7. SEM image of the cross-section of track PF2_1.

According to the EDS results, the phases have complex element compositions. For simplification, only the ratio of Fe and Ti is considered until further detailed discussions.

The simple equiaxed area at the bottom shows an atomic composition of $Fe_{79}Cr_{19}Ni_{10}$, conforming to the chemical composition of the substrate material 316L. The composition in this area is denoted as Fe100.

A dark sphere with a diameter of around $50 \mu m$ is seen at the top left in Fig. 4-7. Its composition is pure Ti, denoted as Fe0. Therefore, the dark sphere is estimated to be a partially melted Ti particle. Other smaller and less regularly shaped Ti particles are seen on the right side too.

Four regions of different Fe/Ti compositions can be identified by EDS between the 316L substrate (Fe100) and the pure Ti regions (Fe0) in the Ti deposition. These reaction regions are shown in Fig. 4-8.

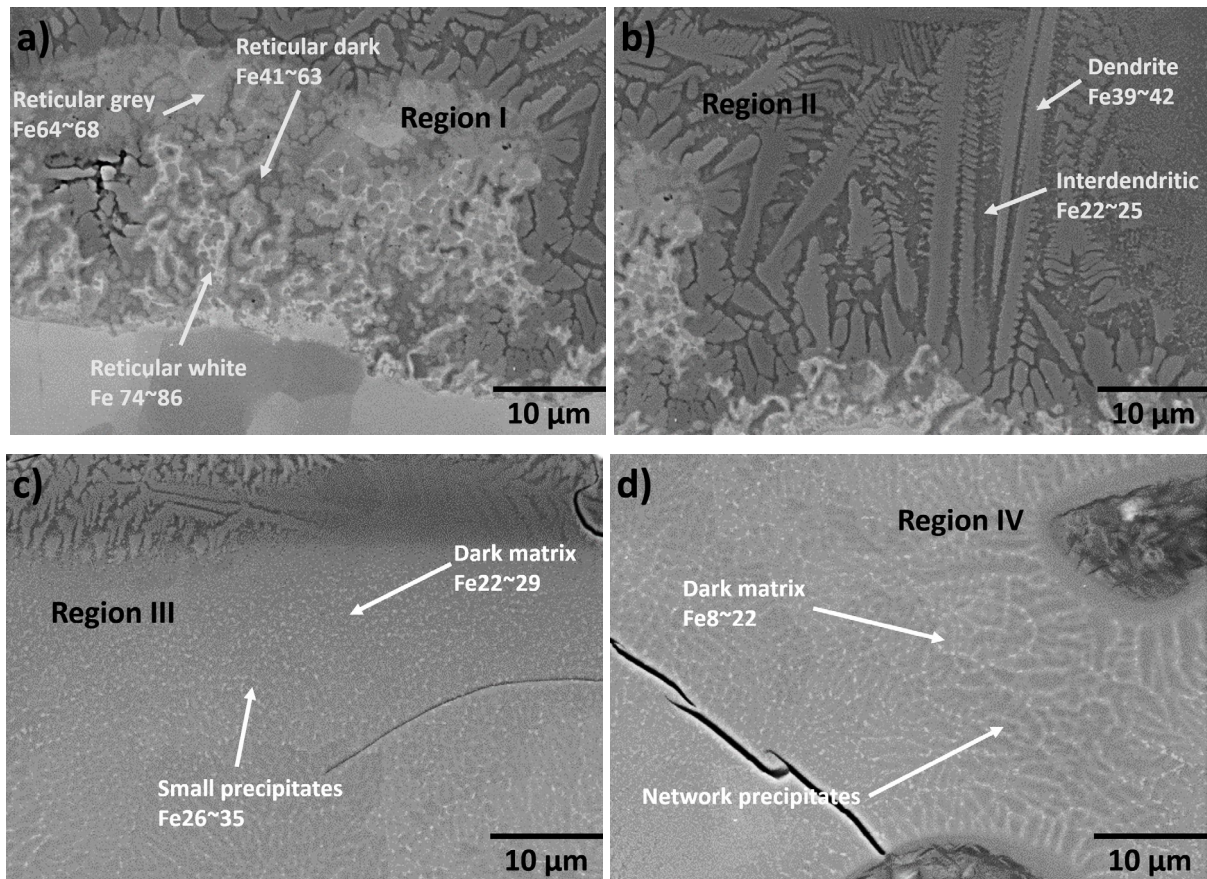


Fig. 4-8. The four reaction regions between the 316L substrate and the Ti particles in Track PF_2_1. Their microstructural features are marked with white arrows.

Region I: **Fig. 4-8a** shows the first region above the equiaxed substrate area. This reticular region is denoted as "Region I". The Region I in Track PF_2_1 has a thickness of 3 to 25 μm and consists of three structures with white, grey and dark contrasts. In a large fraction of the Region I area, the width of these features are easily below 1 μm . The white structure is like river networks. It has a composition of Fe74~86, possibly corresponding to the eutectic of $\text{Fe}_2\text{Ti} + \alpha\text{Fe}$ around $\text{Fe}_{84}\text{Ti}_{16}$ in the Fe-Ti equilibrium phase diagram in **Fig. 4-9**. The grey structure is like diffusion rendering of the white structure. It has a composition of Fe64~68, possibly corresponding to the Fe_2Ti IMC. The dark structure fills the space between the grey structure. It has a composition of Fe41~63 and could correspond to the FeTi IMC.

Region II: **Fig. 4-8b** shows the dendritic region denoted as "Region II" above Region I. The dendrites have brighter contrast than the interdendritic area. The width of the dendrites is below 3 μm . The width of the interdendritic area is below 2 μm . The dendrites in Region II have a composition of Fe39~42, possibly corresponding to the FeTi-rich hypereutectic of $\text{Ti} + \text{FeTi}$ above $\text{Fe}_{29.5}\text{Ti}_{70.5}$. The interdendritic areas in Region II have a composition of Fe22~25 and could correspond to the Ti-rich hypoeutectic of $\text{Ti} + \text{FeTi}$ below $\text{Fe}_{29.5}\text{Ti}_{70.5}$.

Region III: After Region II is a region consisting of a dark matrix and bright precipitates. This region is denoted as "Region III" and shown in **Fig. 4-8c**. The dark matrix in Region III has a composition of Fe22~29 and could correspond to the Ti-rich hypoeutectic of Ti+FeTi below $Fe_{29.5}Ti_{70.5}$. The bright precipitates in Region III show submicron sizes in the SEM image of the cross-section. EDS point analyses on the precipitates indicate slightly higher Fe content of Fe26~35, possibly corresponding to the eutectic of Ti+FeTi around $Fe_{29.5}Ti_{70.5}$.

Region IV: Closest to the dark sphere of pure Ti is a region with a dark matrix and bright network precipitates, denoted as "Region IV". The precipitates show submicron width. Region IV has a composition of Fe8~22, corresponding to the β -Ti or α -Ti+FeTi. The bright network precipitates have slightly higher Fe concentration than the dark matrix.

The abovementioned reaction regions are marked with their compositions in the Fe-Ti binary phase diagram in **Fig. 4-9**.

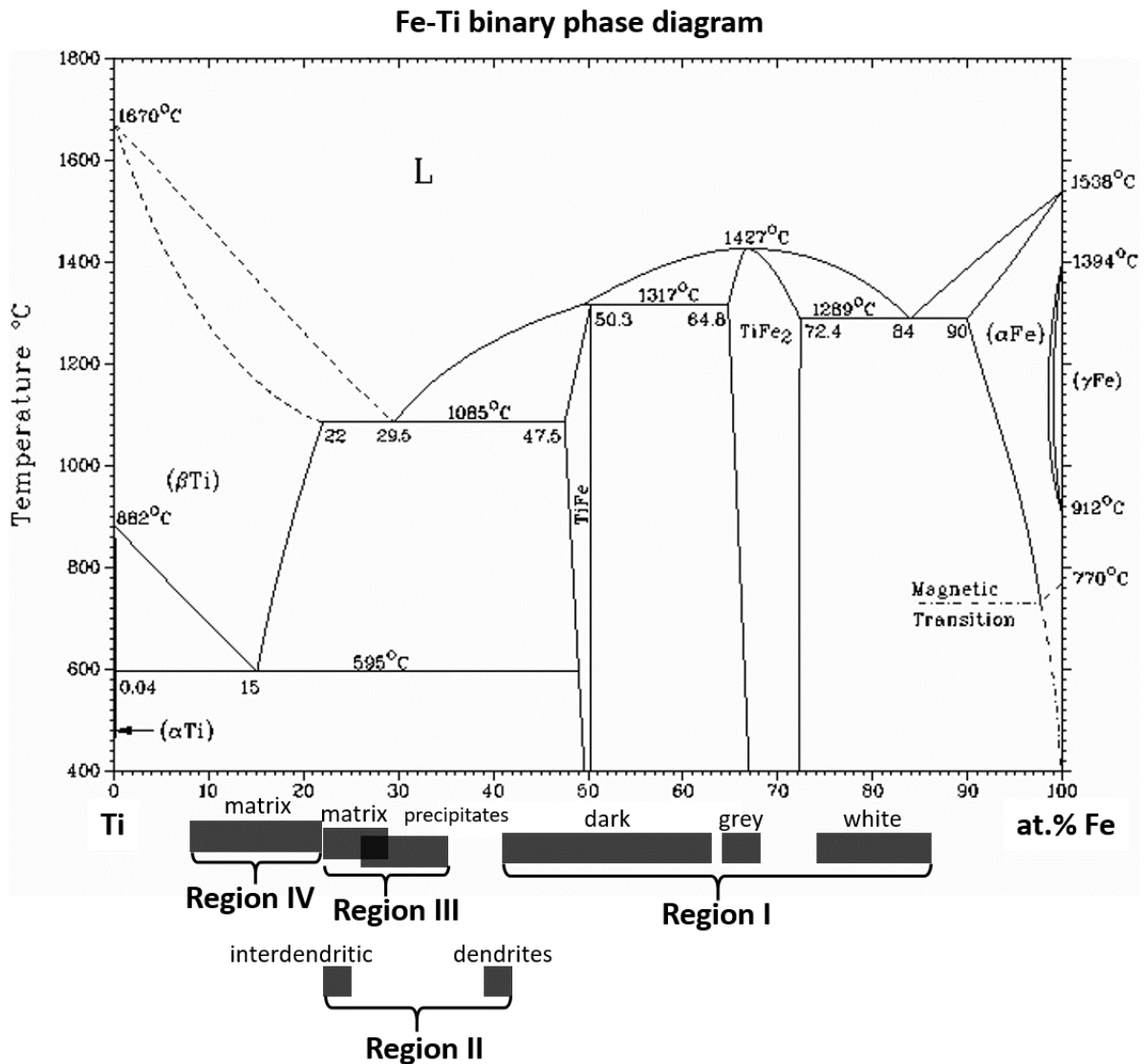


Fig. 4-9. The range of Fe atomic percentage in the features in the reaction regions I, II, III and IV marked on the Fe-Ti binary phase diagram.

4.1.1.3. Types of composition transitions

EDS point analyses were not sufficient for revealing the continuous composition transition in the cross-sections. Therefore, EDS line scans were conducted from the 316L substrate to the top of the tracks to obtain the composition transition profile along the height. The track samples are categorized by three types of transitions depending on the ending composition. In all three types, the composition transition is abrupt at the bottom of the solidified melt pool and gradual in the area above.

Transition ending with high Fe concentration. Track PF3_3 represents this type of transition. The cross-section of PF3_3 is shown in **Fig. 4-10**. These samples only have the reticular Region I and the dendritic Region II. The EDS line scan result from track PF3_3 is shown as overlay in **Fig. 4-10**. The ending Fe concentration is around Fe66 in track PF3_3 and can be down to Fe41 in other samples. Severe cracks have been observed and there are usually voids in these samples. The sharp debris in the voids indicate brittle crack probably due to mechanical cutting.

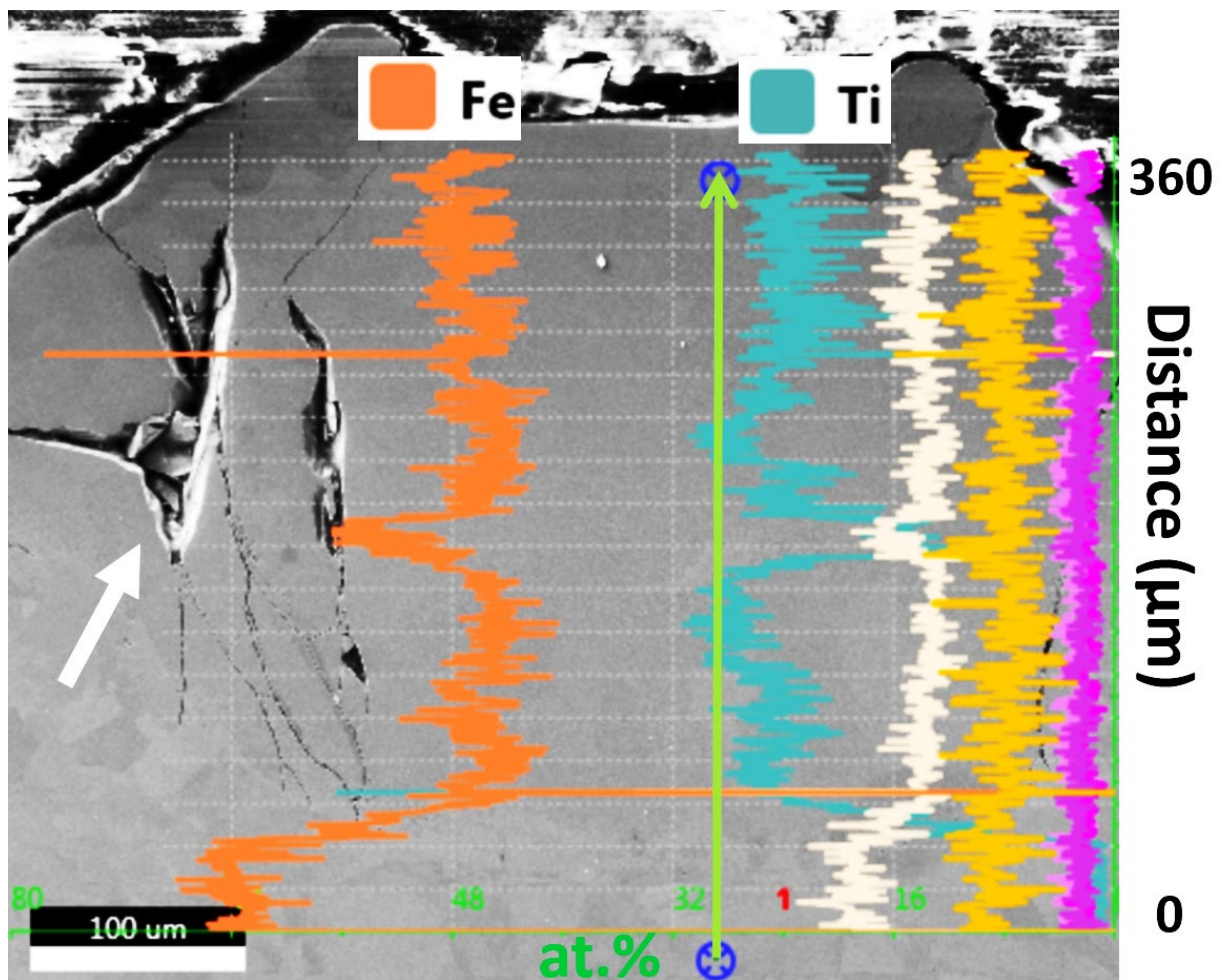


Fig. 4-10. EDS line scan on track PF3_3. The scan was done along the green arrowed line. The horizontal axis is atomic percentage and the vertical axis is distance. The orange and cyan curves correspond to Fe and Ti respectively. The severe cracks with voids are marked with a white arrow.

Transition ending with low Fe concentration. Track PF2_1 represents this type of transition. As its cross-section in **Fig. 4-11** shows, these samples show all four reaction regions clearly. The EDS line scan result from track PF2_1 is shown in **Fig. 4-11**. Apart from the pure Ti particles and the areas surrounding them, the ending concentration in the cross-section is around Fe22, reaching the lower limit in Region III. A crack is observed between two partially melted Ti particles. The shattered top of the deposition is estimated due to mechanical cutting.

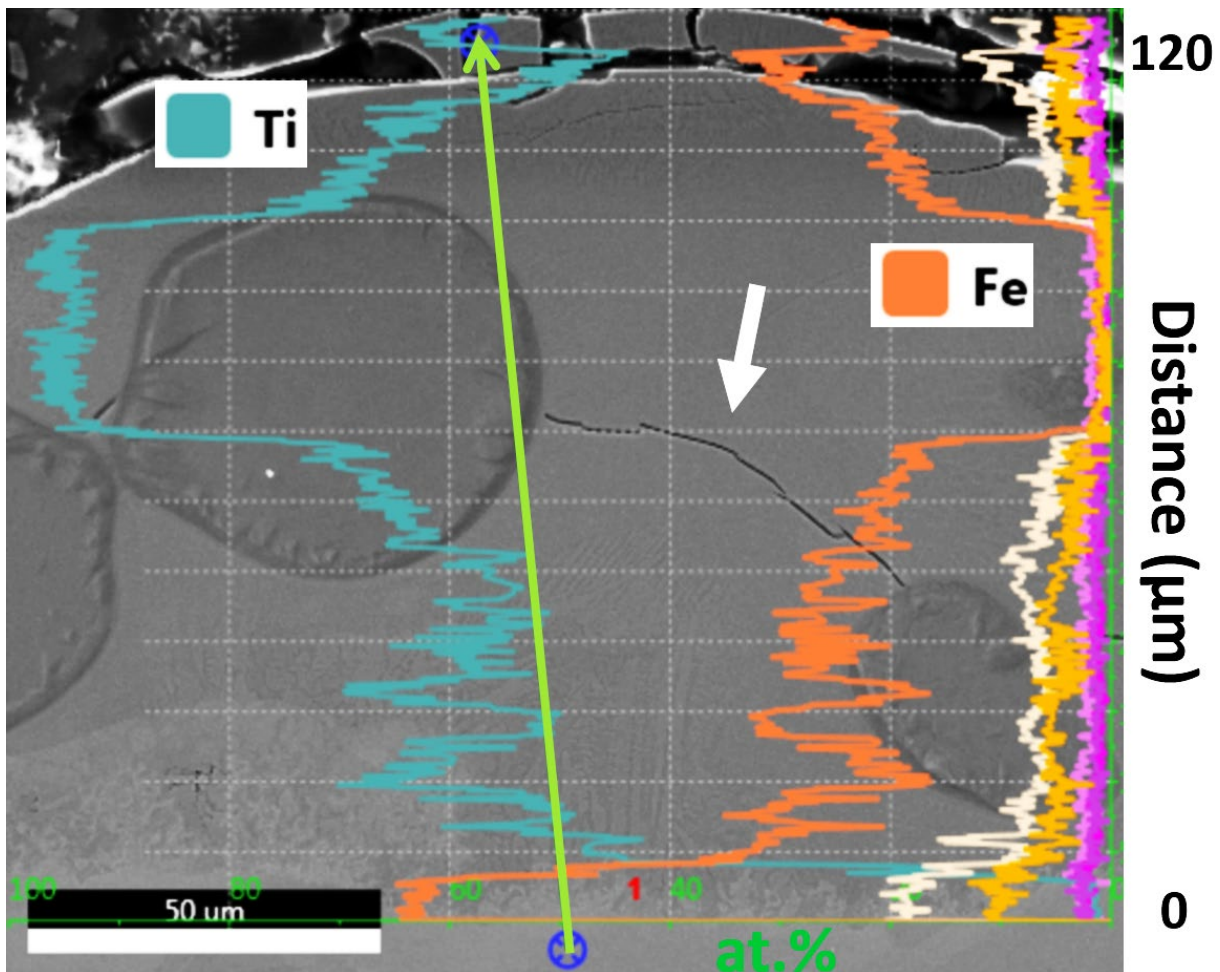


Fig. 4-11. EDS line scan on track PF2_1. A crack between two Ti particles is marked with a white arrow.

Track PF1_2 has the same transition profile and its cross-section is shown in **Fig. 4-12** to better demonstrate that cracks can penetrate all reaction regions. The only regions where the cracks are never observed propagating into are the 316L substrate and Ti particles. It is worth to note that under these processing conditions, i.e. relative low powder feedrate of 2.5 g/min, a lot of partially unmelted particles are still present in the cross-section.

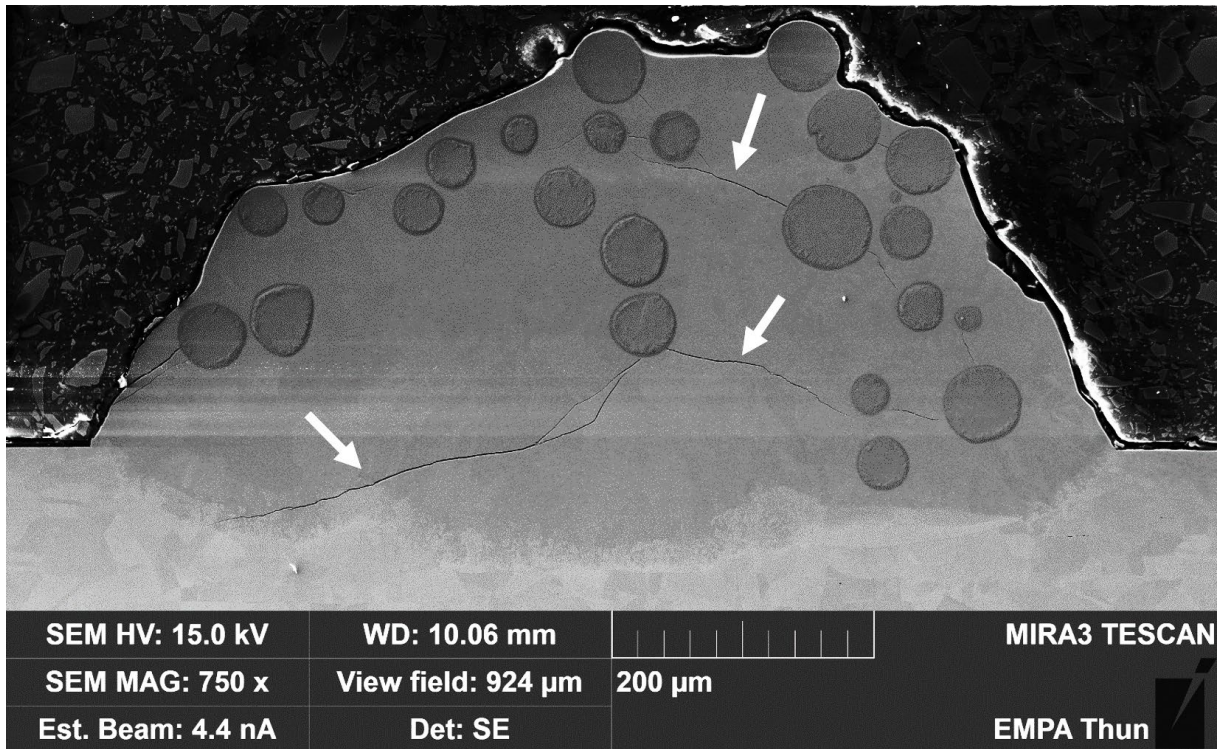


Fig. 4-12. SEM image of the cross-section of Track PF1_2. The cracks are marked with white arrows.

Transition ending with pure Ti. Track NV1_1 represents this type of transition. The cross-section and EDS line scan result of NV1_1 is shown in **Fig. 4-13**. These samples have two transition bands between the 316L substrate and the deposition. The lower band shows microstructural features of Region I and the upper band shows similar microstructural features to Region III. Above the upper band, the microstructure is homogeneous to the top of the deposition. Region II and Region IV are almost never observed in these samples. The lowest Fe concentration in Track NV1_1 is Fe0, which is measured in the area above the upper band. This indicates pure Ti above the upper band. The lower band shows a composition of around Fe45~56, corresponding to the dark structure in Region I. The upper band shows a composition of around Fe23~26, corresponding to Region III. The total thickness of the two bands is around 60 μm in Track NV1_1. For all such samples, the total thickness of the two bands ranges in 20~70 μm. No cracks have been observed in these samples.

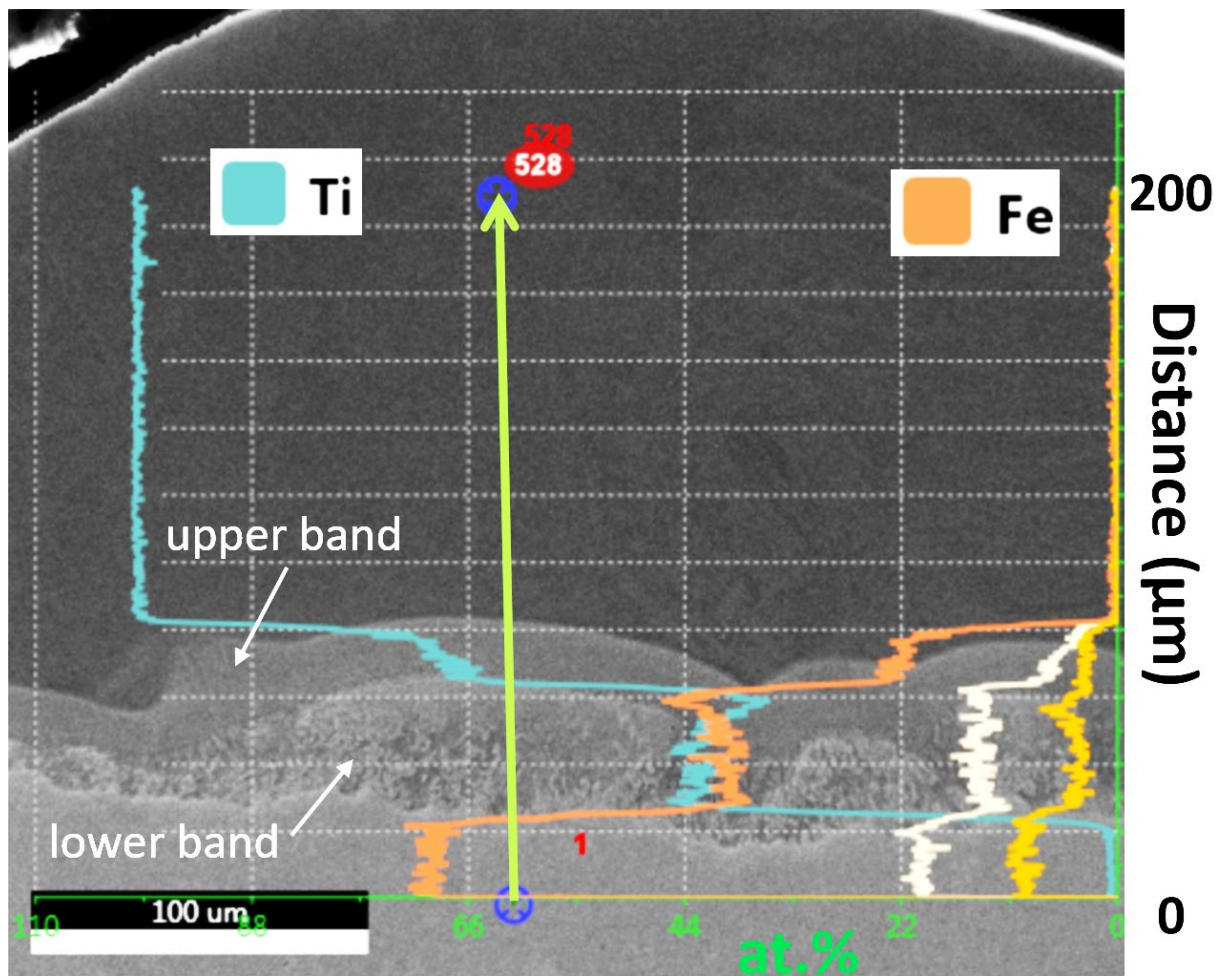


Fig. 4-13. EDS line scan on track NV1_1. The two bands between the substrate and the deposition are marked with white arrows.

4.1.1.4. Microhardness

Microindentation was done in the different regions described above. A small load of 10 g was selected to ensure that the indents were small enough and completely within the measured region. The Vickers microhardness $HV_{0.01}$ measured are summarized in **Fig. 4-14**.

Region I shows the highest microhardness, with an average value of $893HV_{0.01}$. The Regions II, III and IV show moderate microhardness with average values in the range of $391\sim 455HV_{0.01}$. The 316L and Ti regions show lowest microhardness with average values in the range of $185\sim 201HV_{0.01}$. The 316L substrate has similar microhardness to as-cast 316L (around $200HV$) in literature ^[85]. The deposited pure Ti also has similar microhardness to as-cast Ti ($200.26 HV$) in literature ^[86].

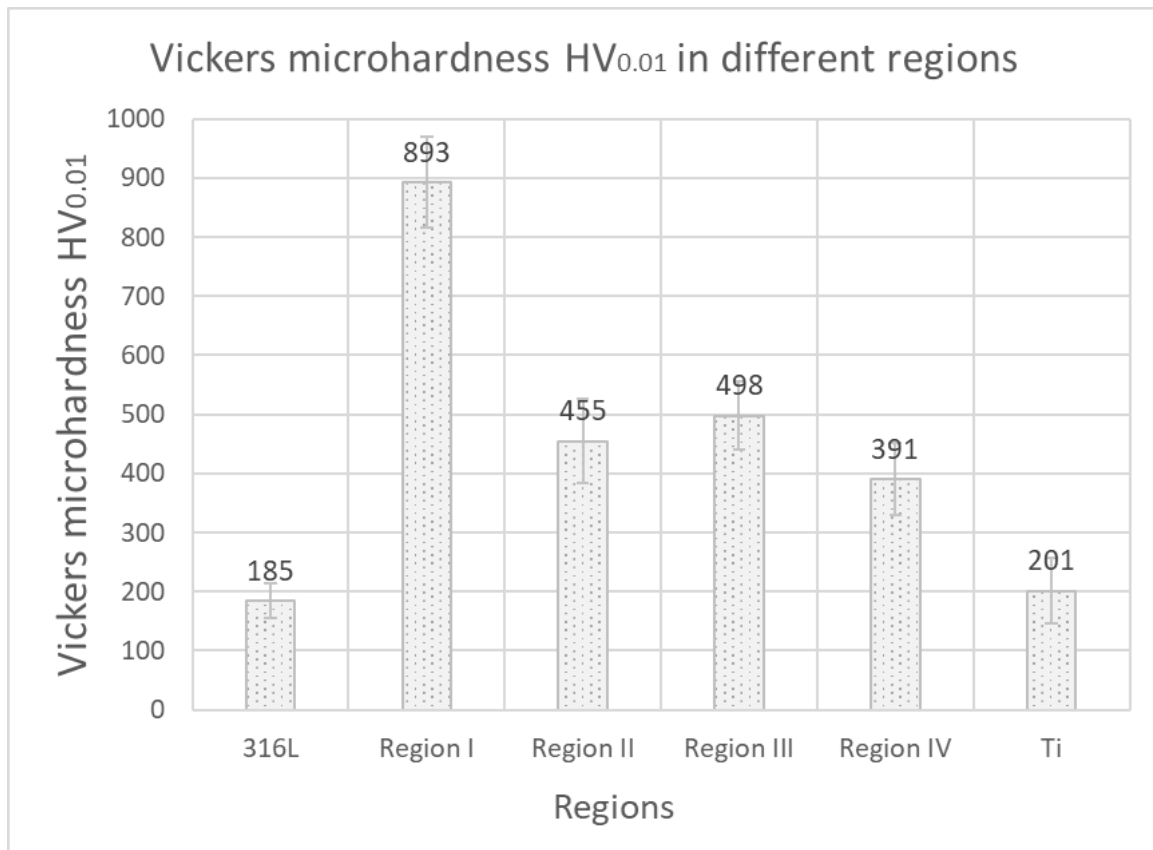


Fig. 4-14. Vickers microhardness HV_{0.01} measured in 316L, Regions I~IV and Ti.

4.1.2. Discussion

4.1.2.1. Microstructures, phases and microhardness

In the DED process, when Ti is mixed with 316L in the liquid state, Fe₂Ti, FeTi and other brittle IMCs form during solidification. Complex microstructures have been observed in the cross-sections of the single tracks produced. The SEM image of track PF2_1 in **Fig. 4-8** demonstrates the four reaction regions between the 316L substrate and the pure Ti in the deposition.

It should be noted that the deviation of the chemical composition from the phases in the equilibrium phase diagram can also result from the size of the EDS analytical area. In this study, the acceleration voltage was set at 30 kV to ensure ionization of atoms of all main elements Ti, Fe, Cr, Ni and Mo ^[87]. The electron beam diameter is around 40 nm. For Ti and Fe, the relationship between the acceleration voltage and the diameter of the interaction volume is given in **Fig. 4-15** ^[88]. With an acceleration voltage of 30 kV, the diameter of the interaction volume for Ti K α , Fe L α and Fe K α are much larger than 1.4 μ m. Therefore, the actual diameter of the interaction volume for the studied samples is estimated to be larger than 1.4 μ m. In areas

Chapter 4. Single track and single wall trials

with microstructural features with dimensions around a few microns, the measured compositions could be influenced by the neighboring features.

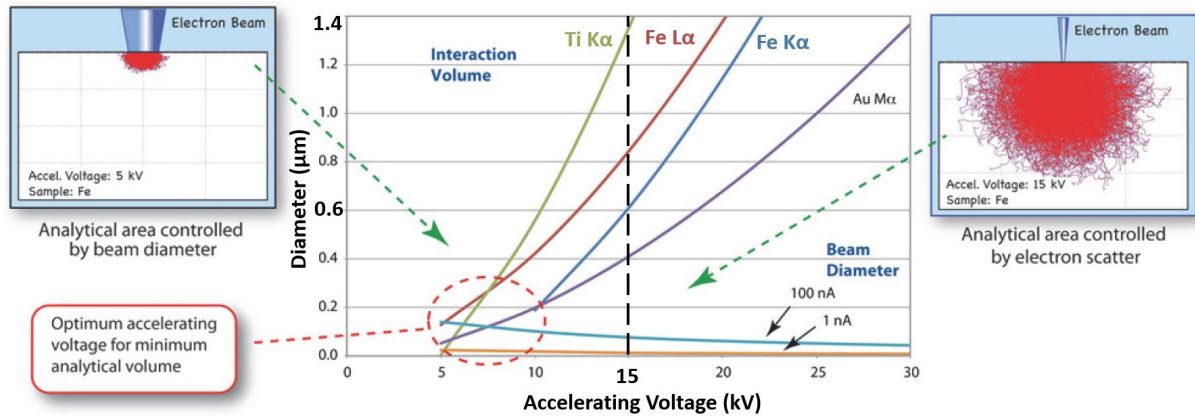


Fig. 4-15. The analytical area is controlled by both the beam diameter and the scatter within the sample. At a higher accelerating voltage, scattering within the sample generates a larger analytical area; at a lower accelerating voltage the expanding beam diameter makes for a larger analytical area. Beam diameters were measured on JEOL JXA-8530F field emission electron microprobe. Size of X-ray generation volume calculated from the Castaing equation ^[89]. 30 kV was used in this study for the EDS analyses, indicating an analytical area with a diameter much larger than 1.4 μm.

Region I shows a complex reticular microstructure with three Fe-rich phases. Such a complex structure has been widely reported in laser welding and additive manufacturing of Fe and Ti based alloys ^{[1] [28]}. The composition of the white structure like river networks has been simplified to Fe74~86 in the results. However, the atomic percentage of Ti in this phase is so low (below 35% of Fe) that it is comparable to or even lower than the second most element in 316L, Cr. Therefore, the Fe-Cr-Ti ternary phase diagram needs to be considered for phase identification. The corrected atomic composition in the white structure is Fe₆₁Cr₂₁Ti₁₈, close to the Ti₅Fe₁₇Cr₅ phase reported in ^[28]. In other literature, the τ phase Ti₅Fe₁₇Cr₇ with slightly higher Cr concentration has also been reported ^{[1] [90] [91] [92]}. The grey structure in Region I has a composition of Fe64~68, well matching the Fe₂Ti IMC phase. The dark structure in Region I has a composition of Fe41~63, fluctuating in a wide range around the equiatomic composition. The phase of this structure can be estimated to be FeTi IMC, since rapid solidification in the DED process can extend the solubility in FeTi ^{[93] [94] [95]}.

Region II contains dendrites with a composition of Fe39~42. The phase of these dendrites is estimated to be supersaturated FeTi. The deviation from equiatomic composition can result from different factors. On one hand, there is extended solubility of Ti in FeTi due to the rapid solidification in DED ^[93]. On the other hand, Cr and Ni with a total atomic percentage of around 40% of Fe (according to the EDS point analysis) can take the position of Fe atoms in the FeTi lattice ^[28]. The interdendritic areas in Region II has a much lower Fe concentration of Fe22~25.

Due to the rapid solidification during the DED process, β -Ti can have extended solubility. The interdendritic regions are thus estimated to be supersaturated β -Ti. This is in agreement with [9]. Satoh also suggested that in the Ti-Fe pair, only a small amount of mixing is required to exceed the 10% Mo-equivalent threshold and stabilize the β -Ti from transforming to α -Ti.

Region III shows a dark matrix with a composition of Fe22~29. The matrix phase is estimated to be supersaturated β -Ti as well. Considering the effective electron interaction area, the bright precipitates should have higher content of Fe than the measured Fe26~35. As the solubility in FeTi is extended in rapid solidification, these precipitates are estimated to be FeTi IMC.

Region IV shows a dark matrix with an Fe content of Fe8~22. Under the rapid solidification condition, the phase is estimated to be β -Ti. The bright coarse networks with higher Fe content are estimated to be precipitated FeTi IMC.

The compositions and phases in the reaction regions are summarized in Table 4-2.

Table 4-2. Compositions and phases in the reaction regions.

Reaction region	Compositions	Phases
Region I	Fe74~86, Fe64~68, Fe41~63	Ti ₅ Fe ₁₇ Cr ₅ , Fe ₂ Ti, FeTi
Region II	Fe39~42, Fe22~25	FeTi, β -Ti
Region III	above Fe26~35, Fe22~29,	FeTi, β -Ti
Region IV	Fe8~22	FeTi, β -Ti

EDS line scans from the substrate to the top of the deposition reveals the transition of composition in the vertical direction. Three types of transitions are found among all track samples and summarized in Table 4-3.

Table 4-3. Types of composition transitions and defects observed

Transition type	Ending composition	Defects
1	High Fe	Severe cracks and voids
2	Low Fe	Cracks
3	Pure Ti	No cracks

In samples with **transition type 1**, the transition ends with high Fe concentration. Severe cracks and voids have been frequently observed. At the bottom of the solidified melt pool, the composition drops from Fe100 to around Fe66 within the first 10~30 μ m. Afterward, the composition fluctuates in the range of Fe41~66 until the top of the deposition. The main phases in the deposition are therefore the brittle Fe₂Ti and FeTi IMCs. Bobbio et al. reported that the CTE mismatch between FeTi and Fe₂Ti, which were intertwined in a dendritic

Chapter 4. Single track and single wall trials

solidification structure, was hypothesized to be the root of major cracking in a Ti-6Al-4V to Invar 36 (64 wt.% Fe, 36 wt.% Ni) functionally graded material ^[96].

In samples with **transition type 2**, the transition ends with low Fe concentration. Brittle cracks are observed in all reaction regions. At the bottom of the solidified melt pool, the composition drops from Fe100 to around Fe66 within the first 3~50 μm and Region I forms in this range. Then, the composition drops to around Fe26 within the next 5~50 μm and Region II forms in this range. Afterwards, the composition fluctuates around Fe26 until the top of the deposition and Region III forms in this range. The main phase in the deposition is supersaturated β -Ti with rather high Fe concentration.

In samples with **transition type 3**, the transition ends with pure Ti. No cracks have been observed in these samples. At the bottom of the solidified melt pool, the composition drops from Fe100 to around Fe50 within the first 3~40 μm and Region I forms in this range as the lower band. Then, the composition drops to around Fe22 within the next 17~30 μm , and Region III forms in this range as the upper band. Afterward, the Fe concentration drops sharply and stabilizes at below Fe8. The composition transition from 316L to pure Ti is abrupt and almost completed within the first 20~70 μm . In this case, the main brittle phase is FeTi IMC in the two bands at the bottom of the melt pool. Similar microstructure and transition has been found in crack-free joint of Ti and CoCrMo by DED with a dilution of 1.4~5% ^[97].

This study did not dig further into the possible phases in the Fe-Ti-Cr ternary phase diagram because most of the measured compositions are close to the Ti side and the Cr concentration is thus neglectable. More detailed phase analyses in Ti-steel joint can be found in literature ^[98] ^[99] ^[100].

The microhardness measured in the reaction regions with intermediate compositions between 316L and Ti are in the range of 298~969HV_{0.01}, significantly higher than the base materials 316L 155~215HV_{0.01} and Ti 147~256HV_{0.01}. Among all the reaction regions, the reticular Region I shows the highest microhardness 817~969HV_{0.01}. This is because the main phases in Region I are the Fe₂Ti and FeTi IMCs. Chen et al. ^[28] reported the microhardness of FeTi and Fe₂Ti to be 600HV and 1000HV, respectively. These highly brittle phases explain the severe cracks and voids in tracks with large areas of Region I. Nonetheless, the cracks could penetrate through all of the four reaction regions despite the difference in their microhardness. The samples with only two bands at the bottom however show no cracks in the cross-sections. They may benefit from the small amount of the IMCs because the main body of the deposition is almost pure Ti.

To conclude, an abrupt composition transition ending with pure Ti is favorable in order to limit the formation of the brittle phases in two transition bands at the bottom of the solidified melt

pool. This helps avoid cracks in the deposition. In other cases where composition transitions end with either high or low Fe concentration, considerable amounts of brittle phases form in the solidified melt pool. The deposition is therefore prone to cracks or even voids after cutting for cross-section.

4.1.2.2. Cross-section geometry

The reproducibility of the penetration depth D and added height H are in the range of 10~20%. The width W varied however only by a few percents.

The influences of laser power LP, nozzle velocity NV and powder feedrate PF on the penetration depth D, added height H, width W, dilution DL and aspect ratio AR are complicated. As is concluded in Section 4.1.2.1. that a transition ending with pure Ti (transition type 3) is favorable for avoiding cracks, the type of composition transition is then used to sort the studied parameter sets. The transition types are listed with the parameters and geometric dimensions in Table 4-4.

Table 4-4. The parameters, geometric dimensions and transition types of the single track samples.

Sample	LP W	NV mm/min	PF g/min	D μm	H μm	W μm	DL %	AR %	Transition type
LP1_3	250	700	5.0	30	556	716	5	78	3
LP2_3	250	1000	5.0	27	406	726	6	56	3
NV1_1	175	1000	2.5	27	218	595	11	37	3
NV2_1	175	1000	3.5	28	212	626	12	34	3
NV3_1	175	1000	5.0	17	441	496	4	92	3
NV3_2	250	1000	5.0	31	419	746	7	57	3
PF1_1	175	700	2.5	47	107	523	31	20	2
PF1_2	250	700	2.5	94	292	786	24	37	2
PF1_3	350	700	2.5	124	444	1122	22	40	2
PF2_1	175	1000	2.5	45	80	478	36	17	2
PF3_1	175	1400	2.5	36	49	326	42	15	2
LP1_1	250	700	2.5	69	371	803	16	46	2
LP1_2	250	700	3.5	67	391	836	15	47	2
LP2_1	250	1000	2.5	56	304	728	16	42	2
LP2_2	250	1000	3.5	63	285	756	18	38	2
LP3_1	250	1400	2.5	48	216	653	18	33	2
LP3_2	250	1400	3.5	54	264	645	17	41	2
LP3_3	250	1400	5.0	43	262	747	14	36	2
NV1_2	250	1000	2.5	56	305	725	15	42	2
NV1_3	350	1000	2.5	87	374	965	19	39	2
NV2_2	250	1000	3.5	64	317	749	17	42	2
NV2_3	350	1000	3.5	101	433	967	19	45	2
NV3_3	350	1000	5.0	97	493	934	16	53	2
PF2_2	250	1000	2.5	110	135	644	45	21	1
PF2_3	350	1000	2.5	159	287	916	36	31	1
PF3_2	250	1400	2.5	125	79	601	61	13	1
PF3_3	350	1400	2.5	237	129	724	65	18	1

First of all, the samples with transition type 3 have the smallest D and DL with a maximum value of 31 μm and 12%, respectively. The small D means that the absolute amount of melted substrate is small. The small DL means that the ratio of the melted substrate to the deposited powder is also small. Both the D and the DL have to be low to form an abrupt transition at the bottom of the solidified melt pool. Among the samples with transition type 3, most of them were deposited with the higher PF of 5.0 g/min. Therefore, high PF is expected to be an important parameter that reduces the dilution of Fe into the melt pool and reduces the formation of IMCs.

The cross-sections of the samples with transition type 3 are shown in **Fig. 4-17**. Tracks LP1_3, LP2_3, NV3_1 and NV3_2 with high AR above 50% show vertical or even overhanging structures (obtuse contact angle) on their edges. This makes it difficult to deposit another track next to them without forming inter-track voids. Therefore, it would be unrealistic to deposit an applicable dense Ti coating on 316L. This phenomenon has been reported in literature ^[101] ^[102]. The influence of contact angle and AR on the deposition quality is illustrated in **Fig. 4-16** ^[103]. An AR below 50% is crucial for achieving an acute contact angle and avoiding inter-track voids.

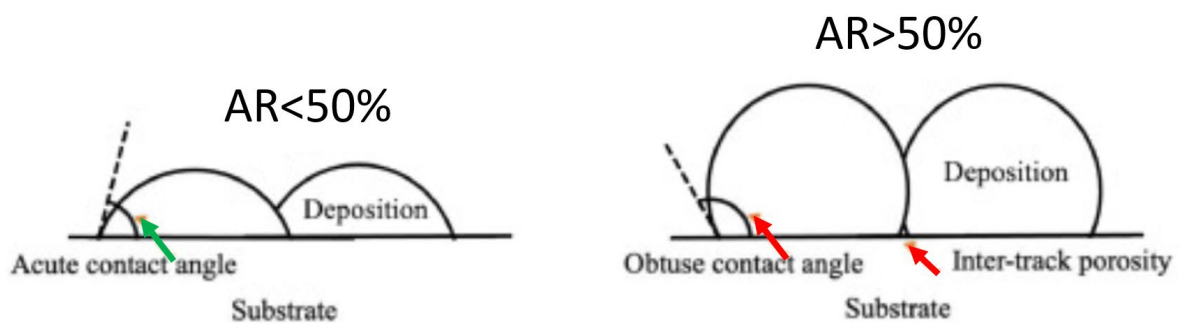


Fig. 4-16. The influence of contact angle and AR on deposition quality. Inter-track porosity is marked in case of obtuse contact angle and AR > 50%.

The tracks NV1_1 and NV2_1 with smaller AR of around 35% show better shapes with relatively sharper contact angles on the edges. But it is difficult to conclude from Table 4-4 alone what LP and NV can lead to small AR given that high PF is already needed to reduce IMC formation.

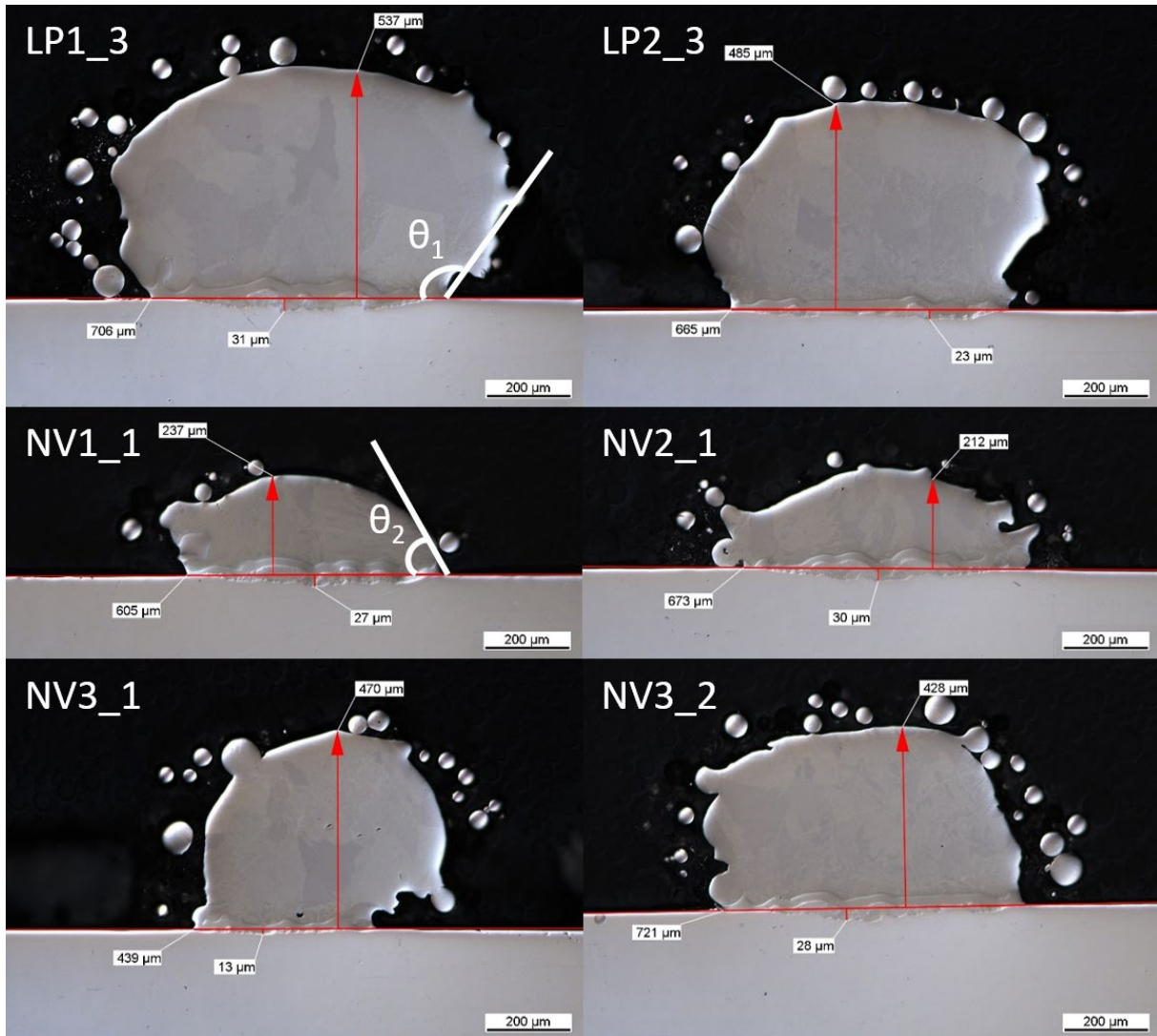


Fig. 4-17. OM images of the cross-section of single tracks with transition type 3 - reaching Ti. θ_1 in LP1_3 indicates an obtuse contact angle and θ_2 in NV1_1 indicates an acute contact angle. The red lines and arrows indicate measurement of the dimensions.

In order to search for LP and NV that lead to small AR with high PF, the geometric dimensions of samples in the LP and NV groups (samples with desired transition type 3 are all in these groups) are then analyzed to explore the process window that gives small D and DL with small AR in a reasonable range. Contour plots of D, DL and AR against the process parameters LP, NV and PF were produced.

In the LP groups, 2nd order polynomial fit of D against PF of samples printed with NV=700 mm/min is done. The same fit is also done for samples printed with NV=1000 mm/min and NV=1400 mm/min. The three curves are then used to produce a contour plot of D against PF and NV with a constant LP=250 W. The contour plots of DL and AR against PF and NV with a constant LP=250 W are produced the same way. Similarly, the contour plots of D, DL and AR for the NV groups (against LP and PF) are produced.

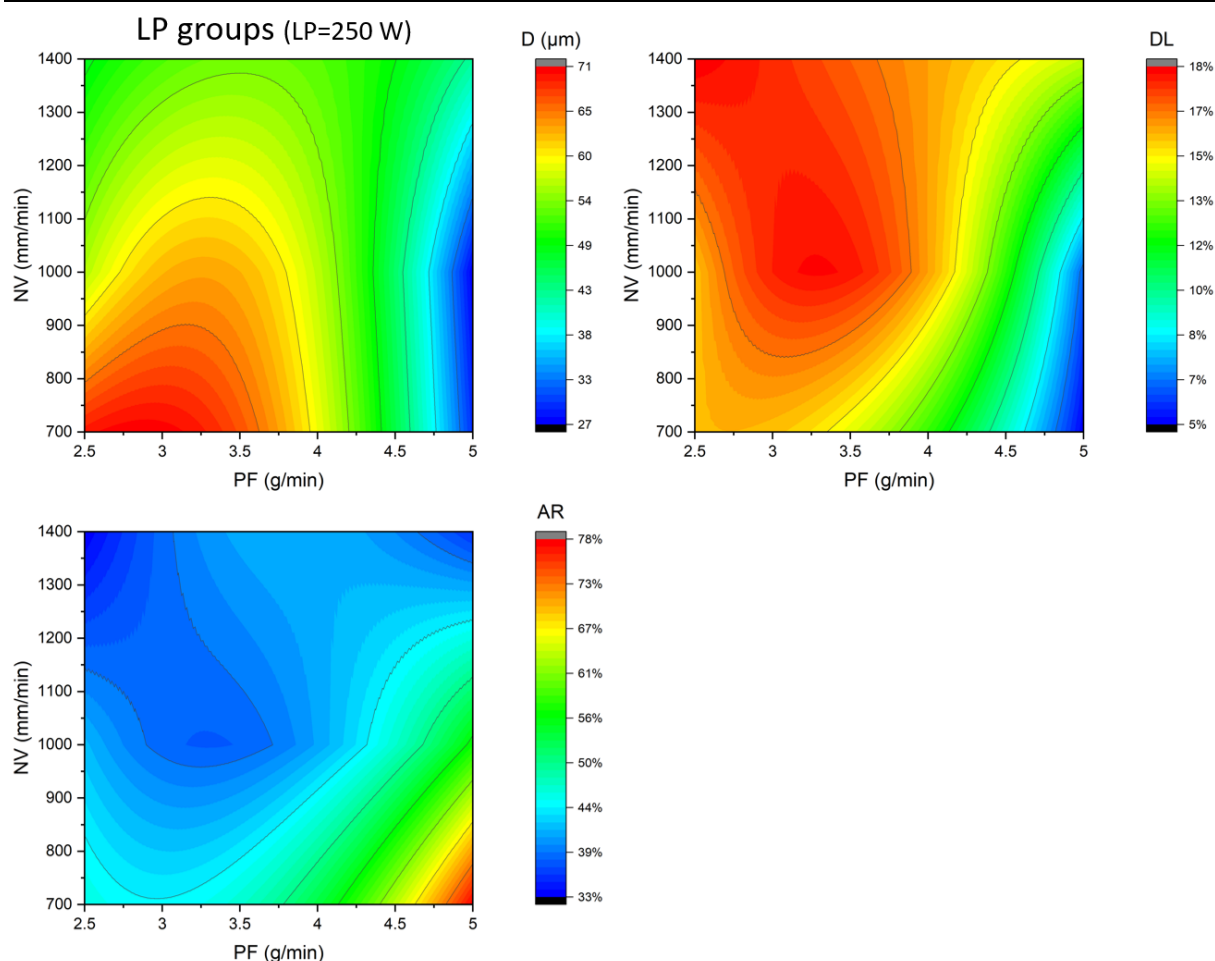


Fig. 4-18. Contour plots of D, DL and AR against PF and NV from LP groups.

The contour plots of D, DL and AR from LP groups with a constant LP=250 W are shown in **Fig. 4-18**. In order to obtain small D and DL, PF has to be increased indeed. Meanwhile, NV has to be increased to avoid high AR on condition of high PF. This is logical because when PF increases, the powder material consumes more energy for melting. Also, the density of flying powder particles in the laser beam increases, blocking the laser and reducing the ratio of energy reaching the substrate. The attenuation due to powder particle shadowing is illustrated in **Fig. 4-19a**. As a result, the melting of the substrate material is reduced. This also conforms with the findings in literature ^[104]. It has been reported that the attenuation of the laser can be achieved by reducing powder size ^[105]. **Fig. 4-19b** shows that the radiated energy by the heated powder flow is higher when powder size is smaller, indicating that the powder jet absorbs more energy from the laser beam and the attenuation is higher. However, because the DED system used in this study does not allow stable transportation of smaller powder (e.g. 15~45 μm), depositing with smaller powder was not further investigated. As more energy is absorbed by the powder material, the amount of deposition increases. The high AR samples in **Fig. 4-17** indicates that

tracks printed with high PF and insufficient NV would have unfavorable contact angles at the edges. Therefore NV needs to be increased to reduce the AR.

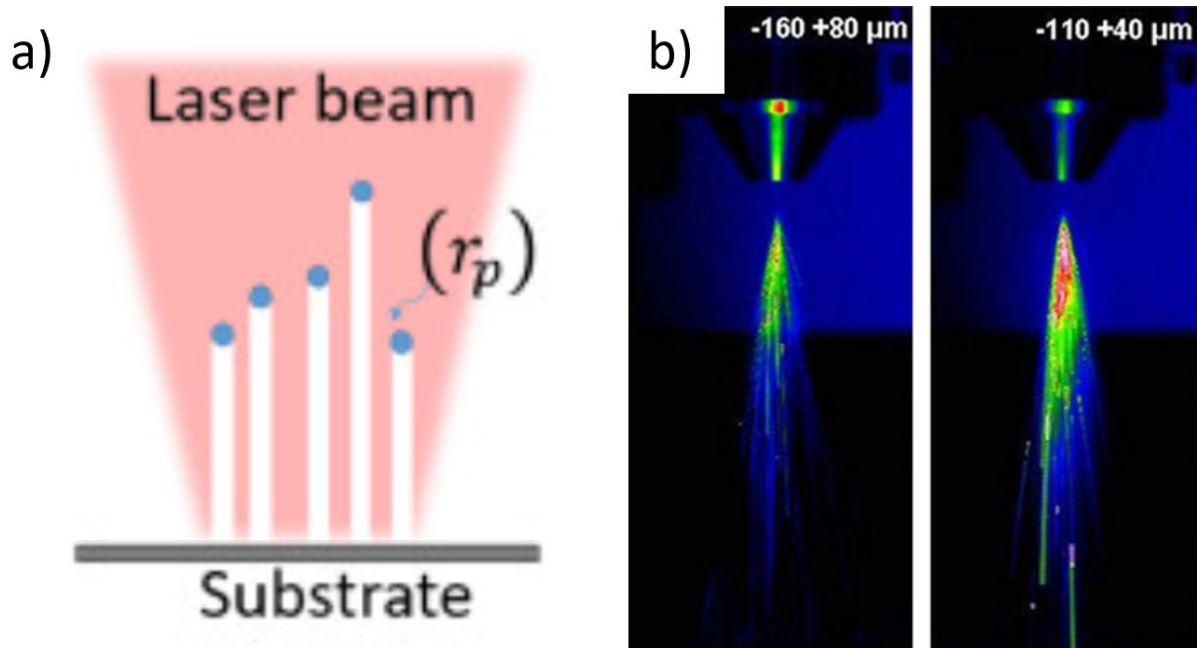


Fig. 4-19. a) Attenuation of laser beam due to powder particle shadowing^[103]. b) Image of the interaction zone obtained with a thermal camera for two powders with different sizes. The red and blue colors indicate higher and lower radiated energy, respectively^[105].

The contour plots of D, DL and AR from NV groups with a constant NV=1000 mm/min are shown in **Fig. 4-20**. In order to obtain small DL, PF has to be increased. With a high PF, LP does not have to be limited at low levels for obtaining a small D. The contour plot of AR indicates that on condition of a high PF, a LP of around 310 W would result in the smallest AR. When LP is low, the melt has lower temperature, which does not allow the melt enough time to collapse and wet the substrate surface and eventually form high AR shapes like NV3_1 in **Fig. 4-17**. As LP increased, the higher temperature of the melt allows it more time to collapse before solidifying, thus reducing the AR. When LP further increases, the increase of the amount of melted powder becomes dominant, leading to more increase in the H than in the W, thus increasing AR.

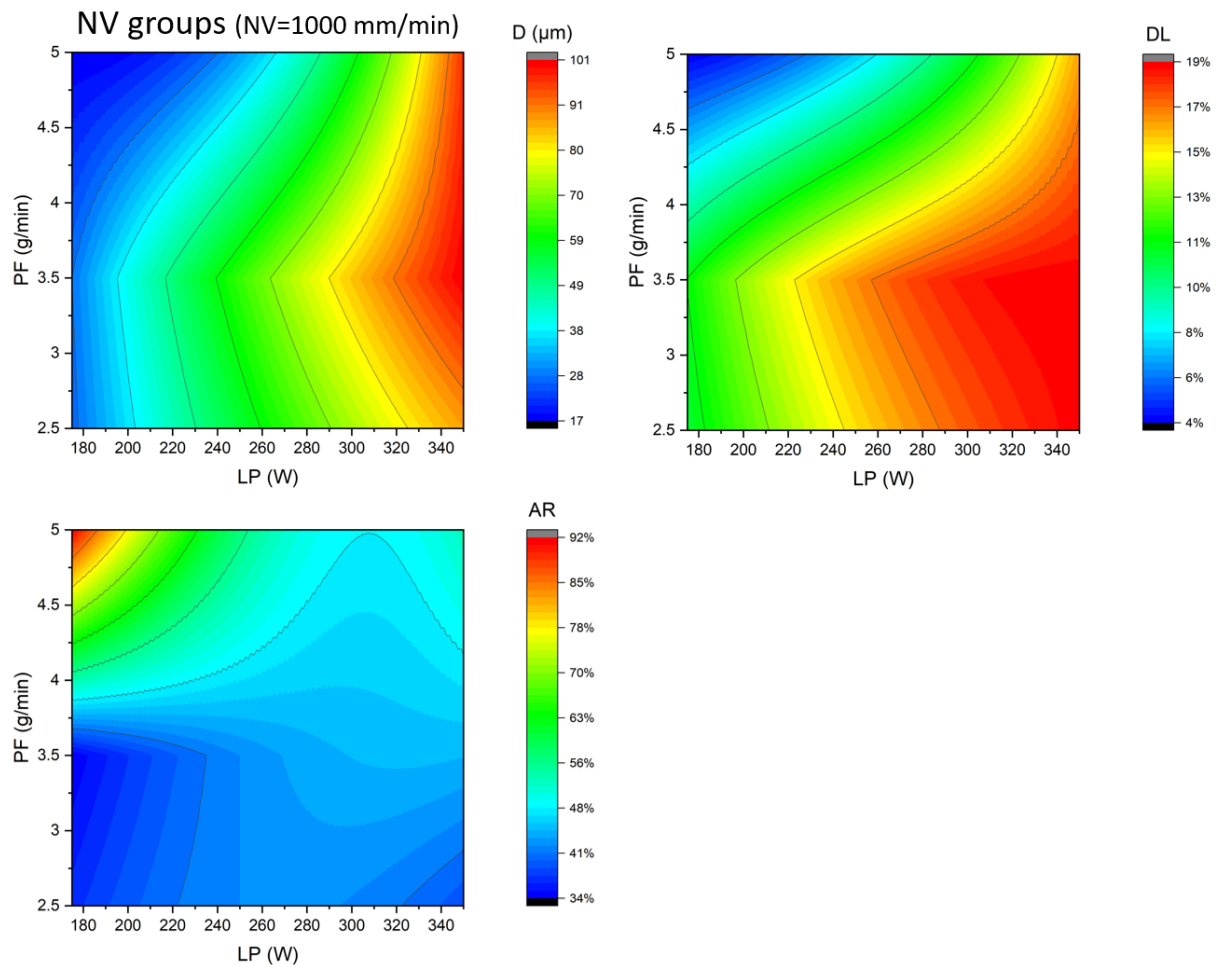


Fig. 4-20. Contour plots of D, DL and AR against LP and PF from NV groups.

To conclude, in order to further decrease D and DL while obtaining a relatively small AR, increasing all of PF, NV and LP at the same time can be a possible direction. This is in accordance with a new variant of DED - EHLA ^[106].

4.1.3. Conclusion

During the DED process, the 316L substrate and Ti powder mix in the liquid state and can form various phases in different reaction regions.

From the 316L side to pure Ti, four possible reaction regions have been identified.

- Region I has a complex reticular microstructure consisting of three features: $Ti_5Fe_{17}Cr_5$ river-shaped network, Fe_2Ti surrounding the river-shaped network and FeTi filling the space left by the Fe_2Ti .
- Region II consists of FeTi dendrites and interdendritic supersaturated β -Ti.

- Region III consists of supersaturated β -Ti as the matrix and FeTi particle precipitates.
- Region IV consists of β -Ti as the matrix and FeTi network precipitates. All these regions exhibit much higher microhardness than 316L and Ti, with Region I showing the highest value of 893HV_{0.01}.

The concentration of Fe decreases from the bottom of the solidified melt pool to its top. Depending on the ending composition, three types of composition transitions are observed.

- Transition type 1 ends with high Fe concentration. Such samples contain a large amount of Fe₂Ti and FeTi IMCs in the deposition and are prone to severe cracks and voids.
- Transition type 2 ends with low Fe concentration. Such samples contain supersaturated β -Ti as the main phase. Cracks can penetrate all reaction regions in these samples.
- Transition type 3 ends with pure Ti. Only Region I and Region III have been observed as thin bands at the bottom of the solidified melt pool. The thin bands have a total thickness of 20~70 μ m. No cracks have been observed in these samples.

An abrupt transition ending with pure Ti is therefore estimated favorable for reducing crack in the deposition. Such a composition transition requires small penetration depth D and dilution DL at the same time. A relatively small aspect ratio AR is desired for avoiding large intertrack voids when printing overlapping tracks. These requirements could be fulfilled by increasing powder feedrate PF, nozzle velocity NV and laser power LP simultaneously. Compared to standard approach, increase of PF, NV and LP could reduce the formation of brittle IMCs in the interface between 316L and Ti.

4.2. Single wall trials

In real applications, 3D structures instead of single tracks have to be produced, thus involving deposition of multiple superposing tracks. In order to investigate the influence of the superposing tracks on the interface formed in the first track, the single track parameters were used to print 5-layer single walls.

4.2.1. Results

Many of the wall samples cracked entirely at the bottom of the solidified melt pool. The results from the single walls are grouped by composition transition type in their corresponding single tracks.

Single walls corresponding to track samples with transition type 1 ending with high Fe concentration are represented by Walls PF2_3 and PF3_3. Their cross-sections are shown in **Fig.**

4-21. Both of the single walls crack at the bottom of the melt pool. A large amount of material is even missing in wall PF2_3 after cutting for the cross-section.

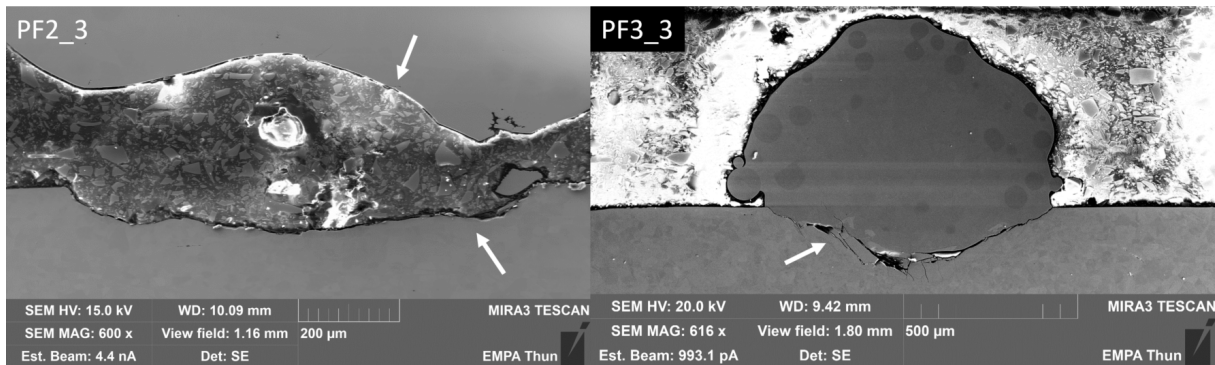


Fig. 4-21. Cross-sections of Wall PF2_3 and PF3_3. The cracks are marked with white arrows.

Single walls corresponding to track samples with transition type 2 ending with low Fe concentration behave differently at the bottom. Some of the single walls do not fracture at the bottom and the others fracture at the bottom.

Single walls that do not fracture are represented by Wall PF2_1. **Fig. 4-22a** shows the cross-section of Wall PF2_1. A large amount of unmelted Ti particles are seen on top of the wall. They are estimated to have stuck to the hot surface of the deposition when the nozzle had already moved away. Wall PF2_1 shows a section of thin interface with almost no penetration depth on each lateral side, forming neither reticular Region I nor dendritic Region II. **Fig. 4-22b** shows the left part of the interfacial region between the deposited wall and the substrate. The reticular Region I is seen close to the middle of the interface. The thickness of Region I reduces toward the left edge, and this region disappears in the white box marked c. EDS mapping of the interfacial region is shown as overlay as well. The composition in the reticular region is Fe73 (blue in the overlay), conforming to that of the same Region I in the single track samples. The composition in the regions above (red overlay) and below (yellow overlay) the reticular regions are Fe<22 and Fe100, conforming to Region IV β -Ti and substrate 316L respectively.

Fig. 4-22c is a high magnification SEM image of the area where the reticular region disappears. A region with dark matrix and bright precipitates and a thickness of around 10 μm is observed above Region I. The composition of the dark matrix and the bright precipitates are Fe24 and Fe33 respectively, conforming to Region III in the track samples. The composition above Region III is around Fe10, conforming to β -Ti.

A high magnification SEM image of the thin interface close to the edge of Wall PF2_1 is shown in **Fig. 4-22d**. A thin band with a thickness of around 200 nm is seen between the substrate

and Region III. EDS point analysis on the thin band gives a composition of around Fe50, corresponding to the FeTi IMC.

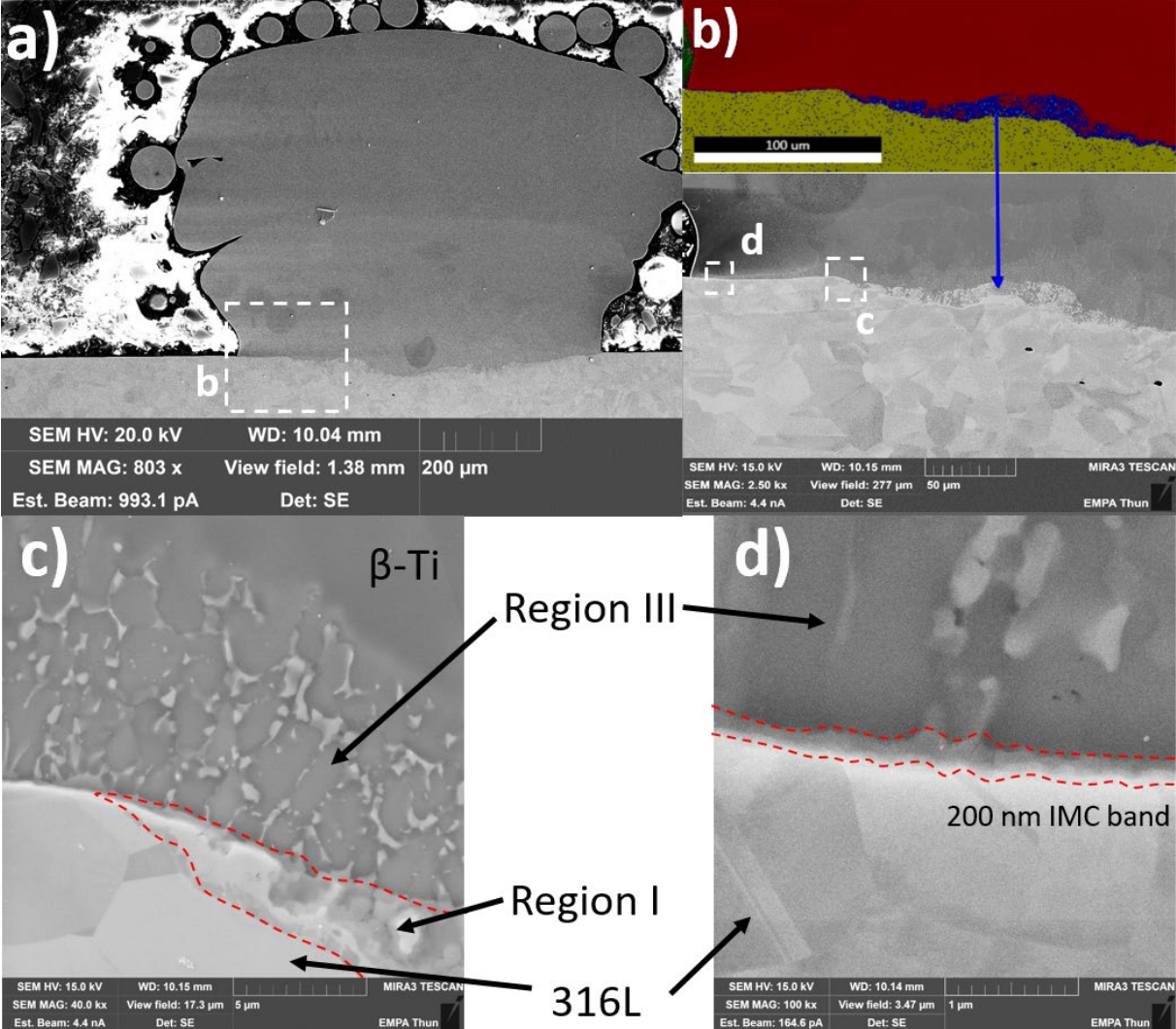


Fig. 4-22. a) SEM image of the cross-section of Wall PF2_1. The positions of b), c) and d) are marked with white boxes. EDS mapping of the interfacial regions in b) is shown on the top of b).

Single walls corresponding to single tracks with transition type 2 and fracture at the bottom are represented by Walls PF1_2 and PF1_3. Their cross-sections are shown in **Fig. 4-23** together with Wall PF2_1.

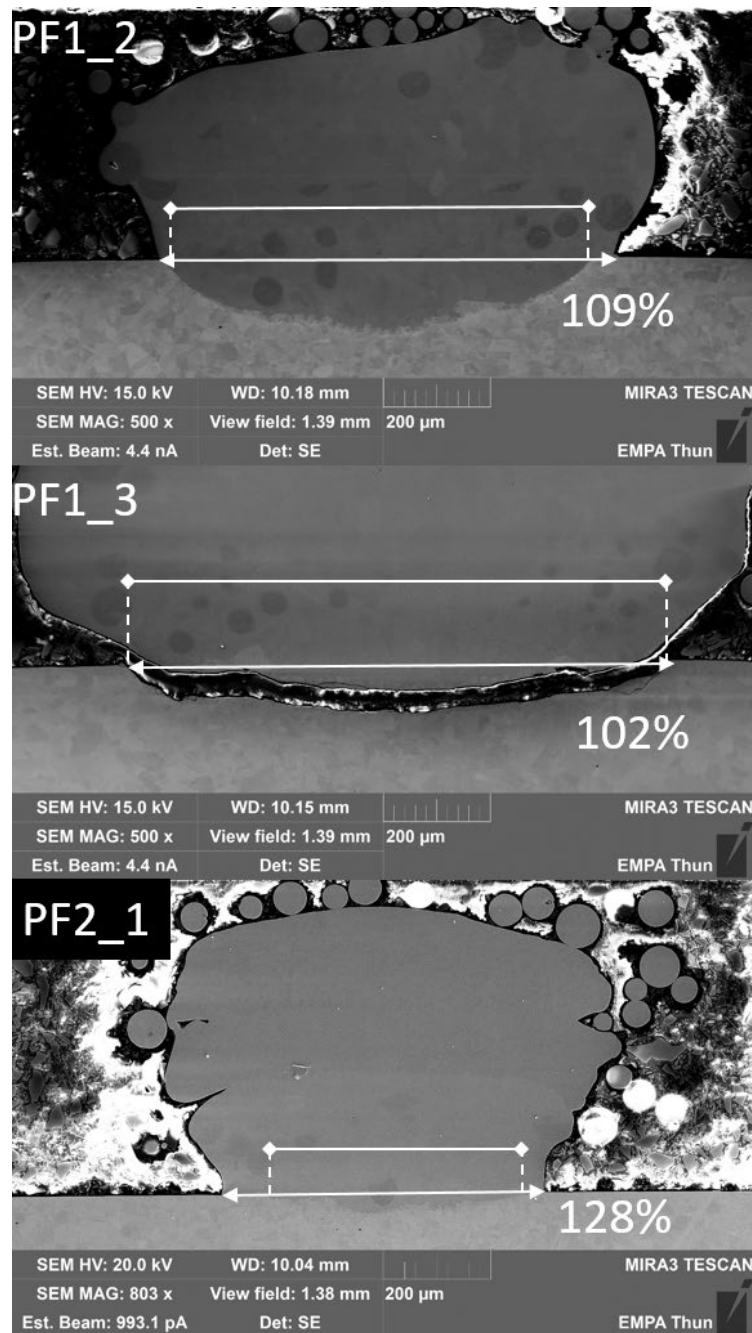


Fig. 4-23. Cross-sections of Wall PF1_2, PF1_3 and PF2_1. The widths of their corresponding single tracks are indicated with diamond-headed white lines. The ratio of the single wall width to the single track width is marked in each image.

Walls PF1_2 and PF1_3 do not look like 5 superposed single tracks. In order to compare these two walls with the expected deposition of 5 superposed tracks, the depth D , height H and width W of these walls are compared with their corresponding single tracks and listed in Table 4-5. The ratios listed are of the wall dimensions to the track dimensions. The W of the tracks are particularly indicated in **Fig. 4-23** in comparison to the W of the walls. The ratio of the single wall width to the single track width for the PF2_1 parameter set is 128%, obviously larger than those for PF1_2 (109%) and PF1_3 (102%).

Table 4-5. The geometric dimensions of track and wall samples printed with PF1_2, PF1_3 and PF2_1 parameter sets. Ratios are the wall dimension to the track dimension.

Dimension Parameter	D (μm)			H (μm)			W (μm)		
	Track	Wall	ratio	Track x 5	Wall	ratio	Track	Wall	ratio
PF1_2	94	152	162%	1460	403	28%	786	854	109%
PF1_3	124	110	89%	2220	1527	69%	1122	1145	102%
PF2_1	45	41	91%	400	535	138%	478	613	128%

Single walls corresponding to track samples with transition type 3 ending with pure Ti are represented by Wall NV1_1. **Fig. 4-24** shows the cross-section of Wall NV1_1. The two-band structure from the first layer remains at the bottom of the deposition. Wall NV1_1 cracked off the substrate at the bottom of the lower band. Cracks are observed both in the lower band and upper band.

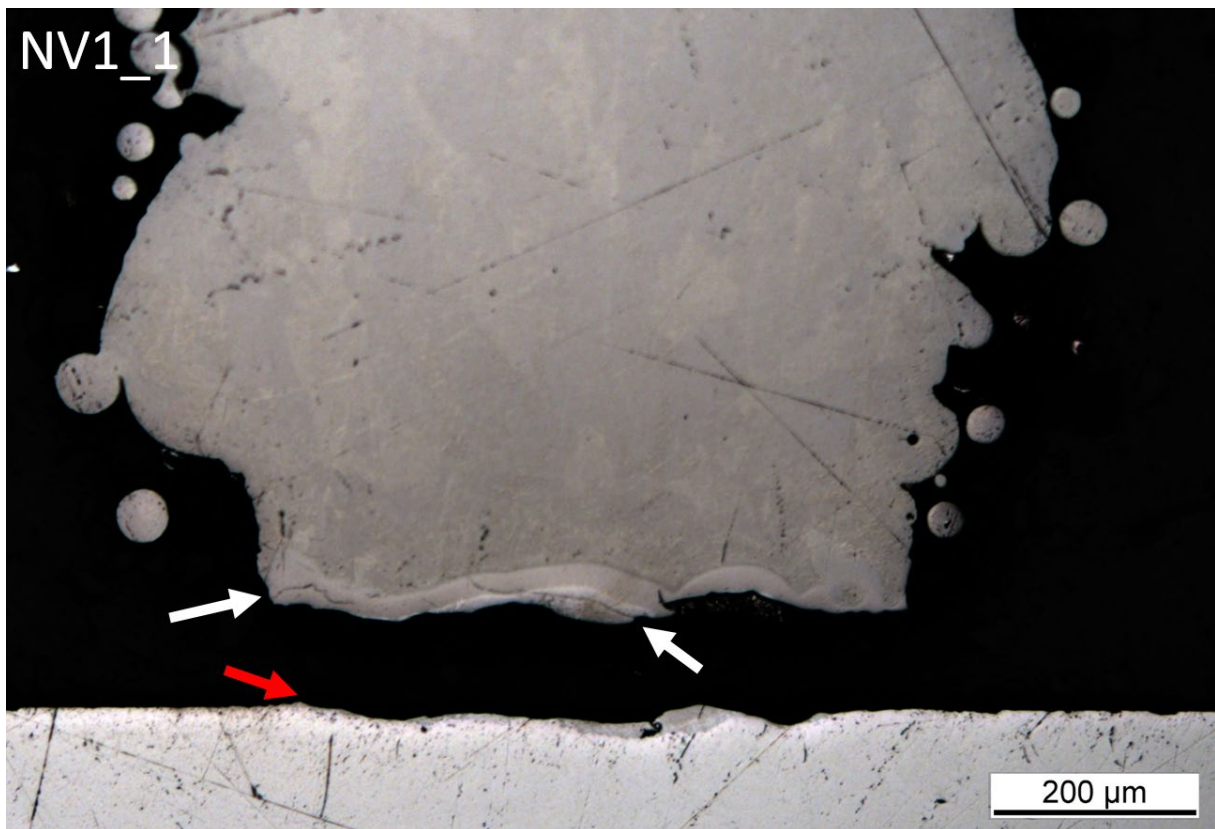


Fig. 4-24. The cross-section of Wall NV1_1. The delamination is marked with a red arrow and the cracks are marked with white arrows.

4.2.2. Discussion

Depositing more tracks on top of the first single track generally induced more cracks at the bottom of the first track. This is estimated as a result of additional thermal expansion and contraction cycles. The coefficient of thermal expansion (CTE) of pure Ti and 316L are 9×10^{-6}

Chapter 4. Single track and single wall trials

K^{-1} and $16 \times 10^{-6} K^{-1}$ respectively [9]. Due to this mismatch of CTE, shape distortion and excessive generation of strain accumulate at the interface during the melting and solidification cycles in the DED process. Therefore, the risk of cracking and delaminating at the bottom of single walls is higher compared to single track samples.

In walls with transition type 1 ending with high Fe concentration in the first layer, a large amount of brittle FeTi and Fe₂Ti exists in the first layer. Subject to multiple thermal cycles, severe cracks and voids were easily induced.

In walls with transition type 2 ending with low Fe concentration in the first layer, the main microstructure is Region III supersaturated β -Ti matrix with small FeTi precipitates. The first layer is generally more resistant to multiple thermal shocks, but the results can vary among different samples. As Table 4-5 shows, the total height H of Wall PF1_2 is only 28% of 5 times of H of Track PF1_2. Therefore, it is unlikely that Wall PF1_2 is superposing of 5 tracks. Meanwhile, the depth D and width W of Wall PF1_2 152 μ m are 162% and 109% of the D and W of Track PF1_2, respectively. During the DED process, the deposited part was observed delaminating and flying away from the substrate when printing the third layer of Wall PF1_2. The final structure of Wall PF1_2 is therefore estimated to be two tracks deposited on the pit left by the detached deposition. Wall PF1_3 has a total H of 1527 μ m, around 69% of 5 times of the H of Track PF1_3. The D and W of Wall PF1_3 are 89% and 102% of the D and W of Track PF1_3. Therefore, the crack in Wall PF1_3 shown in **Fig. 4-23** is estimated to have formed after all 5 tracks printed.

Fig. 4-23 shows that the Ti-316L interface in Wall PF2_1 successfully withstood the deposition of 5 tracks. The bottom of the first track does not seem to be influenced by the subsequent tracks via remelting. An interesting observation is that the W of Wall PF2_1 is 128% of the corresponding track sample. Outside the range of the width of the track, the wall has a section of thin interface on each lateral side with the substrate. **Fig. 4-22c** shows that the interface section start from where the thickness of Region I reduces to zero. It is estimated that when the first track was formed, it could act as a protective layer that avoided further melting into the 316L substrate. The melt pool of the second track flowed to the lateral sides of the first track. Thanks to the low energy density of the Gaussian beam, the temperature of the fresh substrate surface was low enough. The melt pool of the second layer thus solidified shortly after wetting the fresh substrate surface. **Fig. 4-22d** shows the thin interface is an IMC band with a thickness of only 200nm, and it takes only 10 μ m to transition from 316L to β -Ti with a composition of Fe10. The transition distance is comparable to or even smaller than the values obtained by diffusion bonding (a few microns to 55 μ m) [19] [41] [107] [108] and friction stir welding (1 to 6 μ m) [46] [109]. Joint between Ti(-alloys) and steels by these techniques exhibits ultimate

tensile strength in a range of 222~480 MPa or ultimate shear strength in a range of 190 MPa. On the contrary, conventional fusion joining techniques like laser welding generally result in 30~80 μm thick transition distance ^{[27] [28]}. The ultimate tensile strength from laser welded joints falls in a lower range of 65~200 MPa. The joint strength seems to decrease with the increase of the transition distance, which is positively correlated to the amount of brittle IMCs. Therefore, the interface strength would be promising if the 200 nm thin interface sections obtained with DED can be extended to form a full layer. **Fig. 4-25** shows the schematic of such a strategy. A 1st track is deposited with thick interface mainly consisting of reticular Region I with the brittle IMCs (marked in red) at the bottom. Then, a 2nd track is formed on top of the first track and overflows to the lateral sides to form the two sections of thin interface. Each subsequent track is deposited with a small shift in the lateral direction, so that its melt pool is expected to overflow in one direction and extend the thin interface. Eventually, the 200 nm thin interface is expected to be the main form of the interface between a full layer of deposited Ti and the 316L substrate.

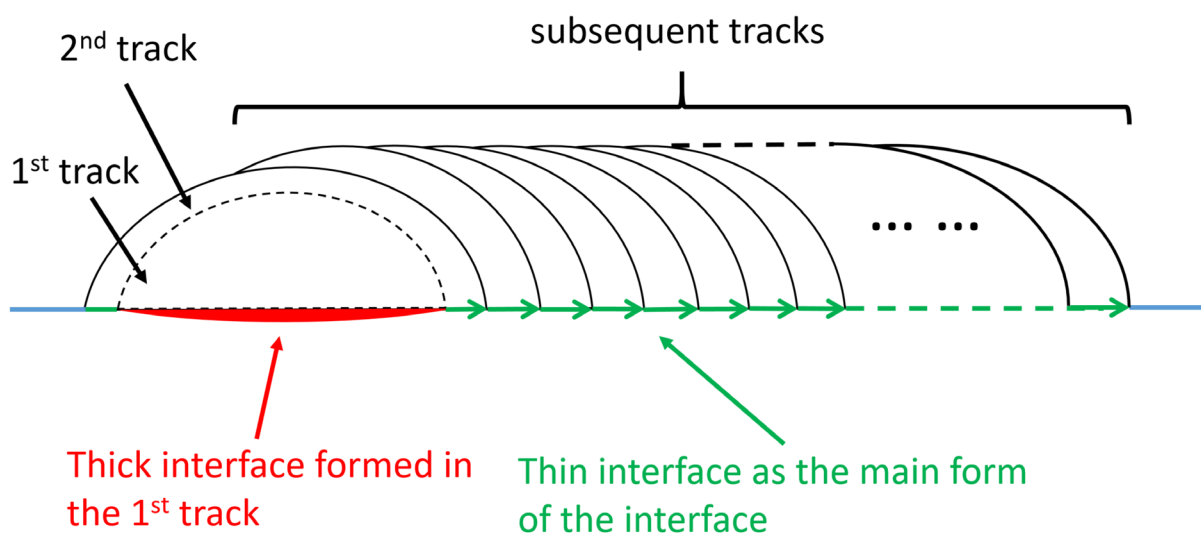


Fig. 4-25. Schematic of the overflowing method for extending the thin interface.

In walls with transition type 3 ending with pure Ti in the first layer, the main feature is two transition bands at the bottom corresponding to reticular Region I with IMCs and Region III with supersaturated β -Ti and FeTi precipitates, respectively. The two band structures of the first track does not seem to be influenced by subsequent tracks via remelting either. However, despite the crack-free observation in the single track samples, the wall samples delaminate from the substrate. The catastrophic cracks are observed in both the lower band (Region I) and the upper band (Region III). It seems that these transition bands with their current thickness were not capable of surviving accumulated thermal stress over multiple thermal cycles.

Chapter 4. Single track and single wall trials

Reducing the thickness of these bands is expected to reduce the amount of IMCs and the thermal stress in them, eventually improving the interface strength.

4.2.3. Conclusion

During deposition of single walls consisting of 5 single tracks, the composition and phases at the bottom of the first track were not influenced by the subsequent tracks by remelting or heat dissipation. The bottom of the first track is exposed to higher risk of cracking and delaminating because of thermal stress accumulated over more thermal cycles.

When a parameter set results in transition type 1 ending with high Fe concentration in the single track, its corresponding single wall is prone to crack because the first layer consists of mainly IMCs.

When a parameter set results in transition type 2 ending with low Fe concentration in the single track, its corresponding single wall can behave differently, with or without cracking at the bottom. An interesting case is that 200 nm thin interface sections form on the lateral sides of the first track, estimated due to overflowing of the second track. This proves that producing an interface with a very abrupt transition with metallurgical bonding is possible with the DED system.

When a parameter set results in transition type 3 ending with pure Ti in the single track, its corresponding single wall cracks at the bottom of the first track, within the two transition bands of IMCs and supersaturated β -Ti with FeTi precipitates. Reducing the thickness of these transition bands could help improve the interface strength.

4.3. Summary

Ti in the forms of single track and single wall has been successfully deposited on 316L substrate with DED. When the substrate material mixes with the powder material in liquid state, brittle IMCs like $\text{Ti}_5\text{Fe}_{17}\text{Cr}_5$, Fe_2Ti and FeTi form in the solidified melt pool. These brittle phases have been observed in four reaction regions with different compositions. Three types of composition transition from 316L to Ti have been observed. The type of composition transition determines the presence of the reaction regions and the phases within.

It has been concluded that an abrupt transition ending with pure Ti is beneficial for reducing the amount of IMCs. Additionally the risk of cracking and delaminating is reduced. Two approaches are proposed basing on the results of the single track and single wall experiments.

1. With a laser power $LP = 175$ W, nozzle velocity $NV = 1000$ mm/min and powder feedrate $PF = 2.5$ g/min, extremely thin IMC interface sections with a thickness of 200 nm have been observed on the lateral sides in single wall deposition. Across these interface sections, the transition from 316L to β -Ti can complete within around 10 μm and this is expected to provide promising interface strength. This interface is estimated to form when the melt pool of the second track overflows to the lateral sides of the first track and solidifies shortly after touching the cold substrate surface. The overflowing strategy aimed at extending this thin interface is explored in Chapter 5.

2. It has been found possible to limit the IMCs inside two transition bands at the bottom of a single track. Such single tracks feature small penetration depth D and dilution ratio DL . To obtain acute contact angles for avoiding inter-track voids when depositing a full layer, small aspect ratio AR in the single track is also desired. Increasing powder feedrate PF , nozzle velocity NV and laser power LP simultaneously is expected to reduce D , DL and AR , which should be good for increasing the interface strength. Therefore, parameter sets outside the conventional DED process window in this chapter are explored in Chapter 6.

Chapter 5. Overflowing upper layer

The possibility of forming a thin interface with an overflowing upper layer described in Section 4.2.2 was explored in this chapter. 2-layer single walls were printed with their 1st layers having the same parameter set of laser power LP = 175 W, nozzle velocity NV = 1000 mm/min and powder feedrate PF = 3.0 g/min. This parameter set was selected due to its relatively small penetration depth D and aspect ratio AR. The 1st layer acted as a base for the 2nd layer to form thin interface on its sides. Different parameter sets for the 2nd layers on top were studied to find conditions where lateral thin interface sections form by the 2nd layer via overflowing and the interface at the bottom of the 1st layer does not change. The parameter sets investigated for the 2nd layer are listed in Table 5-1. PF for the 2nd layer was fixed at 3 g/min for all samples.

Table 5-1. Parameters for the 2nd layers in the DED experiments with overflowing upper layer.

Group	Sample No.	LP (W)	NV (mm/min)
S1	1	175	500
	2	200	500
	3	250	500
	4	300	500
	5	350	500
S2	1	175	700
	2	200	700
	3	250	700
	4	300	700
	5	350	700
S3	1	175	1000
	2	200	1000
	3	250	1000
	4	300	1000
	5	350	1000
S4	1	175	1200
	2	200	1200
	3	250	1200
	4	300	1200
	5	350	1200

The 2nd layer parameters are divided in four groups S1~S4. In each group, the LP increases from 175 W to 350 W. Each group has a common NV. The NV increases from 500 mm/min in S1 to 1200 mm/min in S4.

The 2-layer single wall samples were cut perpendicular to the nozzle scan direction. The cross-sections were grinded and observed with OM.

5.1. Results

The OM image of the 1st layer alone is shown in **Fig. 5-1**. Some partially melted Ti particles are seen in the deposition. The reticular Region I is observed between the deposition and the substrate.

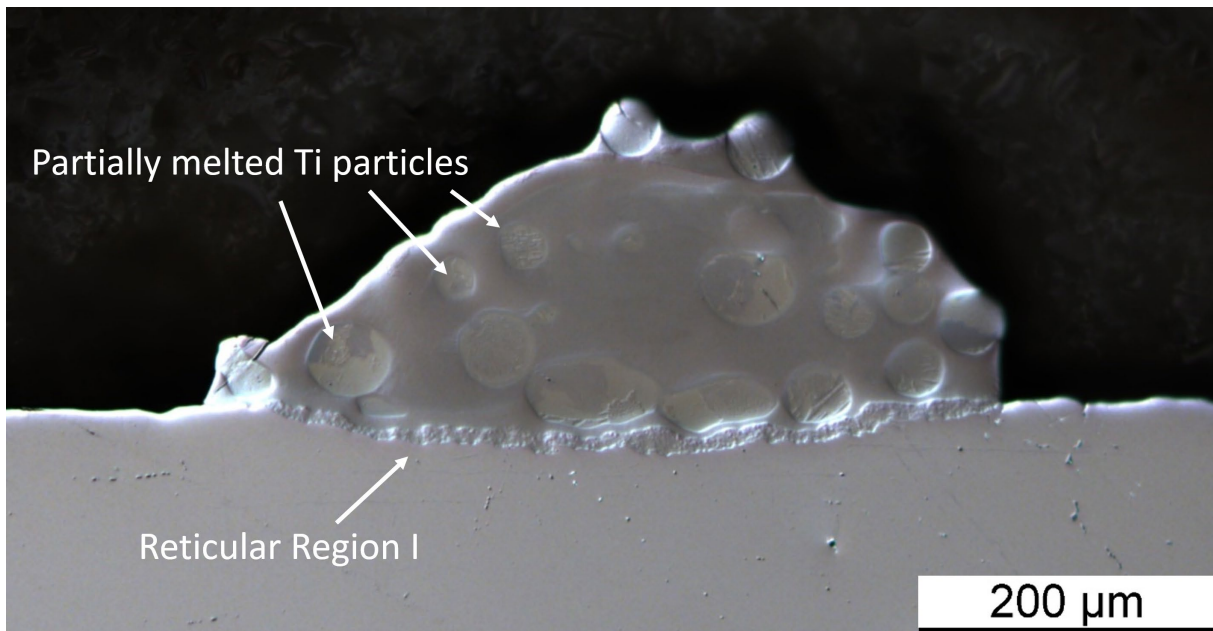


Fig. 5-1. OM image of the cross-section of the 1st layer deposited with LP = 175 W, NV = 1000 mm/min and PF = 3.0 g/min. The partially melted Ti particles and reticular Region I are marked.

OM images of the cross-sections of the 2-layer walls are summarized in **Fig. 5-2**. All of the walls show more or less overhanging structure at the sides. The reticular Region I can be seen at the interface between the deposition and the substrate in almost all samples. Wall S1_1 (NV=500 mm/min and LP=175 W) clearly shows the small 1st layer below. The large 2nd layer on top solidified before touching the 316L substrate. The fusion region between the 1st and 2nd layers is marked with a white broken curve. The reticular Region 1 is also marked. The other walls in group S1 shows that as the LP increased, the 2nd layer collapsed more and more toward the substrate. This trend is observed in the other groups as well. When LP is fixed, as NV increases the height of the 2nd layer decreases.

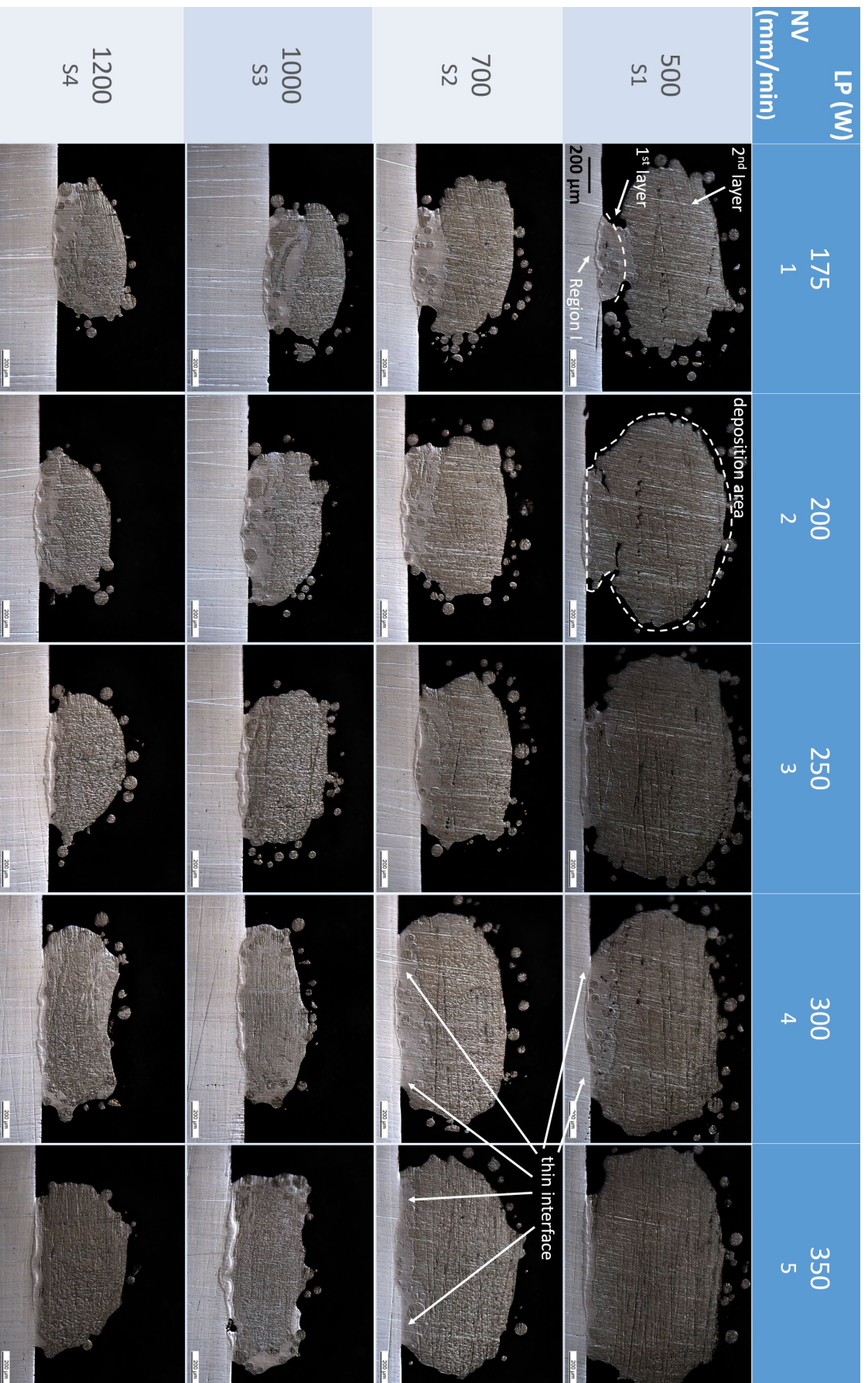


Fig. 5-2. OM images of the cross-sections of 2-layer single wall samples in groups S1~S4. In each group, NV is constant and LP increases from 175 W to 350 W. NV increases from 500 mm/min in S1 to 1200 mm/min in S4. PF is 3.0 g/min for all samples. Magnification is constant for all images

The amount of deposition can be quantified by the area of the deposition above the substrate surface in the cross-section. The deposition area is marked with white broken curve on Wall S1_2 in **Fig. 5-2** for example. The contour plot of the deposition area against LP and NV is shown in **Fig. 5-3**. The amount of deposition generally increased with increasing LP and decreased with increasing NV.

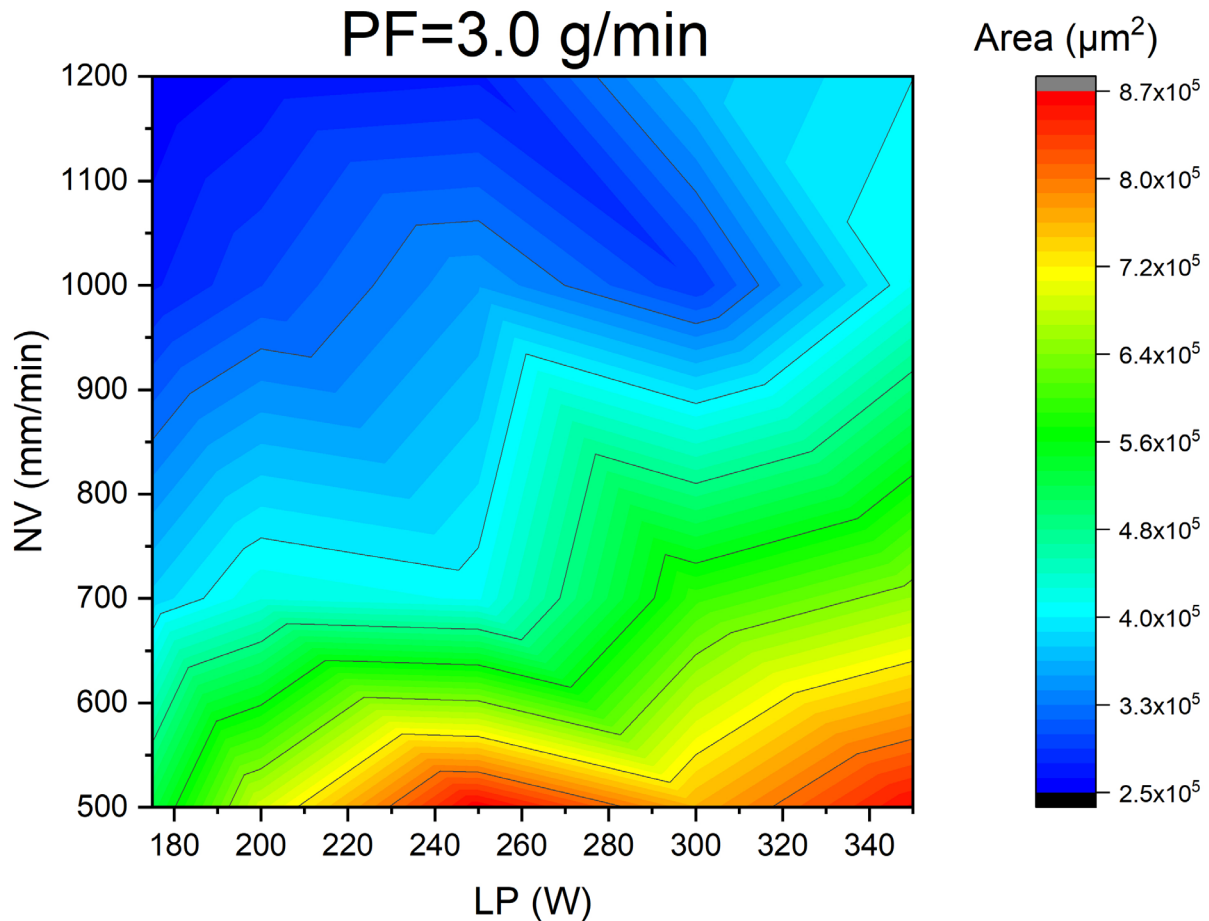


Fig. 5-3. Contour plot of deposition area against LP and NV with a constant PF=3.0 g/min.

Fig. 5-2 shows that in samples like Wall S1_4, S2_4, S2_5, etc., the thin interface appears at the lateral sides as expected and makes up a large fraction of the total width of the wall. The ratio of the total width of the wall at the substrate surface level to the width of the reticular Region I is measured. This "Wall to Reticular region Ratio" is denoted as WRR. The maximum WRR of 213% was obtained with LP=350 W and NV=700 mm/min. The minimum WRR of 100% was obtained with LP=175 W and NV=500 mm/min. The contour plot of WRR against LP and NV is shown in **Fig. 5-4**. When NV is below 1000 mm/min, WRR increases with increasing LP. When NV is 1000 mm/min or higher, WRR does not show a clear correlation with LP. WRR does not show a clear trend with NV at any given LP.

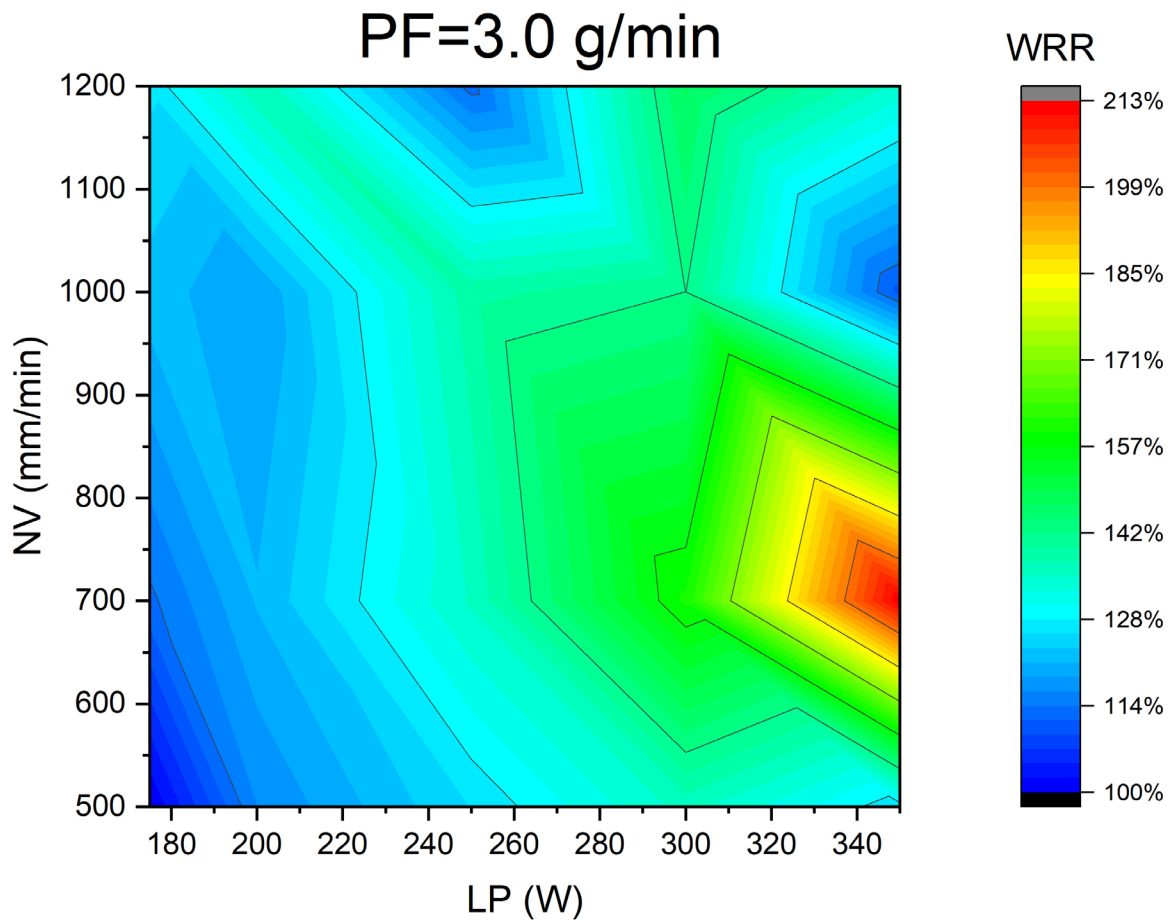


Fig. 5-4. Contour plot of WRR against LP and NV with a constant PF=3.0 g/min.

5.2. Discussion

With the investigated parameters for the 2nd layers, no significant change in the penetration depth D of the 1st layer into the substrate was found.

The cross-sections of the 2-layer walls in group S1 show the formation of the thin interface at the lateral sides of the wall between the Ti deposition and the 316L substrate. **Fig. 5-2** shows that with a constant and low NV of 500 mm/min for S1 samples, LP below 250 W was enough to melt the particles and create a melt. But the short lifetime of the melt does not allow it to collapse and wet the substrate on the lateral sides before solidifying. As LP increased, the melt had increased temperature and longer lifetime to collapse. Eventually, when LP is above 250 W, the melt of the 2nd layer could touch the fresh substrate surface on the lateral sides of the 1st layer, and form the thin interface as expected.

The thin interface sections on the lateral sides have been observed in many samples, validating that the overflowing strategy indeed can produce the desired thin interface sections. However, the 2nd tracks tend to form overhanging structures at the edges, making it difficult to expand

Chapter 5. Overflowing upper layer

the thin interface laterally with adjacent tracks. The schematic in **Fig. 5-5a** illustrates the principle of this problem. Such a phenomenon was indeed observed in attempts aimed to deposit single layers by expanding the thin interface. The top view of some of the single layers in **Fig. 5-5b** show periodic wave-like features. The cross-section of the single layer in **Fig. 5-5c** shows the overhanging structure corresponding to **Fig. 5-5a**. Apparently, the overflowing strategy with the studied parameters could not create dense Ti layers on 316L substrate with a desired interface.

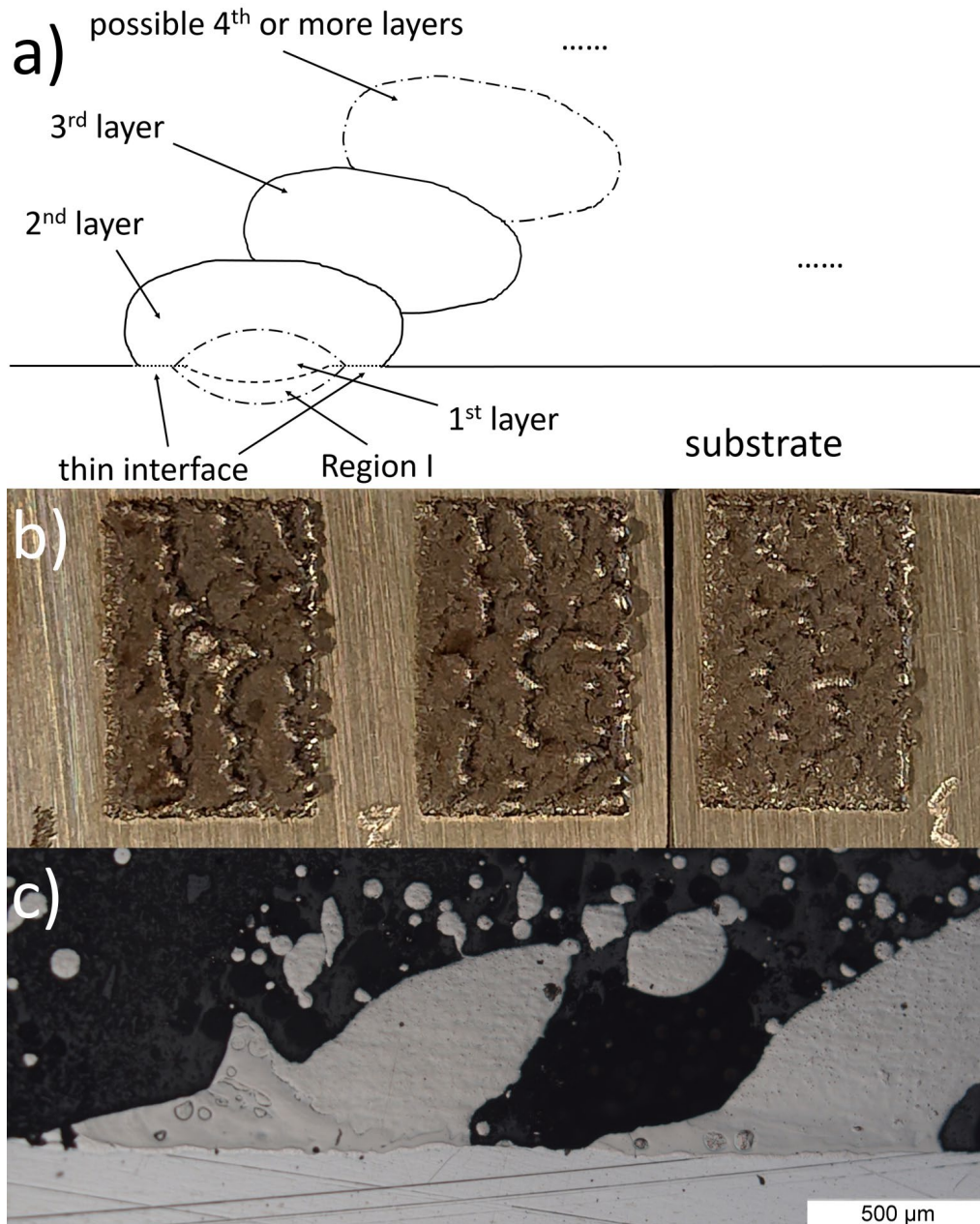


Fig. 5-5. a) Schematic of the overflowing problem after depositing multiple tracks. b) Top view of three single layers printed with the overflowing strategy. c) Cross-section of part of a single layer showing the overhanging problem.

5.3. Conclusion

2-layer single walls of Ti have been deposited on 316L substrate. The hypothesis in Section 4.2.2 on the formation of the thin interface sections has been validated - the melt pool of the upper layer collapses and overflows to the lateral sides of the 1st layer, solidifies upon wetting the fresh substrate surface and forms the thin interface.

The total width of the 2-layer wall could reach 213% of the reticular Region I formed by the 1st layer. However, with the studied parameters, the subsequent tracks piled up and formed periodic overhanging structure. Dense Ti layers on 316L substrate with a desired interface could not be produced.

Chapter 6. High powder feedrate DED

6.1. Entering the high powder feedrate regime

As discussed in Section 4.3., depositing Ti on 316L with high powder feedrate PF together with increased nozzle velocity NV and laser power LP could be an approach to improving the interface strength.

A series of Ti single tracks were deposited on a 316L substrate to study the effect of entering the high PF regime.

The parameters are summarized in Table 6-1.

Table 6-1. Parameters for single tracks showing the effect of entering the high PF regime.

Group	Sample No.	LP (W)	NV (mm/min)	PF (g/min)
M	1	250	700	2.5
	2	250	700	21
	3	250	13000	21
	4	500	13000	21

The M group track samples were cut perpendicular to the nozzle scan direction. The cross-sections were polished and observed with OM.

6.1.1. Results

Fig. 6-1 shows the OM images of the cross-section of the M group track samples.

Track M1 was deposited with parameters in the typical range for DED and has a normal track geometry with a penetration depth D of 51 μm. A reticular Region I is observed at the bottom of the solidified melt pool. Several partially melted particles are observed in the deposition.

Track M2 was deposited with significantly increased PF compared to M1. M2 detached from the substrate immediately. Its cross-section in **Fig. 6-1** is nearly a circle with a diameter of around 1100 μm. No trace of penetration was observed on the substrate side.

Track M3 was deposited with significantly increased NV compared to M2. M3 has a much smaller cross-section (an area of $9.3 \times 10^4 \mu\text{m}^2$) than M2 (an area of $1.0 \times 10^6 \mu\text{m}^2$). M3 does not bond with the substrate either.

Track M4 was deposited with doubled LP comparing to M3. M4 bonds to the substrate with a very small D of 12 μm maximum. The track forms an acute contact angle with the substrate.

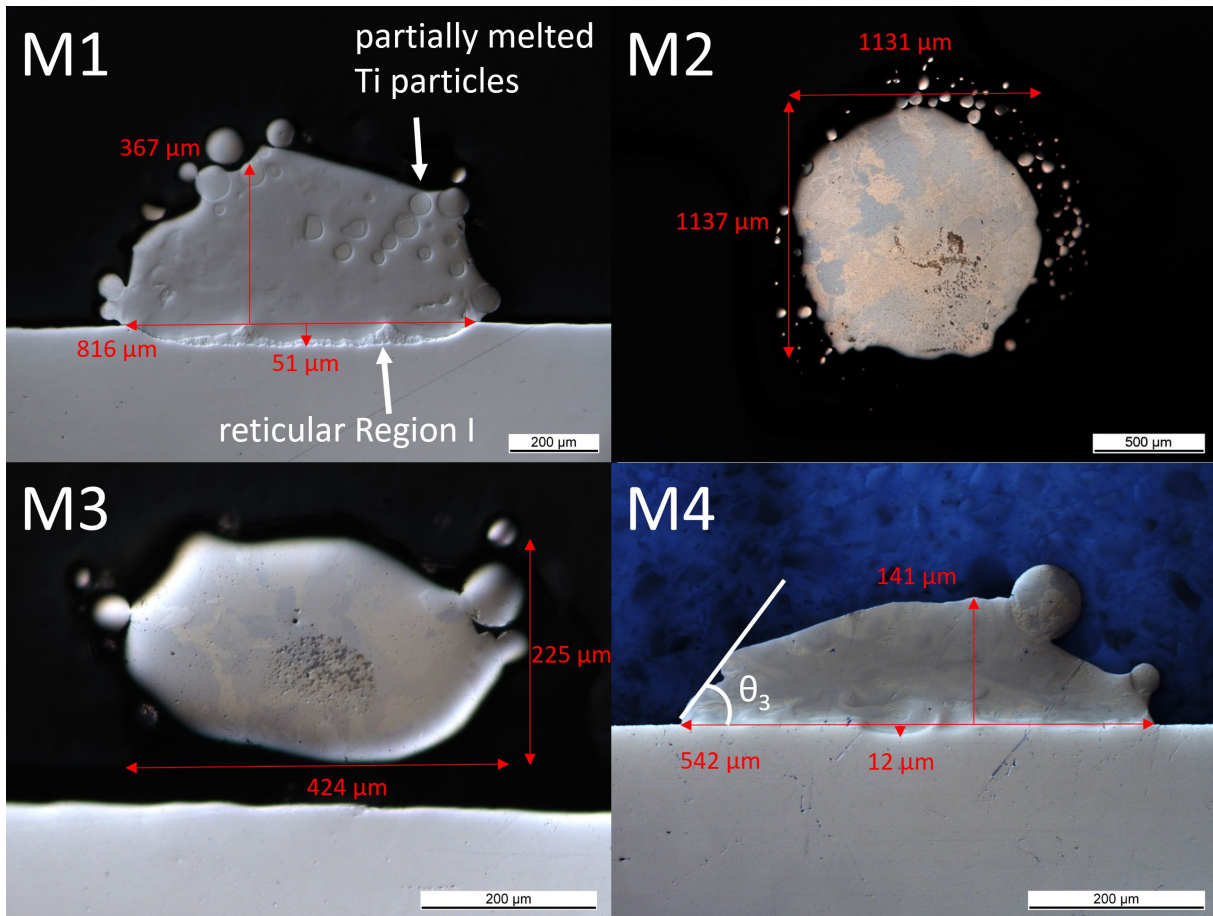


Fig. 6-1. The OM images of the cross-section of the M group single tracks. The acute contact angle in M4 is marked as θ_3 .

6.1.2. Discussion

As the PF increased from 2.5 g/min for Track M1 dramatically to Track M2, the amount of deposited material increased significantly while no penetration has been observed on the substrate. This indicates that more fraction of the laser energy was absorbed by the powder material. The fraction of laser energy absorbed by the substrate was not enough to create a melt pool on it.

Compared with Track M2, Track M3 shows much less deposited material. This is because M3 was deposited with much higher NV, which effectively reduced the powder material supply per unit length. The aspect ratio AR of M3 is $H/D=53\%$, close to suitable for a single track geometry. The substrate was not melted, which is a good sign considering the composition issue. However, the Track M3 is still not bonding with the substrate, indicating insufficient energy input.

The M4 parameter set with doubled LP comparing to M3 seems to have provided enough energy for the melted powder material to collapse and wet the substrate before solidifying. The schematic for the hypothesized powder melting mechanism is shown in **Fig. 4-19**. Track M4 forms a very shallow and uniform interface with the substrate. **Fig. 6-1** shows that the maximum penetration is only 12 μm , indicating that the substrate material is scarce in the solidified melt pool. The acute contact angle makes it promising to deposit adjacent tracks with fewer and smaller voids. Compared with M1, M4 also shows no unmelted particles in the deposition. Therefore, M4 seems to be a good base layer for further depositing a 3D structure on top.

6.1.3. Conclusion

A large increase of the powder feedrate PF dramatically reduced the melting of the 316L substrate due to the interaction between the powder jet and the laser beam. Meanwhile, the nozzle velocity NV had to be increased to avoid building up cylindrical Ti single tracks with little contact and bonding with the substrate. Laser power was increased simultaneously to allow sufficient melting of the powder particles and wetting of the melt on the substrate. Entering the high PF regime has been validated promising for depositing Ti single tracks on 316L substrate with a small melting depth down to 12 μm and an acute contact angle on the edges.

6.2. High powder feedrate single tracks

Far from the conventional process window provided by the DED system manufacturer for depositing bulk Ti, the parameters powder feedrate PF, nozzle velocity NV and laser power LP were tested to the upper limit of the DED system used in this study.

Two series of DED experiments depositing Ti single tracks on 316L substrate were conducted to search for optimal parameter sets in the high powder feedrate regime.

F series: 5 groups with PF increasing from 6 g/min for group Fa to 32 g/min for group Fe. NV increases from 4000 mm/min to 30000 mm/min within each group. LP is 500 W for all tracks.

P series: 5 groups with LP increasing from 300 W for group Pa to 500 W for group Pe. NV increases from 4000 mm/min to 30000 mm/min within each group. PF is 32 g/min for all tracks.

These parameters for the F series and P series are summarized in Table B-1 and Table B-2 in Appendix B, respectively.

Chapter 6. High powder feedrate DED

It is to be noted that that 32 g/min, 30000 mm/min and 500 W are the maximum values of PF, NV and LP on the BeAM DED system.

The high PF single tracks were cut perpendicular to the nozzle scan direction. The cross-sections were polished and observed with OM.

6.2.1. Results

The photos of the as-printed high PF single tracks in groups Fc and Pc are shown in **Fig. 6-2** for example. In group Fc, NV increases from 4000 mm/min for Track Fc_1 to 30000 mm/min for Track Fc_6. It is the same for all groups. In each group, as NV increased, the tracks become more and more discontinuous.

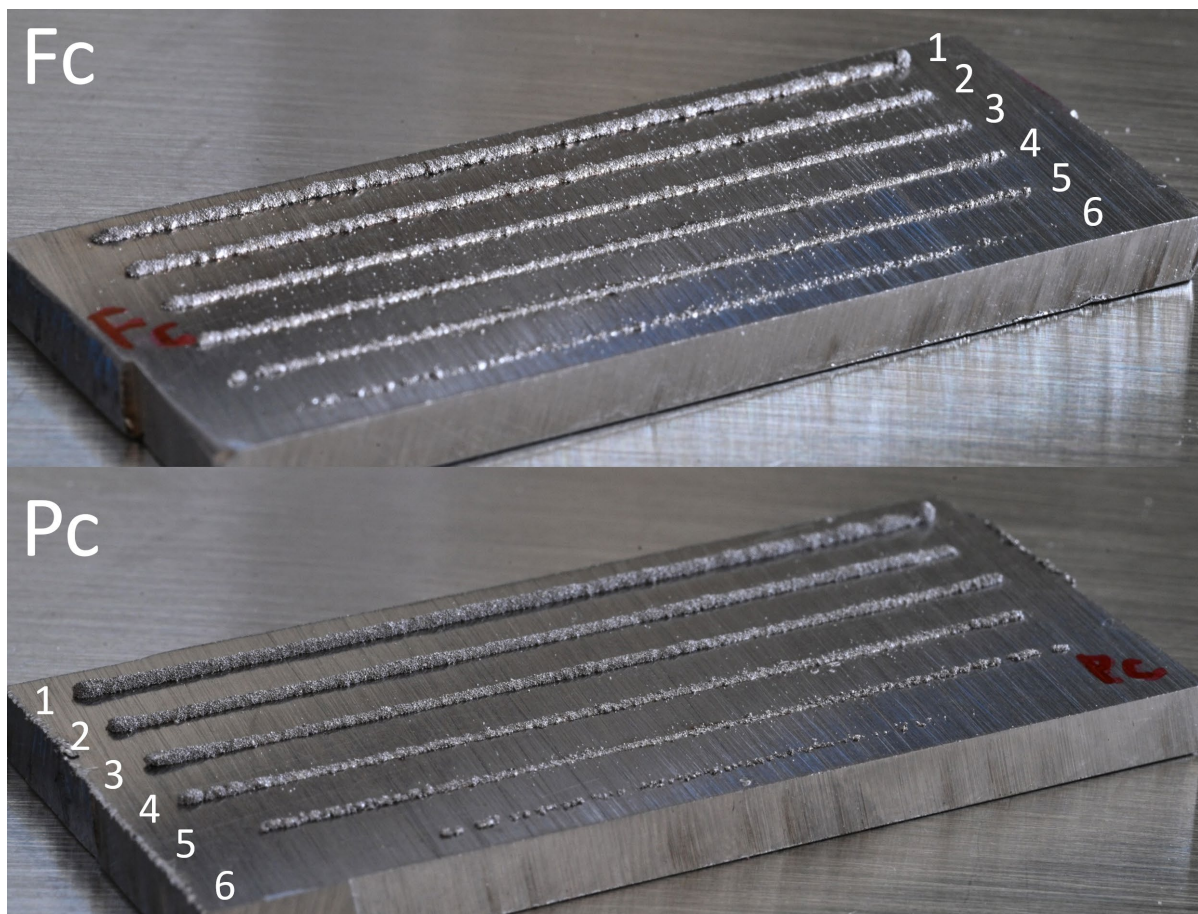


Fig. 6-2. Photos of the as-printed high PF single tracks in groups Fc and Pc.

The cross-sections of samples in groups Fa~Fe imaged with OM are summarized in **Fig. 6-3**. In these F groups, LP is fixed at the maximum value of 500 W for all samples.

In each F group, as NV increases, the amount of deposited material shows a clear decreasing trend. In all F groups, single tracks printed with 30000 mm/min show discontinuity in the photos in **Fig. 6-2**. The OM images of the very small and irregular cross-sections in the last column in **Fig. 6-3** confirm this.

In F samples with the same NV, as the PF increases, the amount of deposited material increases. The adhesion between the deposited tracks and the substrate has a tendency of deterioration too. Taking F samples with NV = 6000 mm/min for example, Fa_2 and Fb_2 form acute contact angles with the substrate. Fc_2 almost forms a right angle with the substrate. Fd_2 and Fe_2 show obtuse contact angles with the substrate and obviously overhanging structures on the lateral sides.

The cross-sections of samples in groups Pa~Pe imaged with OM are summarized in **Fig. 6-4**. In these P groups, PF is fixed at the maximum value of 32 g/min for all samples.

In each P group, as NV increases, the amount of deposited material shows a clear decreasing trend similar to the F groups. In most groups, single tracks printed with 13000 mm/min or a higher NV show discontinuity as can be seen in the photos in **Fig. 6-2**. This observation is also supported by the strongly irregular shape or absence of the cross-section of the tracks in OM images in **Fig. 6-4**.

In P samples with the same NV, as the LP increases, the amount of deposited material slightly increases without a clear trend. The adhesion between the deposited tracks and the substrate also increases, especially in samples with a NV of below 30000 mm/min. Taking P samples with NV = 9000 mm/min for example, Pa_3 and Pb_3 form discontinuous interfaces with the substrate, barely adhering to the it. Pc_3 forms a continuous and flat interface with the substrate. Pd_3 and Pe_3 show further melting into the substrate.

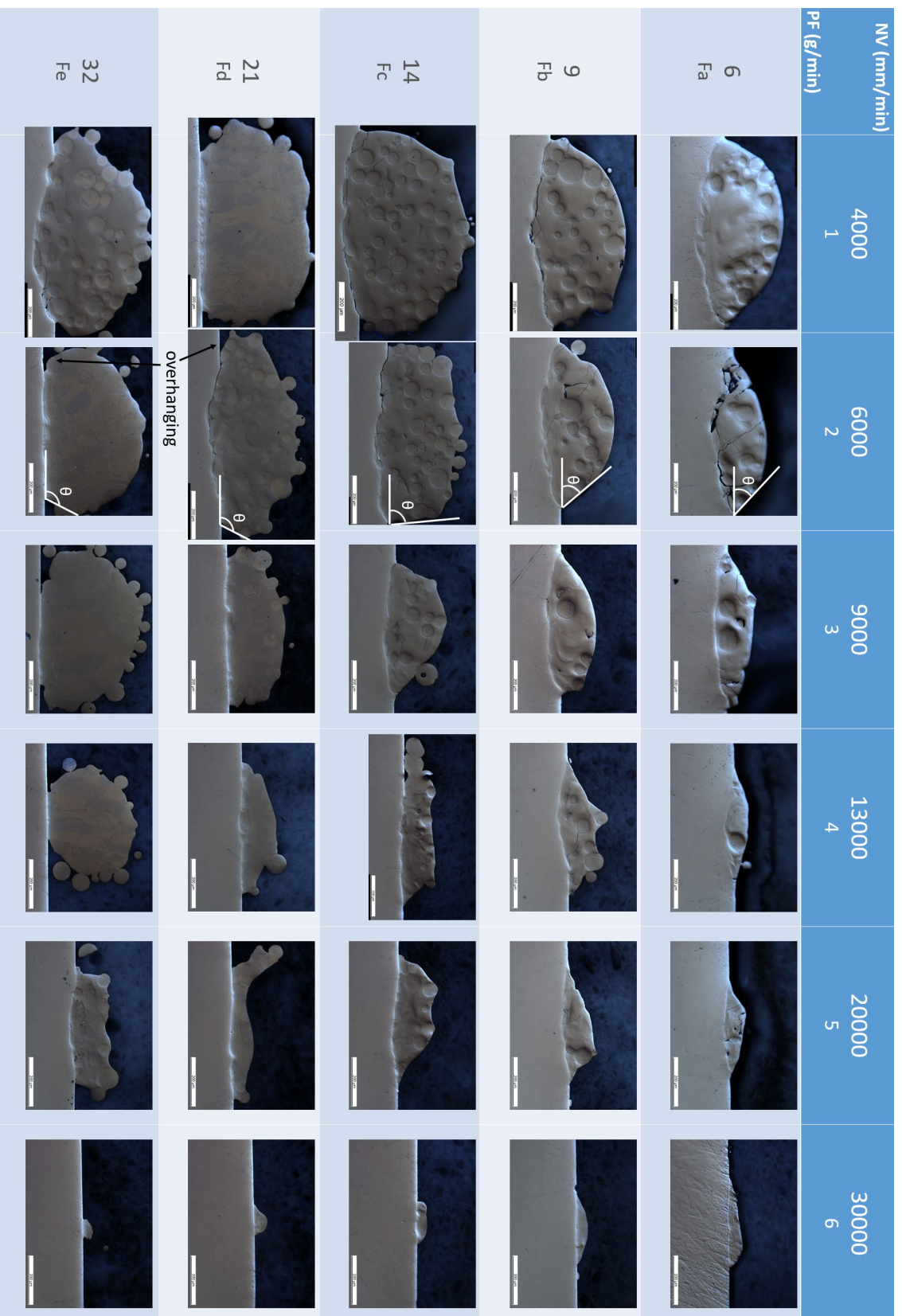


Fig. 6-3. OM images of the cross-sections of samples in groups Fa~Fe. In each group, PF is constant and NV increases from 4000 mm/min to 30000 mm/min. PF increases from 6 g/min in Fa to 32 g/min in Fe. LP is at the maximum value 500 W for all samples.

NV (mm/min)	4000	6000	9000	13000	20000	30000
LP (W)	1	2	3	4	5	6
300 Pa				-		
350 Pb						-
400 Pc						
450 Pd						
500 Pe						

Fig. 6-4. OM images of the cross-sections of samples in groups Pa~Pe. In each group, LP is constant and NV increases from 4000 mm/min to 30000 mm/min. LP increases from 300 W in Pa to 500 W in Pe. PF is at the maximum value 32 g/min for all samples.

Apart from the samples with extremely high NV and irregular shape or almost no deposition like Track Fd_6 and Pb_5, the other tracks can be divided into three types depending on the microstructures.

Track type 1 is represented by Track Fa_1 shown in **Fig. 6-5**. Dendrites are the main microstructure in the deposition. Cracks and partially melted Ti particles are also marked.

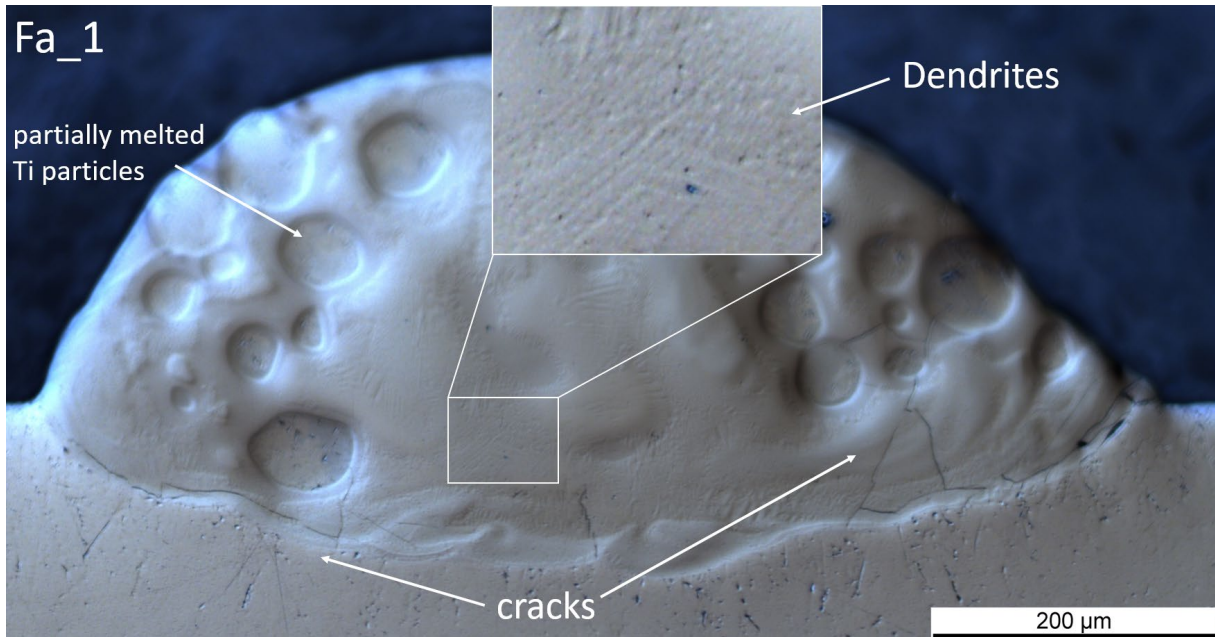


Fig. 6-5. OM image of Track Fa_1.

Track type 2 is represented by Track Fd_1 shown in **Fig. 6-6**. The interface of samples of this type is similar to the interface of the single tracks in Section 4.1.1.3 showing transition type 3 ending with pure Ti. A smooth band takes the place of reticular Region I where it is discontinuous in the lower band. An upper band is observed below the Ti region that makes up the main body of the deposition. The total thickness of the two bands is around 30 μm. Some small vertical cracks are found in the bands.

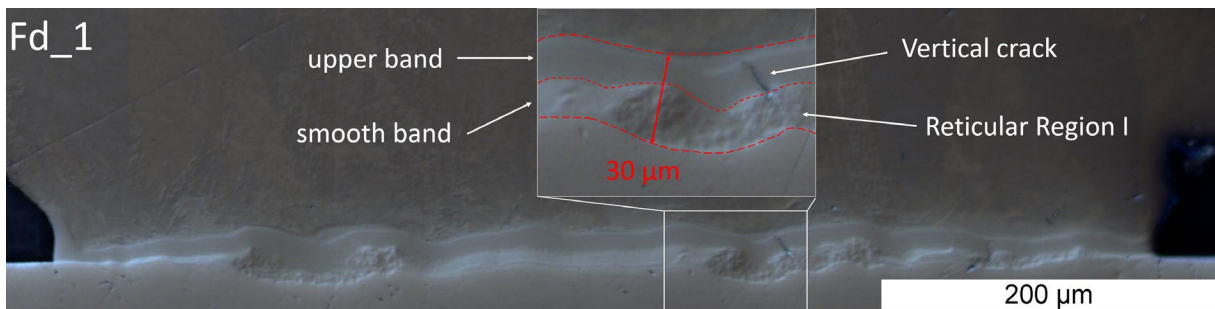


Fig. 6-6. OM image of the interface between track Fd_1 and the 316L substrate. In some parts of the lower band closer to 316L, reticular Region I is observed.

Track type 3 is represented by Track Fd_4 shown in **Fig. 6-7**. Track Fd_4 is completely free from reticular Region I. The interface consists of only the smooth band and the upper band. Both bands are much thinner than in track type 2. The total thickness of the two bands in Track Fd_3 is around 10 μm . A few vertical cracks are also observed within the bands.

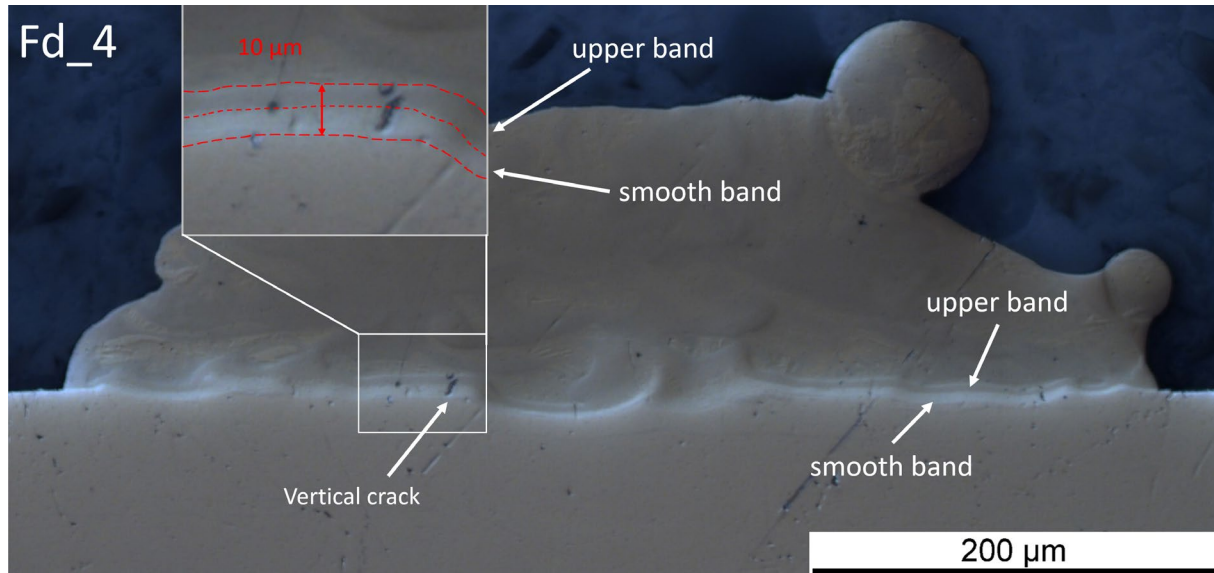


Fig. 6-7. OM image of track Fd_4. Two smooth bands can be observed.

6.2.2. Discussion

The single tracks deposited with extremely high nozzle velocity NV close to 30000 mm/min are unusable due to the poor geometry and amount of deposition. The rest of the tracks fall into three types depending on their microstructures.

In track type 1, the energy absorbed by the substrate was high enough to melt into the substrate. A considerable amount of Fe in the substrate entered the melt pool and formed dendrites that are estimated to be brittle IMCs as have been shown in **Fig. 4-8b**. Cracks propagate easily in the deposition and the interface. This is similar to tracks with transition type 1 and 2 deposited with parameters in the normal DED process window in Chapter 4.

In track type 2, only a small amount of the substrate was melted and two transition bands are observed at the interface. The transition from 316L to Ti was completed within around 30 μm . The upper band is estimated to be supersaturated β -Ti as in Region III shown in **Fig. 4-13**. The band below consists of two structures: the reticular Region I with the $\text{Ti}_5\text{Fe}_{17}\text{Cr}_5$, Fe_2Ti and FeTi IMCs and the smooth sections estimated to be $\text{Ti}_5\text{Fe}_{17}\text{Cr}_5$. Such IMC phases have been reported to be found in the interface between laser welded titanium alloy and stainless steel too ^[28].

In track type 3, the melting of the substrate is even less and two bands are observed at the interface similar to track type 2. The difference is that the lower band in type 3 tracks is completely smooth without reticular Region I. It takes only around 10 μm to transition from 316L to $\beta\text{-Ti}$ with $\text{Fe}<22$. The transition in these tracks is the most abrupt thanks to the very small melting depth of the substrate.

Small vertical cracks are seen only constrained in the interfacial bands in track type 2 and type 3. Connection of cracks is thus avoided and catastrophic cracking that can detach the deposition from the substrate does not happen. The cracks do not tend to propagate parallel to the interface and could indicate improved bonding.

In order to print a continuous layer consisting of parallel single tracks with good bonding with the substrate, the single track need to fulfill two requirements

1. In terms of the geometry, if the deposition is too high and forms obtuse angles with the substrate, the space near to the foot of the deposition can not be filled by the next track. This has been illustrated in **Fig. 4-16** in Section 4.1.2.2. In the studied parameter range where the laser hardly melts the substrate, the space is even more difficult to fill. Therefore, the single track needs to form an acute contact angle with the substrate.

2. In terms of the interface morphology, as IMCs cannot be completely avoided anyway, tracks showing two continuous thin bands without reticular regions are preferred. Brittle IMCs are mostly reduced this way.

Basing on the geometric and interface criteria, several parameter sets for the high PF single tracks were selected for depositing continuous single layers as the basis for printing 3D Ti structure on 316L substrate.

6.3. High powder feedrate single layer with cuboids on top

In the high PF single track experiments in Section 6.2, six single tracks forming acute contact angles with the substrate and showing an interface consisting of two continuous thin bands (Pd_3, Pe_4, Pe_5, Fc_5, Fd_3 and Fd_4) have been produced. As the stress condition would be different from single tracks to applicable 3D structures, the parameter sets for these single tracks were then used to deposit single layers. On top of each single layer, Ti cuboids were deposited with the reference parameters for pure Ti on Ti substrate provided by the DED system manufacturer. The aim is to validate the interface strength given by the selected parameter sets in the case of real 3D structure deposition.

The parameters for depositing the selected single layers described are summarized in Table 6-2. The hatch spacing HS was selected as 75% of the measured width of each single track. The reference parameters for printing the Ti cuboids are also summarized in the last row.

Table 6-2. Parameters for the Ti single layers. Reference parameters for the Ti cuboids on top are in the last row.

Group	Sample No.	LP (W)	NV (mm/min)	PF (g/min)	HS (mm)	ΔZ (mm)
Pd	3	450	9000	32	0.459	-
Pe	4	500	13000	32	0.425	-
	5	500	20000	32	0.392	-
Fc	5	500	20000	14	0.358	-
Fd	3	500	9000	21	0.500	-
	4	500	13000	21	0.431	-
Cuboid	-	325	2000	4	0.500	0.200

For each parameter set:

1. Cross-sections of the part with solely the layer and the part with the Ti cuboid on top were prepared for observation with OM, SEM and EDS.

2. Five identical specimens of the cuboid on the single layer were extracted by EDM for shear tests. The schematic of the top view of the deposition layout and cutting plan is shown in **Fig. C-1** in Appendix C.

These samples are referred to as room temperature RT samples.

Residual stress level can play a crucial role at the interface. As heating processes can significantly alleviate the residual stresses and lessen cracks ^{[110] [111] [112]}, the same layers with cuboids on top were also deposited with preheating and controlled cooling. These samples are referred to as high temperature HT samples. Before printing the HT samples, the 316L substrate was fixed on a hot plate, preheated to 520°C and kept at this temperature for 1 h. After all samples were printed, the substrate was kept at 520°C for another 1 h, and then cooled down at 25°C/5min to room temperature. They were prepared the same way as the RT samples for cross-section observation and shear tests.

6.3.1. Results

Fig. 6-8 shows two cuboids deposited on two different single layers. These samples were cut off from the substrate at the single layer. The geometry of the layers and cuboids generally

conform to the designed geometry of $7 \times 80 \text{ mm}^2$ and $5 \times 5 \times 3 \text{ mm}^3$. There is slight over-deposition on the sides of the cuboids that does not influence the interface investigated.

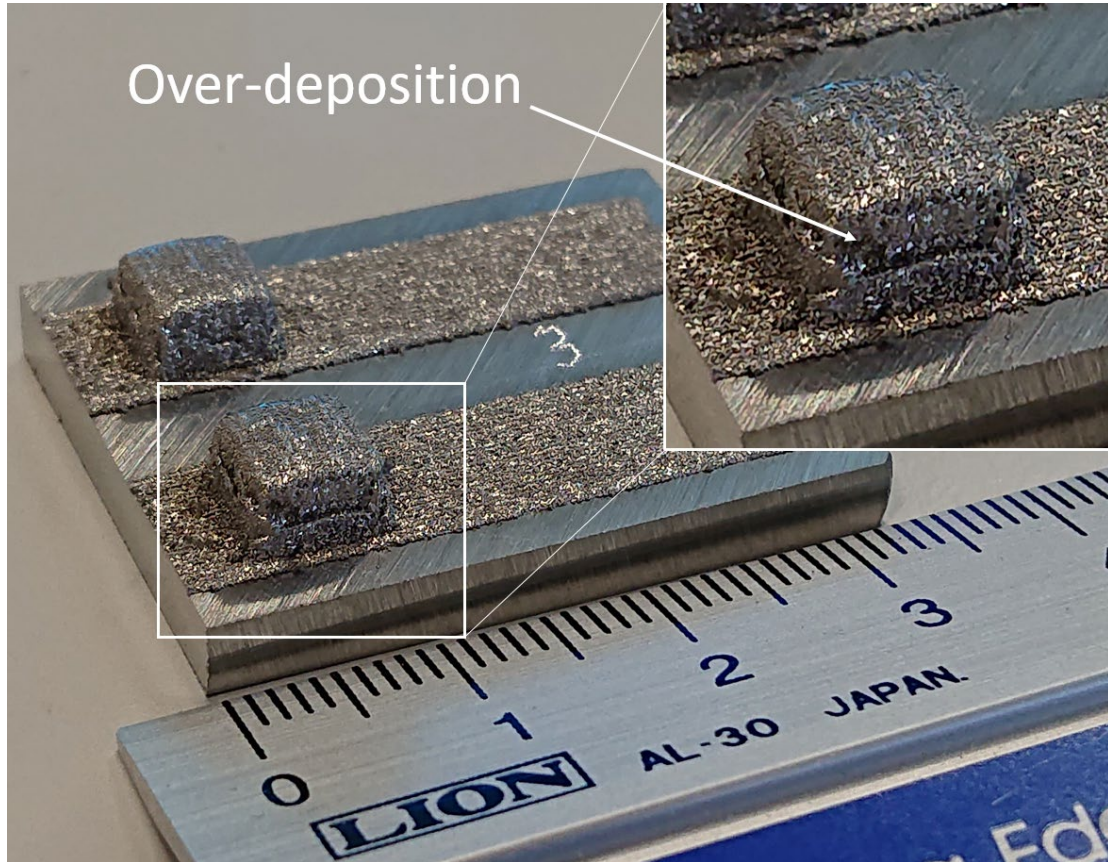


Fig. 6-8. Two Ti cuboids deposited on different Ti single layers on the 316L substrate.

6.3.1.1. Interface Morphology

All single layers show a good adherence to the 316L substrate and many cuboid samples delaminate at the interface after mechanical cutting. The single layer and cuboid samples produced under different temperature conditions with the same parameter set can behave differently at the interface with the substrate. The samples produced with the Fd_4 parameter set were investigated as an example.

The OM images of the Ti-316L interface in single layer RT_Fd_4, cuboid RT_Fd_4, single layer HT_Fd_4 and cuboid HT_Fd_4 are shown in **Fig. 6-9**. Layers RT_Fd_4 and HT_Fd_4 both show a good adherence to the substrate. Some small vertical cracks are however observed in RT_Fd_4. Cuboid RT_Fd_4 delaminated from the substrate at the interface, while the preheated HT_Fd_4 shows a good adherence with the substrate. Partially melted Ti particles and inter-track voids are observed in the first layer in almost all samples.

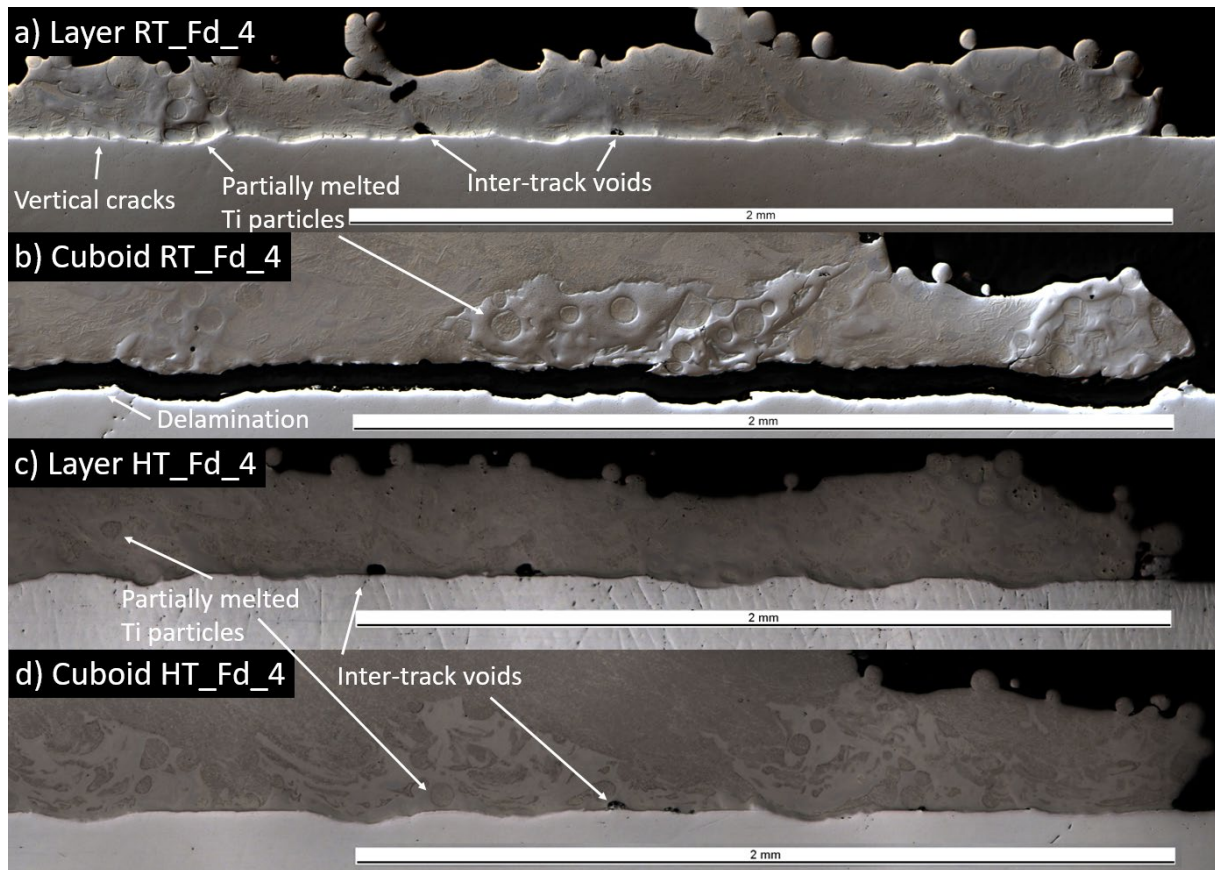


Fig. 6-9. OM images of the Ti-316L interface in a) single layer RT_Fd_4, b) cuboid RT_Fd_4, c) single layer HT_Fd_4 and d) cuboid HT_Fd_4.

A SEM image of the interfacial area in single layer HT_Fd_4 is shown in **Fig. 6-10**. An EDS line scan was performed along the green line and the results are shown on the right. At the bottom is the 316L substrate. Above the 316L substrate is a smooth band of $Ti_5Fe_{17}Cr_5$ IMC with a thickness below $2\ \mu m$. The reticular Region I as has been described in **Fig. 4-8a** occurs above the $Ti_5Fe_{17}Cr_5$ layer occasionally as small islands. EDS point analysis shows that the phases in the reticular region are $Ti_5Fe_{17}Cr_5$, Fe_2Ti and $FeTi$ IMCs, also conforming to the results in the single track trials. Above the smooth band is a band with the same characteristics as the upper band of Region III in **Fig. 4-13**. This upper band has a composition of $Fe_{22\sim 29}$ and the phase is identified as supersaturated β -Ti. Like single layer RT_Fd_4 shown in **Fig. 6-9a**, vertical cracks at the interface of all samples stop at the upper border of upper band. Above the upper band, the Fe composition drops abruptly into a range of $Fe_{8\sim 22}$ and then even lower, corresponding to β -Ti. Above a few or tens of microns of β -Ti, the transition to pure Ti is completed.

6.3.1.2. Transition distance

According to previous studies on joining of Ti(-alloys) and steels [48], it is expected that a shorter transition distance will give a better interface strength. The distance it takes to transition from the 316L substrate to the upper border of the upper band was measured on the results from EDS line scans. The transition distance is measured from the point where Fe concentration starts dropping to where it reaches Fe22. The ranges in chemical composition and corresponding area are marked with the red boxes in the EDS result and the SEM image in **Fig. 6-10**. The transition distance in single layer HT_Fd_4 is measured to be around 10 μm in the location marked in **Fig. 6-10**.

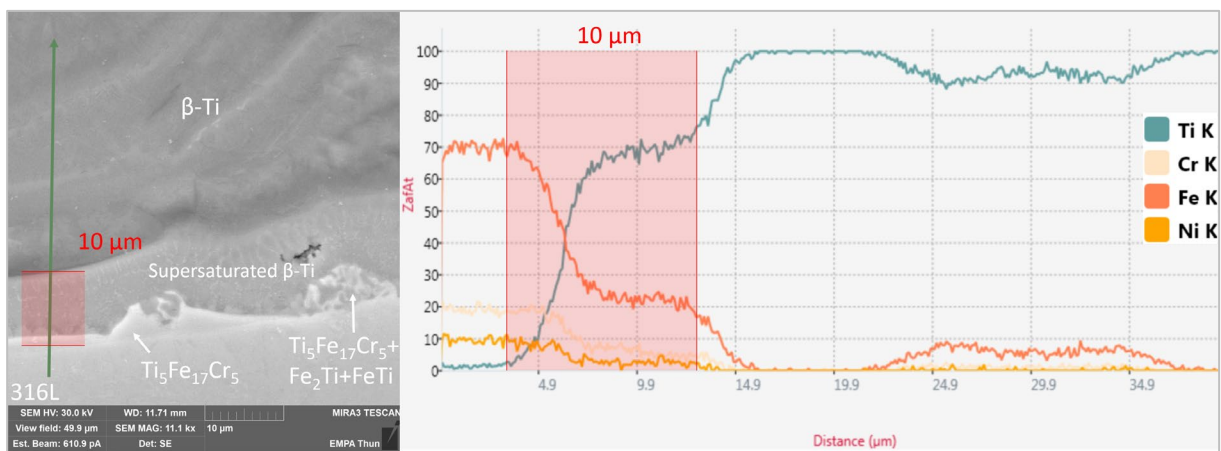


Fig. 6-10. SEM image of the Ti-316L interface in single layer HT_Fd_4. The chemical composition profile along the green line is shown on the right. The red boxes mark the area and range of Fe22~100.

The transition distance in the single layer and cuboid samples fabricated under RT and HT conditions are summarized in **Fig. 6-11**. In most samples, the transition distance is below 18 μm . There seems to be a very slight increase in transition distance in cuboid samples than in layer samples. The transition distance in HT samples are slightly higher than that in RT samples as well.

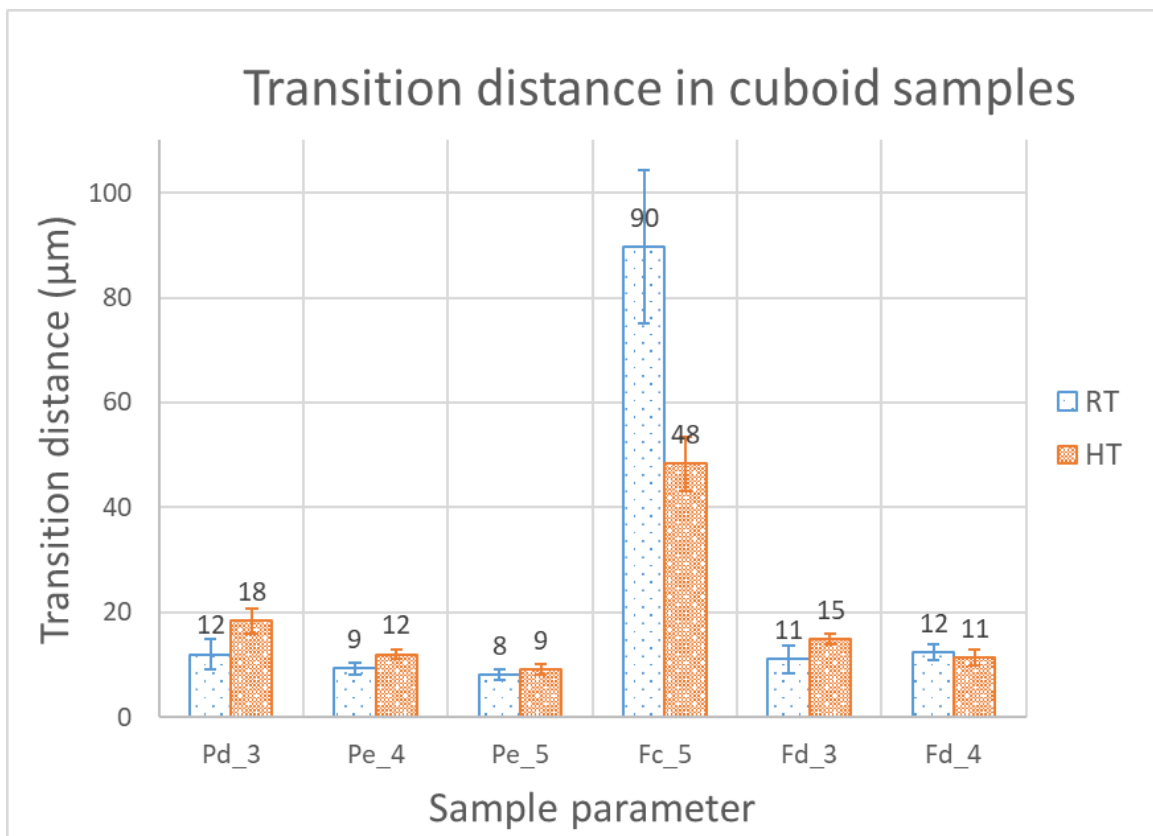
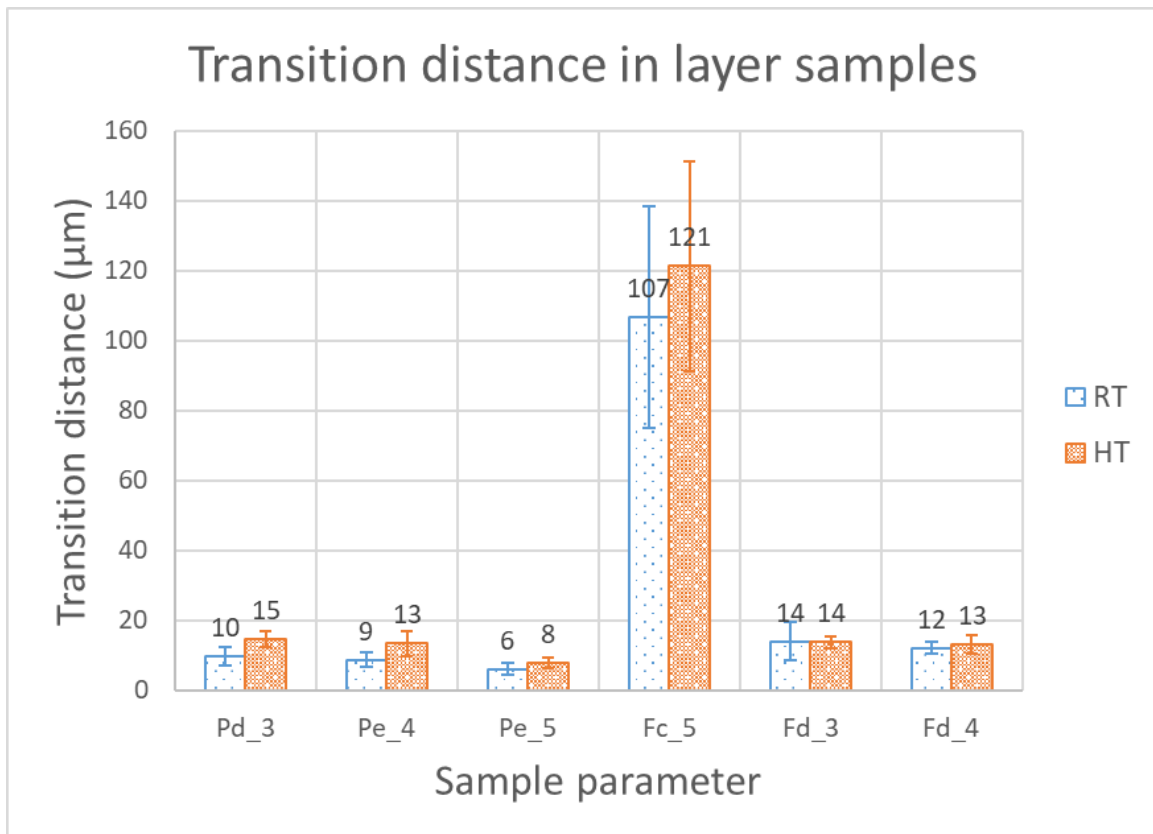


Fig. 6-11. The transition distance in the single layer and cuboid samples fabricated with RT and HT conditions.

Samples printed with the Fc_5 parameter set exhibit significantly larger transition distance than the others. **Fig. 6-12a.** shows the interface in cuboid HT_Fc_5 for example. **Fig. 6-12b** is a high magnification image of the area marked with the white box in **Fig. 6-12a**. Partially melted Ti particles are observed close to the bottom of the deposition. Areas with similar microstructures to Region IV and Region III as described in **Fig. 4-8** are marked in **Fig. 6-12b**. According to the EDS results, the Fe22 border is marked with the red broken line. The distance between the 316L substrate and the Fe22 border is roughly 50 μm .

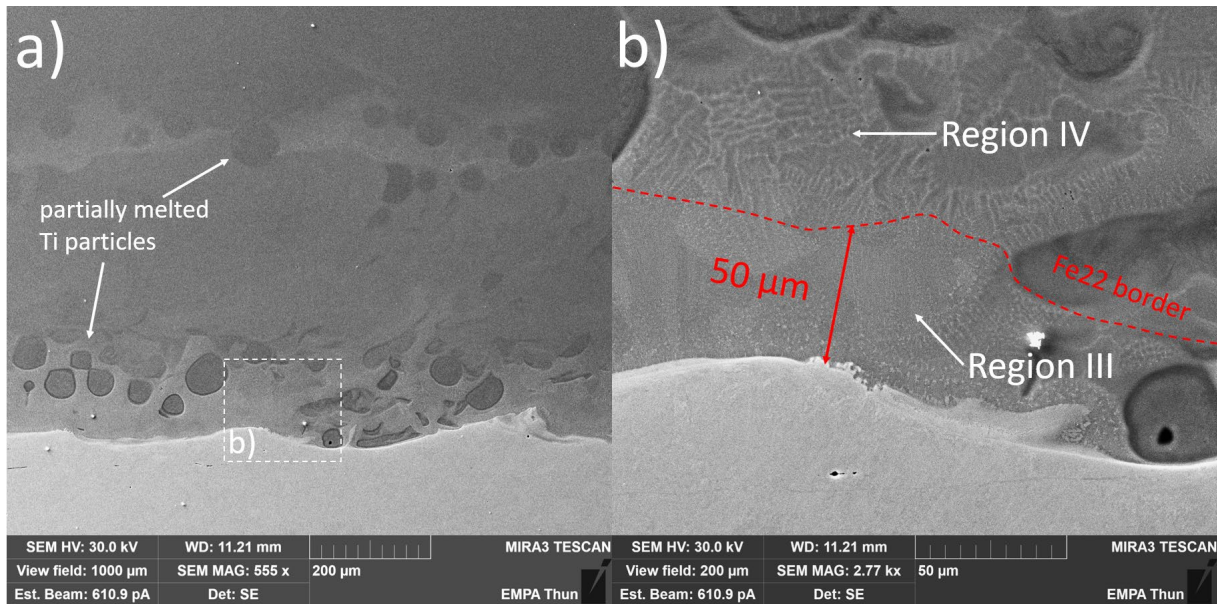


Fig. 6-12. SEM image of the Ti-316L interface in cuboid HT_Fc_5. The Fe22 border is marked with red broken curves. b) is the area marked with the white box in a).

There is no significant influence of the added cuboid on the transition distance when comparing to the single layer samples.

There is not a clear correlation between the transition distance and the printing parameters LP, NV and PF in general. However, cuboids Pd_3, Pe_4 and Pe_5 printed with both the RT and HT conditions show that the transition distance decreases with increasing NV.

Preheating generally resulted in a slight increase of the transition distance.

6.3.1.3. Ultimate shear strength

5 identical cuboid specimens were produced for each condition. The cuboid samples were cut with EDM to particularly avoid inflicting crack initiation at the cross-sections. The EDM-cut samples were characterized with shear tests for the strength of the interface. The pressure head

of the shear tester was positioned as close to the substrate surface as possible, but not touching the top of the first layer in each sample.

Photos of four sheared specimens RT_Pe_4, RT_Fd_4, HT_Pe_4 and HT_Fd_4 are shown in **Fig. 6-13** for example. It can be noted that there is almost no shear between the cuboid and the first layer in the RT samples. Obvious shear between the cuboid and the first layer in the HT samples is observed.

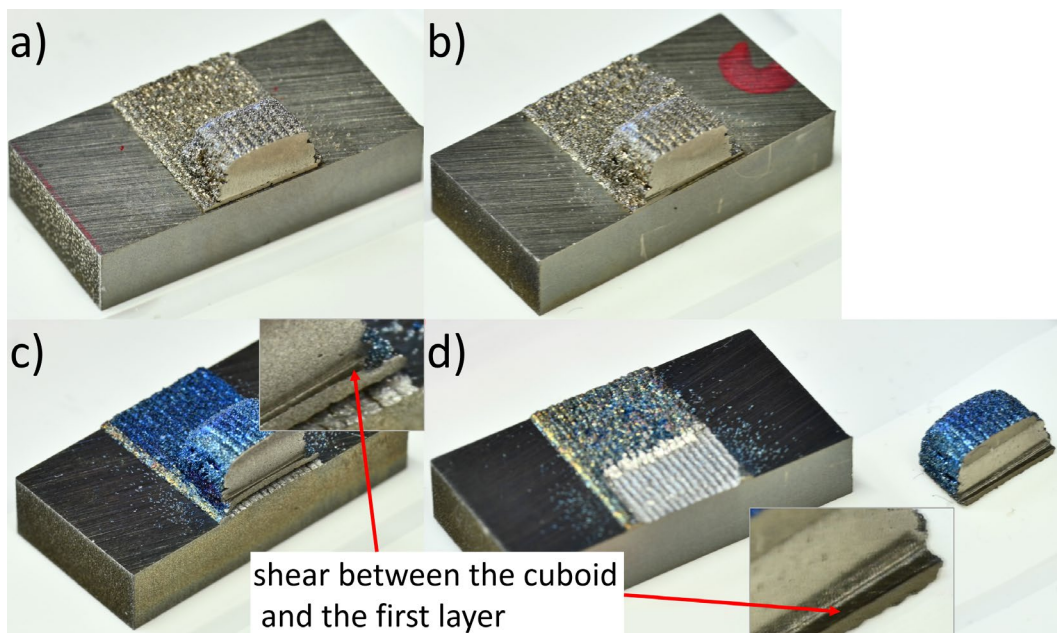


Fig. 6-13. Specimens after shear test: a) RT_Pe_4, b) RT_Fd_4, c) HT_Pe_4 and d) HT_Fd_4.

Fig. 6-14 shows the shear force - displacement curves obtained from the four specimens RT_Pe_4, RT_Fd_4, HT_Pe_4 and HT_Fd_4 for example. Both HT specimens reached much higher shear force than the RT specimens. The maximum shear forces are 2559 N, 4069 N, 7939 N and 9897 N respectively. The two RT specimens failed immediately the shear force reached the maximum value. The two HT specimens failed shortly after the shear force reached the maximum value and started decreasing.

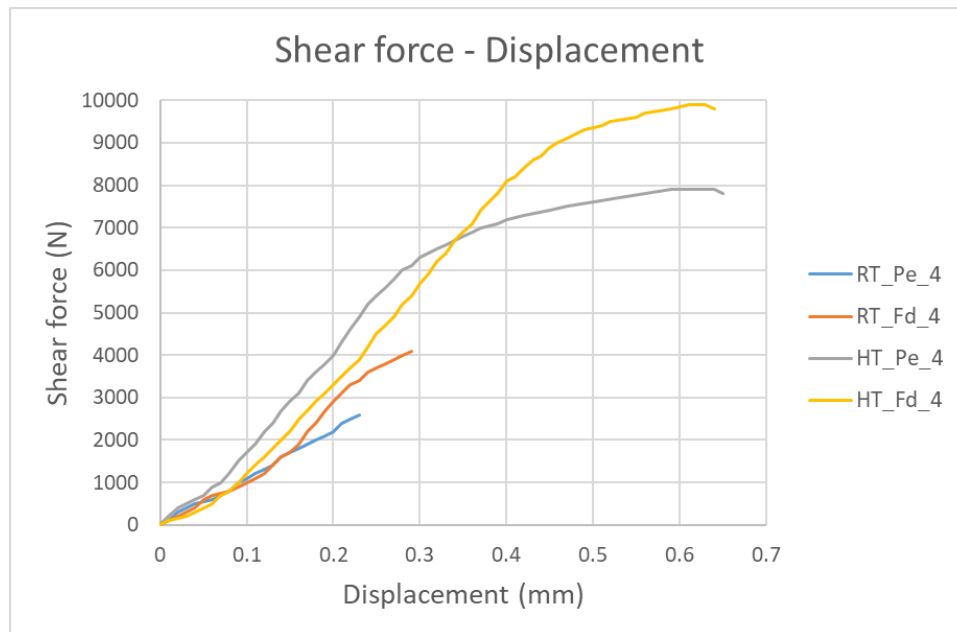


Fig. 6-14. Shear force - displacement response of four specimens RT_Pe_4, RT_Fd_4, HT_Pe_4 and HT_Fd_4.

The maximum shear forces F_{max} of all samples are summarized in **Fig 6-15**. Delaminated surface area A was measured for each sample and fall in a range of 24~70 mm². The ultimate shear strength is calculated as $USS = F_{max}/A$ (in Section 3.3.8) and also summarized in **Fig. 6-15**. The USS of the RT samples are in a range of 45~153 MPa. The HT samples have significantly higher USS in a range of 173~381 MPa. The interface in HT_Fd_4 cuboids have the highest USS of 381±24 MPa, higher than the weaker base material pure Ti (371 MPa^[113]) but lower than 316L (517 MPa^[114]).

Cuboid samples Pd_3, Pe_4 and Pe_5 printed with both the RT and HT conditions show that the USS increased with decreasing transition distance, also with increasing NV. But there is no clear correlation between the USS and the transition distance in all cuboid samples in general. HT_Fc_5 with the relatively high USS and largest transition distance indicates that the transition distance may not be crucial for the USS.

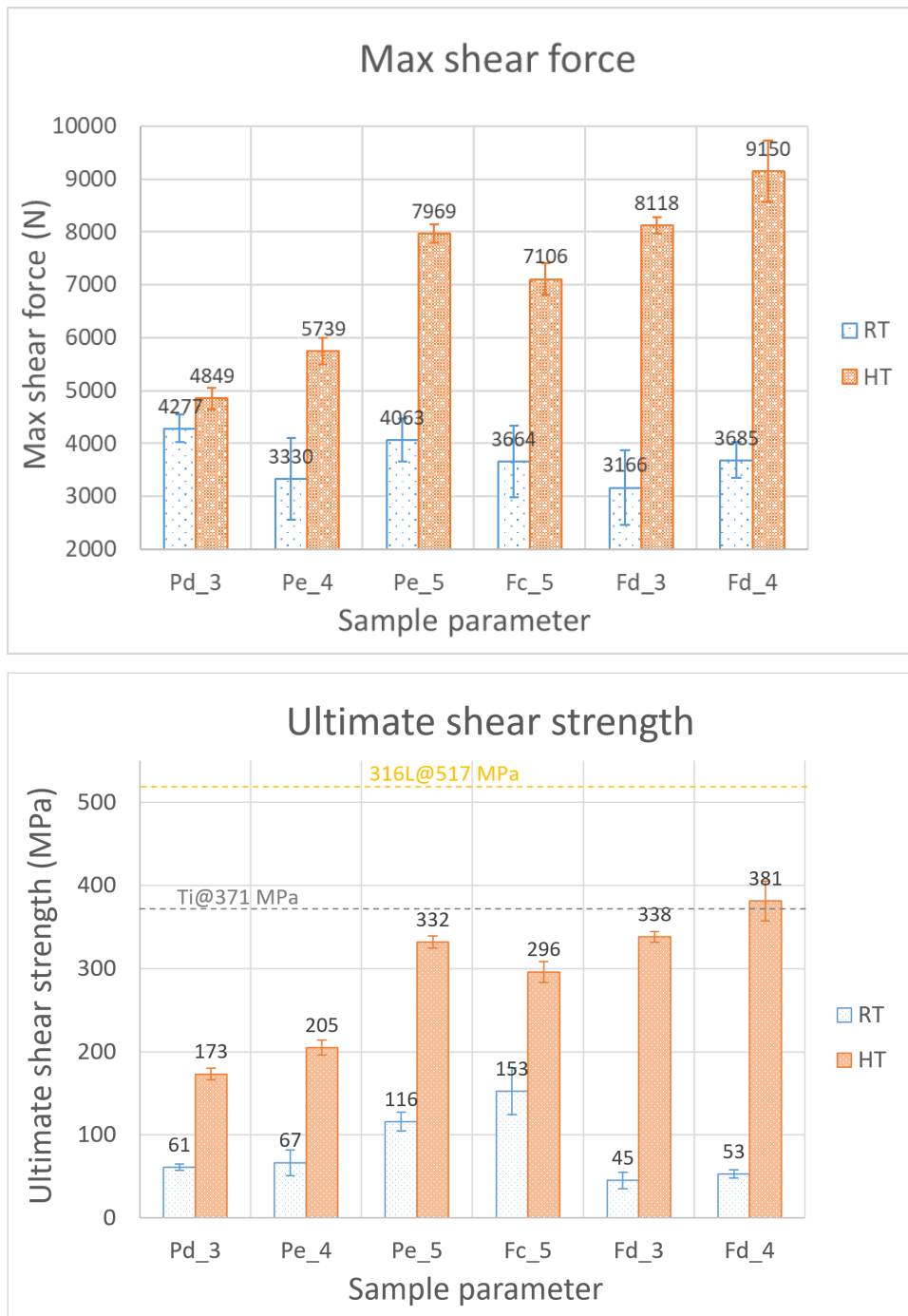


Fig. 6-15. The maximum shear force and ultimate shear strength measured from the cuboid samples.

6.3.1.4. Macro failure features

Three macro failure features have been observed in the sheared cuboids.

- i. Shear between the cuboid and the top of the first layer;
- j. Detachment of the bottom of the first layer (with the cuboid on top) from the substrate;

k. Detachment of the single layer part (without the cuboid on top) from the substrate.

Three combination of the failure features **ij**, **j** and **jk** are concluded. Three samples are shown in **Fig. 6-16** to demonstrate the combinations of failure features.

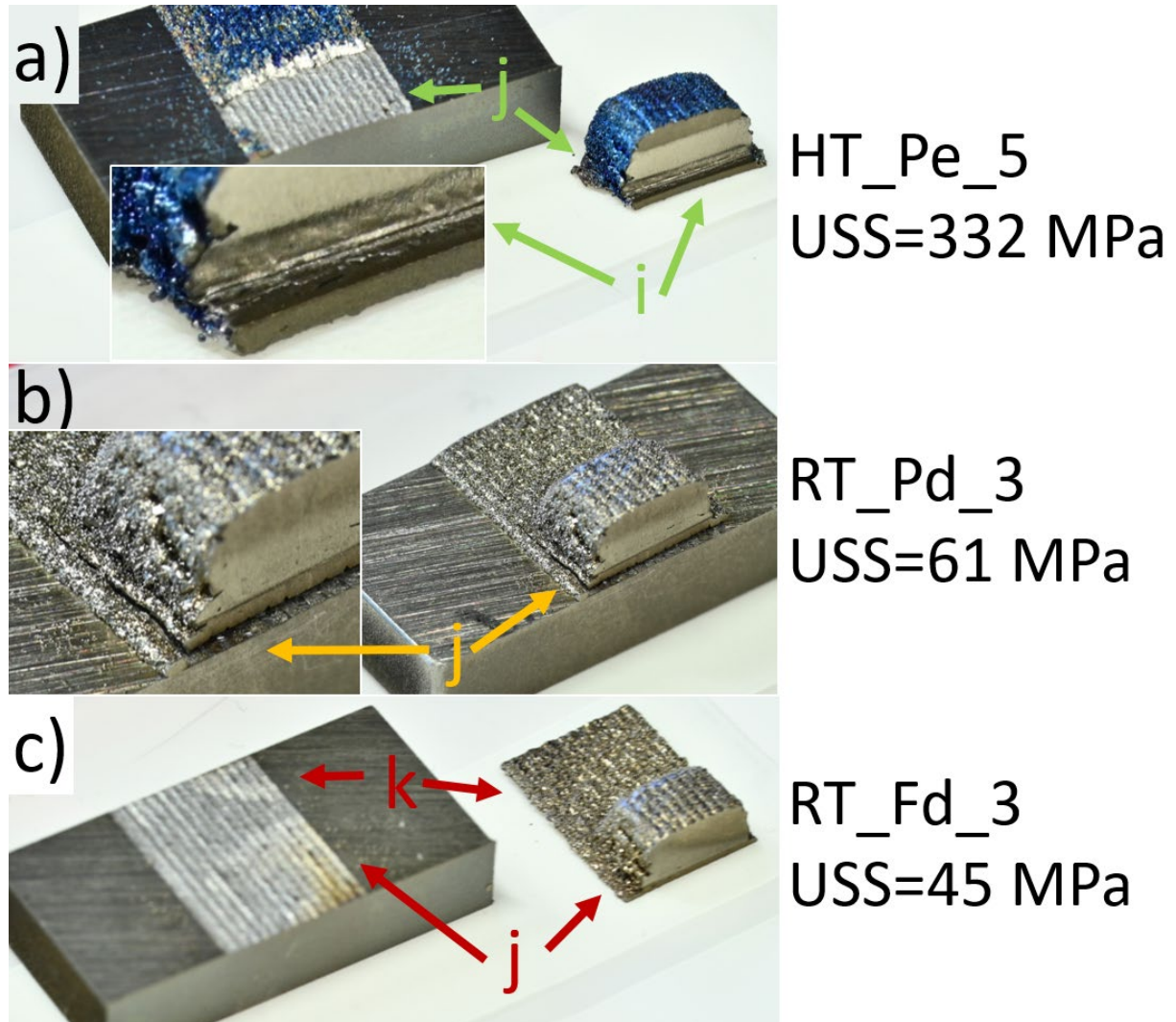


Fig. 6-16. Cuboid samples with their failure features marked. a) HT_Pe_5 with features **ij** and USS=332 MPa, b) RT_Pd_3 with feature **j** and USS=61 MPa, c) RT_Fd_3 with features **jk** and USS=45 MPa.

The presence of the failure feature combinations are summarized in Table 6-3 with the ultimate shear strength USS of the samples. Samples with feature combinations **ij**, **j** and **jk** are marked in green, yellow and red, respectively. In some HT_Fd_3 samples, only feature **i** is observed. A HT_Fd_3 specimen is shown in **Fig. 6-17** as an example with only feature **i**.

Table 6-3. The USS and combinations of failure features in the cuboid samples after shear tests.

Printing conditions		USS (MPa)	i	j	k
RT	Pd_3	61	-	√	-
	Pe_4	67	-	√	-
	Pe_5	116	-	√	-
	Fc_5	153	-	√	-
	Fd_3	45	-	√	√
	Fd_4	53	-	√	√
HT	Pd_3	173	-	√	-
	Pe_4	205	√	√	-
	Pe_5	332	√	√	-
	Fc_5	296	√	√	-
	Fd_3	338	√	some	-
	Fd_4	381	√	√	-

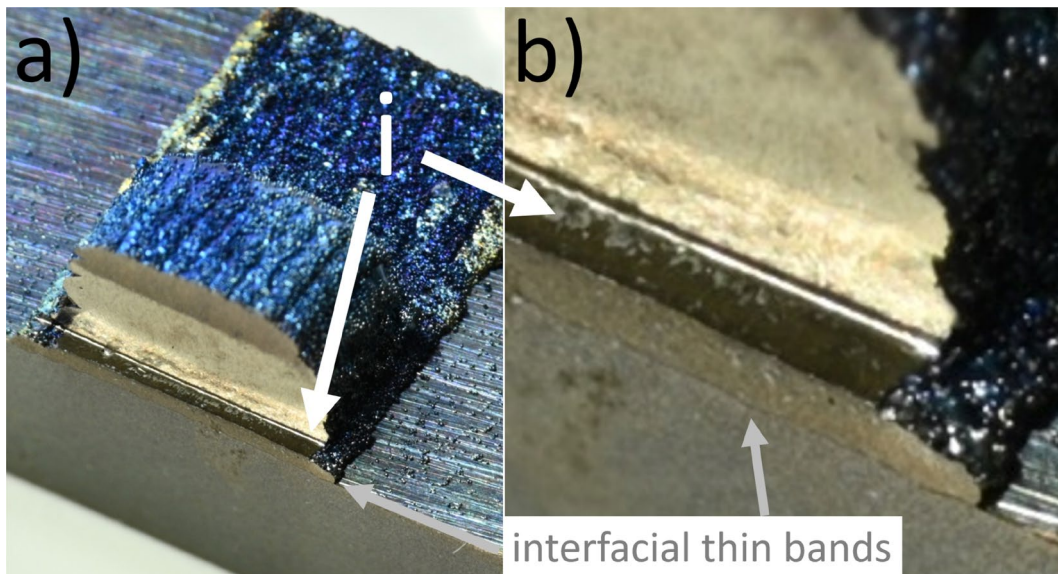


Fig. 6-17. A Cuboid HT_Fd_3 specimen with its failure feature **i** and the interfacial thin bands. USS=338 MPa.

6.3.1.5. Microstructure and chemical composition

The top view of a shear fractured HT_Pe_4 specimen is shown in **Fig. 6-18a**. The two steps formed during the shear test can be seen. The upper and lower steps correspond to features **i** and **j**, respectively. High magnification images taken from the small boxes on the two steps are shown in **Fig. 6-18b** and **Fig. 6-18c** respectively. **Fig. 6-18d** shows fluted fracture on the upper step. **Fig. 6-18e** shows cleavage and micro cracks.

Periodic fracture features with the same interval as the hatch spacing are observed on the lower step and marked in **Fig. 6-18c**. EDS point analysis shows that the composition on these periodic fracture features is around Fe93. These fractures are estimated to be the naked 316L substrate under the inter-track voids.

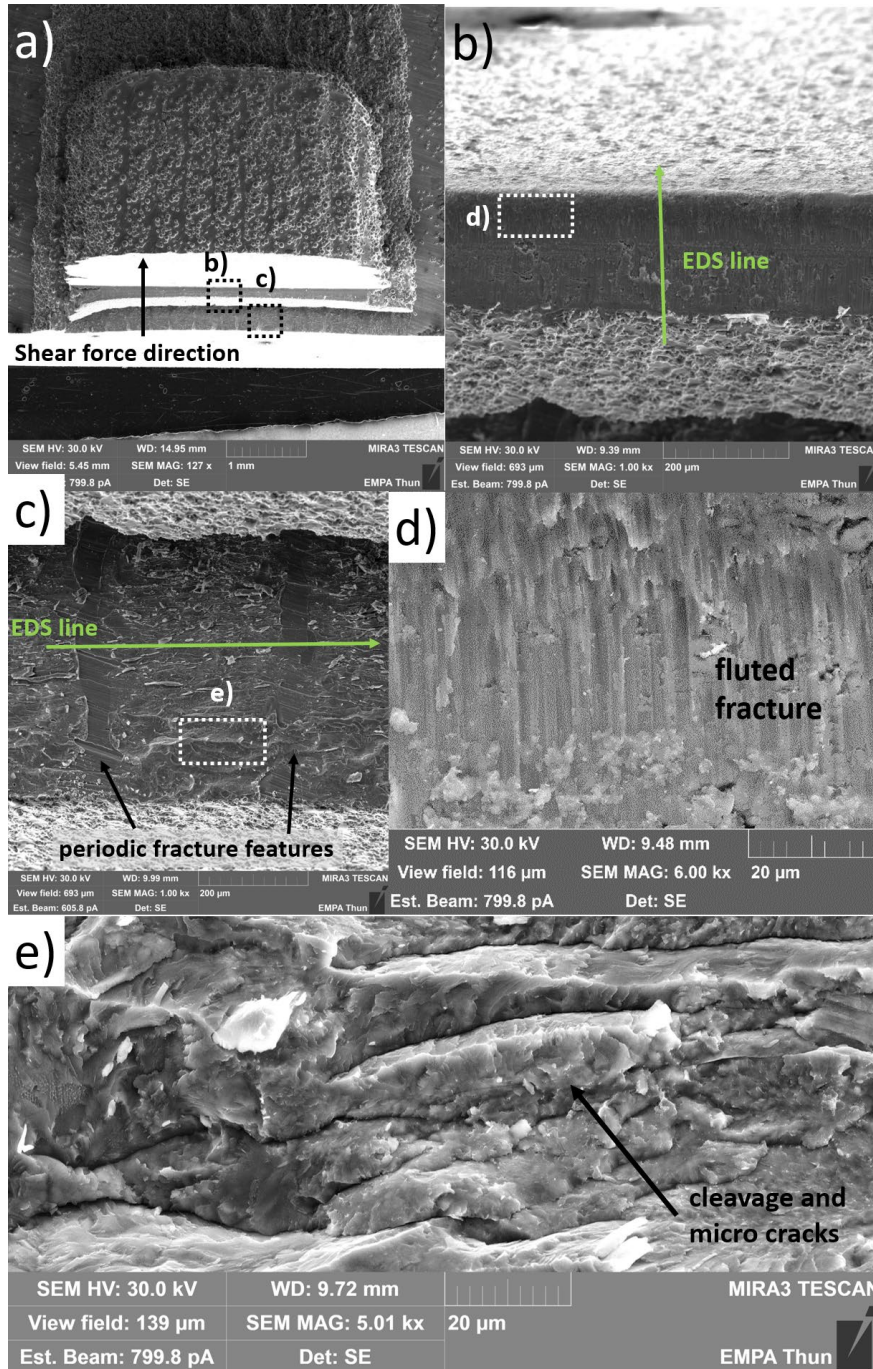


Fig. 6-18. a) Top view of a shear fractured HT_Pe_4 specimen. b) high magnification image of feature i, the shear between the cuboid and the first layer, c) high magnification image of feature j, the detachment of the first layer from the substrate. d), e) high magnification images of the areas marked in b) and c) respectively.

EDS line scans were performed along the green lines in **Fig. 6-18b** and **Fig. 6-18c**. The EDS results are shown in **Fig. 6-19a** and **Fig. 6-19b** respectively. The upper step (feature i) consists

of almost pure Ti, and this applies to all samples with feature **i**. The composition on the surface of the lower step (feature **j**) fluctuates in a large range of Fe18~88 in areas except the periodic fracture features. The periodic fracture features are marked with grey overlay and not considered in subsequent EDS results or discussion, because they are not the main form of interface between the deposition and the substrate.

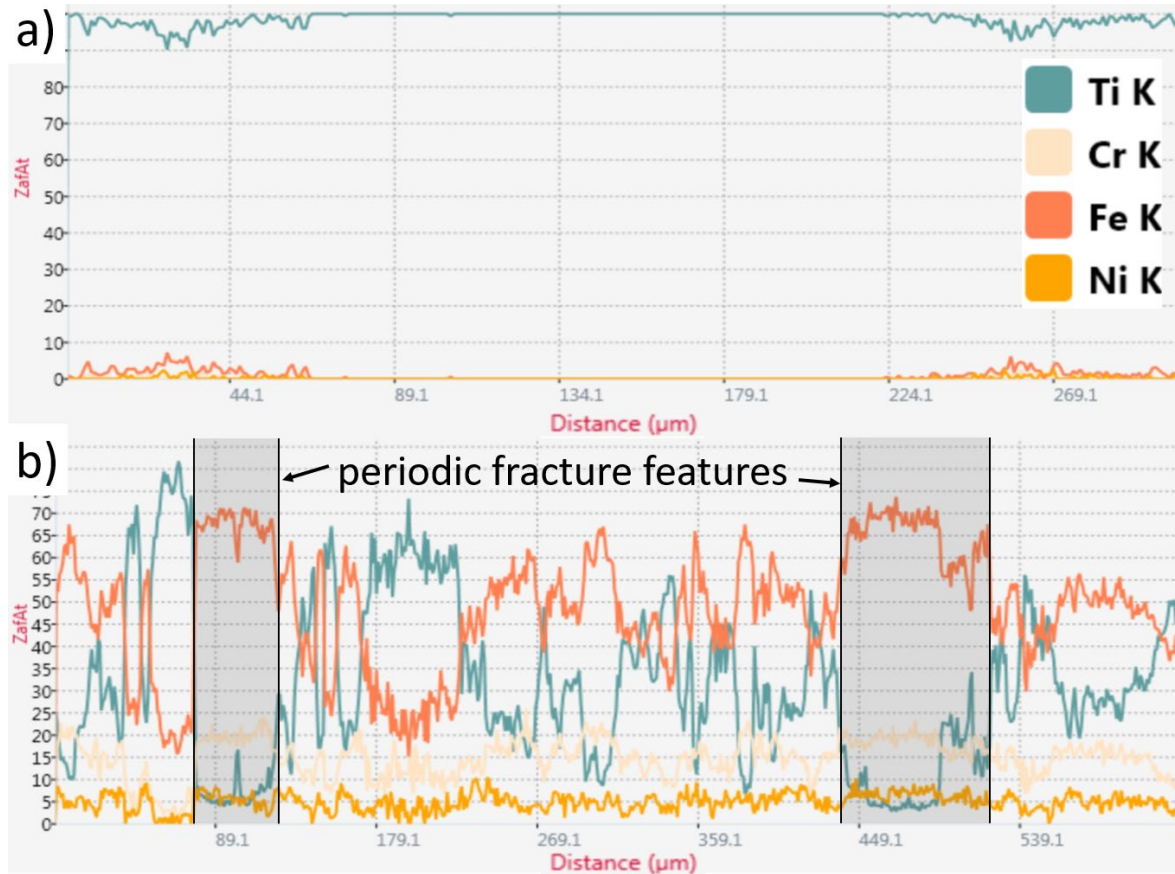


Fig. 6-19. a) and b) are the EDS line scan results from the green lines in Fig. 6-18b and Fig. 6-18c in HT_Pe_4, respectively. The periodic fracture features are marked with grey overlay.

Fig. 6-20 shows the results of EDS line scans on the 316L side of the fracture surface (i.e. the lower step in feature **j**) of six samples RT/HT_Pe_4, RT/HT_Fd3 and RT/HT_Fd_4. The results from the RT samples with $USS \leq 67$ MPa show lower fraction of Fe-rich phases in the fracture surface than the HT samples with $USS \geq 205$ MPa. There is also a trend in the HT samples that the higher the USS, the higher the fraction of Fe-rich phases in the fracture surface. In HT_Fd_4, which has the highest USS in this study, Fe-rich phases dominate the fractured surface on the 316L side.

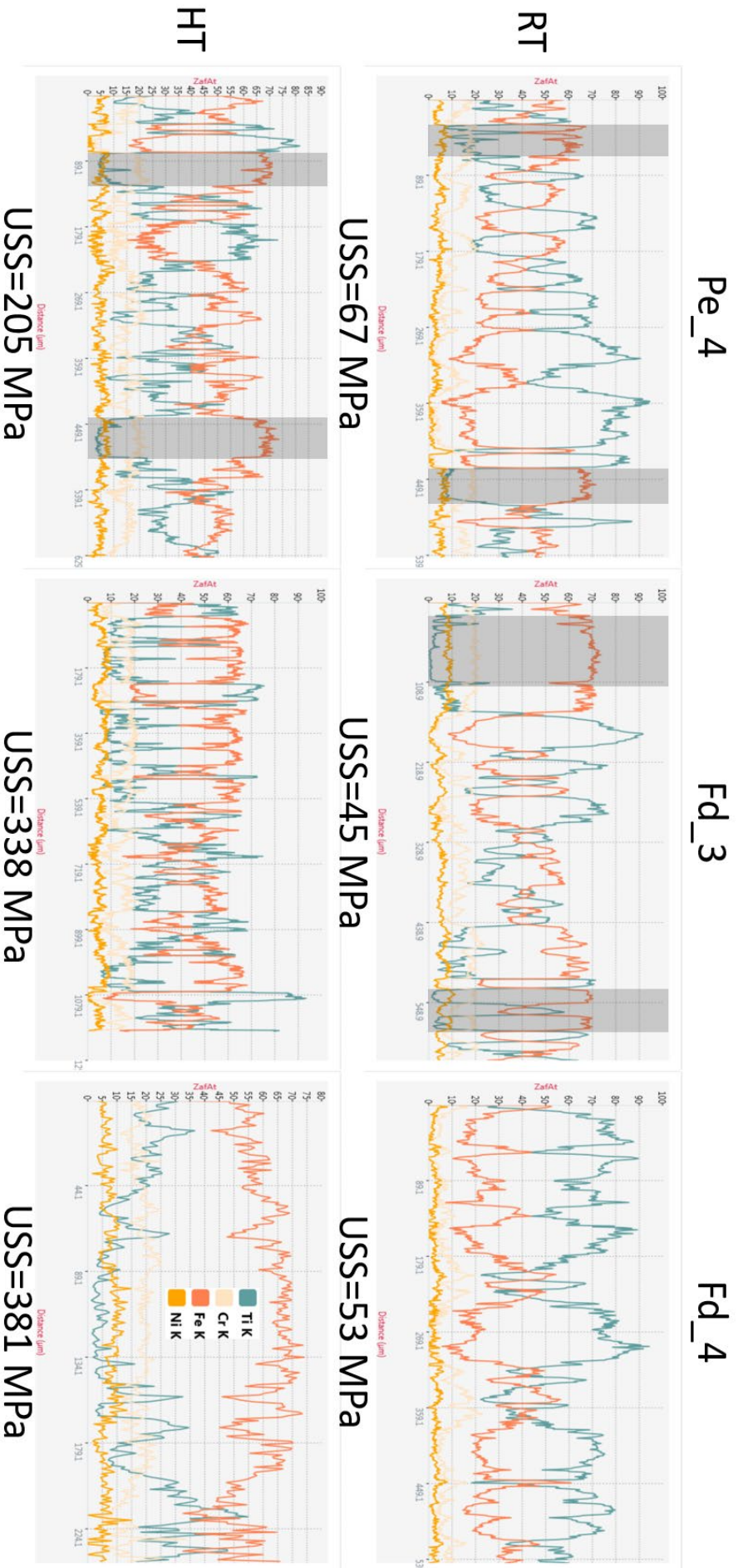


Fig. 6-20. Results of EDS line scans on the 316L side of the fracture surface in cuboid samples Pe_4, Fd_3 and Fd_4 produced at both RT and HT. The periodic fracture features are marked in grey and not considered.

EDS mapping has been done on the 316L side of the fracture surface. The results of Fe and Ti from samples RT/HT_Pe_4 and RT/HT_Fd_4 are shown in **Fig. 6-21**. The overall atomic ratio of Fe : Fe+Ti in these areas are: 45% in RT_Pe_4, 37% in RT_Fd_4, 52% in HT_Pe_4 and 61% in HT_Fd_4.

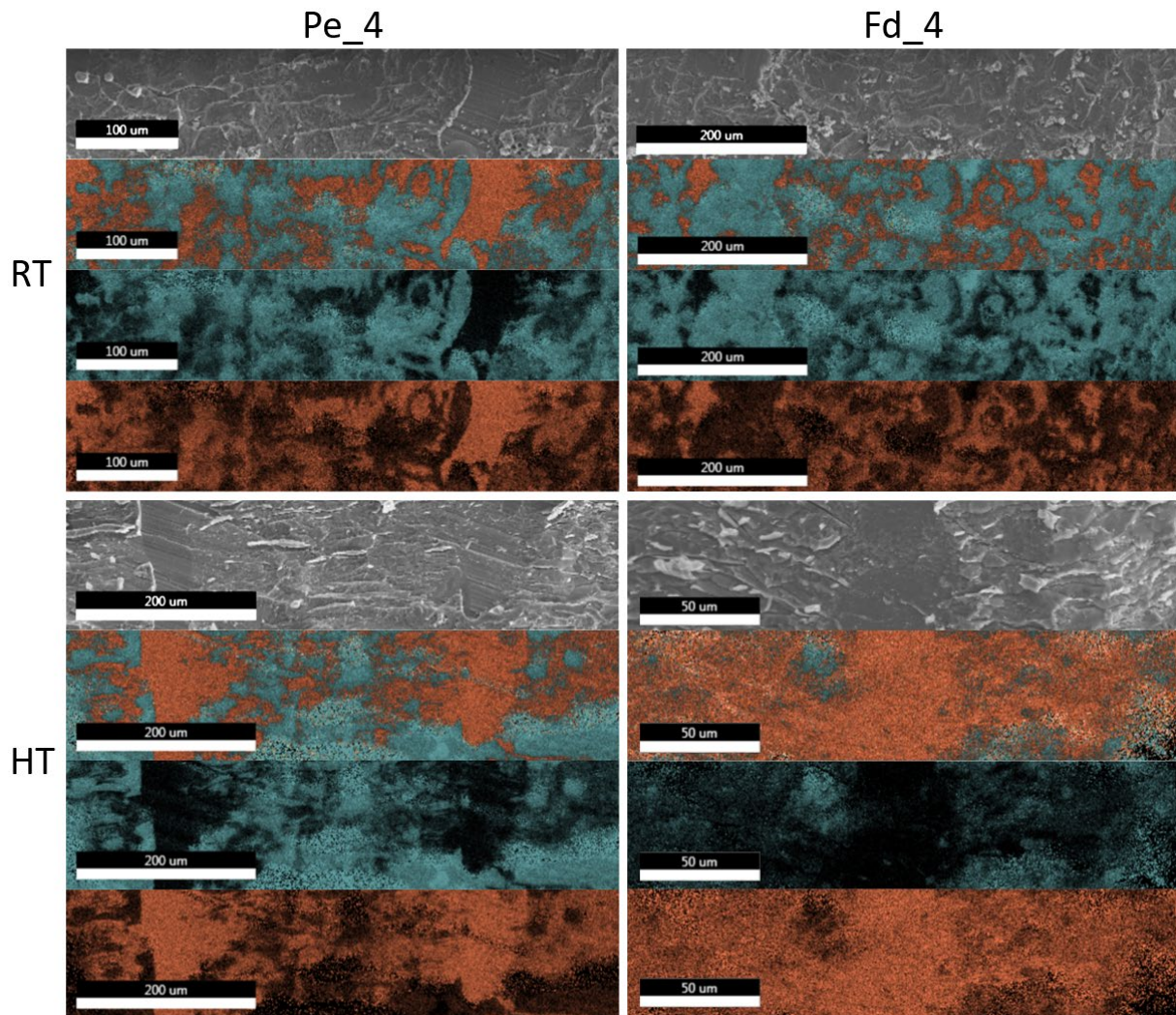


Fig. 6-21. EDS mapping results from samples RT/HT_Pe_4 and RT/HT_Fd_4. For each samples, the four images from top to bottom are the SEM image, the overlapped distribution of Ti and Fe, the distribution of Ti, and the distribution of Fe. The concentration in the insets are in at.%.

The atomic ratios Fe : Fe+Ti on the fracture surface of the 316L side from samples RT/HT_Pe_4 and RT/HT_Fd_4 are plotted against the sample USS in **Fig. 6-22**. The USS of pure Ti and 316L from literature are plotted at 0% and 100%, respectively. For the studied samples, the USS increases as the ratio increases.

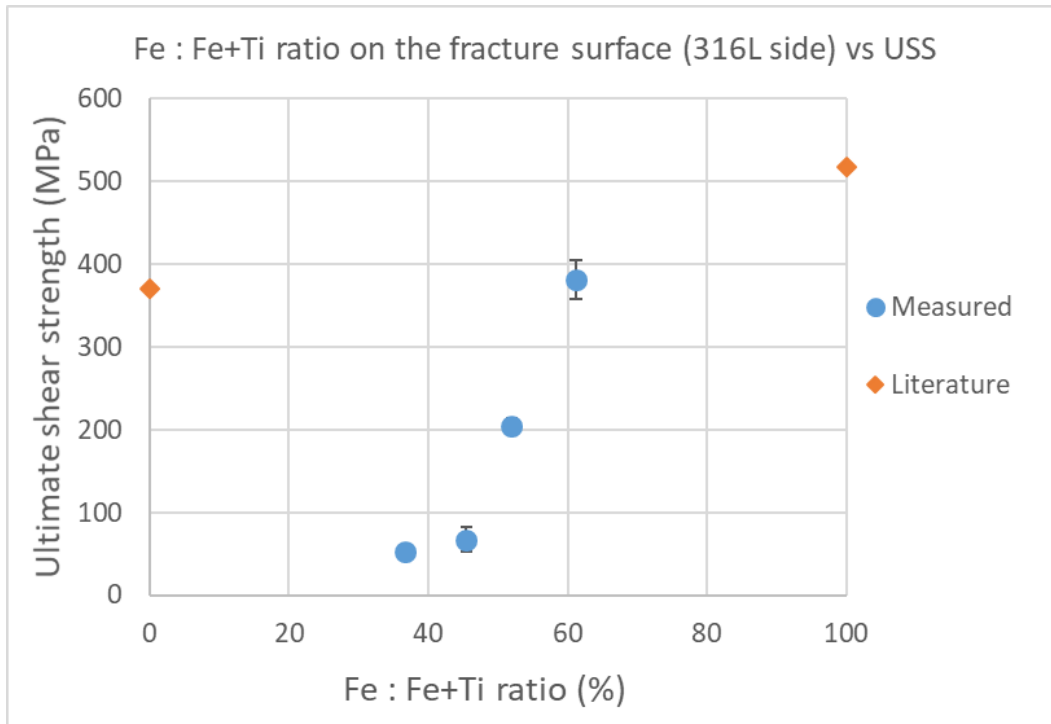


Fig. 6-22. The atomic ratio Fe : Fe+Ti and USS from samples RT/HT_Pe_4 and RT/HT_Fd_4. The USS of Ti and 316L from literature are also plotted.

To conclude, the delamination between the cuboid and the substrate due to the shear force happened in the IMC regions formed in the first layer. The delamination in samples with higher USS happened closer to the 316L substrate side, showing higher Fe concentration on the fracture surface.

6.3.1.6. Dimple network in HT samples

Dimples indicating ductile fracture have been found on the substrate side in all HT samples in the Fe-rich areas. Such features were not found in any RT samples. A high magnification SEM image of the substrate side from a shear fractured HT_Fd_4 specimen is shown in **Fig. 6.23a**. An EDS line scan was performed along the green line in **Fig. 6-23a**. The result is shown in **Fig. 6-23b** with the dimple and cleavage areas marked. The dimple area has a composition of Fe96. The nearby cleavage area has a composition of Fe85.

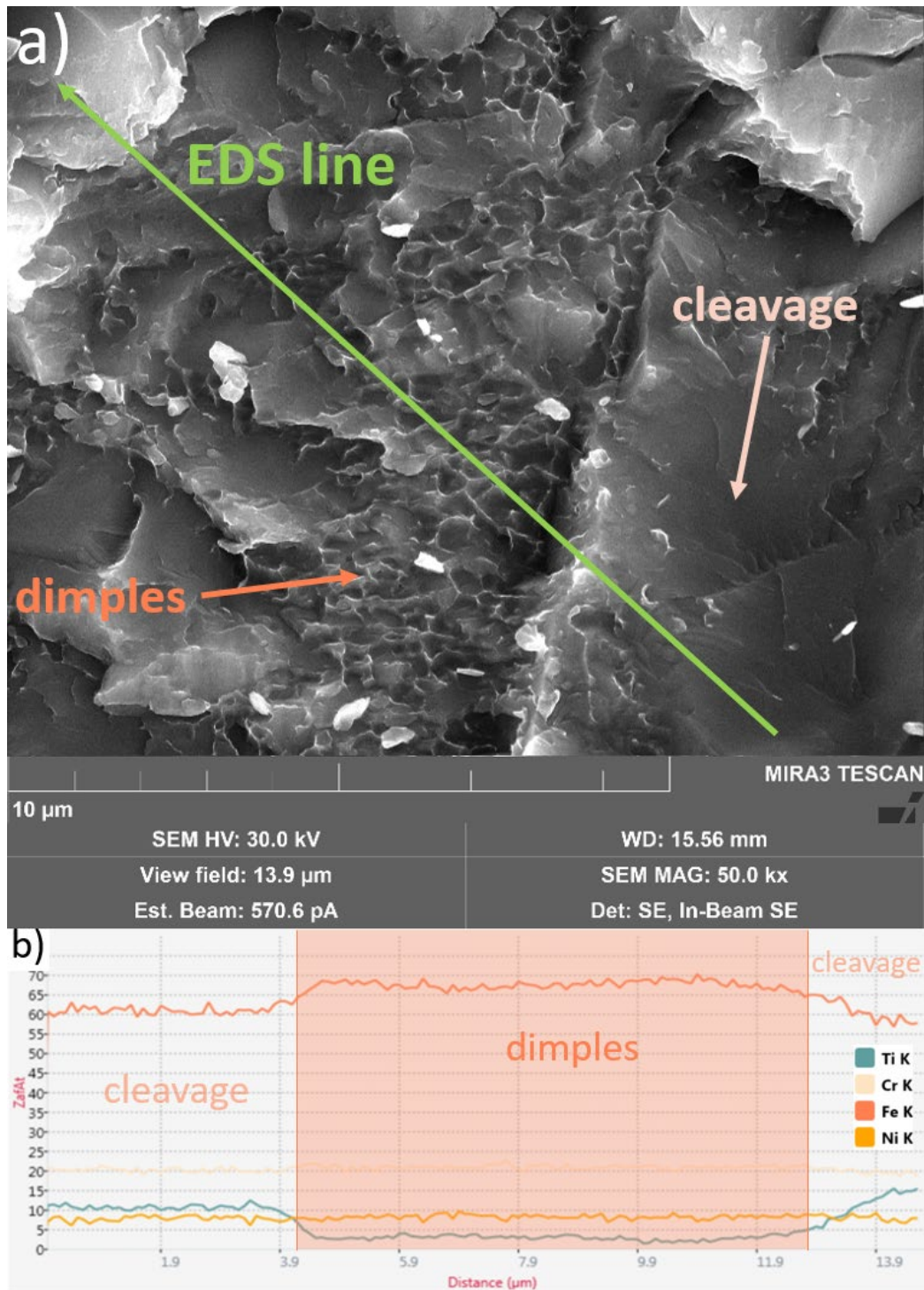


Fig. 6-23. a) SEM image of the substrate side from a shear fractured HT_Fd_4 specimen. b) EDS line scan result from the green line in a).

6.3.2. Discussion

6.3.2.1. Cross-section

Ti single layers have been deposited directly on 316L substrate. The thin bands interfacial features are similar to those observed in their corresponding single tracks investigated in 6.2.

The composition of Fe indicates the presence of $Ti_5Fe_{17}Cr_5$ in the smooth band close to the substrate and supersaturated β -Ti with FeTi IMC precipitation in the upper band. There is usually a few or tens of microns of β -Ti above the upper band. Then the composition completely transitions to pure Ti. The transition distance in the cuboid samples are slightly higher than in the layer samples, and the transition distance in HT samples are generally higher than in RT samples. As no remelting of the two interfacial bands at the bottom has been observed, the broadening of the bands is estimated to be a result of interdiffusion of the Fe and Ti elements at elevated temperature during deposition of the cuboids (15 layers in total) on top.

The thickness of the diffusion reaction layer (X) can be roughly calculated as the diffusion distance of Fe in β -Ti as follows ^{[115] [116]},

$$\text{Diff} = \text{Diff}_0 \times \exp(-Q/RT)$$

$$X = (\text{Diff} \times t)^{1/2}$$

where Diff is the diffusion coefficient, Diff_0 is the diffusion constant ($1.2 \times 10^{-6} \text{ m}^2 \text{ s}^{-1}$), Q is the activation energy of diffusion ($137000 \text{ J mol}^{-1}$), R is the gas constant ($8.314 \text{ J K}^{-1} \text{ mol}^{-1}$), T is the temperature in K and t is time in s. In this study, T is 793.15 K (520°C) and t is 3600 s (1h). The calculated thickness of the reaction layer X is 2.0 μm . This is very close to the difference in transition distance between the RT and HT samples.

Although the parameters used to deposit the single layers were selected for avoiding inter-track voids, such defects have been observed periodically at the interface. This is estimated due to the relatively small process window. Overhanging structures might have formed in random locations in the scan direction on the edges of the single tracks during deposition of the full single layers and created the inter-track voids.

Other defects like small vertical cracks in the two interfacial thin bands and partially melted Ti particles in the deposition are also observed. Despite the presence of these defects, the single layer samples bond to the substrate after mechanically cut for their cross-section. But when Ti cuboids are added on top of the single layers, most of the samples delaminated at the interface between the first layer and the substrate at the interface. This is a result of thermal stress accumulated over the many more thermal cycles and in larger volumes as the deposition goes from 2D layer to a 3D structure.

The transition distance in the investigated samples are mostly in a range of 6~18 μm . This is close to or even lower than the Fe-Ti interface thickness in joints obtained by many solid-state joining techniques. The Fc_5 samples behave differently from the other samples. This is because Fc_5 single layer penetrated deeper into the substrate and took more substrate material into

the melt. As a result, the supersaturated β -Ti band occasionally expands upward up to the top of the first layer. When the cuboids were deposited on top of the Fc_5 first layer with a small remelting depth, the 316L elements were further diluted in the melt pool of the second layer. The transition distance is thus increased and fluctuates in a large range.

6.3.2.2. Ultimate shear strength and fracture analysis

The ultimate shear strength USS of the RT samples are in a range of 45~153 MPa, lower than half of the USS of pure Ti 371 MPa. Preheating of the substrate and controlled cooling (25°C/5min) after deposition significantly increased the USS of the interfaces. The HT samples have an USS in a range of 173~381 MPa, with the highest strength exceeding pure Ti but below SS316 (USS=517 MPa). No clear correlation is found between the USS and the transition distance in the studied process window.

After shear testing, three possible macro failure features have been observed in the samples. Three combinations of the failure features, **ij**, **j** and **jk** are found. The relationship between USS and the failure feature combinations is plotted in **Fig. 6-24**.

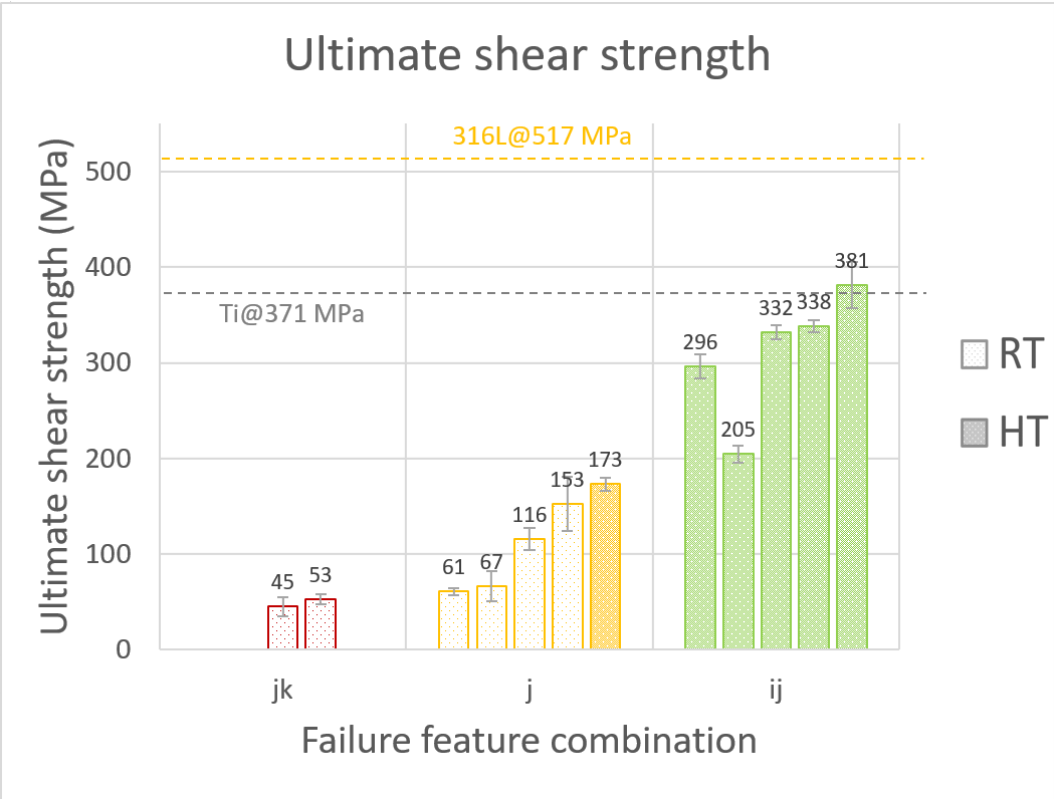


Fig. 6-24. The ultimate shear strength measured from the cuboid samples grouped by failure feature combination.

Samples with features **jk** effectively crack off the substrate completely at the bottom of the first layer. Only RT samples exhibit this failure feature combination. The large areas of cleavage on the **jk** features indicates that brittle cracks propagated through the whole interface and caused the failure. The strength of the interface is quite low with an USS of 45~53 MPa.

Samples with feature combination **j** crack at the bottom of the first layer too, but the delamination is constrained only under the cuboid. Despite the delamination under the cuboid, the interface in the single layer part withstood the maximum shear force during the test. Such a feature combination occurs in both RT and HT samples. These RT and HT samples show higher USS of 61~153 MPa and 173 MPa, respectively.

Samples with feature combination **ij** show both an obvious shear at the level of the pressure head and delamination at the interface between the first layer and the substrate. These features are effectively the upper and lower steps in **Fig. 6-18a**, respectively. Only HT samples exhibit this feature combination. During the shear test, the pressure head was mostly stopped manually after a loud sound of the brittle crack. In these samples, the highest shear force was already printed before the sound, conforming to the shear force - displacement curves of e.g. HT_Pe_4 and HT_Fd_4 in **Fig. 6-14**. It is estimated that the brittle crack in the interface happened during strain hardening of the pure Ti. Therefore, the interface in these samples is estimated to be stronger than the deposited pure Ti on top in terms of yield strength. The USS of these samples are significantly higher in a range of 205~381 MPa. Particularly, HT_Fd_4 samples have an average USS of 381 MPa, higher than the USS of pure Ti in literature ^[113].

Fluted fracture is observed on the step formed due to the shear between the cuboid and the first layer. A SEM image of the observed flutes is shown in **Fig. 6-25a**. Flutes are elongated dimples commonly seen in hcp structures and considered in connection with ductile fracture ^{[37] [117] [118] [119] [120] [121]}. EDS line scan results in **Fig. 6-19a** confirm that the fluted fracture happened in pure Ti. **Fig. 6-25b** shows a similar fluted structure on the Ti side of the fractured joint reported in hot-roll diffusion of pure Ti and carbon steel with nickel interlayer ^[62].

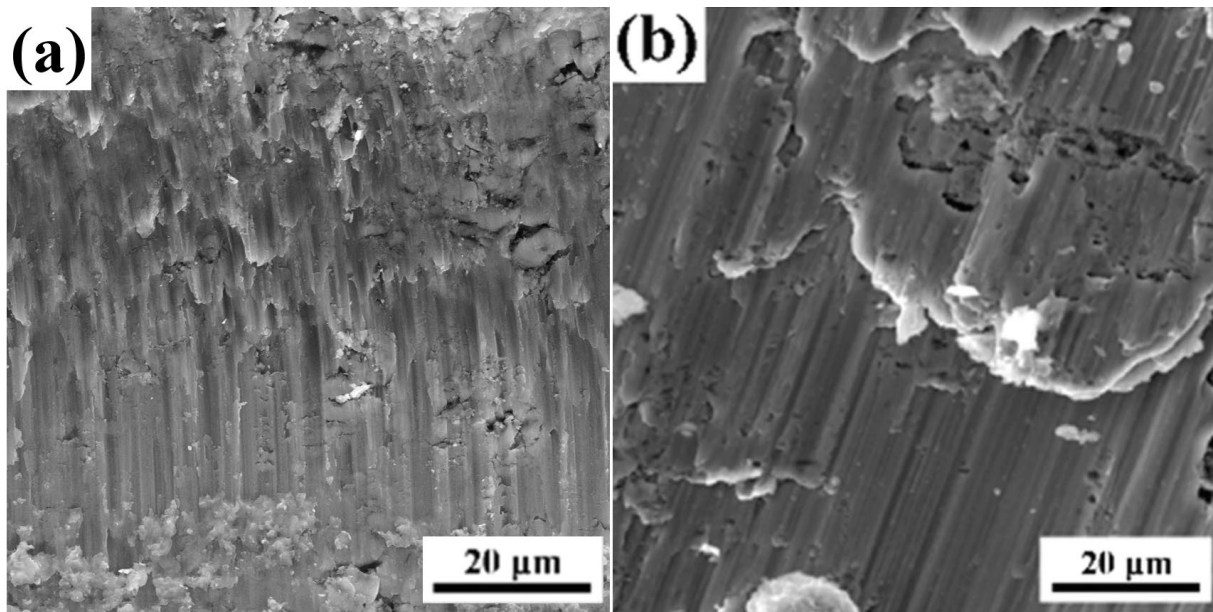


Fig. 6-25. Flutes in the fracture on the Ti side of a) HT_Pe_4 in this study and b) a hot-roll diffusion bonded Ti/carbon steel joint with nickel interlayer in literature [62].

The crack surface at the interface between the substrate and the first layer is full of cleavage fractures and tear ridges for all samples that crack here. **Fig. 6-26** shows similar fracture surfaces in this study and reported in laser welded joints of Ti and stainless steels [28] [122]. EDS line scans across these surfaces show that the composition fluctuates in a wide range of Fe18~96 (considering the sum Fe and Ti as 100 at.%), covering almost all the phases from 316L to β -Ti, with a large amount of FeTi and Fe₂Ti IMCs.

This indicates that the brittle cracks penetrated all the phases between the substrate and the deposited pure Ti.

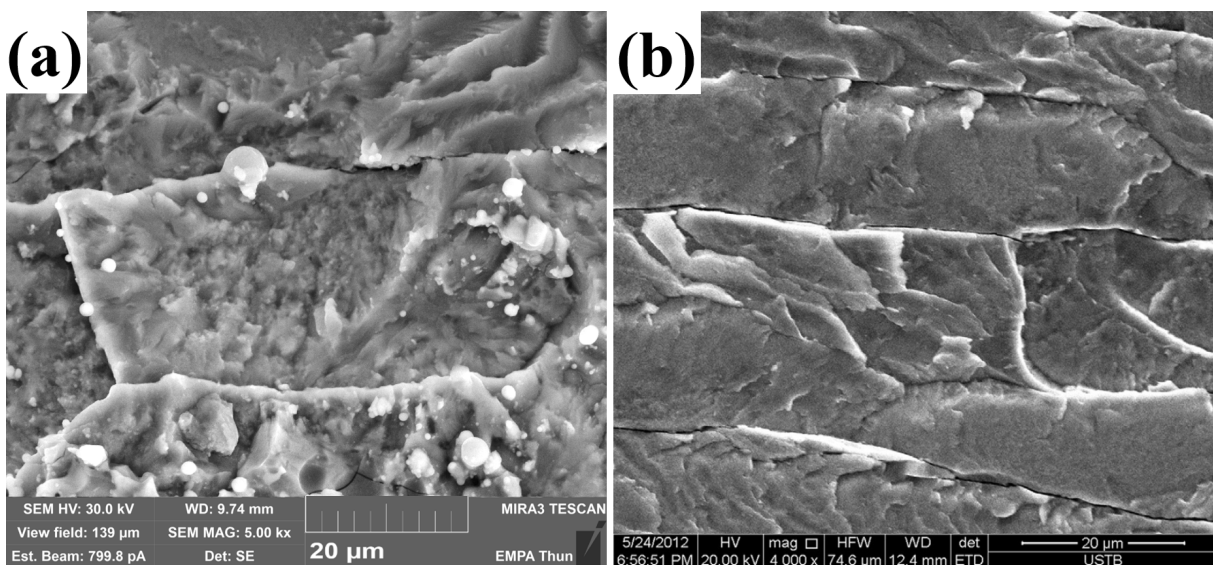


Fig. 6-26. Cleavage fractures in the interface in a) RT_Pe_4 in this study and b) a laser welded joint between Ti6Al4V and SS 201 in literature [28].

Nonetheless, small areas of dimples shown in **Fig. 6-27a** have been observed distributed in Fe-rich areas on the fracture surfaces of the interfaces on the 316L side in HT samples. No such areas have been found in RT samples. The dimple areas show a composition of Fe96 with little Ti and is considered almost 316L. Dimples are typical microscopic features of ductile fracture and are observed in many studies on AM of 316L or dissimilar joints involving 316L [3] [50] [123] [124] [125] [126] [127] [128] [129] [130] [131] [132] [133] [134]. Dimples on the fracture surfaces in 316L produced by selective laser melting (SLM) and DED are shown in **Fig. 6-27** [135] [136]. As is shown in **Fig. 6-22**, fracture surface on the 316L side with higher Fe : Fe+Ti ratio is correlated with higher ultimate shear strength USS. It is inferred that the higher this ratio, the larger the area where Fe concentration can reach Fe96 corresponding to the dimple area. The more ductile fracture then explains the increased USS. In samples with lower USS, the cracks propagated more in the brittle IMC areas.

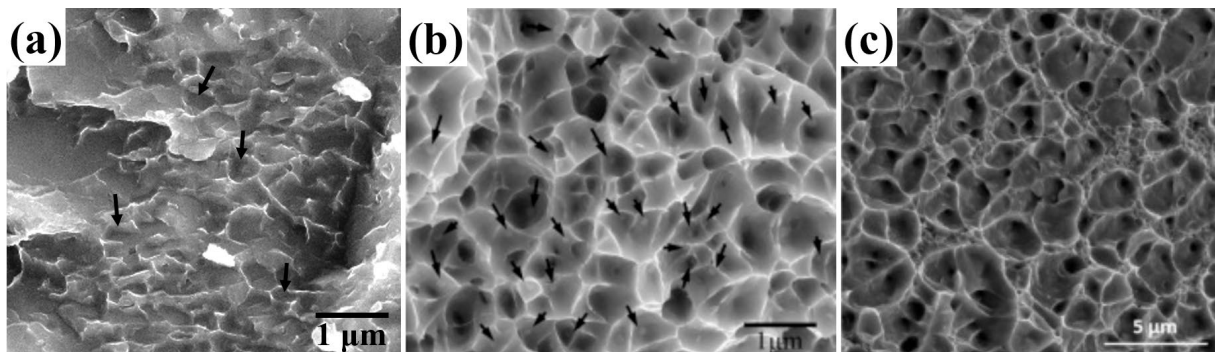


Fig. 6-27. Dimples on the fracture surface of a) the interface of HT_Fd_4 in this study, b) 316L prepared by SLM [135] and c) 316L prepared by DED [136]

6.3.2.3. Preheating and controlled cooling

Substrate preheating is a commonly used method for mitigating distortion and reducing cracks [137] [138]. Preheating the substrate to 400°C led to a reduction in residual stress by 40% in a study on DED of SS 304 [139].

Fig. 6-15 shows that the HT samples have significantly improved USS compared to their RT counterparts. Preheating and controlled cooling can benefit the interface in multiple aspects.

FeTi has been found to be the main IMC phase in the two interfacial bands. The brittle-to-ductile transition temperature of FeTi is reported in a range between 500°C and 600°C [140]. **Fig. 6-28** shows the change in hardness and yield stress of FeTi with temperature. The hardness of FeTi remains in a small range around 400HV up to 300°C and decreases with elevating temperature. FeTi behaves in brittle manner below 500°C and becomes completely ductile above 600°C. For the HT samples in this study, the substrate was effectively preheated to 520°C before deposition started. Given the continuous heat input of the deposition process, the

temperature in the interfacial regions is estimated to be maintained in the ductile range of FeTi during the DED process. In addition, the amplitude of temperature variation in the solid and the thermal gradient are reduced due to elevated base temperature. Thermal stress due to CTE mismatch and cycles of thermal expansion and contraction is thus reduced. As a result, the risk of hot cracks during the DED process is reduced thanks to preheating.

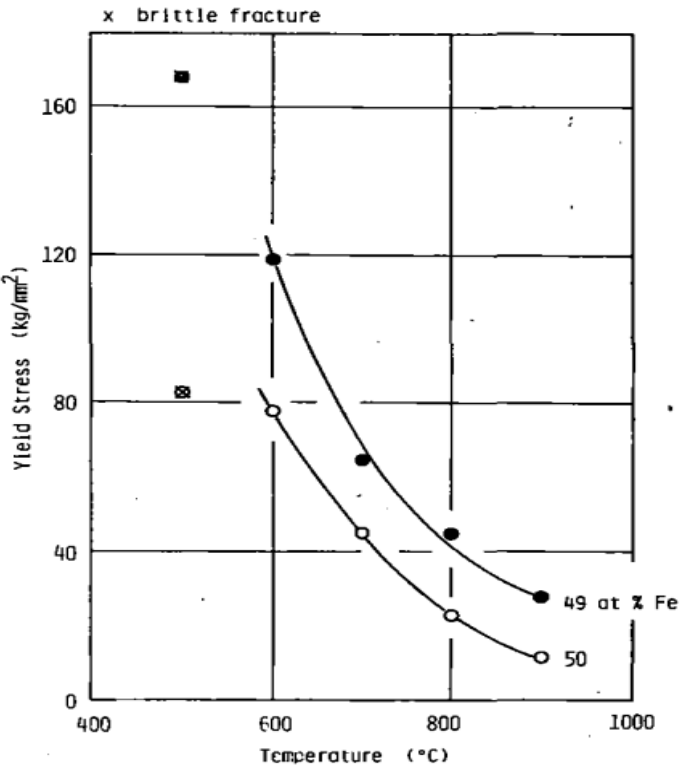
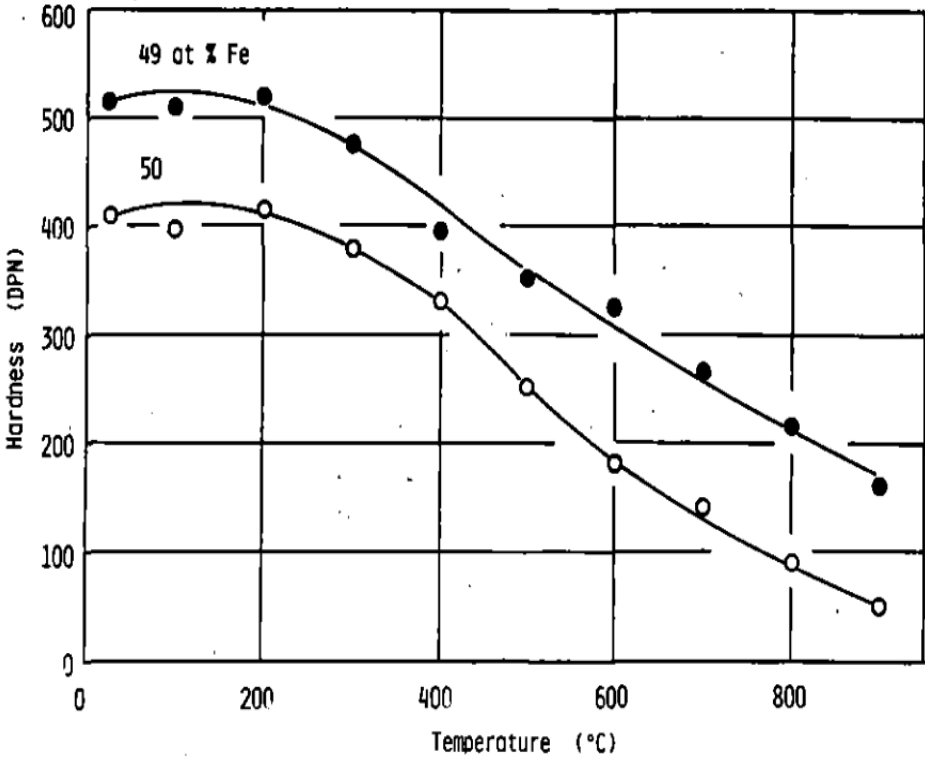


Fig. 6-28. Temperature dependence of hardness and yield stress of FeTi [140]

The influence of annealing on the Ti/steel clad plates produced by cold spray additive manufacturing and hot-rolling has been studied in literature [3]. It is reported that annealing at 550°C for 3 h promoted the recovery and recrystallization mechanisms in the joint. It also reduced the dislocation density, resulting in more ductility. However when annealing was done with 650°C, the mechanical properties of the joint was adversely affected due to the growth of undesired TiC. In this study, the HT samples were also kept at 520°C for an additional hour after the deposition was finished. This is effectively in-situ annealing of the deposition. The highest USS obtained is 381 MPa, much higher than 280 MPa reported in the above mentioned literature. This could be a result of reduced holding time at annealing temperature, which avoided overgrowth of detrimental phases.

With the abovementioned thermal management, the risk of crack formation in the interfacial regions with brittle IMCs in the as-deposited parts is reduced. It is estimated that the HT samples have fewer cracks in the interfacial regions than RT samples. During shear testing of the RT samples, the existing cracks in the interfacial regions easily propagated to cause catastrophic fracture, exhibiting low ultimate shear strength USS without shear between the Ti cuboid and the first layer. On the contrary, the interfacial regions in the HT samples with fewer cracks could withstand higher stress until pure Ti yielded. Therefore, almost all samples in which the shear between the Ti cuboid and the first layer is observed exhibit higher USS than the yield strength 217 MPa of pure Ti [113]. The bottom of the interface close to 316L eventually fractured during strain hardening of the pure Ti.

6.3.3. Conclusion

As single tracks or even single layers are not representative of a real 3D structure, cuboids (5 x 5 x 3 mm³) were deposited on single layers optimized according to the high PF strategy described in Chapter 4. Some parameter sets could be found with which the printed 3D structures show good interfacial strength with the 316L substrate.

In the cuboid samples, the transition from 316L to Ti is mostly completed at the bottom of the first layer. The transition distance in cuboid samples falls mostly in a range of 8~18 μm. Preheating the substrate generally increased the transition distance by around 2 μm via atomic diffusion.

The ultimate shear strength USS of RT samples is in a range of 45~153 MPa. The USS of HT samples is in a significantly higher range of 173~381 MPa, with a maximum value of 381±24 MPa exceeding 371 MPa, the USS of pure Ti in literature.

The low USS samples without preheating exhibit only cleavage and tear ridges on the 316L side of the fracture surface, indicating brittle fracture. The fracture surface shows lower Fe concentration which indicates that the fracture happened mainly in the IMC regions in the middle of the interface. The high USS samples with preheating exhibit dimples in addition to the features observed in the low USS samples, indicating both brittle and ductile fracture modes. The fracture surface shows higher Fe concentration with the highest concentration Fe₉₆ found in the dimple areas. This indicates that the fracture happened closer to the bottom of the interface, involving ductile fracture of the near-316L regions.

Preheating played the role of in-situ annealing. It is estimated to help increase the interface strength by processing in the ductile range of the IMC phases, reducing thermal stress and dislocation density.

Chapter 7. Conclusions and outlooks

7.1. Conclusions

It appears that for dissimilar metal deposition with IMCs, a special strategy has to be applied for controlling the interface. The IMC regions should be as thin as possible for achieving a sufficient interfacial strength. Standard deposition recipe can be applied for the subsequent 3D structure on top as the interfacial region is not changed anymore.

In this research, deposition of pure Ti cuboids on stainless steel 316L substrate with a strong interface is achieved by directed energy deposition (DED). Using the high powder feedrate (PF) strategy for the interfacial layer, the melting depth of the substrate is as low as around 12 μm . In this way, the dilution of Fe from the substrate into the melt pool is limited to a very low extent. The brittle intermetallic compounds (IMCs) like $\text{Ti}_5\text{Fe}_{17}\text{Cr}_5$, Fe_2Ti and FeTi still form with the inevitable intermixing of Fe and Ti. But these detrimental phases are constrained within two thin bands with a total thickness of 8~18 μm at the bottom of the solidified melt pool. Ultimate shear strength (USS) of 45~153 MPa has been achieved. Furthermore, preheating of the substrate and controlled cooling at 25°C/5min after deposition reduced the risk of cracking during the DED process and residual stress at room temperature. With the thermal management, the USS of the interface has been improved to 173~381 MPa. The highest USS of the interface produced is 381 ± 24 MPa, exceeding the USS of the weaker base material pure Ti (371 MPa) and below that of the stronger base material 316L (517 MPa).

Beside this main conclusion on the necessity of applying a special strategy for controlling the interfacial region in dissimilar metal deposition, sub conclusions can be extracted from this study.

As the 3D structures produced by DED is composed of single tracks as the elementary unit, this study was started from DED of Ti single tracks on 316L substrate. The main results before achieving deposition of Ti cuboids are summarized in this section.

Deposition of Ti single tracks on 316L substrate was experimented within the conventional DED process window to study the influence of process parameters on the geometry of the deposition, distribution of the microstructure, chemical composition and phases. The main results can be summarized as follows.

- From the 316L side to pure Ti, four possible reaction regions have been observed in the deposition. Region I has a reticular microstructure which consists of three features:

river-shaped network estimated to be $Ti_5Fe_{17}Cr_5$, Fe_2Ti surrounding the river-shaped network and $FeTi$ that fills the space left by the Fe_2Ti . Region II consists of $FeTi$ dendrites and interdendritic supersaturated β -Ti. Region III consists of supersaturated β -Ti as the matrix and $FeTi$ particle precipitates. Region IV consists of β -Ti as the matrix and $FeTi$ network precipitates.

- The Fe concentration decreases from the bottom to the top of the deposition. Three types of composition transitions depending on the ending Fe concentration have been found. Insufficient composition transitions with a concentration of Fe22 (meaning the atomic fraction of Fe is 22%, counting the sum of Fe and Ti as 100%) at the end leaves large amounts of IMCs in the deposition. Cracks are observed in such samples with voids in severe cases. A complete and abrupt transition with pure Ti in the main part of the deposition constrains the IMCs in two thin bands with a total thickness of 20~70 μm at the bottom of the solidified melt pool. After the upper band, the concentration of Fe quickly reduces to neglectable level. No cracks are observed in these samples. Therefore, an abrupt and complete transition in composition is estimated favorable for reducing crack in the deposition.
- A complete and abrupt transition in composition requires small penetration depth and dilution ratio. A small aspect ratio (the ratio of the height to the width) of the deposition is necessary to create acute contact angles on the edges of the single tracks. This helps avoid overhanging structures that cause inter-track voids when depositing parallel single tracks to form a single layer. To fulfill these requirements, increased powder feedrate, nozzle velocity and laser power were determined as the direction for subsequent experiments.

Deposition of Ti single walls on 316L was also experimented to investigate the influence of subsequent tracks on top of the first track. The main results can be summarized as follows.

- More cracks and delamination in the first track of the single walls have been observed than in single tracks.
- 200 nm thin interface has been observed in the lateral sections of the whole interface in single walls with insufficient composition transition in the first track. This thin interface was estimated to have formed between the 2nd track overflowing to the lateral sides and the fresh substrate surface. This phenomenon proves that producing an interface with a very abrupt composition transition is possible with the DED system used in this study.

- All the single walls with the first tracks forming two IMC-containing thin bands at the bottom with a total thickness of 20~70 μm as described before show catastrophic cracks within the two bands. It was estimated that the interface fractured because the contained IMCs could not withstand the higher thermal stress accumulated over multiple thermal cycles than in the single tracks.

Based on the results from the single track and single wall DED experiments, two strategies were then explored for obtaining thin interface with abrupt composition transition from 316L to Ti.

1. Overflowing strategy: Extension of the 200 nm thin interface sections on the lateral sides with overflowing upper layer.
2. High powder feedrate strategy: Entering the high powder feedrate regime with simultaneously increased nozzle velocity and laser power. The parameter combination is expected to lead to low dilution ratio with low aspect ratio by shielding the substrate from the laser and distributing less powder material along unit deposition length.

The main results from overflowing strategy can be summarized as follows.

- The total width of the 2-layer wall could reach 213% of the reticular IMC Region I formed by the 1st layer.
- Subsequent tracks aimed to extend the thin interface laterally turned out piling up and forming periodic overhanging structures. Conditions for forming dense Ti layer on 316L substrate with this strategy as the base for further Ti deposition were not found in this study.

Parameter sets with the high powder feedrate strategy were investigated aiming to achieve thin interface with abrupt and complete composition transition. The main results are summarized below.

- Single tracks with two IMC-containing thin bands with a total thickness, namely the transition distance, of around 30 μm have been deposited. Different from the lower reticular band featuring observed in the conventional process window, this lower band is mostly smooth, with reticular regions appearing only occasionally. When the

transition distance reduces to around 10 μm , the lower band is completely smooth and identified as $\text{Ti}_5\text{Fe}_{17}\text{Cr}_5$ IMC. Ti single layers consisting of overlapping parallel single tracks have also been deposited with transition distance around 10 μm .

- Ti cuboids were deposited on the single layers within a single DED process. The ultimate shear strength (USS) of such room temperature (RT) samples is in a range of 45~153 MPa. HT samples were prepared with preheating of the substrate to 520°C and keeping the samples at this temperature for another hour before cooling down at a controlled cooling rate of 25°C/5min. HT samples exhibit significantly improved USS in a range of 173~381 MPa.

On one hand, the composition in the deposition has been controlled by DED with high powder feedrate to reduce the thickness of interfacial bands containing brittle IMCs like $\text{Ti}_5\text{Fe}_{17}\text{Cr}_5$, FeTi and Fe_2Ti . On the other hand, thermal management has been adopted to produce the interface in its ductile temperature range and reduce the thermal stress during and after the process. As a result, the cracking problem in dissimilar DED of Ti on 316L has been solved using the combination of the two methods.

7.2. Outlooks

The previous section presents successful deposition of Ti on 316L with DED. Future work in different aspects is recommended below.

- ❖ Process optimization
 - DED parameters like laser power, nozzle velocity and powder feedrate can be further optimized to reduce the transition distance further below 10 μm .
 - The influence of thermal management on the ultimate shear strength can be further investigated. Parameters include preheating temperature, holding time after deposition and cooling rate.
- ❖ In-depth characterization
 - Localized phase identification in the thin bands at the interface can be carried out with transmission electron microscopy.

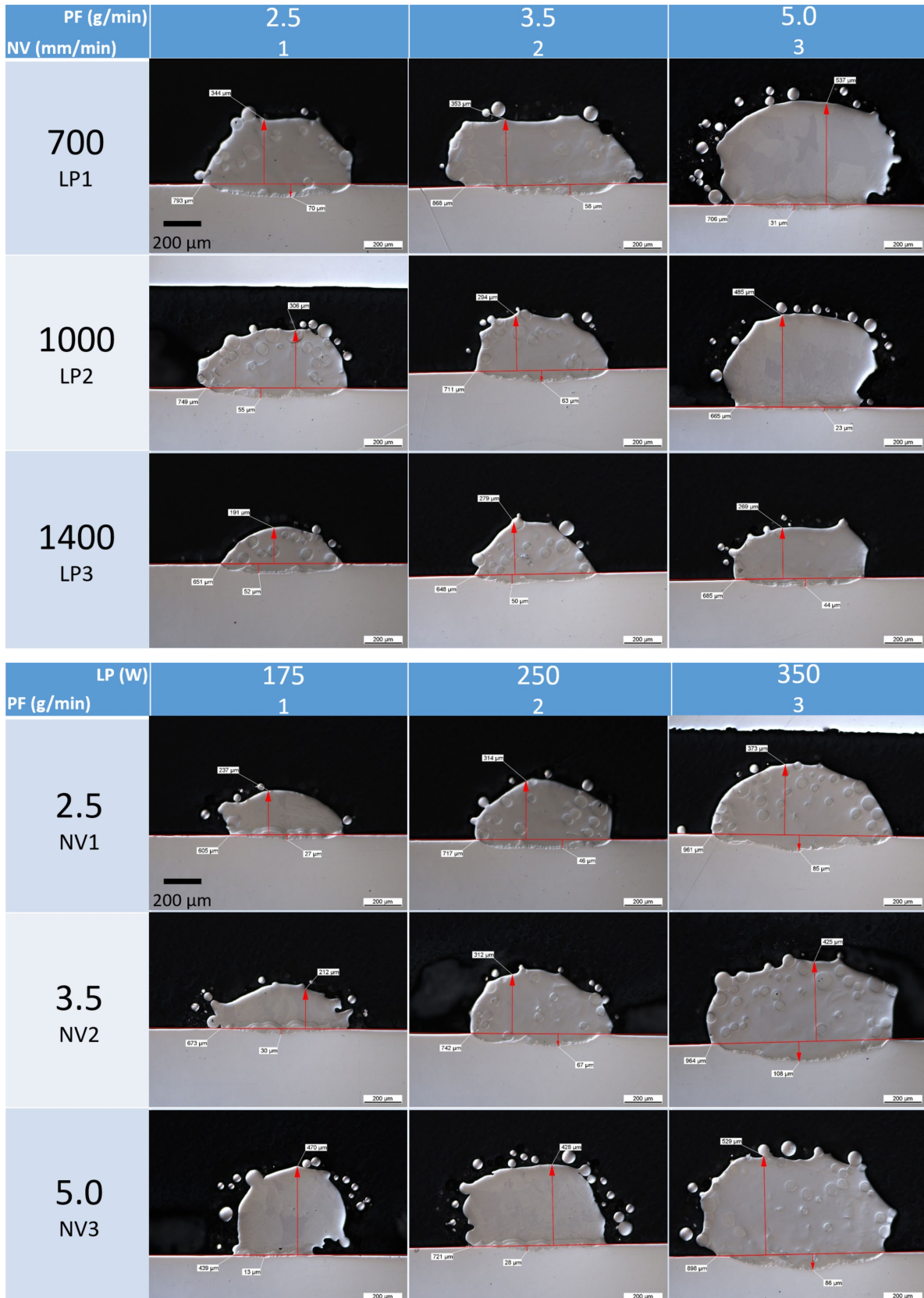
- Residual stress at the interface can be measured and modeled to further understand the contribution of thermal management.

❖ Knowledge transfer

- The high powder feedrate strategy can be transferred to dissimilar deposition of other material pairs where brittle IMCs can form, such as Ti(-alloys) with other steels, Inconel, Invar, CoCrMo, etc.

Appendix A - Single track trials

The pictures of the single track cross-sections used in Section 4.1.1.1. are displayed in **Fig. A-1** below.



Appendix A - Single track trials

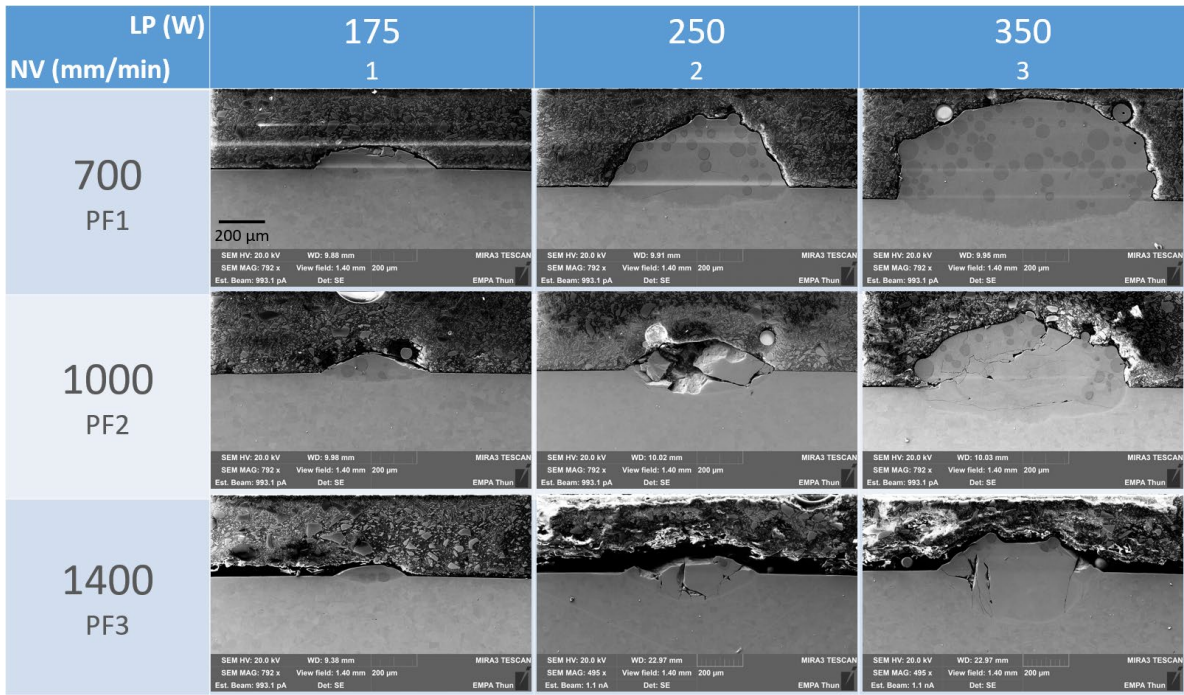


Fig. A-1. Microscopic images of the cross-sections of the single track samples described in 4.1.1. LP groups have a constant LP of 250 W. NV groups have a constant NV of 1000 mm/min. PF groups have a constant PF of 2.5 g/min.

Appendix B - High powder feedrate DED

The parameters for DED of the high powder feedrate PF single tracks described in Section 6.2 are summarized in Table. B-1.

Table B-1. Parameters for the high PF single tracks in the F series.

Group	Sample No.	LP (W)	NV (mm/min)	PF (g/min)
Fa	1	500	4000	6
	2	500	6000	6
	3	500	9000	6
	4	500	13000	6
	5	500	20000	6
	6	500	30000	6
Fb	1	500	4000	9
	2	500	6000	9
	3	500	9000	9
	4	500	13000	9
	5	500	20000	9
	6	500	30000	9
Fc	1	500	4000	14
	2	500	6000	14
	3	500	9000	14
	4	500	13000	14
	5	500	20000	14
	6	500	30000	14
Fd	1	500	4000	21
	2	500	6000	21
	3	500	9000	21
	4	500	13000	21
	5	500	20000	21
	6	500	30000	21
Fe	1	500	4000	32
	2	500	6000	32
	3	500	9000	32
	4	500	13000	32
	5	500	20000	32
	6	500	30000	32

Appendix B - High powder feedrate DED**Table B-2.** Parameters for the high PF single tracks in the P series.

Group	Sample No.	LP (W)	NV (mm/min)	PF (g/min)
Pa	1	300	4000	32
	2	300	6000	32
	3	300	9000	32
	4	300	13000	32
	5	300	20000	32
	6	300	30000	32
Pb	1	350	4000	32
	2	350	6000	32
	3	350	9000	32
	4	350	13000	32
	5	350	20000	32
	6	350	30000	32
Pc	1	400	4000	32
	2	400	6000	32
	3	400	9000	32
	4	400	13000	32
	5	400	20000	32
	6	400	30000	32
Pd	1	450	4000	32
	2	450	6000	32
	3	450	9000	32
	4	450	13000	32
	5	450	20000	32
	6	450	30000	32
Pe	1	500	4000	32
	2	500	6000	32
	3	500	9000	32
	4	500	13000	32
	5	500	20000	32
	6	500	30000	32

Appendix C - EDM cutting plan

The schematic of the top view of the depositing layout and cutting plan in Section 6.3 is shown in **Fig. C-1**. The grey rectangle is the Ti single layer on the 316L substrate. The black squares are the Ti cuboids deposited on top of the single layer. The red boxes are the overlay of the cutting path for extracting specimens for shear tests.

The scanning direction of the nozzle was parallel to the long edge of the grey rectangle when depositing the single layers. The scanning direction was parallel to the short edge of the grey rectangle when depositing the first layer of the cuboids, and was rotated by 90° after each layer of the cuboid was finished.

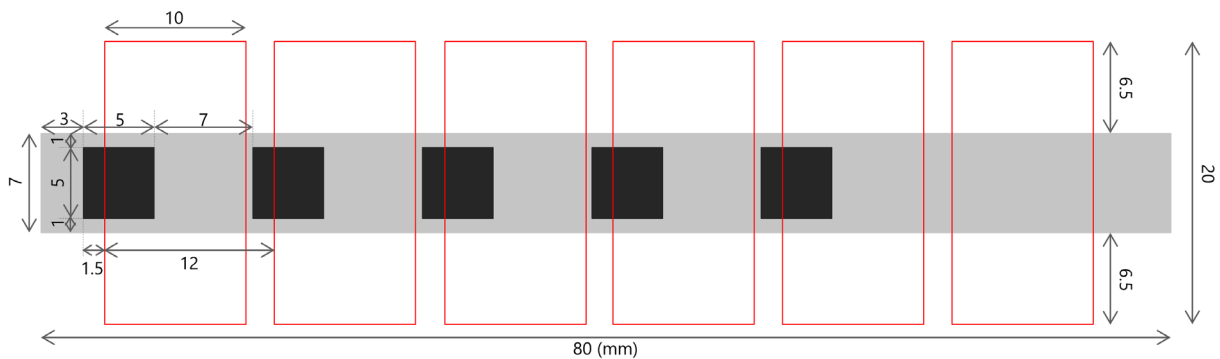


Fig. C-1. The schematic of the top view of a single layer sample with five cuboids on top of it. The red boxes are the cutting path for extracting the shear test samples with EDM.

References

- [1] Mannucci, A.; Tomashchuk, I.; Mathieu, A.; Cicala, E.; Boucheron, T.; Bolot, R.; Lafaye, S. Direct Laser Welding of Pure Titanium to Austenitic Stainless Steel. *Procedia CIRP* **2018**, *74*, 485–490.
- [2] Lee, M. K.; Lee, J. G.; Lee, J. K.; Hong, S. M.; Lee, S. H.; Park, J. J.; Kim, J. W.; Rhee, C. K. Formation of Interfacial Brittle Phases Sigma Phase and IMC in Hybrid Titanium-to-Stainless Steel Joint. *Transactions of Nonferrous Metals Society of China* **2011**, *21*, s7–s11.
- [3] Zhao, Z.; Tariq, N. ul H.; Tang, J.; Ren, Y.; Liu, H.; Tong, M.; Yin, L.; Du, H.; Wang, J.; Xiong, T. Influence of Annealing on the Microstructure and Mechanical Properties of Ti/Steel Clad Plates Fabricated via Cold Spray Additive Manufacturing and Hot-Rolling. *Materials Science and Engineering: A* **2020**, *775*, 138968.
- [4] Yang, X.; Shi, C.; Ge, Y.; Sabuj, M. N. H. Comparison of Microstructure and Mechanical Properties of Titanium/Steel Composite Plates by Two Manufacturing Processes. *J. Iron Steel Res. Int.* **2018**, *25* (3), 347–356.
- [5] Yang, D.; Luo, Z.; Xie, G.; Wang, M.; Misra, R. D. K. Effect of Vacuum Level on Microstructure and Mechanical Properties of Titanium–Steel Vacuum Roll Clad Plates. *J. Iron Steel Res. Int.* **2018**, *25* (1), 72–80.
- [6] Li, W.; Yan, L.; Karnati, S.; Liou, F.; Newkirk, J.; Taminger, K. M. B.; Seufzer, W. J. Ti-Fe Intermetallics Analysis and Control in Joining Titanium Alloy and Stainless Steel by Laser Metal Deposition. *Journal of Materials Processing Technology* **2017**, *242*, 39–48.
- [7] Gilbert, S. M. Solid-state joining of titanium alloy to stainless steel. 91.
- [8] Kundu, S.; Chatterjee, S. Effects of Temperature on Interface Microstructure and Strength Properties of Titanium–Niobium Stainless Steel Diffusion Bonded Joints. *Materials Science and Technology* **2011**, *27* (7), 1177–1182.
- [9] Satoh, G.; Yao, Y. L.; Qiu, C. Strength and Microstructure of Laser Fusion-Welded Ti–SS Dissimilar Material Pair. *Int J Adv Manuf Technol* **2013**, *66* (1), 469–479.
- [10] Zhou, Q.; Liu, R.; Zhou, Q.; Fan, K.; Xie, J.; Chen, P.; Rittel, D. Tensile Behavior of the Titanium-Steel Explosive Welded Interface under Quasi-Static and High-Strain Rate Loading. *International Journal of Solids and Structures* **2022**, *254–255*, 111870.
- [11] Wu, T.; Yang, C. Influence of Pulse TIG Welding Thermal Cycling on the Microstructure and Mechanical Properties of Explosively Weld Titanium/Steel Joint. *Vacuum* **2022**, *197*, 110817.
- [12] Murray, J. L. The Fe–Ti (Iron-Titanium) System. *Bulletin of Alloy Phase Diagrams* **1981**, *2* (3), 320–334.
- [13] Loh, G. H.; Pei, E.; Harrison, D.; Monzón, M. D. An Overview of Functionally Graded Additive Manufacturing. *Additive Manufacturing* **2018**, *23*, 34–44.

References

- [14] Cui, D.; Mohanta, A.; Leparoux, M. Interface Control in Additive Manufacturing of Dissimilar Metals Forming Intermetallic Compounds—Fe-Ti as a Model System. *Materials* **2020**, *13* (21), 4747.
- [15] Cui, D.; Lanfant, B.; Leparoux, M.; Favre, S. Additive Manufacturing of Ti-Nb Dissimilar Metals by Laser Metal Deposition. In *Industrializing Additive Manufacturing*; Meboldt, M., Klahn, C., Eds.; Springer International Publishing: Cham, 2021; pp 96–111.
- [16] Onuike, B.; Bandyopadhyay, A. Additive Manufacturing of Inconel 718 – Ti6Al4V Bimetallic Structures. *Additive Manufacturing* **2018**, *22*, 844–851.
- [17] Special Metals Corporation: INCONEL® Alloy 718 Product Brochure, Publication Number SMC-045
- [18] Peters, M.; Kumpfert, J.; Ward, C. h.; Leyens, C. Titanium Alloys for Aerospace Applications. *Advanced Engineering Materials* **2003**, *5* (6), 419–427.
- [19] Tomashchuk, I.; Sallamand, P. Metallurgical Strategies for the Joining of Titanium Alloys with Steels. *Advanced Engineering Materials* **2018**, *20* (6), 1700764.
- [20] Sidambe, A. T. Biocompatibility of Advanced Manufactured Titanium Implants—A Review. *Materials (Basel)* **2014**, *7* (12), 8168–8188.
- [21] Wiegand, M.; Marks, L.; Sommer, N.; Böhm, S. Dissimilar Micro Beam Welding of Titanium to Nitinol and Stainless Steel Using Biocompatible Filler Materials for Medical Applications. *Weld World* **2023**, *67* (1), 77–88.
- [22] Steen, W. M.; Mazumder, J. *Laser Material Processing*, 4th Edition.; Springer: London, 2010.
- [23] Oliveira, J. P.; Fernandes, F. M. B.; Miranda, R. M.; Schell, N.; Ocaña, J. L. Residual Stress Analysis in Laser Welded NiTi Sheets Using Synchrotron X-Ray Diffraction. *Materials & Design* **2016**, *100*, 180–187.
- [24] Touzé, S.; Rauch, M.; Hascoët, J.-Y. Methodology for Complexity and Cost Comparison between Subtractive and Additive Manufacturing Processes. *J Intell Manuf* **2022**.
- [25] Chen, H.-C.; Pinkerton, A. J.; Li, L. Fibre Laser Welding of Dissimilar Alloys of Ti-6Al-4V and Inconel 718 for Aerospace Applications. *Int J Adv Manuf Technol* **2011**, *52* (9), 977–987.
- [26] Gao, M.; Wang, Z. M.; Li, X. Y.; Zeng, X. Y. Laser Keyhole Welding of Dissimilar Ti-6Al-4V Titanium Alloy to AZ31B Magnesium Alloy. *Metall Mater Trans A* **2012**, *43* (1), 163–172.
- [27] Chen, H.-C.; Bi, G.; Lee, B. Y.; Cheng, C. K. Laser Welding of CP Ti to Stainless Steel with Different Temporal Pulse Shapes. *Journal of Materials Processing Technology* **2016**, *231*, 58–65.
- [28] Chen, S.; Zhang, M.; Huang, J.; Cui, C.; Zhang, H.; Zhao, X. Microstructures and Mechanical Property of Laser Butt Welding of Titanium Alloy to Stainless Steel. *Materials & Design* **2014**, *53*, 504–511.

- [29] Zhang, Y.; Sun, D.; Gu, X.; Li, H. Strength Improvement and Interface Characteristic of Direct Laser Welded Ti Alloy/Stainless Steel Joint. *Materials Letters* **2018**, *231*, 31–34.
- [30] Cook, G. O.; Sorensen, C. D. Overview of Transient Liquid Phase and Partial Transient Liquid Phase Bonding. *J Mater Sci* **2011**, *46* (16), 5305–5323.
- [31] Mo, D.; Song, T.; Fang, Y.; Jiang, X.; Luo, C. Q.; Simpson, M. D.; Luo, Z. A Review on Diffusion Bonding between Titanium Alloys and Stainless Steels. *Advances in Materials Science and Engineering* **2018**, *2018*, 1–15.
- [32] Shirzadi, A. A.; Laik, A.; Tewari, R.; Orsborn, J.; Dey, G. K. Gallium-Assisted Diffusion Bonding of Stainless Steel to Titanium; Microstructural Evolution and Bond Strength. *Materialia* **2018**, *4*, 115–126.
- [33] Mukherjee, A. B.; Laik, A.; Kain, V.; Chakravartty, J. K. Shrinkage-Stress Assisted Diffusion Bonds Between Titanium and Stainless Steel: A Novel Technique. *J. of Materi Eng and Perform* **2016**, *25* (10), 4425–4436.
- [34] Kundu, S.; Chatterjee, S. Diffusion Bonding between Commercially Pure Titanium and Micro-Duplex Stainless Steel. *Materials Science and Engineering: A* **2008**, *480* (1), 316–322.
- [35] Ghosh, M.; Chatterjee, S. Characterization of Transition Joints of Commercially Pure Titanium to 304 Stainless Steel. *Materials Characterization* **2002**, *48* (5), 393–399.
- [36] Vigraman, T.; Ravindran, D.; Narayanasamy, R. Effect of Phase Transformation and Intermetallic Compounds on the Microstructure and Tensile Strength Properties of Diffusion-Bonded Joints between Ti–6Al–4V and AISI 304L. *Materials & Design (1980-2015)* **2012**, *36*, 714–727.
- [37] Ferrante, M.; Pigoretti, E. V. Diffusion Bonding of Ti-6Al-4V to AISI 316L Stainless Steel: Mechanical Resistance and Interface Microstructure. *Journal of Materials Science* **2002**, *37* (13), 2825–2833.
- [38] Kundu, S.; Sam, S.; Chatterjee, S. Evaluation of Interface Microstructure and Mechanical Properties of the Diffusion Bonded Joints of Ti–6Al–4V Alloy to Micro-Duplex Stainless Steel. *Materials Science and Engineering: A* **2011**, *528* (15), 4910–4916.
- [39] Kundu, S.; Sam, S.; Chatterjee, S. Interface Microstructure and Strength Properties of Ti–6Al–4V and Microduplex Stainless Steel Diffusion Bonded Joints. *Materials & Design* **2011**, *32* (5), 2997–3003.
- [40] Norouzi, E.; Atapour, M.; Shamanian, M. Effect of Bonding Time on the Joint Properties of Transient Liquid Phase Bonding between Ti–6Al–4V and AISI 304. *Journal of Alloys and Compounds* **2017**, *701*, 335–341.

References

- [41] Velmurugan, C.; Senthilkumar, V.; Sarala, S.; Arivarasan, J. Low Temperature Diffusion Bonding of Ti-6Al-4V and Duplex Stainless Steel. *Journal of Materials Processing Technology* **2016**, *234*, 272–279.
- [42] Wang, M.; Luo, Z.; Yang, J.; Xie, G.; Liu, Z. Diffusion Behavior and Formation Mechanism of Compounds in Titanium-Steel Bonding Process at High Temperature. *Materials Letters* **2023**, *330*, 133309.
- [43] Kumar, R. R.; Gupta, R. K.; Sarkar, A.; Prasad, M. J. N. V. Vacuum Diffusion Bonding of A-titanium Alloy to Stainless Steel for Aerospace Applications: Interfacial Microstructure and Mechanical Characteristics. *Materials Characterization* **2022**, *183*, 111607.
- [44] Akbarimousavi, S. A. A.; GohariKia, M. Investigations on the Mechanical Properties and Microstructure of Dissimilar Cp-Titanium and AISI 316L Austenitic Stainless Steel Continuous Friction Welds. *Materials & Design* **2011**, *32* (5), 3066–3075.
- [45] Gao, Y. F.; Nakata, K. Microstructural Characterization and Mechanical Properties of Friction-Stir-Welded Dissimilar Lap Joint of CP-Ti and Steel. In *Proceedings of the 1st International Joint Symposium on Joining and Welding*; Fujii, H., Ed.; Woodhead Publishing, 2013; pp 259–265.
- [46] Ishida, K.; Gao, Y.; Nagatsuka, K.; Takahashi, M.; Nakata, K. Microstructures and Mechanical Properties of Friction Stir Welded Lap Joints of Commercially Pure Titanium and 304 Stainless Steel. *Journal of Alloys and Compounds* **2015**, *630*, 172–177.
- [47] Li, S.; Chen, Y.; Zhou, X.; Kang, J.; Huang, Y.; Deng, H. High-Strength Titanium Alloy/Steel Butt Joint Produced via Friction Stir Welding. *Materials Letters* **2019**, *234*, 155–158.
- [48] Borrisutthekul, R.; Yachi, T.; Miyashita, Y.; Mutoh, Y. Suppression of Intermetallic Reaction Layer Formation by Controlling Heat Flow in Dissimilar Joining of Steel and Aluminum Alloy. *Materials Science and Engineering: A* **2007**, *467* (1), 108–113.
- [49] Szmul, M.; Stan-Glowinska, K.; Janusz-Skuza, M.; Bigos, A.; Chudzio, A.; Szulc, Z.; Wojewoda-Budka, J. The Interface Zone of Explosively Welded Titanium/Steel after Short-Term Heat Treatment. *Metall Mater Trans A* **2021**, *52* (5), 1588–1595.
- [50] Zhou, Q.; Liu, R.; Zhou, Q.; Chen, P.; Zhu, L. Microstructure Characterization and Tensile Shear Failure Mechanism of the Bonding Interface of Explosively Welded Titanium-Steel Composite. *Materials Science and Engineering: A* **2021**, *820*, 141559.
- [51] Guoyin, Z.; Xi, S.; Jinghua, Z. Interfacial Bonding Mechanism and Mechanical Performance of Ti/Steel Bimetallic Clad Sheet Produced by Explosive Welding and Annealing. *Rare Metal Materials and Engineering* **2017**, *46* (4), 906–911.
- [52] Chen, X.; Inao, D.; Tanaka, S.; Li, X.; Bataev, I. A.; Hokamoto, K. Comparison of Explosive Welding of Pure Titanium/SUS 304 Austenitic Stainless Steel and Pure Titanium/SUS 821L1

Duplex Stainless Steel. *Transactions of Nonferrous Metals Society of China* **2021**, 31 (9), 2687–2702.

[53] Bai, Y.-L.; Liu, X.-F.; Shi, Z.-Z. Stress-Induced Alternating Microstructures of Titanium/Steel Bonding Interface. *Materials Letters* **2021**, 298, 130019.

[54] Wu, Y.; Wang, T.; Ren, Z.; Liu, Y.; Huang, Q. Evolution Mechanism of Microstructure and Bond Strength Based on Interface Diffusion and IMCs of Ti/Steel Clad Plates Fabricated by Double-Layered Hot Rolling. *Journal of Materials Processing Technology* **2022**, 310, 117780.

[55] Wang, M.; Luo, Z.; Li, D.; Xie, G.; Misra, R. D. K. Investigation on the Interfacial Microstructure and Mechanical Properties of Ti Alloy/HSLA Steel Clad Plates Fabricated by Vacuum Roll-Cladding. *Materials Science and Engineering: A* **2022**, 853, 143774.

[56] Sahasrabudhe, H.; Harrison, R.; Carpenter, C.; Bandyopadhyay, A. Stainless Steel to Titanium Bimetallic Structure Using LENSTM. *Additive Manufacturing* **2015**, 5, 1–8.

[57] Rashkovets, M.; Mazzarisi, M.; Nikulina, A. A.; Casalino, G. Analysis of Laser Direct Stainless Steel Powder Deposition on Ti6Al4V Substrate. *Materials Letters* **2020**, 274, 128064.

[58] Kundu, S.; Chatterjee, S.; Olson, D.; Mishra, B. Effects of Intermetallic Phases on the Bond Strength of Diffusion-Bonded Joints between Titanium and 304 Stainless Steel Using Nickel Interlayer. *Metall Mater Trans A* **2007**, 38 (9), 2053–2060.

[59] He, P.; Zhang, J.; Zhou, R.; Li, X. Diffusion Bonding Technology of a Titanium Alloy to a Stainless Steel Web With an Ni Interlayer. *Materials Characterization* **1999**, 43 (5), 287–292.

[60] Kundu, S.; Chatterjee, S. Interfacial Microstructure and Mechanical Properties of Diffusion-Bonded Titanium–Stainless Steel Joints Using a Nickel Interlayer. *Materials Science and Engineering: A* **2006**, 425 (1), 107–113.

[61] Kundu, S.; Chatterjee, S. Characterization of Diffusion Bonded Joint between Titanium and 304 Stainless Steel Using a Ni Interlayer. *Materials Characterization* **2008**, 59 (5), 631–637.

[62] Lin, C.-M.; Rizi, M. S.; Chen, C.-K. Effects of Temperature on Interfacial Evolution and Mechanical Properties of Pure Titanium and Carbon Steel Sheets Bonded via New Multi-Pass Continuous Hot-Roll Diffusion with Nickel Interlayer. *Int J Adv Manuf Technol* **2022**, 119 (5), 2811–2823.

[63] Kundu, S.; Mishra, B.; Olson, D. L.; Chatterjee, S. Interfacial Reactions and Strength Properties of Diffusion Bonded Joints of Ti64 Alloy and 17-4PH Stainless Steel Using Nickel Alloy Interlayer. *Materials & Design* **2013**, 51, 714–722.

[64] Kundu, S.; Ghosh, M.; Laik, A.; Bhanumurthy, K.; Kale, G. B.; Chatterjee, S. Diffusion Bonding of Commercially Pure Titanium to 304 Stainless Steel Using Copper Interlayer. *Materials Science and Engineering: A* **2005**, 407 (1), 154–160.

References

- [65] Elrefaey, A.; Tillmann, W. Solid State Diffusion Bonding of Titanium to Steel Using a Copper Base Alloy as Interlayer. *Journal of Materials Processing Technology* **2009**, *209* (5), 2746–2752.
- [66] Xia, Y.; Dong, H.; Hao, X.; Li, P.; Li, S. Vacuum Brazing of Ti6Al4V Alloy to 316L Stainless Steel Using a Ti-Cu-Based Amorphous Filler Metal. *Journal of Materials Processing Technology* **2019**, *269*, 35–44.
- [67] Lee, J. G.; Hong, S. J.; Lee, M. K.; Rhee, C. K. High Strength Bonding of Titanium to Stainless Steel Using an Ag Interlayer. *Journal of Nuclear Materials* **2009**, *395* (1), 145–149.
- [68] He, P.; Yue, X.; Zhang, J. H. Hot Pressing Diffusion Bonding of a Titanium Alloy to a Stainless Steel with an Aluminum Alloy Interlayer. *Materials Science and Engineering: A* **2008**, *486* (1), 171–176.
- [69] Taufiqurrahman, I.; Lenggo Ginta, T.; Mustapha, M. The Effect of Holding Time on Dissimilar Resistance Spot Welding of Stainless Steel 316L and Ti6Al4V Titanium Alloy with Aluminum Interlayer. *Materials Today: Proceedings* **2021**, *46*, 1563–1568.
- [70] Shiue, R. K.; Wu, S. K.; Shiue, J. Y. Infrared Brazing of Ti–6Al–4V and 17-4 PH Stainless Steel with (Ni)/Cr Barrier Layer(s). *Materials Science and Engineering: A* **2008**, *488* (1), 186–194.
- [71] Kundu, S.; Thirunavukarasu, G. Structure and Properties Correlation of Diffusion Bonded Joint of Duplex Stainless Steel and Ti–6Al–4V with and without Ni–17Cr–9Fe Alloy Interlayer. *Weld World* **2016**, *60* (4), 793–811.
- [72] Lee, M. K.; Lee, J. G.; Choi, Y. H.; Kim, D. W.; Rhee, C. K.; Lee, Y. B.; Hong, S. J. Interlayer Engineering for Dissimilar Bonding of Titanium to Stainless Steel. *Materials Letters* **2010**, *64* (9), 1105–1108.
- [73] Fang, Y.; Jiang, X.; Song, T.; Mo, D.; Luo, Z. Pulsed Laser Welding of Ti-6Al-4V Titanium Alloy to AISI 316L Stainless Steel Using Cu/Nb Bilayer. *Materials Letters* **2019**, *244*, 163–166.
- [74] Mannucci, A.; Tomashchuk, I.; Bolot, R.; Mathieu, A.; Lafaye, S. Microstructure and Mechanical Properties of Dissimilar Ti/Nb/Cu/Steel Laser Joints. *Procedia CIRP* **2020**, *94*, 644–648.
- [75] Song, T. F.; Jiang, X. S.; Shao, Z. Y.; Fang, Y. J.; Mo, D. F.; Zhu, D. G.; Zhu, M. H. Microstructure and Mechanical Properties of Vacuum Diffusion Bonded Joints between Ti-6Al-4V Titanium Alloy and AISI316L Stainless Steel Using Cu/Nb Multi-Interlayer. *Vacuum* **2017**, *145*, 68–76.
- [76] Li, P.; Li, J.; Xiong, J.; Zhang, F.; Raza, S. H. Diffusion Bonding Titanium to Stainless Steel Using Nb/Cu/Ni Multi-Interlayer. *Materials Characterization* **2012**, *68*, 82–87.
- [77] Lee, J. G.; Lee, J. K.; Hong, S. M.; Lee, M. K.; Rhee, C. K. Microstructure and Bonding Strength of Titanium-to-Stainless Steel Joints Brazed Using a Zr–Ti–Ni–Cu–Be Amorphous Filler Alloy. *J Mater Sci* **2010**, *45* (24), 6837–6840.

- [78] Li, W.; Karnati, S.; Kriewall, C.; Liou, F.; Newkirk, J.; Brown Taminger, K. M.; Seufzer, W. J. Fabrication and Characterization of a Functionally Graded Material from Ti-6Al-4V to SS316 by Laser Metal Deposition. *Additive Manufacturing* **2017**, *14*, 95–104.
- [79] Bobbio, L. D.; Bocklund, B.; Simsek, E.; Ott, R. T.; Kramer, M. J.; Liu, Z.-K.; Beese, A. M. Design of an Additively Manufactured Functionally Graded Material of 316 Stainless Steel and Ti-6Al-4V with Ni-20Cr, Cr, and V Intermediate Compositions. *Additive Manufacturing* **2022**, *51*, 102649.
- [80] Gushchina, M. O.; Klimova-Korsmik, O. G.; Turichin, G. A. Direct Laser Deposition of Cu-Mo Functionally Graded Layers for Dissimilar Joining Titanium Alloys and Steels. *Materials Letters* **2022**, *307*, 131042.
- [81] Li, X.; Pan, C.; Fu, D.; Wang, M.; Zhang, Z.; Qu, S.; Yang, C. Fabrication of Highly Dissimilar TC4/Steel Joint with V/Cu Composite Transition Layer by Laser Melting Deposition. *Journal of Alloys and Compounds* **2021**, *862*, 158319.
- [82] Hannon, P. A Brief Review of Current Orthopedic Implant Device Issues: Biomechanics and Biocompatibility. *Biol Eng Med* **2016**, *1* (1).
- [83] *Standard Specification for Titanium and Titanium Alloy Bars and Billets*. <https://www.astm.org/standards/b348>.
- [84] *Cp-Ti Grade 1*. Advanced Powders. <https://www.ge.com/powders/titanium/cp-ti1>.
- [85] Luo, J.; Jia, X.; Gu, R.; Zhou, P.; Huang, Y.; Sun, J.; Yan, M. 316L Stainless Steel Manufactured by Selective Laser Melting and Its Biocompatibility with or without Hydroxyapatite Coating. *Metals* **2018**, *8* (7), 548.
- [86] da Rocha, S. S.; Adabo, G. L.; Henriques, G. E. P.; Nóbilo, M. A. de A. Vickers Hardness of Cast Commercially Pure Titanium and Ti-6Al-4V Alloy Submitted to Heat Treatments. *Braz Dent J* **2006**, *17* (2), 126–129.
- [87] https://www.epfl.ch/research/facilities/cime/wp-content/uploads/2019/02/EDX_2009.pdf
- [88] McSwiggen, P. Characterisation of Sub-Micrometre Features with the FE-EPMA. *IOP Conf. Ser.: Mater. Sci. Eng.* **2014**, *55*, 012009.
- [89] Castaing, R. Electron Probe Microanalysis. In *Advances in Electronics and Electron Physics*; Marton, L., Marton, C., Eds.; Academic Press, 1960; Vol. 13, pp 317–386.
- [90] Zeng, L.; Liu, L.; Huang, S.; Zhang, L. Experimental Investigation of Phase Equilibria in the Ti-Fe-Cr Ternary System. *Calphad* **2017**, *58*, 58–69.
- [91] Boriskina, N. G.; Kornilov, I. I. Investigation of the Iron-Chromium-Titanium Phase Diagram in a Region of Iron- and Chromium-Rich Alloys. *ARS Journal* **1961**, *31* (7), 961–966.
- [92] *Handbook of Ternary Alloy Phase Diagrams (10 Volume Set) - ASM International*. https://www.asminternational.org/search/-/journal_content/56/10192/57706G/PUBLICATION.

References

- [93] Ray, R.; Giessen, B. C.; Grant, N. J. The Constitution of Metastable Titanium-Rich Ti-Fe Alloys: An Order-Disorder Transition. *Metall Mater Trans B* **1972**, *3* (3), 627–629.
- [94] Vilar, R. 10.07 - Laser Powder Deposition. In *Comprehensive Materials Processing*; Hashmi, S., Batalha, G. F., Van Tyne, C. J., Yilbas, B., Eds.; Elsevier: Oxford, 2014; pp 163–216.
- [95] Reichardt, A.; Shapiro, A. A.; Otis, R.; Dillon, R. P.; Borgonia, J. P.; McEnerney, B. W.; Hosemann, P.; Beese, A. M. Advances in Additive Manufacturing of Metal-Based Functionally Graded Materials. *International Materials Reviews* **2021**, *66* (1), 1–29.
- [96] Bobbio, L. D.; Otis, R. A.; Borgonia, J. P.; Dillon, R. P.; Shapiro, A. A.; Liu, Z.-K.; Beese, A. M. Additive Manufacturing of a Functionally Graded Material from Ti-6Al-4V to Invar: Experimental Characterization and Thermodynamic Calculations. *Acta Materialia* **2017**, *127*, 133–142.
- [97] Sartika, V. D.; Choi, W. S.; Choi, G.; Han, J.; Chang, S.-J.; Ko, W.-S.; Grabowski, B.; Choi, P.-P. Joining Dissimilar Metal of Ti and CoCrMo Using Directed Energy Deposition. *Journal of Materials Science & Technology* **2022**, *111*, 99–110.
- [98] Pasang, T.; Pramana, S. S.; Kracum, M.; Misiolek, W. Z.; Aziziderouei, M.; Mizutani, M.; Kamiya, O. Characterisation of Intermetallic Phases in Fusion Welded Commercially Pure Titanium and Stainless Steel 304. *Metals* **2018**, *8* (11), 863.
- [99] Materials Science International Team, MSIT®; Ivanchenko, V.; Pryadko, T. Chromium – Iron – Titanium. In *Iron Systems, Part 3*; Effenberg, G., Ilyenko, S., Eds.; Landolt-Börnstein - Group IV Physical Chemistry; Springer Berlin Heidelberg: Berlin, Heidelberg, 2008; Vol. 11D3, pp 365–381.
- [100] Wang, S.; Wang, K.; Chen, G.; Li, Z.; Qin, Z.; Lu, X.; Li, C. Thermodynamic Modeling of Ti-Fe-Cr Ternary System. *Calphad* **2017**, *56*, 160–168.
- [101] Picasso, M.; Marsden, C. F.; Wagniere, J. D.; Frenk, A.; Rappaz, M. A Simple but Realistic Model for Laser Cladding. *MMTB* **1994**, *25* (2), 281–291.
- [102] Abioye, T. E.; Folkes, J.; Clare, A. T. A Parametric Study of Inconel 625 Wire Laser Deposition. *Journal of Materials Processing Technology* **2013**, *213* (12), 2145–2151.
- [103] Vundru, C.; Singh, R.; Yan, W.; Karagadde, S. A Comprehensive Analytical-Computational Model of Laser Directed Energy Deposition to Predict Deposition Geometry and Integrity for Sustainable Repair. *International Journal of Mechanical Sciences* **2021**, *211*, 106790.
- [104] Goodarzi, D. M.; Pekkarinen, J.; Salminen, A. Effect of Process Parameters in Laser Cladding on Substrate Melted Areas and the Substrate Melted Shape. *Journal of Laser Applications* **2015**, *27* (S2), S29201.
- [105] Taberero, I.; Lamikiz, A.; Martínez, S.; Ukar, E.; López de Lacalle, L. N. Modelling of Energy Attenuation Due to Powder Flow-Laser Beam Interaction during Laser Cladding Process. *Journal of Materials Processing Technology* **2012**, *212* (2), 516–522.

- [106] Li, T.; Zhang, L.; Bultel, G. G. P.; Schopphoven, T.; Gasser, A.; Schleifenbaum, J. H.; Poprawe, R. Extreme High-Speed Laser Material Deposition (EHLA) of AISI 4340 Steel. *Coatings* **2019**, *9* (12), 778.
- [107] Orhan, N.; Khan, T. I.; Eroğlu, M. Diffusion Bonding of a Microduplex Stainless Steel to Ti–6Al–4V. *Scripta Materialia* **2001**, *45* (4), 441–446.
- [108] Ghosh, M.; Bhanumurthy, K.; Kale, G. B.; Krishnan, J.; Chatterjee, S. Diffusion Bonding of Titanium to 304 Stainless Steel. *Journal of Nuclear Materials* **2003**, *322* (2–3), 235–241.
- [109] Fazel-Najafabadi, M.; Kashani-Bozorg, S. F.; Zarei-Hanzaki, A. Joining of CP-Ti to 304 Stainless Steel Using Friction Stir Welding Technique. *Materials & Design* **2010**, *31* (10), 4800–4807.
- [110] Mahmood, M. A.; Chioibas, D.; Ur Rehman, A.; Mihai, S.; Popescu, A. C. Post-Processing Techniques to Enhance the Quality of Metallic Parts Produced by Additive Manufacturing. *Metals* **2022**, *12* (1), 77.
- [111] Bermingham, M. J.; Nicastro, L.; Kent, D.; Chen, Y.; Dargusch, M. S. Optimising the Mechanical Properties of Ti-6Al-4V Components Produced by Wire + Arc Additive Manufacturing with Post-Process Heat Treatments. *Journal of Alloys and Compounds* **2018**, *753*, 247–255.
- [112] Ma, P.; Prashanth, K. G.; Scudino, S.; Jia, Y.; Wang, H.; Zou, C.; Wei, Z.; Eckert, J. Influence of Annealing on Mechanical Properties of Al-20Si Processed by Selective Laser Melting. *Metals* **2014**, *4* (1), 28–36.
- [113] Suryawanshi, J.; Singh, G.; Msolli, S.; Jhon, M. H.; Ramamurty, U. Tension-Compression Asymmetry and Shear Strength of Titanium Alloys. *Acta Materialia* **2021**, *221*, 117392.
- [114] *Shear Strength Metal Specifications | UniPunch Tooling Systems*. UniPunch. <https://unipunch.com/support/charts/material-specifications/>.
- [115] Li, S.; Chen, Y.; Kang, J.; Huang, Y.; Gianetto, J. A.; Yin, L. Interfacial Microstructures and Mechanical Properties of Dissimilar Titanium Alloy and Steel Friction Stir Butt-Welds. *Journal of Manufacturing Processes* **2019**, *40*, 160–168.
- [116] Alemán, B.; Gutiérrez, L.; Urcola, J. J. Interface Microstructures in Diffusion Bonding of Titanium Alloys to Stainless and Low Alloy Steels. *Materials Science and Technology* **1993**, *9* (8), 633–641.
- [117] Schur, R.; Ghods, S.; Schultz, E.; Wisdom, C.; Pahuja, R.; Montelione, A.; Arola, D.; Ramulu, M. A Fractographic Analysis of Additively Manufactured Ti6Al4V by Electron Beam Melting: Effects of Powder Reuse. *J Fail. Anal. and Preven.* **2020**, *20* (3), 794–803.
- [118] Pilchak, A. L.; Williams, J. C. Crystallography of Fluted Fracture in Near- α Titanium Alloys. *Metall Mater Trans A* **2010**, *41* (1), 22–25.

References

- [119] Valoppi, B.; Zhang, Z.; Deng, M.; Ghiotti, A.; Bruschi, S.; Ehmann, K. F.; Cao, J. On the Fracture Characterization in Double-Sided Incremental Forming of Ti6Al4V Sheets at Elevated Temperatures. *Procedia Manufacturing* **2017**, *10*, 407–416.
- [120] Haase, F.; Siemers, C.; Klinge, L.; Lu, C.; Lang, P.; Lederer, S.; König, T.; Rösler, J. Aluminum- and Vanadium-Free Titanium Alloys for Medical Applications. *MATEC Web Conf.* **2020**, *321*, 05008.
- [121] Nixon, R. C. C.; Hawkins, D. N. Nature of Fluted Fracture Observed in Welds in Titanium Plate. *Materials Science and Technology* **1989**, *5* (3), 288–292.
- [122] Zhang, Y.; Zhou, J.; Sun, D.; Gu, X. Nd:YAG Laser Welding of Dissimilar Metals of Titanium Alloy to Stainless Steel without Filler Metal Based on a Hybrid Connection Mechanism. *Journal of Materials Research and Technology* **2020**, *9* (2), 1662–1672.
- [123] Yadollahi, A.; Shamsaei, N.; Thompson, S. M.; Seely, D. W. Effects of Process Time Interval and Heat Treatment on the Mechanical and Microstructural Properties of Direct Laser Deposited 316L Stainless Steel. *Materials Science and Engineering: A* **2015**, *644*, 171–183.
- [124] Li, P.; Gong, Y.; Liang, C.; Yang, Y.; Cai, M. Effect of Post-Heat Treatment on Residual Stress and Tensile Strength of Hybrid Additive and Subtractive Manufacturing. *Int J Adv Manuf Technol* **2019**, *103* (5), 2579–2592.
- [125] Aversa, A.; Saboori, A.; Librera, E.; de Chirico, M.; Biamino, S.; Lombardi, M.; Fino, P. The Role of Directed Energy Deposition Atmosphere Mode on the Microstructure and Mechanical Properties of 316L Samples. *Additive Manufacturing* **2020**, *34*, 101274.
- [126] Saboori, A.; Aversa, A.; Bosio, F.; Bassini, E.; Librera, E.; De Chirico, M.; Biamino, S.; Ugues, D.; Fino, P.; Lombardi, M. An Investigation on the Effect of Powder Recycling on the Microstructure and Mechanical Properties of AISI 316L Produced by Directed Energy Deposition. *Materials Science and Engineering: A* **2019**, *766*, 138360.
- [127] Yang, N.; Yee, J.; Zheng, B.; Gaiser, K.; Reynolds, T.; Clemon, L.; Lu, W. Y.; Schoenung, J. M.; Lavernia, E. J. Process-Structure-Property Relationships for 316L Stainless Steel Fabricated by Additive Manufacturing and Its Implication for Component Engineering. *J Therm Spray Tech* **2017**, *26* (4), 610–626.
- [128] Morrow, B. M.; Lienert, T. J.; Knapp, C. M.; Sutton, J. O.; Brand, M. J.; Pacheco, R. M.; Livescu, V.; Carpenter, J. S.; Gray, G. T. Impact of Defects in Powder Feedstock Materials on Microstructure of 304L and 316L Stainless Steel Produced by Additive Manufacturing. *Metall Mater Trans A* **2018**, *49* (8), 3637–3650.
- [129] Mani, C.; Balasubramani, S.; Karthikeyan, R.; Kannan, S. Digital Image Correlation of Tensile Properties for Monel 400/SS 316L Dissimilar Metal Welding Joints. *Materials* **2021**, *14* (6), 1560.
- [130] Peng, J.; Peng, J.; Li, K.-S.; Pei, J.-F.; Zhou, C.-Y. Temperature-Dependent SRS Behavior of 316L and Its Constitutive Model. *Acta Metall. Sin. (Engl. Lett.)* **2018**, *31* (3), 234–244.

- [131] Hilders, O. A.; Zambrano, N.; Caballero, R. Microstructure, Strength, and Fracture Topography Relations in AISI 316L Stainless Steel, as Seen through a Fractal Approach and the Hall-Petch Law. *International Journal of Metals* **2015**, *2015*, e624653.
- [132] Su, Y. Y.; Wang, Z. F.; Xie, J. C.; Xu, G.; Xing, F.; Luo, K. Y.; Lu, J. Z. Microstructures and Mechanical Properties of Laser Melting Deposited Ti6Al4V/316L Functional Gradient Materials. *Materials Science and Engineering: A* **2021**, *817*, 141355.
- [133] Kumar, D.; Jhavar, S.; Arya, A.; Prashanth, K. G.; Suwas, S. Mechanisms Controlling Fracture Toughness of Additively Manufactured Stainless Steel 316L. *Int J Fract* **2022**, *235* (1), 61–78.
- [134] Vashishtha, H.; Taiwade, R. V.; Sharma, S.; Patil, A. P. Effect of Welding Processes on Microstructural and Mechanical Properties of Dissimilar Weldments between Conventional Austenitic and High Nitrogen Austenitic Stainless Steels. *Journal of Manufacturing Processes* **2017**, *25*, 49–59.
- [135] Zhong, Y.; Liu, L.; Wikman, S.; Cui, D.; Shen, Z. Intragranular Cellular Segregation Network Structure Strengthening 316L Stainless Steel Prepared by Selective Laser Melting. *Journal of Nuclear Materials* **2016**, *470*, 170–178.
- [136] Barkia, B.; Aubry, P.; Haghi-Ashtiani, P.; Auger, T.; Gosmain, L.; Schuster, F.; Maskrot, H. On the Origin of the High Tensile Strength and Ductility of Additively Manufactured 316L Stainless Steel: Multiscale Investigation. *Journal of Materials Science & Technology* **2020**, *41*, 209–218.
- [137] Corbin, D. J.; Nassar, A. R.; Reutzel, E. W.; Beese, A. M.; Michaleris, P. Effect of Substrate Thickness and Preheating on the Distortion of Laser Deposited Ti–6Al–4V. *Journal of Manufacturing Science and Engineering* **2018**, *140* (6).
- [138] Le Dantec, M. C. L. Additive Fabrication of Silicon Pillars on Monocrystalline Silicon by Direct Laser Melting, EPFL, Lausanne, **2018**.
- [139] Vasinonta, A.; Beuth, J. L.; Griffith, M. Process Maps for Predicting Residual Stress and Melt Pool Size in the Laser-Based Fabrication of Thin-Walled Structures. *Journal of Manufacturing Science and Engineering* **2006**, *129* (1), 101–109.
- [140] Suzuki, T.; Uehara, S. Mechanical Properties of FeTi, CoTi, and NiTi at Elevated Temperatures. *Proceedings of the 4th International* **1980**, *2* (5), 9.

References

Appendix D - Interface Control in Additive Manufacturing of Dissimilar Metals Forming Intermetallic Compounds—Fe-Ti as a Model System

Di Cui, Antaryami Mohanta and Marc Leparoux*

Empa–Swiss Federal Laboratories for Materials Science and Technology, Laboratory for Advanced Materials Processing, Feuerwerkerstrasse 39, CH–3602 Thun, Switzerland

* Correspondence: marc.leparoux@empa.ch; Tel.: +4158-765-62-47

Abstract: Laser metal deposition (LMD) has demonstrated its ability to produce complex parts and to adjust material composition within a single workpiece. It is also a suitable additive manufacturing (AM) technology for building up dissimilar metals directly. However, brittle intermetallic compounds (IMCs) are formed at the interface of the dissimilar metals fabricated by LMD. Such brittle phases often lead to material failure due to thermal expansion coefficient mismatch, thermal stress, etc. In this work, we studied a Fe-Ti system with two brittle phases, such as FeTi and Fe₂Ti, as a model system. Fe was grown on top of Ti at various process parameters. The morphologies and microstructures were characterized by optical microscopy (OM) and scanning electron microscopy (SEM). No cracks along the interface between pure Ti and bottom of the solidified melt pool were observed in the cross-sectional images. Chemical composition in the fabricated parts was measured by Energy-dispersive X-ray spectroscopy (EDS). Electron backscatter diffraction (EBSD) was performed in addition to EDS to identify the crystalline phases. The Vickers hardness test was conducted in areas with different phases. The chemical composition in the melt pool region was found to be a determining factor for the occurrence of major cracks.

Keywords: laser metal deposition; dissimilar metals; intermetallic compounds; chemical composition; microhardness

1. Introduction

Laser metal deposition (LMD) is an advanced powder-injective laser additive manufacturing (AM) technology, which is capable of directly producing dense metal parts with complex geometry and especially with varying composition. The ability of LMD has been demonstrated in the fields of rapid manufacturing, repairing, and remanufacturing of metallic components [1]. Thanks to convenient switching of powder feedstock during the deposition process, LMD has a unique advantage in fabricating a workpiece of dissimilar metals.

Titanium alloys exhibit a high strength-to-weight ratio, biocompatibility, and superior heat and corrosion resistance. Therefore, they are considered as excellent engineering materials in biomedical, aerospace, automobile, nuclear, and many other industries [1]. Stainless steel (SS) has been widely used in the fields of automobile, petrochemical, construction, power generation, and medical devices due to its excellent mechanical properties, corrosion resistance, good weldability, and low cost [2]. In order to combine good

mechanical and metallurgical properties with a more affordable cost, there is increasing interest in joining Ti (-alloy) and SS [3] [4] [5] [6].

Various techniques, including LMD, have been employed to join Ti (-alloy) and SS [1,4,7,8]. All have been confronted with cracking issues due to the presence of FeTi and Fe₂Ti brittle intermetallic compounds (IMCs) at the interface. A Fe-Ti phase diagram showing the different phases that may form at equilibrium is presented in Figure 1 [9].

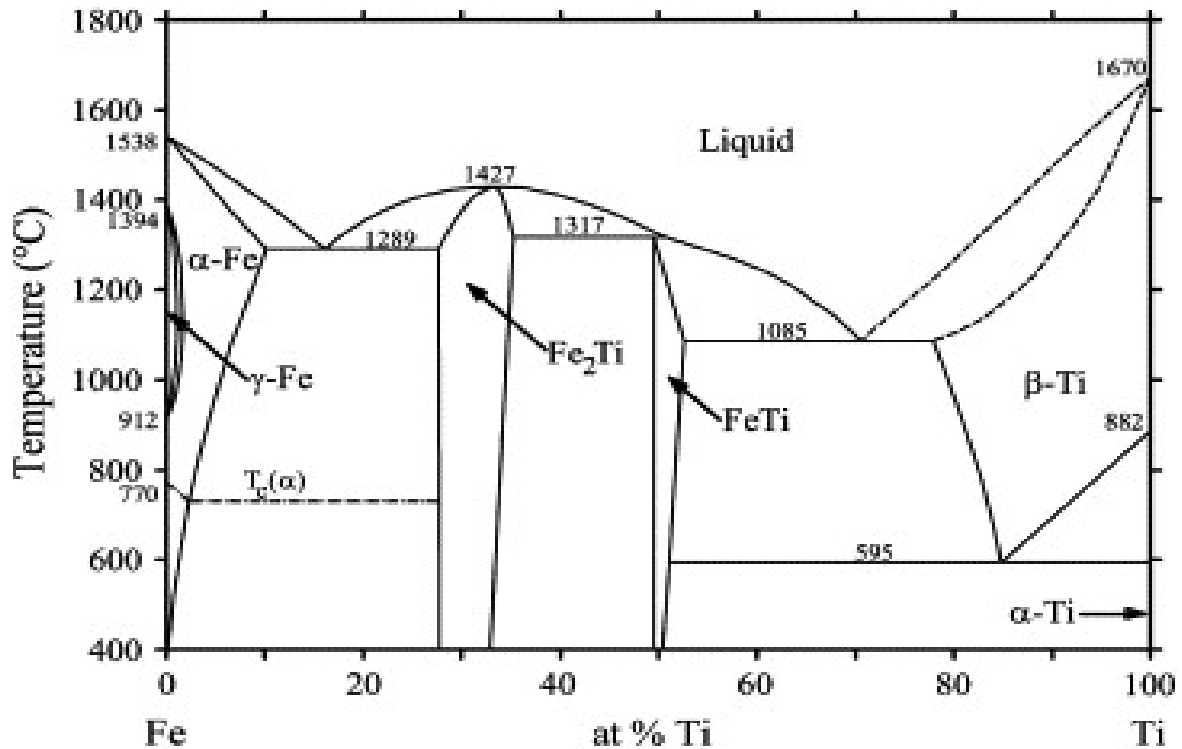


Figure 1. Phase diagram of Fe-Ti binary system. Reprinted from [9] with permission from Elsevier.

Chen et al. [4] used direct laser welding to join Ti and SS304 with the laser beam centered on the contact line. The ultimate tensile strength (UTS) of the joint was only 65 MPa, and continuous distribution of large amounts of Ti-Fe IMCs was found at the interface. Offsetting the laser beam by 0.6 mm toward SS304 increased the UTS to 150 MPa. Smaller and discontinuous Ti-Fe IMC zones were formed in the weld thanks to the reduction of melted Ti. Zhang et al. [8] achieved a UTS of 336 MPa in a joint between Ti6Al4V and SS301L by offsetting the laser beam by 0.45 mm toward Ti6Al4V. They inferred that the temperature at the contact line was below the melting point of Ti6Al4V and above that of the β-Ti + FeTi eutectic. Atomic interdiffusion promoted by the elevated temperature created eutectic liquid locally at the contact line, which later expanded. Fe and Ti in the liquid further diffused into Ti6Al4V and SS301L, respectively, to form a β-Ti(Fe) solid solution and Fe₂Ti IMC. The UTS increased thanks to the finer eutectic structure. Li et al. [1] tried to directly deposit SS316 on Ti6Al4V using LMD with a 2 mm wide laser beam. The deposited layer fell off from the substrate with a clear cracking sound. The researchers then inferred that it is impossible to join the two directly with their setup, and proceeded with a transition route with three filler materials (Ti6Al4V-V-Cr-Fe-SS316) to avoid the formation of Ti-Fe IMCs. A smooth gradient in hardness and composition was achieved from Ti6Al4V through interlayers to SS316. This approach provided a solution for crack-free joining under certain circumstances. However, the non-

biocompatible elements V and Cr used as adaptation layers limited the application of this solution in the medical industry [8].

Despite the interest of building parts out of Ti and stainless steel, no direct joining using an additive manufacturing approach has been reported to the best of the authors' knowledge. Most of the elements of the stainless steel may form intermetallic compounds among them, like σ FeCr, or by reaction with Titanium like α Cr₂Ti, β Cr₂Ti, γ Cr₂Ti, Ti₅Cr₇Fe₁₇, Ti₅Cr₈Fe₁₆, etc. [10] In this fundamental study aiming at understanding the formation of the different phases at the interfacial zone during a laser deposition process, the material system has been simplified to Ti and Fe. Iron is indeed the main constituent of SS and both the FeTi and Fe₂Ti IMCs, reported as main critical brittle phases during the joining of Ti(-alloy) and SS, may also form during the laser processing. The morphology, microstructure, chemical composition, and microhardness of the material and the interfacial zone were investigated as a function of the main AM processing parameters.

2. Materials and Methods

2.1. Materials

Ti Grade 1 plates with a thickness of 4mm (Zapp AG, Ratingen, Germany) were used as substrate for depositing Fe. Non-spherical Fe micropowder (Shanghai Knowhow Powder-tech Co., Ltd., Shanghai, China) sieved for 45–125 μ m was used as feedstock for the deposition. According to the provider's certificate, Fe purity is 99.5 wt.%.

2.2. Deposition of Fe on Ti

A commercial LMD machine (Mobile 1.0, BeAM, Strasbourg, France) was used for building the 3D structures in the shape of single tracks and single walls.

An airtight process chamber of the LMD system offered the possibility to work under a controlled atmosphere. A continuous wave (CW) fiber laser with a maximum power of 500 W, operating at a wavelength of 1068 nm (YLR-Series, IPG Photonics), was used as the energy source. The laser has a Gaussian transverse profile and the focal spot diameter of the laser is about 800 μ m. A volumetric powder feeder (Medicoat AG, Mägenwil, Switzerland) was equipped with two powder containers. The interior of the process chamber and the powder feeder with two powder containers are shown in Figure 2.

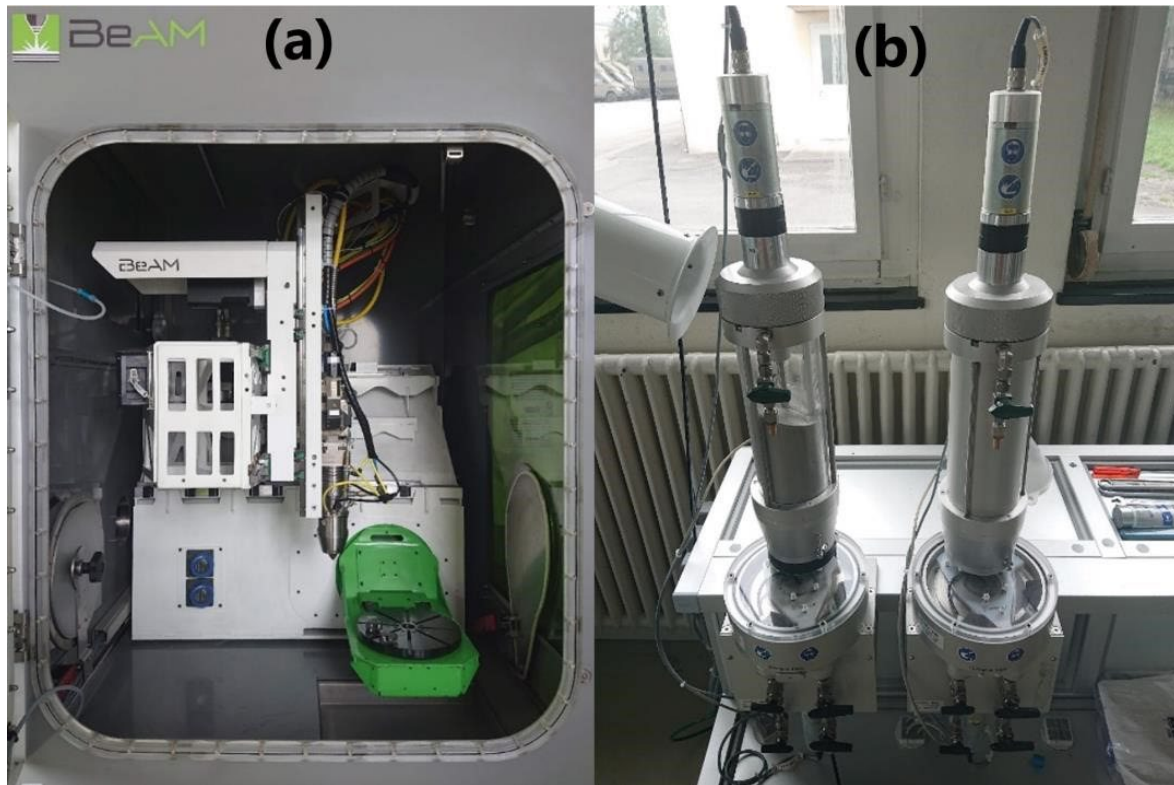


Figure 2. (a) The interior of the process chamber of the laser metal deposition (LMD) machine. (b) The powder feeder with two powder containers.

The Fe microscale powder was fed by the volumetric conventional powder feeder and injected coaxially to the laser spot in the process zone through a specific conical nozzle. The focus distance of both the laser beam and the nozzle for the powder jet was 3.5 mm. The nozzle was supported by a 3 axes system (x, y, z) and the substrate was fixed on a 2 rotative-axes holder (a, b). The samples were produced in argon atmosphere (40 ppm O₂, 200 ppm H₂O).

The key parameters of the deposition process are scan speed (S), laser power (P), and powder feed rate (F). The ratio P/S characterizes the linear energy (LE). Additionally, for wall samples, NL is the final number of layers deposited on the same position. Each spot on the line was irradiated once during the deposition of each layer of the wall, and the interval between two subsequent irradiations is the cooling time (CT). All single tracks and walls were designed to be 10 mm long. During printing of the walls, the nozzle always moved up by 0.2 mm to start a subsequent layer. Speed, power, and feed rate were studied in groups Line_S, Line_P, Line_LE, and Line_F, respectively. In group Wall_NL, NL increased from 1 to 5 with a CT of 3 s for all walls. In group Wall_CT, CT decreased from 8 to 1 s with an NL of 3 for all walls. The parameters for all samples are summarized in Table 1. The combination of power of 150 W, speed of 1000 mm/min, and feed rate of 4.8 g/min is referred to as the standard parameter. Single tracks and walls deposited with the standard parameters are marked light and dark grey, respectively, in Table 1.

Table 1. Parameters used for all samples.

Group	No.	P (W)	S (mm/min)	F (g/min)	NL	CT (s)	LE (J/mm)
Line_S	1	150	500	4.8	1	/	18.0
	2	150	750	4.8	1	/	12.0
	3	150	1000	4.8	1	/	9.0
	4	150	1500	4.8	1	/	6.0
	5	150	2000	4.8	1	/	4.5
Line_P	1	75	1000	4.8	1	/	4.5
	2	100	1000	4.8	1	/	6.0
	3	150	1000	4.8	1	/	9.0
	4	200	1000	4.8	1	/	12.0
	5	300	1000	4.8	1	/	18.0
Line_LE	1	75	500	4.8	1	/	9.0
	2	100	665	4.8	1	/	9.0
	3	150	1000	4.8	1	/	9.0
	4	200	1330	4.8	1	/	9.0
	5	300	2000	4.8	1	/	9.0
Line_F	1	150	1000	2.4	1	/	9.0
	2	150	1000	3.6	1	/	9.0
	3	150	1000	4.8	1	/	9.0
	4	150	1000	5.8	1	/	9.0
	5	150	1000	6.8	1	/	9.0
Wall_NL	1	150	1000	4.8	1	3	9.0
	2	150	1000	4.8	2	3	9.0
	3	150	1000	4.8	3	3	9.0
	4	150	1000	4.8	4	3	9.0
	5	150	1000	4.8	5	3	9.0
Wall_CT	1	150	1000	4.8	3	8	9.0
	2	150	1000	4.8	3	5	9.0
	3	150	1000	4.8	3	3	9.0
	4	150	1000	4.8	3	2	9.0
	5	150	1000	4.8	3	1	9.0

2.3. Characterization Methods

The produced samples were cut perpendicular to the laser scanning directions into halves. Each sample then had two parts. The cross-sections were then embedded in Demotec 4000 resin, ground up to 2500 grit with SiC grinding paper, and polished with 6 and 3 μm diamond pastes, and finally, with an OPS solution (0.04 μm SiO_2 with 10% H_2O_2).

Cross-sectional morphology and microstructure were examined with an optical microscope (OM) (ZEISS Axioplan, Munich, Germany) and a scanning electron microscope (SEM—Mira Tescan 3, Brno, Czech Republic). An energy-dispersive X-ray spectrometer (EDS—Ametek Edax Octane plus, Mahwah, NJ, USA) was used to investigate the elemental spatial distribution. An electron backscatter diffraction camera (EBSD—Ametek, Mahwah, NJ, USA) was used to investigate the crystalline structure. The Vickers hardness was measured with a load of 10 or 100 g and a dwell time of 10 s (ESI Prüftechnik GmbH, LMA-302-VLX, Wendlingen, Germany).

3. Results and Discussion

As seen in Table 1, one standard processing condition set was repeated at least five times for assessing the reproducibility of the LMD process. Therefore, two geometrical characteristics, such as deposition height and penetration depth, were measured for each cross-section. The deposition height (H) is the height of the solidified melt pool above the surface of the substrate and has an average of $67\ \mu\text{m}$, a standard deviation of $13\ \mu\text{m}$, and a coefficient of variation of 19.5. The penetration depth (D) is the depth of the solidified melt pool below the surface of the substrate and has an average of $35\ \mu\text{m}$, a standard deviation of $3\ \mu\text{m}$, and a coefficient of variation of 7.7. $H + D$ corresponds to the total height of the deposited material including the mixing with the substrate material. In the following, a general error on the geometrical measurements for H and D is defined based on these coefficients of variation for all the experiments.

3.1. Group Line_S

Single line samples (group Line_S) were fabricated with increasing scan speed at a constant laser power and powder feed rate. OM images of cross-sections and measured geometries, i.e., the penetration depth D into the substrate and the height of the deposited layer H , of these samples are shown in Figure 3.

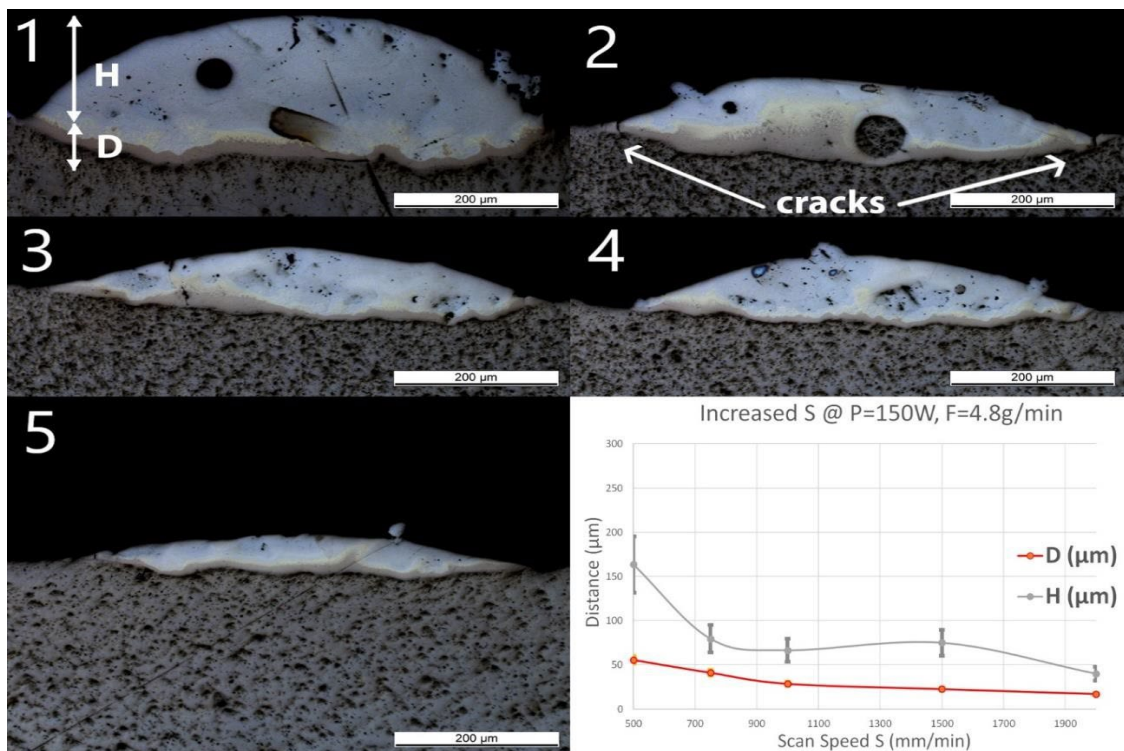


Figure 3. Optical microscopy (OM) images of cross-sections of samples Line_S_1 to Line_S_5 (The inserted number 1 to 5 corresponds to the sample number in Table 1). The last diagram (bottom right) shows the influence of speed (S) on penetration depth (D) and deposition height (H) of the tracks.

A spherical pore with a diameter of around $50\ \mu\text{m}$ was observed in Line_S_1. One unmelted particle with a diameter around $70\ \mu\text{m}$ observed in Line_S_2 was identified as Nb contamination from previous

experiments. In this experimental series, neither cracks nor delamination at the interface between the substrate and the deposited track could be observed, even though small and discontinuous cracks have been found in the deposited layer. Some long straight lines crossing the substrate and the layer might still be observed on the cross-sections as, for instance, in Figure 3(Line_S_1). These lines were produced by the polishing process.

As the scan speed increased, both H and D of the single track decreased. H decreased from 164 ± 33 to 40 ± 8 μm , whereas D decreased from 56 ± 4 to 17 ± 1 μm . A brown thin band with varying thickness appeared at the bottom of each track. EDS line scans have been done across the interface and the deposition to obtain atomic concentrations of Ti and Fe. All scan lines were vertical, starting from pure Ti slightly below the interface to the top of the deposition. The EDS line scan across the sample Line_S_1 is shown as an example in Figure 4 on the right. The scale of the line scan has been adapted to the layer thickness of the corresponding sample shown in Figure 4 on the left.

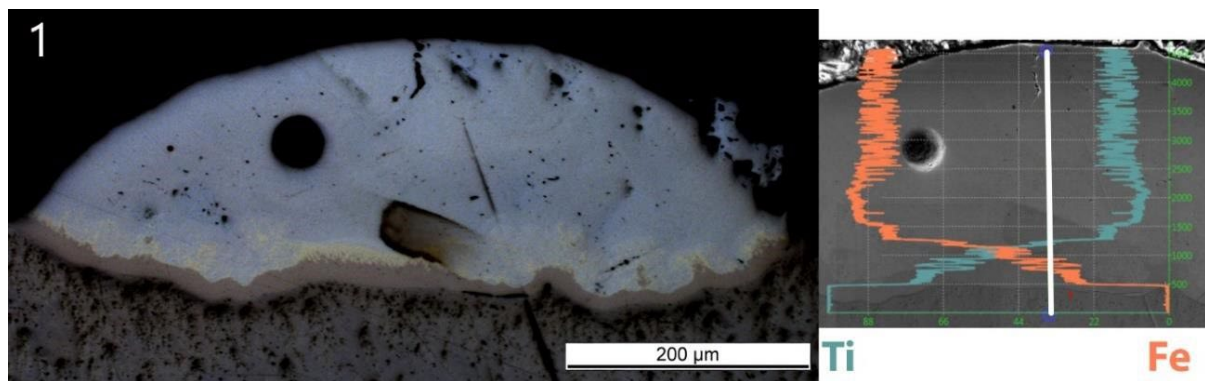


Figure 4. OM image of Sample Line_S_1 (left) and its energy-dispersive X-ray spectrometry (EDS) line scan result with the same scale (right). The scan was conducted along the white line. Vertical coordinate is the position on the scan line. Horizontal coordinate is the atomic concentration with 100 on the left. The cyan curve starting from 100 at the bottom (Ti substrate) is atomic concentration of Ti. The orange curve starting from 0 at the bottom is atomic concentration of Fe.

The composition changes sharply from Ti in the substrate to $\text{Fe}_{30}\text{Ti}_{70}$ (at.) in the brown band corresponding to the $\beta\text{-Ti} + \text{FeTi}$ eutectic in the phase diagram. On top of the Ti-rich eutectic band, a discontinuous yellowish phase was observed with a composition corresponding to $\text{Fe}_{50}\text{Ti}_{50}$ by EDS point analysis. Further up to the top of the deposited track, the concentration changes to $\text{Fe}_{90}\text{Ti}_{10}$, corresponding to the solubility limit of Ti in $\alpha\text{-Fe}$, and fluctuates around that. The upper part of all tracks exhibits a similar light grey color.

3.2. Group Line_P

No material was deposited for $P \leq 100$ W (samples Line_P1 and P2). Thus, only the samples deposited at higher powers are presented in Figure 5. A spherical pore with a diameter of around 60 μm was observed in Line_P_3. No crack or delamination at the interface was observed for all the samples. A crack crossing the entire deposited track was found in Line_P_4 and Line_P_5. No crack penetrated into the Ti substrate.

As the laser power increased, D predominantly increased from 30 ± 2 to $280 \pm 20 \mu\text{m}$, whereas the influence of the power on H was not significant. The same Ti-rich eutectic band was found in all three samples, and this band in Line_P_5 is obviously wider. The optically visible features and chemical composition profile of Line_P_3 are in accordance with Line_S_3, which was fabricated with the standard parameters. As P increased, the amount of yellowish phase increased. In Line_P_4, the composition changes from Ti to $\text{Fe}_{30}\text{Ti}_{70}$ in the brown band, then fluctuates between $\text{Fe}_{30}\text{Ti}_{70}$ and $\text{Fe}_{50}\text{Ti}_{50}$, and finally, between $\text{Fe}_{50}\text{Ti}_{50}$ and $\text{Fe}_{60}\text{Ti}_{40}$. In Line_P_5, the composition changes from Ti to $\text{Fe}_{30}\text{Ti}_{70}$ in the brown band, then fluctuates between $\text{Fe}_{30}\text{Ti}_{70}$ and $\text{Fe}_{50}\text{Ti}_{50}$, and finally, between $\text{Fe}_{50}\text{Ti}_{50}$ and $\text{Fe}_{40}\text{Ti}_{60}$.

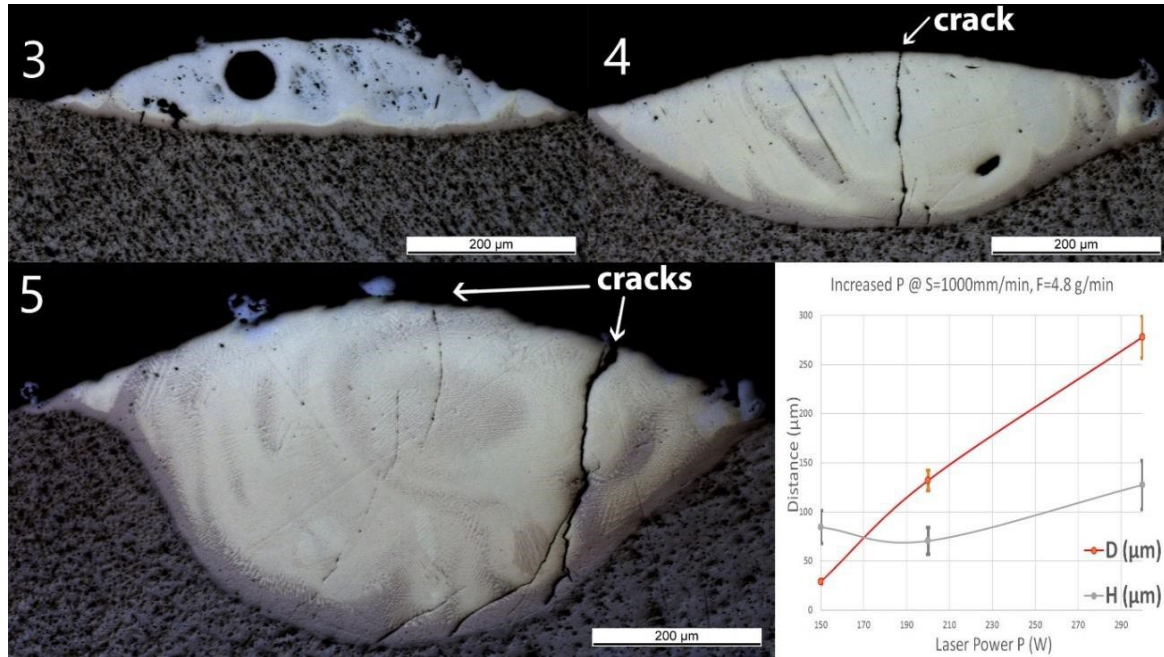


Figure 5. OM images of cross-sections of samples Line_P_3 to Line_P_5 (corresponding to the inserts 3 to 5 in the images above). The last diagram (bottom right) shows the influence of power (P) on penetration depth (D) and deposition height (H) of the tracks.

3.3. Group Line_LE

The results in the Line_LE samples produced with a constant P/S but variation of P and S were very similar to that of Line_P samples. OM images of the cross-sections with atomic concentration overlay and measured geometries are shown in Figure 6. Spherical pores with diameters of around $10 \mu\text{m}$ were observed in Line_LE_3. Pores with diameters of around $50 \mu\text{m}$ were observed in both Line_LE_3 and Line_LE_5. No cracks or delamination at the interface were observed for all the samples. A crack crossing almost the entire deposited track was found in Line_LE_4 and Line_LE_5. No crack penetrated into the Ti substrate.

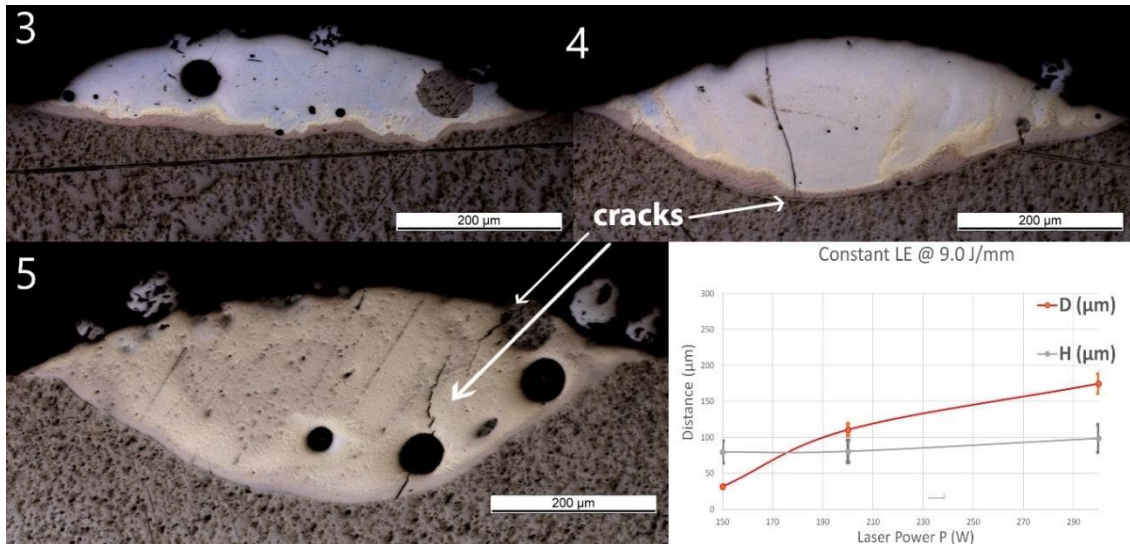


Figure 6. OM images of cross-sections of samples Line_LE_3 to Line_LE_5. The last diagram (bottom right) shows the influence of power (P) (together with proportionally increased speed S, maintaining a constant laser energy of $LE = 9.0 \text{ J/mm}$) on penetration depth (D) and deposition height (H) of the tracks.

As P and S increased proportionally, H increased slightly from 80 ± 16 to $99 \pm 20 \mu\text{m}$. D increased, however, significantly from 32 ± 2 to $111 \pm 9 \mu\text{m}$, and finally, to $175 \pm 13 \mu\text{m}$. The optically visible features and chemical composition profile of Line_P_3 are in accordance with standard samples, confirming the reproducibility of the process. In Line_LE_4, the composition changes from Ti to $\text{Fe}_{30}\text{Ti}_{70}$ in the brown band, then fluctuates around $\text{Fe}_{60}\text{Ti}_{40}$ up to the top of the layer. In Line_LE_5, the composition changes from Ti to $\text{Fe}_{30}\text{Ti}_{70}$ in the brown band, then fluctuates between $\text{Fe}_{30}\text{Ti}_{70}$ and $\text{Fe}_{50}\text{Ti}_{50}$.

3.4. Group Line_F

Samples in group Line_F have been fabricated with an increasing powder feed rate at a constant laser power and scan speed. No cracks or delamination at the interface were observed for all the samples. As F increased from 2.4 to 6.8 g/min, H decreased from 86 ± 17 to $52 \pm 10 \mu\text{m}$, and D fluctuated around $30 \mu\text{m}$ with no obvious trend. The composition transitions are similar for all samples and comparable to the changes observed in the standard samples. The composition in the upper part of Line_F_5 is $\text{Fe}_{66}\text{Ti}_{33}$, indicating the presence of a Fe_2Ti IMC for the highest investigated feed rate of 6.8 g/min.

3.5. Group Wall_NL

After single track experiments, multilayer walls have been produced using the standard parameters. The number of layers has been increased from 1 to 5 and a constant cooling time of 3 s between two subsequent depositions has been applied. OM pictures of the cross-sections with measured geometries are shown in Figure 7. A few small cracks were found in Wall_NL_3 and Wall_NL_4 through the Ti-rich eutectic band and a few large spherical pores are visible. No cracks or delamination through the interface were observed for all samples.

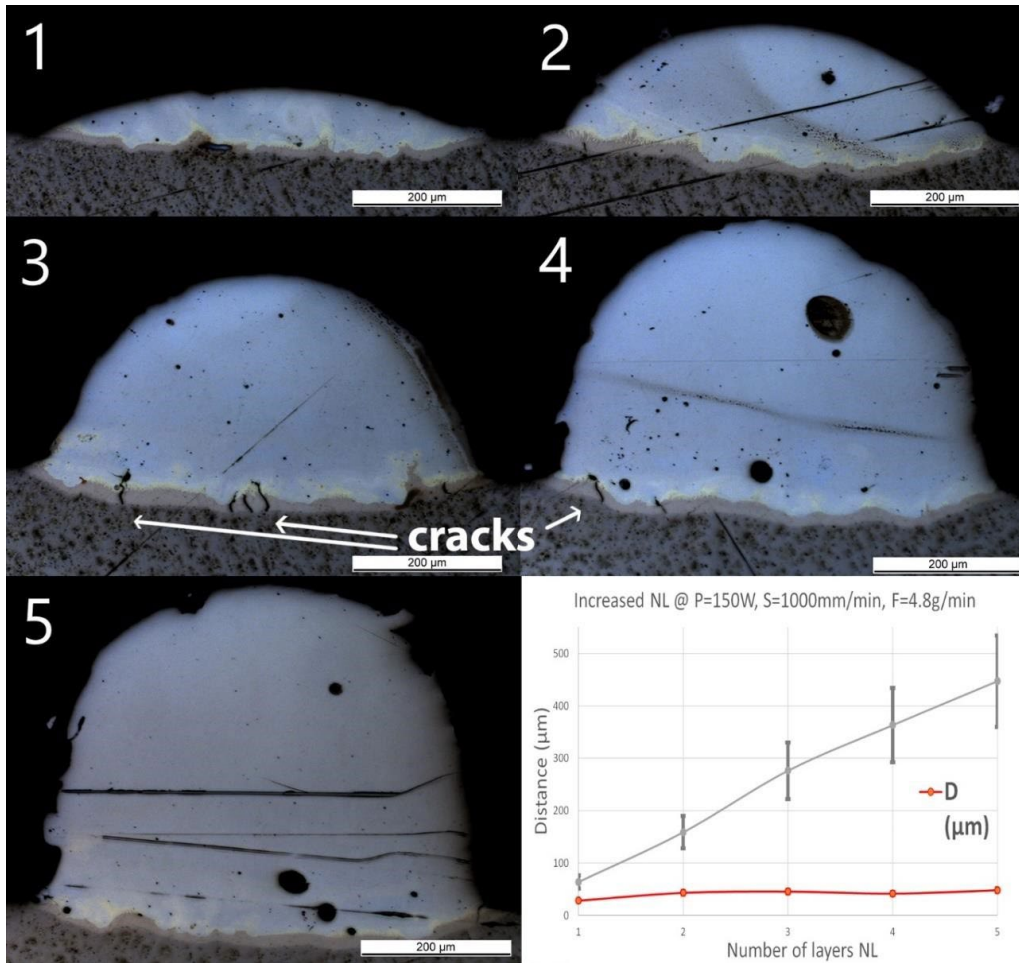


Figure 7. OM images of cross-sections of samples Wall_NL_1 to Wall_NL_5. The last diagram (bottom right) shows the influence of number of layers (NL) on penetration depth (D) and deposition height (H) of the tracks.

The optical microscope pictures did not allow distinction of the interface between the two subsequent layers. However, H increased almost linearly with the number of layers from 60 ± 12 to 450 ± 90 μm, showing an average increase of around 100 μm per additional layer. D slightly increased from 30 ± 2 μm for one layer (Wall_NL_1) to 40 ± 3 μm for the two-layer sample (Wall_NL_2). The deposition of additional layers does not seem to increase the penetration depth, which remains around 40 μm. Composition in Wall_NL_1 reached Fe₈₀Ti₂₀ within the first 50 μm and this composition remained until the top of the track. For the other samples, the compositions all reached Fe₉₀Ti₁₀ in the first 100 μm, and then, gradually shifted to almost pure Fe.

3.6. Group Wall_CT

Considering the standard deposition parameters, the cooling time between two deposition steps was varied from 8 to 1 s. Only three layers were deposited. Similar to the previous samples, small cracks and voids were observed, although no delamination or cracks were observed along the interface. The cooling time seems to have no influence on the penetration depth and only a slight increase in height is observed for CT < 3 s. Additionally, the composition transitions are similar to the one measured in Wall_NL samples. Therefore, the cross-sections of these samples were not depicted here.

3.7. Microhardness, EDS, and EBSD Results from Line_P_5 and Wall_NL_5

To assess the hardness of the different IMCs as well as the pure metals, indents were performed on some samples. The corresponding local Vickers microhardness values are presented in Figure 8 for the samples Line_P_5 and Wall_NL_5.

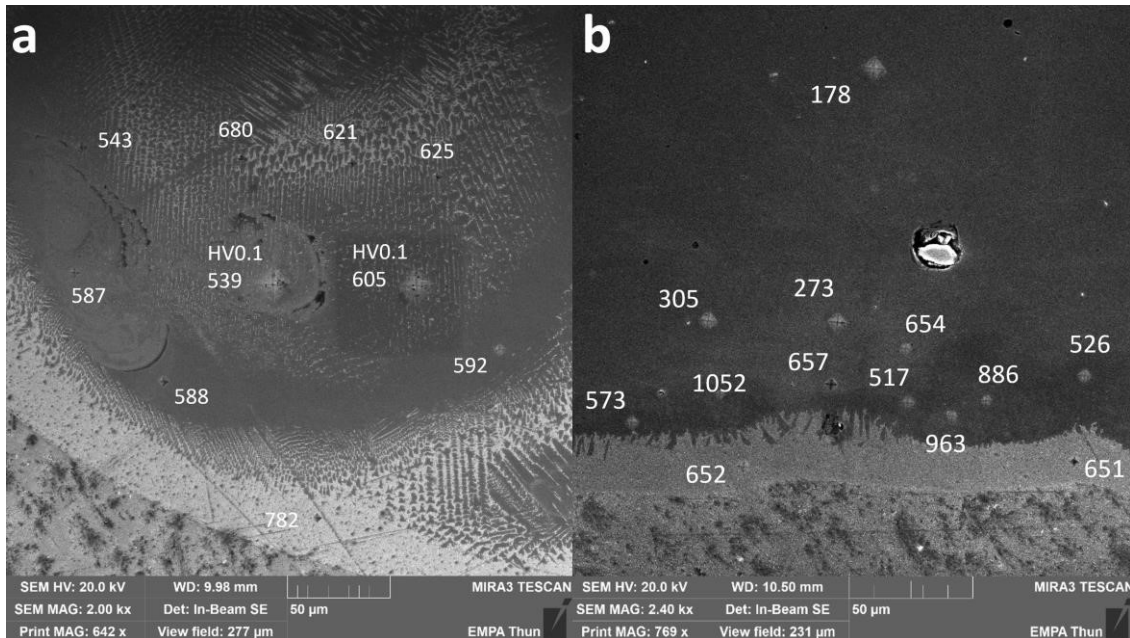


Figure 8. SEM images of cross-sections of (a) Line_P_5 and (b) Wall_NL_5. Numbers without specification are HV0.01 values. Two points were measured as HV0.1 to compare with results from multiple grains covered.

In Line_P_5, 736 ± 46 HV_{0.01} was measured in the Ti-rich eutectic band and 598 ± 82 HV_{0.01} in the main body of the track with an estimated composition fluctuating between Fe₃₀Ti₇₀ and Fe₅₀Ti₅₀.

In Wall_NL_5, microhardness is 652 ± 1 HV_{0.01} in the Ti-rich eutectic band. A jump to as high as 1052 HV_{0.01} was found slightly above the band, where the average microhardness is 967 ± 85 HV_{0.01}. Then, the microhardness decreases gradually to 178 ± 10 HV_{0.01} in the wall body.

Multipoint EDS measurements have been done in the bottom left area in Figure 8b around the highest measured microhardness, i.e., 1052 HV_{0.01}. Corresponding microhardness and possible phases are shown in Table 2. Crystal structures are taken from the Springer Materials database [11].

Table 2. Compositions obtained by EDS point analyses with corresponding microhardness and possible phases with their crystalline structure that can be found in the Fe-Ti phase diagram in Figure 1.

Composition (Atomic Ratio)	HV _{0.01}	Phases
Ti	154 ± 18	α-Ti (h.c.p.)
Fe ₃₀ Ti ₇₀	652 ± 1	Eutectic of β-Ti (b.c.c.) and FeTi (b.c.c.)
Fe ₅₀ Ti ₅₀	539 ± 22	FeTi (b.c.c.)
Fe ₇₃ Ti ₂₇	967 ± 85	Solubility limit of Fe in Fe ₂ Ti (h.c.p.)
Fe ₈₄ Ti ₁₆	656 ± 2	Eutectic of Fe ₂ Ti (h.c.p.) and α-Fe (b.c.c.)
Fe ≥ 90%	252 ± 74	Basically α-Fe (b.c.c.)

A SEM image taken at the upper border of the Ti-rich eutectic band in Wall_NL_5 is shown in Figure 9a. EBSD was performed in a slightly larger area. An image quality (IQ) map obtained from EBSD is shown in Figure 9b, whereas the phase map with the Confidence Index (CI) is shown in Figure 9c. As phases with the same atom arrangement and similar lattice parameters cannot be distinguished with EBSD, b.c.c. generic and h.c.p. generic were used for indexing. Morphologies observed in the SEM image (Figure 9a) are also found in the IQ map (Figure 9b). The $\text{Fe}_{30}\text{Ti}_{70}$ area according to EDS measurements was indexed as b.c.c. with relatively low CI, corresponding to the eutectic between $\beta\text{-Ti}$ (b.c.c.) and FeTi (b.c.c.). The $\text{Fe}_{50}\text{Ti}_{50}$ area was indexed as b.c.c. with the same structure as FeTi. The thin $\text{Fe}_{73}\text{Ti}_{27}$ band was indexed as h.c.p. with relatively low CI and could correspond to Fe_2Ti . In the $\text{Fe}_{84}\text{Ti}_{16}$ area, two lamella structures with thickness of 100~300 nm were observed. The lamella structure with higher IQ (brighter in the IQ map) was indexed as b.c.c. with high CI, corresponding to $\alpha\text{-Fe}$. The other lamella structure with lower IQ was indexed as h.c.p. with low CI, corresponding to Fe_2Ti . The transition through FeTi and Fe_2Ti IMCs is limited within a small thickness of 4 μm in the investigated area.

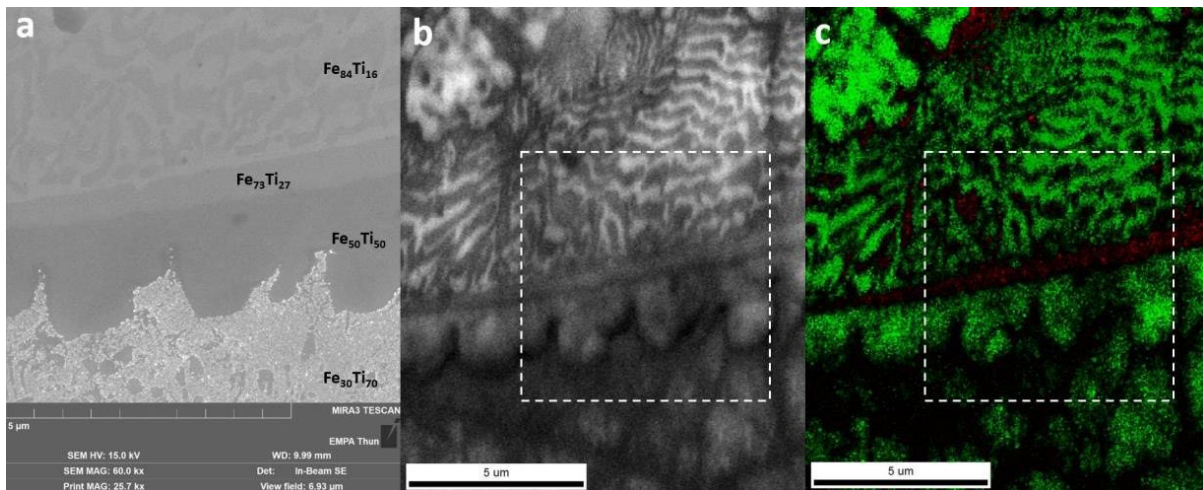


Figure 9. (a) SEM image of the upper border of the Ti-rich eutectic band in Wall_NL_5. Compositions are indicated by atomic ratios. This area is indicated by white boxes in the following electron backscatter diffraction (EBSD) maps. (b) EBSD image quality (IQ) map. (c) EBSD phase map (green for b.c.c. generic and red for h.c.p. generic) with CI (brightness indicates confidence of indexing).

3.8. Discussion

Within the investigated process parameters window and despite the possible formation of brittle IMCs in the Fe-Ti material system, neither delamination nor cracks could be observed along the interfacial zone between these two metals. Only a few large pores and small cracks within the layers could be seen by optical microscopy. However, these pores and cracks could not be correlated to specific energy inputs. This good interfacial bonding appears in contradiction with the extensive delamination reported by Li et al. [1], while investigating the LMD processing of the Ti-SS material system. These authors used, however, large laser diameter and power, 2 mm and 1000 W, respectively, which ensured melting a large amount of Ti. Their scan speed and powder feed rate were also relatively low, i.e., 200 mm/min and 5.1 g/min, respectively, which indicates the melting of a large amount of SS316.

It can be inferred that a large melt pool had formed with an efficient mixing of both Fe and Ti promoting the formation of brittle IMCs.

The additive manufacturing process requires a metallurgical bonding between the deposited layers for building 3D parts. It is then necessary to melt the support layer and to achieve an overlapping zone between the two subsequent layers. However, as described above, an enrichment of the melt pool by both metals will promote the formation of the IMCs. Therefore, the penetration depth into the bottom layer has to be controlled carefully. Wolff proposed a qualification of the metallurgical bonding by introducing a dimensionless parameter called dilution (d), being [12]:

$$d = \frac{D}{H + D} \quad (1)$$

where D is the penetration depth and H is the height of the material deposited above the substrate as described previously in this study. The optimum, according to Wolff, should be a dilution between 10 and 30. In the present investigation, this dilution varies between almost 20 and more than 60. The high dilution values are obtained for high-energy inputs, especially for the highest powers investigated. Indeed, it seems that power is the most critical process parameter influencing the penetration depth. At high powers, a large amount of Ti coming from the substrate is available for building IMCs. For the highest power investigated here, i.e., 300 W, the composition up to the top of the single track is even richer in Ti than in Fe ($\text{Fe}_{40}\text{Ti}_{60}$). The tracks deposited with high powers show one or even many cracks, starting from the interface and propagating straight up to the top of the deposited layer. However, no cracks along the interface between the Ti substrate and the iron deposition could be seen. The brittle IMCs FeTi and Fe_2Ti have been identified based on compositional EDS measurements and their respective crystalline structures could be confirmed by EBSD analyses. These phases are always observed above a first Ti-rich phase present along the interface and having a similar or even higher hardness as compared to the FeTi phase.

Although laser power is the dominant factor influencing the penetration depth, the highest heights of single tracks are obtained for lower scan speeds. No correlation could be drawn regarding the formation of large pores found in a few samples. As these pores are spherical, they may form due to gas trapping during the printing process. Further investigations are then required to avoid their formation by adjusting the shielding gas flow rate used to protect the optical setup of the laser head as well as the carrier gas flow to transport the metal powders.

To achieve 3D structures, more than one layer is normally required. The deposition of additional Fe layers leads to a partial remelting of the sub-layer down to the interfacial zone. Indeed, under the standard processing conditions used in this study, the penetration depth slightly increases from 30 to 40 μm after the second deposition step. This penetration does not change anymore with the application of the additional layers. The height seems to increase linearly with the number of layers, even if the first layer in contact with the substrate may be slightly thinner, i.e., 60 μm instead of 100 μm under the standard deposition conditions. It was not possible to distinguish the successive layers on the cross-sections to assess this linear increase. The cooling time variations indicate that already after 1 s, the sublayers are probably completely solidified. For all the produced multilayered walls, the composition changes gradually from Ti in the substrate to almost pure Fe within a thin transition zone. Despite the high cooling

rates making additive manufacturing a non-equilibrium process, all the specific compositions of the phase diagram could be identified as seen in Table 2. However, the defined processing parameters for building 3D parts allow the confinement of the brittle IMCs FeTi and Fe₂Ti within a thickness of only 4 μm, which could avoid cracking. The remelting of part of the first layer leads to the dilution of titanium in iron and the composition moves from Fe₈₀Ti₂₀ to Fe₉₀Ti₁₀ within the first 100 μm before changing to pure Fe. Above this, the composition is close to pure Fe, where Ti is no longer present.

4. Conclusions

This work shows the capability of direct deposition of Fe walls on Ti substrate. Laser power and scan speed have been found to be dominant in determining the amount of Ti and Fe in the melt pool, respectively. The investigated parameters induced a sharp and gradual composition change at the interface with the Ti substrate. All the crystalline phases of the binary phase diagram could be found at the interface thanks to EDS and EBSD characterizations, despite the non-equilibrium state of the laser process, however with different thicknesses depending mainly on the laser power driving the penetration depth. The brittle IMCs are thus confined within a thin zone that may avoid extensive crack formation and propagation. The deposition of subsequent layers does not influence the interfacial zone anymore, indicating that the printing parameters could then be optimized for depositing the second metal. This study demonstrates then that the first 2–3-layer deposition tailors the interface between two dissimilar metals where cracks and delamination would occur. It is worth noting that for larger dimensions of the printed parts, the stresses may be more important. This will be investigated in a future study aiming at also evaluating the mechanical performances of the printed structures.

Author Contributions

D. C. and A. M.: methodology, experiments, analysis, and writing (original draft preparation, review, and editing). M.L.: supervision, review, and editing.

Funding

This research received no external funding.

Acknowledgments

The authors are thankful to Bernhard von Gunten and Peter Ramseier (Laboratory for Advanced Materials Processing—EMPA Thun) for the support with sample fabrication and metallographic preparation. The authors would also like to thank MatExpert GmbH, Thun, for the support with hardness measurements and Xavier Maeder from EMPA for the support with EBSD analyses.

Conflicts of Interest

The authors declare no conflict of interest.

References

- [1] Li, W.; Yan, L.; Karnati, S.; Liou, F.; Newkirk, J.; Taminger, K.M.B.; Seufzer, W.J. Ti-Fe intermetallics analysis and control in joining titanium alloy and stainless steel by Laser Metal Deposition. *J. Mater. Process. Technol.* 2017, 242, 39–48.
- [2] Kale, G.; Patil, R.; Gawade, P. Interdiffusion studies in titanium–304 stainless steel system. *J. Nucl. Mater.* 1998, 257, 44–50.
- [3] Schutz, R.W.; Baxter, C.F.; Boster, P.L.; Fores, F.H. Applying titanium alloys in drilling and offshore production systems. *JOM* 2001, 53, 33–35.
- [4] Hui-Chi, C.; Bi, G.; Lee, B.Y.; Cheng, C.K. Laser welding of CP Ti to stainless steel with different temporal pulse shapes. *J. Mater. Process. Technol.* 2016, 231, 58–65.
- [5] Gao, Y.; Nakata, K.; Nagatsuka, K.; Liu, F.; Liao, J. Interface microstructural control by probe length adjustment in friction stir welding of titanium and steel lap joint. *Mater. Des.* 2015, 65, 17–23.
- [6] Zhang, Y.; Zhou, J.; Sun, D.; Gu, X. Nd:YAG laser welding of dissimilar metals of titanium alloy to stainless steel without filler metal based on a hybrid connection mechanism. *J. Mater. Res. Technol.* 2020, 9, 1662–1672.
- [7] Zhang, Y.; Sun, D.; Gu, X.; Li, H. Strength improvement and interface characteristic of direct laser welded Ti alloy/stainless steel joint. *Mater. Lett.* 2018, 231, 31–34.
- [8] Sidambe, A.T. Biocompatibility of Advanced Manufactured Titanium Implants—A Review. *Materials* 2014, 7, 8168–8188.
- [9] Cacciamani, G.; De Keyser, J.; Ferro, R.; Klotz, U.E.; Lacaze, J.; Wollants, P. Critical evaluation of the Fe–Ni, Fe–Ti and Fe–Ni–Ti alloy systems. *Intermetallics* 2006, 14, 1312–1325.
- [10] Zeng, L.; Liu, L.; Huang, S.; Zhang, L. Experimental investigation of phase equilibria in the Ti-Fe-Cr ternary system. *Calphad* 2017, 58, 58–69.
- [11] Springer. Materials. Available online: <https://materials.springer.com> (accessed on 29 April 2020).
- [12] Wolff, S.J. *Laser-Matter Interactions in Directed Energy Deposition*; Northwestern University Press: Evanston, IL, USA, 2018.

Appendix E - Additive Manufacturing of Ti-Nb Dissimilar Metals by Laser Metal Deposition

Di Cui^{1*}, Briac Lanfant¹, Marc Leparoux¹, Sébastien Favre²

1. Empa-Swiss Federal Laboratories for Materials Science and Technology, Laboratory for Advanced Materials Processing, 3602 Thun, Switzerland

2. Medtronic Europe Sàrl, 1131 Tolochenaz, Switzerland

* Correspondence: di.cui@empa.ch

Abstract: Conventional technologies for joining dissimilar metals have become insufficient, as the need for designing and fabricating products with complex shape and integrated composition variation have arisen. Laser metal deposition (LMD), a powder injecting additive manufacturing (AM) technology, is capable to build complex geometries and tailor material composition locally within one single workpiece. In this work, thin walls transitioning from titanium to niobium were made by LMD with controlled injection of Ti and Nb powders. The morphologies and microstructures were observed with optical microscopy (OM) and scanning electron microscopy (SEM). The cross-sections showed fully dense deposition, without cracks in any of the transition area. Deposition of Nb powder resulted in partially melted Nb particles embedded in the transition area, which was a result of the significantly higher melting point of Nb. Energy-dispersive spectroscopy (EDS) confirmed metallurgical bonding at the transition areas and showed variation of composition along the build direction. In the transition area, microhardness was 204 ± 5 HV at the Ti-rich side, 155 ± 6 HV in the solid solution, with an atomic composition of $\text{Ti}_{70}\text{Nb}_{30}$, and 120 ± 16 HV at the Nb-rich side. Electron backscattered diffraction (EBSD) results revealed hcp structure in the pure Ti region and bcc structure in the transition and pure Nb regions. Columnar growth was revealed in the pure metal regions and equiaxed growth in the transition region. X-ray computed tomography (X-CT) showed 3D element distribution and revealed very small number of pores in the transition area, which were not observed by previous microscopy on cross-sections.

Keywords: dissimilar metals, laser metal deposition, metallurgical bonding, microhardness, EBSD.

1. Introduction

Laser additive manufacturing (AM) is a solid freeform manufacturing technology. It enables direct fabrication of detailed work pieces by accurately depositing desired material at set positions within a pre-determined domain [1]. Laser metal deposition (LMD) is an advanced powder-injecting laser AM technology capable of directly producing dense metal parts with complex geometries, and, of special interest, variation of composition through the control of the powder type injection. A variety of materials can be manufactured by LMD for numbers of applications in the fields of medical device, automobiles and aerospace.

Despite the lower flexibility in geometry complexity compared to powder bed fusion technologies, LMD has the advantage of mixing at least two different powders with the desired composition to synthesize alloys in-situ [2], metal matrix nanocomposites [3] and functionally graded materials (FGM) [4]. Many binary systems have been studied to produce FGM with LMD. Ti+Ta deposition by LMD was carried out on Ti6Al4V substrate [5]. An increase of Ta concentration resulted in an increase of minimum laser power for successful deposition and resulted in good biocompatibility, Young's modulus and 0.2 offset yield strength. Ti6Al4V-Inconel 625 FGM was fabricated but cracks appeared due to formation of brittle intermetallic phases such as in the Ti-Ni and Ti-Fe material systems [6]. Schneider-Maunoury et al. reported a study on LMD of Ti-Nb samples with several incremental increases of Nb content [7]. Many unmelted Nb particles were observed in the produced bimetal part. Microhardness of the samples decreased with the increase of Nb content. The lowest elastic modulus of 58 ± 8 GPa was found at the composition of Ti40Nb wt. The adaptation of the elastic modulus of Ti-Nb parts to the human bone (10-30 GPa) is of prime interest for orthopedic parts and additive manufacturing offers additionally a customization to the individual patient.

This paper summarizes the preliminary results on the fabrication of Ti-Nb assemblies using LMD process with separate injection of Ti and Nb powders. The focus of this study is the investigation of the interfacial zones between these two materials and the occurrence of cracks depending of main process parameters.

2. Materials and Methods

2.1. Materials

The powders utilized were Cp-Ti grade 1 powder (oxygen < 0.08 wt., Hall flow 0.1 inch 23 s) with a diameter around 45-106 μ m supplied by AP&C Advanced Powders & Coatings Inc., Canada, and AMPERTEC MAP Nb powder (oxygen = 373 ppm, Hall flow 0.1 inch 13s) with a diameter of 63-100 μ m, supplied by H.C. Starck Tantalum and Niobium GmbH, Germany. Powder particles of both titanium and niobium were primarily spherical, with minor satellites (Fig. 1), exhibiting desirable flowability for powder transportation during the LMD process. Pure niobium and titanium bulk foils with various thicknesses have been used as substrates.

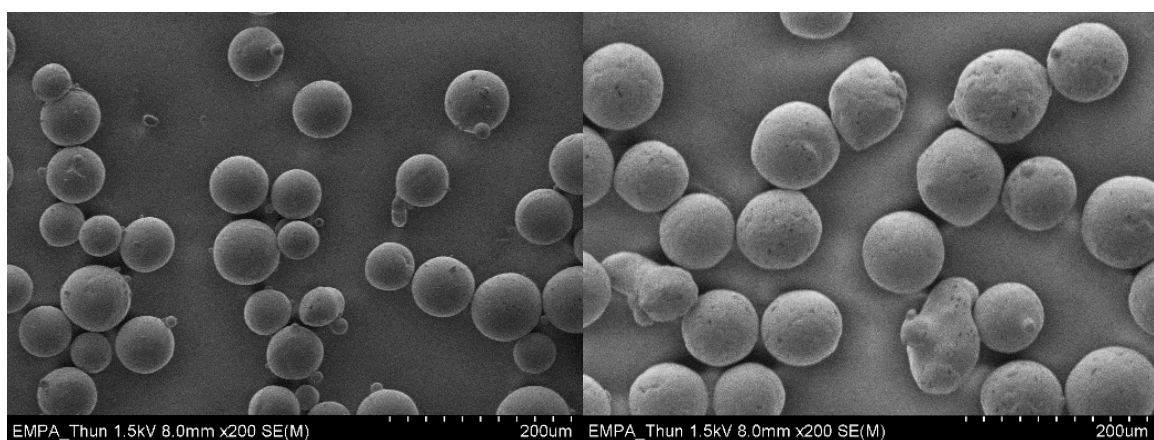


Fig. 1. SEM images of titanium (left) and niobium (right) powder particles.

2.2. Fabrication of thin walls

A commercial LMD machine (Mobile 1.0, BeAM, France) has been used to build the 3D structures. This LMD system uses a continuous wave (CW) fiber laser with a maximum power of 500 W operating at a wavelength of 1068 nm (YLR-Series, IPG Photonics, USA) as the heating source. The laser has a focal spot diameter of 800 μm and a Rayleigh range of 18 mm. The powders are feed through a volumetric powder feeder (Medicoat, Switzerland) with two powder containers. The conventional microscale powders are then transported by a carrier gas (argon) through two tubes which are joined by a Y junction into one single line connected to the processing head. A specific conical nozzle focuses the powder jet at 3.5 mm below its exit at the same position as the laser focus. The processing head is mounted on a 3-axis system (x,y,z) and the substrate holder has 2 rotative axes. The printing process takes place in an airtight chamber that offers possibility to work under low level of oxygen, which is crucial for processing materials with high affinity of oxygen like titanium. Images of the system and schematic of the nozzle are presented in Fig. 2.

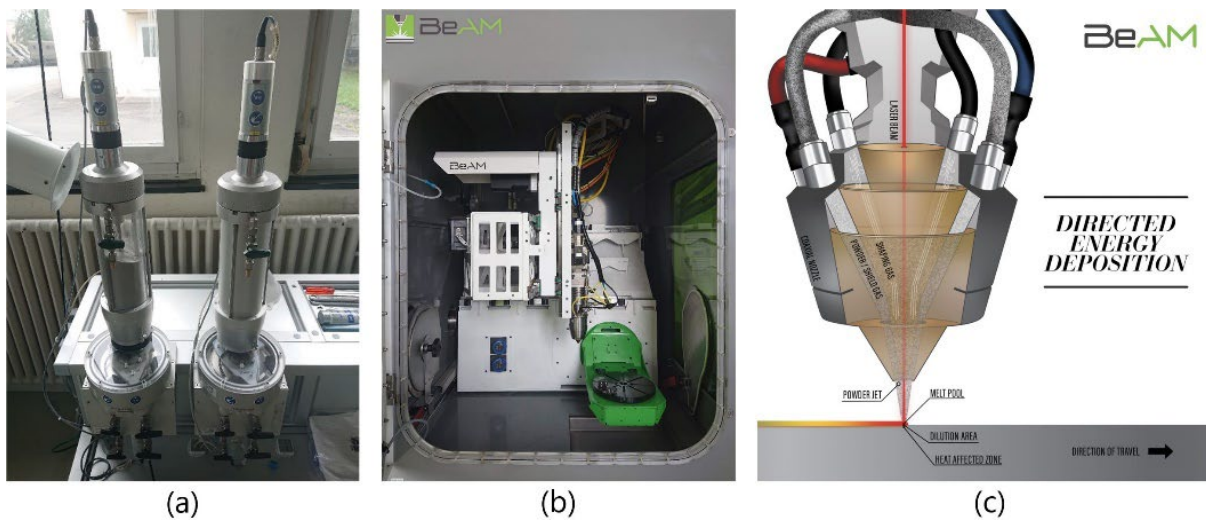


Fig. 2. Laser Metal Deposition (LMD) machine: (a) Dual-container powder feeder; (b) interior of the printing chamber; (c) schematic of the coaxial nozzle.

4 groups of samples have been fabricated as illustrated in Fig. 3:

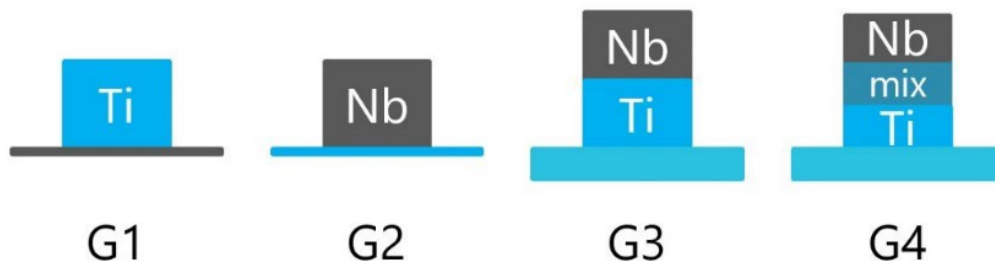


Fig. 3. Schematics of the printed structures.

G1 - deposition of a Ti wall on a Nb foil (200 μm);

G2 - deposition of a Nb wall on a Ti foil (300 μm);

G3 - deposition of Ti followed by Nb, using a Ti grade 23 plate (4 mm) as substrate;

G4 - deposition of Ti and then a mixing area Ti+Nb followed by a pure Nb structure using a Ti grade 23 plate (4 mm) as substrate.

All of the samples have been produced under argon ($O_2 < 30$ ppm, $H_2O < 170$ ppm, argon filling overpressure ≈ 3 mbar).

The targeted dimensions of the samples were lengths of 6 mm, and a height of 4 mm for the pure Ti and Nb walls of samples G1, G2 and G3. The pure material structures were targeted to be 2 mm high with an intermediate mixing zone of 4 mm for the G4 sample. The z step-increment of the nozzle, i.e. designed layer thickness, has been fixed at 0.2 mm for all samples.

Beside the laser power, the linear axis moving speed and the powder feedrates were varied. For comparing the used conditions, a linear energy is defined as power divided by speed, reflecting input laser energy per unit length. Accordingly, a linear feedrate is defined as feedrate divided by speed, which reflects input powder mass per unit length. Finally, energy per feed is defined as power divided by feed rate, reflecting input laser energy per input powder mass. The printing parameters were selected according to a previous study performed with Titanium powder [3] and are summarized in Table 1 (samples G1 to G3) and Table 2 (sample G4). For all the G3 samples, a power of 325 W, speed of 2000 mm/min and feed rate of 3.6 g/min have been employed to deposit the first 4 mm height of Ti on the substrate. A delay of 10 s was then necessary to switch the powder feeder from pure Ti to Nb and to stabilize the powder flow before depositing the next 4 mm of Nb on top of the as-deposited Ti using the parameters presented in Table 1.

It should be noted when analyzing the results that the input laser energy is distributed in four fractions: (1) absorbed by substrate or previously deposited material; (2) absorbed by powder particles during flight; (3) scattered by powder particles and directed away; (4) reflected by substrate or previously deposited material.

Table 1. Printing parameters for G1, G2 and G3

Group	Sample	Power (W)	Speed (mm/min)	Feedrate (g/min)	Linear Energy (J/mm)	Linear Feedrate (mg/mm)	Energy per feed (J/mg)
G1	1	325	2000	3.9	9.8	2.0	4.9
	2	360	2000	3.9	10.8	2.0	5.4
G2	1	150	1000	6.0	9.0	6.0	1.5
	2	188	1000	6.0	11.3	6.0	1.9
	3	213	1000	6.0	12.8	6.0	2.1
	4	248	1000	6.0	14.9	6.0	2.5
	5	94	500	6.0	11.3	12.0	0.9
	6	281	1500	6.0	11.3	4.0	2.8
	7	375	2000	6.0	11.3	3.0	3.8
	8	281	1500	7.0	11.3	4.6	2.3
	9	375	2000	7.0	11.3	3.5	2.8
G3	1	375	1200	6.0	18.8	5.0	3.8
	2	425	1200	6.0	21.3	5.0	4.3
	3	475	1200	6.0	23.8	5.0	4.8
	4	475	1400	7.0	20.4	5.0	4.1

Table 2. Printing parameters for G4

Sample	Powder	Height (mm)	Power (W)	Speed (mm/min)	Feedrate (g/min)	Linear Energy (J/mm)	Linear Feedrate (mg/mm)	Energy per feed (J/mg)
G4_1	Ti	2	325	2000	3.9	9.8	2.0	4.9
	Ti+ Nb	4	375	1040	1.9+ 3.5	21.6	1.8+ 3.4	4.2
	Nb	2	375	1500	4.8	15.0	3.2	4.7

2.3. Characterization Methods

The produced samples have been cut perpendicular to the laser scanning directions. The cross-sections have then been embedded in Demotec 10 resin, ground up to grit 2500 SiC grinding paper, and polished with 6 μm and 3 μm diamond pastes and finally with an OPS solution (0.04 μm SiO_2 with 10% H_2O_2).

Cross-section morphology and microstructure have been examined with an optical microscope (OM) (ZEISS Axioplan, Germany) and a scanning electron microscope (SEM–Hitachi S-4800, Japan). An energy-dispersive spectrometer (EDS–Ametek Edax Octane plus, USA) has been used to investigate the elemental spatial distribution. Microhardness HV0.2 has been measured with a load of 200 g and a dwell time of 10 s. An electron backscattered diffraction camera (EBSD–Ametek, USA) has been used to investigate the grain morphology and the crystalline structure. X-ray computed tomography (X-CT-RX Solutions EasyTom XL Ultra, France) has been used on one sample to visualize the elemental distribution in three dimensions and examine for potential pores.

3. Results and Discussion

3.1. Ti walls deposited on Nb foil

Side views and cross-sections of G1 by OM are presented in Fig. 4. Samples G1_1 and G1_2 exhibited good adherence to the Nb foil. They both have dimensions close to the programmed ones ($L \times H = 6 \text{ mm} \times 4 \text{ mm}$) with a length of 6.5 mm and height of 3.8 mm. Widths of G1_1 and G1_2 are 800 μm and 940 μm , respectively, similar to the provided laser beam diameter of around 800 μm . The 18 wall width difference between the samples is the result of an increase of 11 in laser power, and therefore energy at the sample level. At the interface with the Nb foil, both Ti walls are slightly thinner, as a result of enhanced heat dissipation through the metallic substrate. Both of the walls appear crack-free and dense in the cross-sections, but thermal deformation of the substrate can be observed with thin foils.

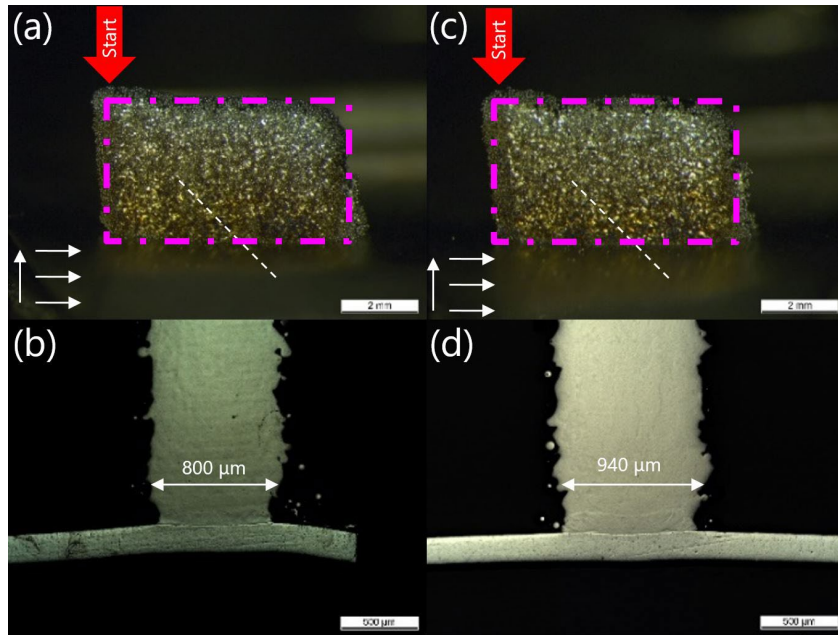


Fig. 4. OM images of G1 samples. (a) and (b) are side view and cross-section of G1_1; (c) and (d) are side view and cross-section of G1_2. Arrows in the lower left caption indicate direction of laser movement in the horizontal plane and building direction. Purple broken frames indicate designed dimension of $L \times H = 6 \text{ mm} \times 4 \text{ mm}$. White broken lines indicate positions of the cross-sections in the as-built thin wall.

Several SEM images of the interface between Ti wall and Nb foil are presented in Fig. 5. SEM imaging of the Ti/Nb interface in G1_1 reveals a thin band of intermediate contrast between Ti wall and Nb foil (Fig. 5(a-c)). Thickness of this band is usually around $0.5 \mu\text{m}$. Occasionally, the band protrudes into the pure Ti part, reaching a thickness approximately $30 \mu\text{m}$ (Fig. 5(c)). EDS line analysis shows variation of relative concentrations of Ti and Nb across the band, confirming metallurgical bonding with mixing of the two elements in the band.

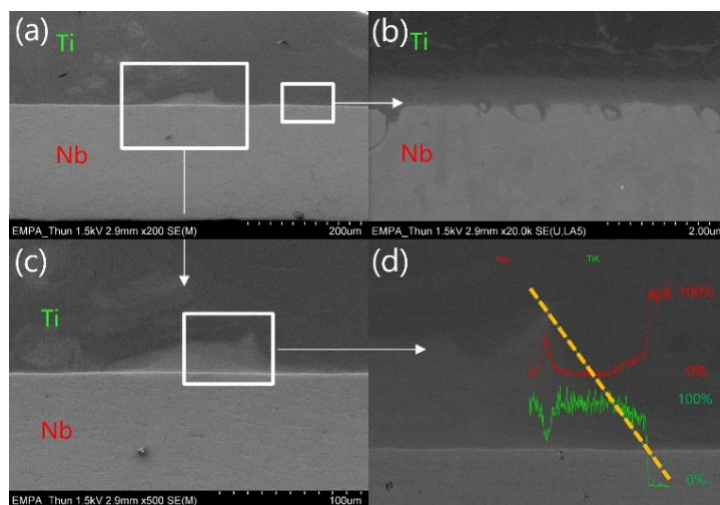


Fig. 5. (a) SEM image of the interface between Ti wall and Nb foil. (b) The thin band with a thickness of $0.5 \mu\text{m}$. (c) thin band protruding into pure Ti part, reaching a thickness of $30 \mu\text{m}$. (d) EDS line analysis along the yellow broken line across the protrusion; red and green curves show variation of intensities of NbL and TiK signals respectively, demonstrating their correspondence with SEM image contrast.

3.2. Nb walls deposited on Ti foil

Samples G2_1 to G2_9 exhibited good adherence to the Ti foil.

Influence of power. Samples G2_1 to G2_4 have been fabricated with increasing power while keeping constant the speed and feed rate. Fig. 6 shows bottom parts of cross-sections of the samples.

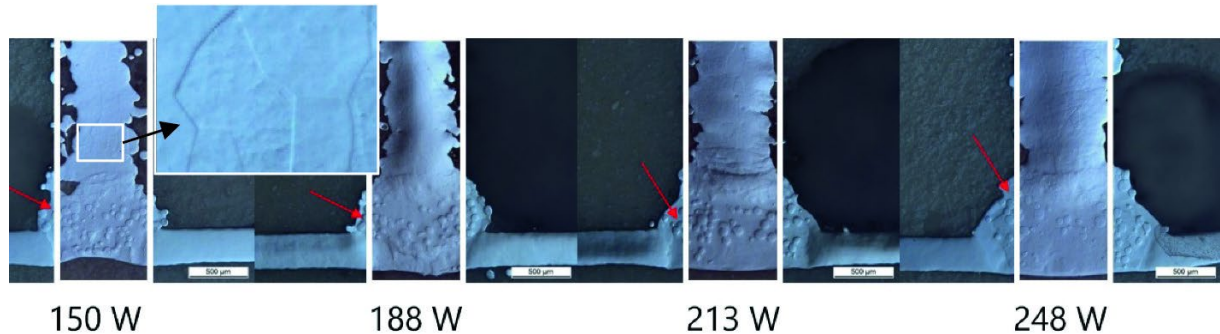


Fig. 6. OM of cross-sections of G2_1 to G2_4 with processing power indicated. Distances between bold white lines indicate laser beam diameter. Red arrows show spherical features in the transition area. The inserted image shows grain boundaries in the wall.

All Ti foils appear melted through at the bottom of the Nb wall deposition. A higher energy density is indeed required for depositing Nb compared to Ti due to the higher melting temperature of Nb (2742 K instead of 1941 K for Ti). Additionally, many spherical features are present in this transition area. These features are unmelted or partially melted Nb inlet particles as confirmed by EDS analyses. Grain boundaries in the main body of the pure Nb walls were revealed by polishing.

In the studied parameters range, a power increase induces an increase of the width of melted part in the substrate, the volume of the transition area and the width of the wall as previously observed with Ti.

Influence of proportionally changing power and speed. Samples G2_5, G2_2, G2_6 and G2_7 have been produced by proportionally increasing power and speed, while keeping the feedrate constant. The samples have been fabricated with the same linear energy, but with a decreasing linear feedrate. Fig. 7 shows bottom parts of cross-sections of the samples. Similar to previous samples, all Ti foils are melted and partially melted Nb particles are observed.

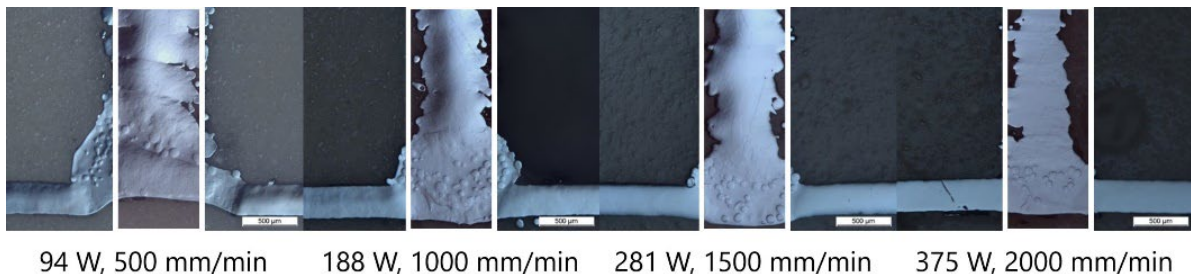


Fig. 7. OM of cross-sections of G2_5, G2_2, G2_6 and G2_7 with processing power and speed indicated. They all have an identical linear energy of 11.3 J/mm. Distances between bold white lines indicate laser beam diameter.

In sample G2_5, the Ti foil has been melted and severely deformed, and traces of individual deposited layers are observed in the wall body, exhibiting poor homogeneity of the wall. As the linear energy was sufficient to create a melt pool within the used parameter range, the lower power for G2_5 could have created a cooler melt pool. The slower speed then allowed this cooler melt pool to exist for longer time thus increasing the probability of melted metals to flow sideways before solidifying, resulting in the protrusions on both sides of G2_5. Compared to other samples where power and speed increased proportionally, the width of melted substrate and the volume of transition area decreased. The width of wall body decreased dramatically, corresponding to the greatly decreased linear feedrate.

Influence of feedrate. Samples G2_6 and G2_8 as well as G2_7 and G2_9 have been produced respectively with the same power and speed, but different feedrates.

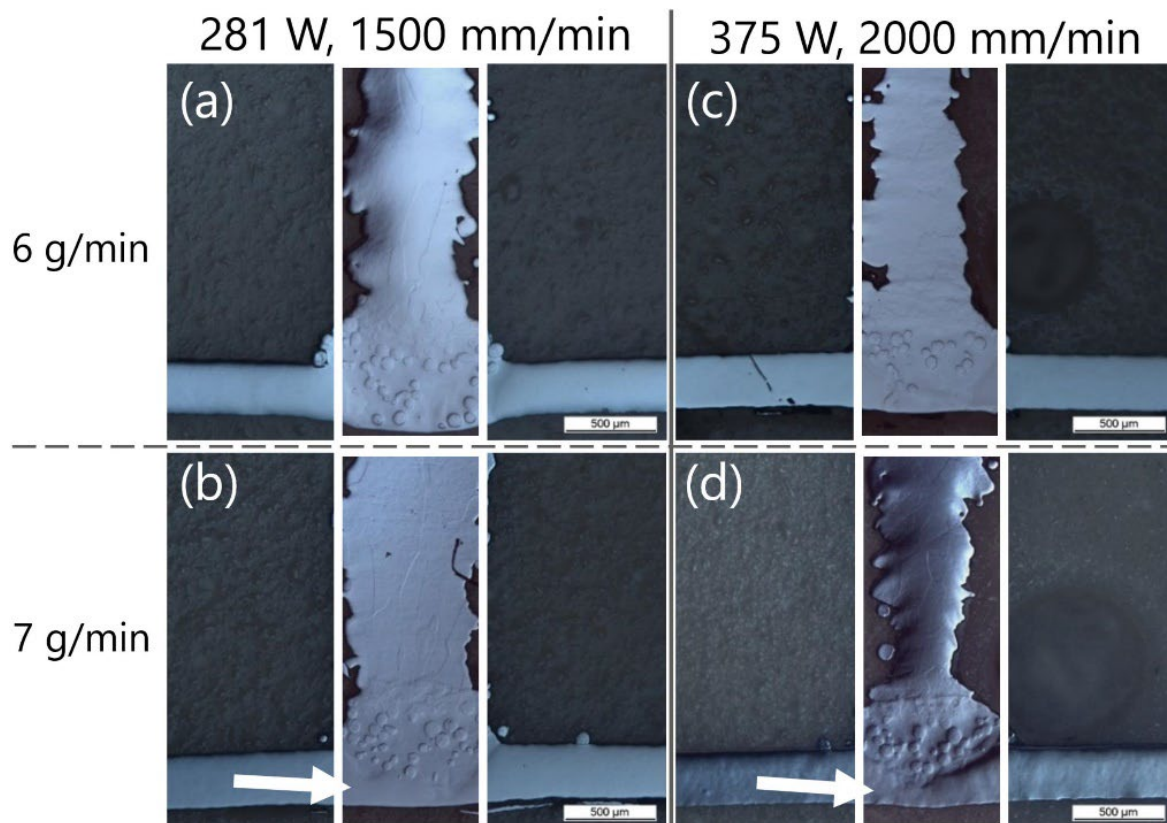


Fig. 8. OM of cross-sections of (a) G2_6, (b) G2_8, (c) G2_7 and (d) G2_9. Distances between bold white lines indicate laser beam diameter.

Fig. 8 shows bottom parts of cross-sections of the samples. Full penetration of the Ti substrate was observed for the lower feedrate 6 g/min while increasing the feedrate to 7 g/min prevents the full penetration (white arrow). Large Nb particles were observed in the mixing zone between Nb and Ti, and their quantity appears to be larger for lower power and speed. The wall thickness and homogeneity is smaller for higher power and speed but no significant changes were observed depending on the feedrate in the investigated range.

Unmelted or partially melted Nb particles. For all samples in G2, meaning where Nb was injected above Ti, Nb particles have been observed in the transition area, but not in the main body of the walls. This indicates that conditions with the lowest energy input in any aspect (power down to 94 W, linear

energy down to 9.0 J/mm or energy per feed down to 0.9 J/mg) have been sufficient to melt Nb inlet particles completely.

To explain the presence of Nb particles only in the transition area and not in the wall body, different effects could be considered:

1. The heat dissipation at the bottom is higher than the upper in the wall body because of larger heat transfer through the bulk substrate. This induces the necking observed at the bottom of the walls built on bulk substrates as seen for instance in Fig. 4.
2. The heat accumulated layer by layer induces a higher melt pool temperature in layers upper in the wall.
3. The boiling point of Nb (5015 K) is significantly higher than that of Ti (3560 K). Potential boiling or overheating of a melt pool of Ti+Nb mixture could dissipate more heat, compared to a melt pool of pure Nb which is hot, but not boiling. Therefore, melt pool of pure Nb can reach potentially much higher temperature than that of Ti+Nb mixture. Additionally Ti vapors may absorb the infrared laser wavelength leading to less energy in the melt pool [8].

These above mentioned effects are all related to heat accumulation and dissipation due to the presence of the substrate. Obviously, these physical phenomena occur not only individually but are combined promoting the non-fully melting of the niobium particles. Higher energy input in the system could however overheat the titanium substrate leading to perforation, extensive evaporation and enhanced instability of the melt pool. Smaller Nb particle sizes that would need less energy for melting could be considered for the transition area.

3.3. Deposition directly changing from Ti to Nb

A pure Ti wall is first deposited on a Ti grade 23 substrate, and then Nb is deposited onto it (scheme G3 – Fig. 3). All samples have similar dimensions close to the target programmed. Fig. 9 presents optical micrographs of the cross-sections of the transition areas between the deposited Ti and Nb walls for the different processing conditions in Table 1. Negligible cracks nor delamination at the interface between the substrate and the printed structure have been observed. Furthermore, negligible cracking nor porosity have been observed within the printed structures as well. In all samples, there is a transition area between pure Ti part and pure Nb part, with a sharp interface at the pure Ti side but no well-defined interface at the pure Nb side. Several Nb particles are observed in this transition area, but not in the pure Nb wall side located on the top of the manufactured structures.

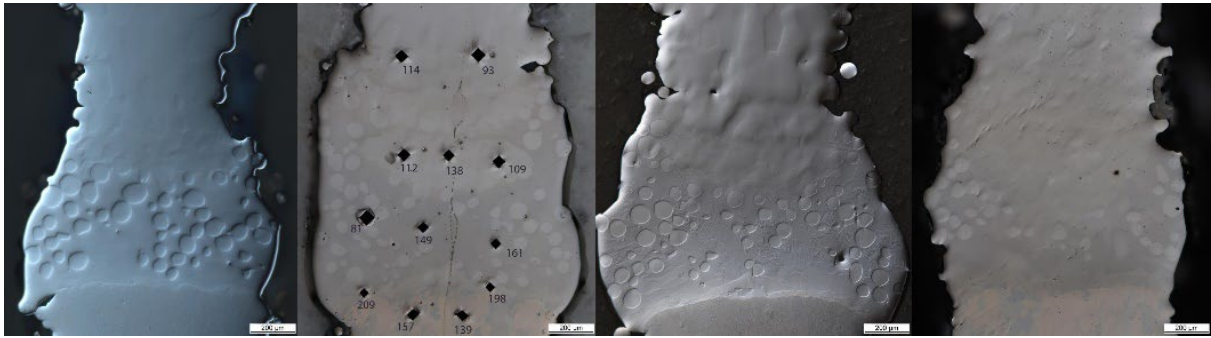


Fig. 9. OM of cross-sections of samples G3_1 to G3_4 (from left to right). The color and morphology difference is due to different polarization when taking the images. Black dots on G3_2 are indents for microhardness measurements.

X-CT has been done on a part of the G3_3 sample to visualize the 3D elemental distribution and check for potential pores. This sample and its reconstructed image are shown on the left in Fig. 10. Nb with a higher atomic number has a brighter contrast in the reconstructed image, while Ti appears darker. Six horizontal slices of the reconstructed image (indicated by the dashed lines) are presented on the right side of Fig. 10. Slice 1 shows fully dense Ti part with a few Nb particles sticking on the side. An area with intermediate contrast appears in slice 2, indicating emergence of Ti/Nb solid solution. Slices 3 to 5 are characteristic of the transition from Ti to Nb. Several bright spheres in these slices correspond to the Nb particles observed in OM images. A few pores with sizes of tens of microns are observed in slice 4, which were not observed in cross-section OM images. The stepped contrast in slice 5 shows traces of a few different scanning tracks, indicating stepped composition gradient in the transition area. Slice 6 shows the dense pure Nb part.

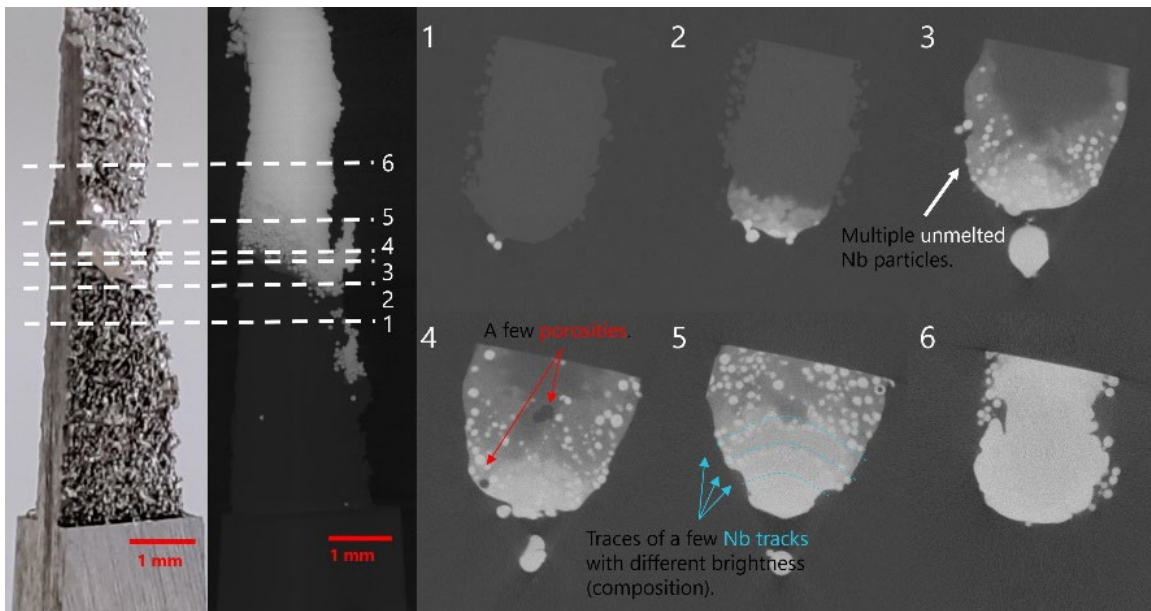


Fig. 10. Photograph of the G3_3 sample part and its reconstructed image by X-CT. 6 slices of the reconstructed image are shown on the right. There positions are indicated by the white dashed lines.

Coupled EDS and EBSD have been performed on sample G3_4. The results are shown in Fig. 11. It can be noticed that, hcp structure (α -Ti) is only present where no Nb element is detected. However as soon as Nb appears in the area, a bcc (Nb or β -Ti) phase is observed, regardless of the presence of Ti. This is in agreement with Nb being a β -stabilizer for Ti. A sharp interface is observed between the transition area and pure Ti part, as shown in samples presented in Fig. 9. These interfaces could then be explained by a mismatch of both crystal structures. This interface would be an interesting subject of testing in future mechanical tests. The inverse pole figure (IPF) maps in Fig. 11 show a tendency of columnar growth in pure Ti and pure Nb parts, and equiaxed growth in the transition area.

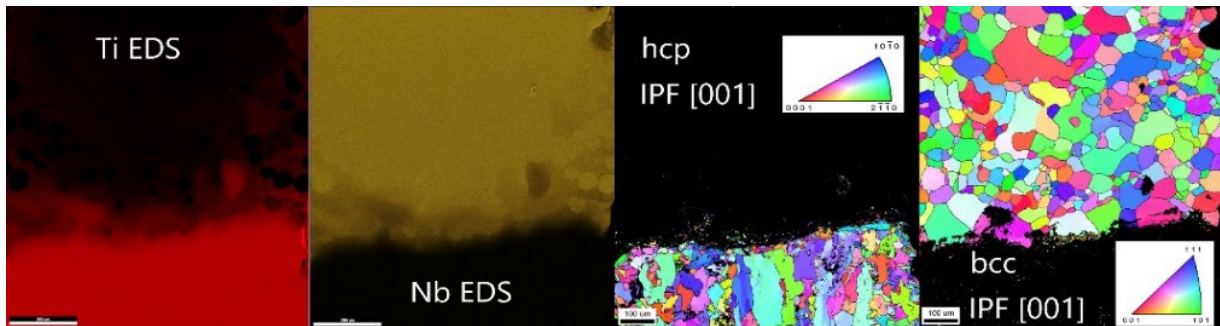


Fig. 11. Coupled EDS and EBSD mapping of Ti and Nb in transition area of G3_4.

EDS line scan, mapping and microhardness measurements have been done on sample G3_2. The results are shown in Fig. 12. The line scan (Fig. 12 middle) reveals a basically 3-step transition in the transition area. Immediately above pure Ti part with an average microhardness of 148 ± 9 HV is a band with a width of $40 \sim 100 \mu\text{m}$, where the atomic composition is $\text{Ti}_{90}\text{Nb}_{10}$. Microhardness in this area is highest, with an average of 204 ± 5 HV. Then in the main part of the transition area, An atomic composition is $\text{Ti}_{70}\text{Nb}_{30}$ was observed in the primary part of the transition area. The atomic ratio converted to mass ratio is $\text{Ti}:\text{Nb} = 55:45$, essentially the same as a Ti grade 36 alloy composition. This area exhibits an average microhardness of 155 ± 6 HV. The embedded Nb particle has an average microhardness of 81 ± 1 HV which could indicate weak points in future mechanical tests. Further up in the structure, traces of a Nb-rich track ($\text{Nb} > 95$ at.) wrapped in the Ti grade 36 were observed, with an average microhardness of 120 ± 16 HV. Finally, the pure Nb part has an average microhardness of 100 ± 12 HV. The highest microhardness in the $\text{Ti}_{90}\text{Nb}_{10}$ band could result from finer grains due to crystal structure mismatch, as it is transitioning from hcp α -Ti to bcc $\text{Ti}_{70}\text{Nb}_{30}$.

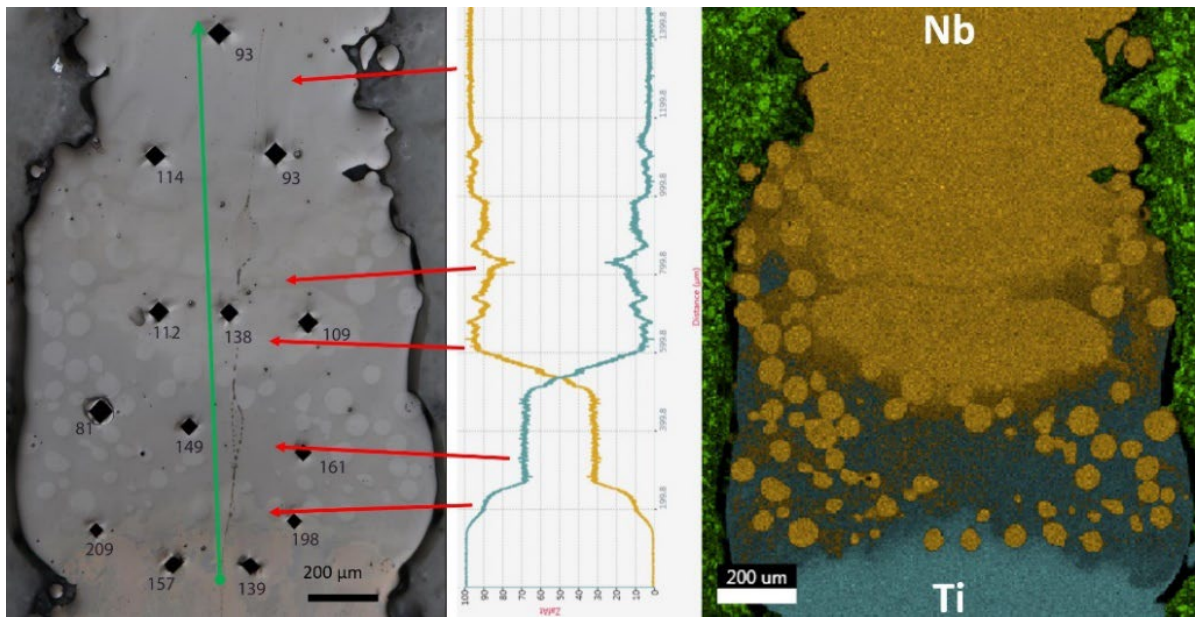


Fig. 12. OM image of G3_2 with microindents corresponding HV0.2 numbers. The EDS line scan was done along the green arrowed line, and atomic composition of Nb and Ti (yellow and teal curves, respectively) are shown in the chart. Key composition points are directed by red arrows to corresponding areas in the OM image, indicating a composition-contrast correlation. EDS mapping of Nb and Ti on the right shows similar element distribution to that of G3_4, with slightly more Nb particles.

Unmelted or partially melted Nb particles. For all G3 samples, Nb has been deposited on as-deposited Ti walls. Therefore, enhanced heat dissipation through the bulk substrate should not play a role anymore as compared to the deposition of Nb directly on a Ti substrate (samples type G2). In this configuration, the heat dissipated in the Ti-Nb mixing zone due to overheating of Titanium could explain the presence of non-fully melted Nb particles. Above this transition zone, in the pure Nb wall, no non-fully melted niobium particles could be observed as for G2 samples.

3.4. Deposition changing from Ti to Nb with a mixing area in between

In sample G4_1, a pure Ti wall has been first deposited on a Ti grade 23 substrate. Nb powder feeder has then been activated and a waiting time of 10 s has been imposed before beginning deposition in the mixing area, in order to guarantee a stable flow of sufficiently mixed powder in the feeding line. After finishing the mixing area, the Ti feeder was turned off and Nb feeder was adjusted to the desired feedrate, but no waiting time has then been imposed at this transition. The parameters listed in Table 2 have been employed to immediately deposit the Nb part of the structure. Fig. 13(a) shows cross-section of the sample G4_1.

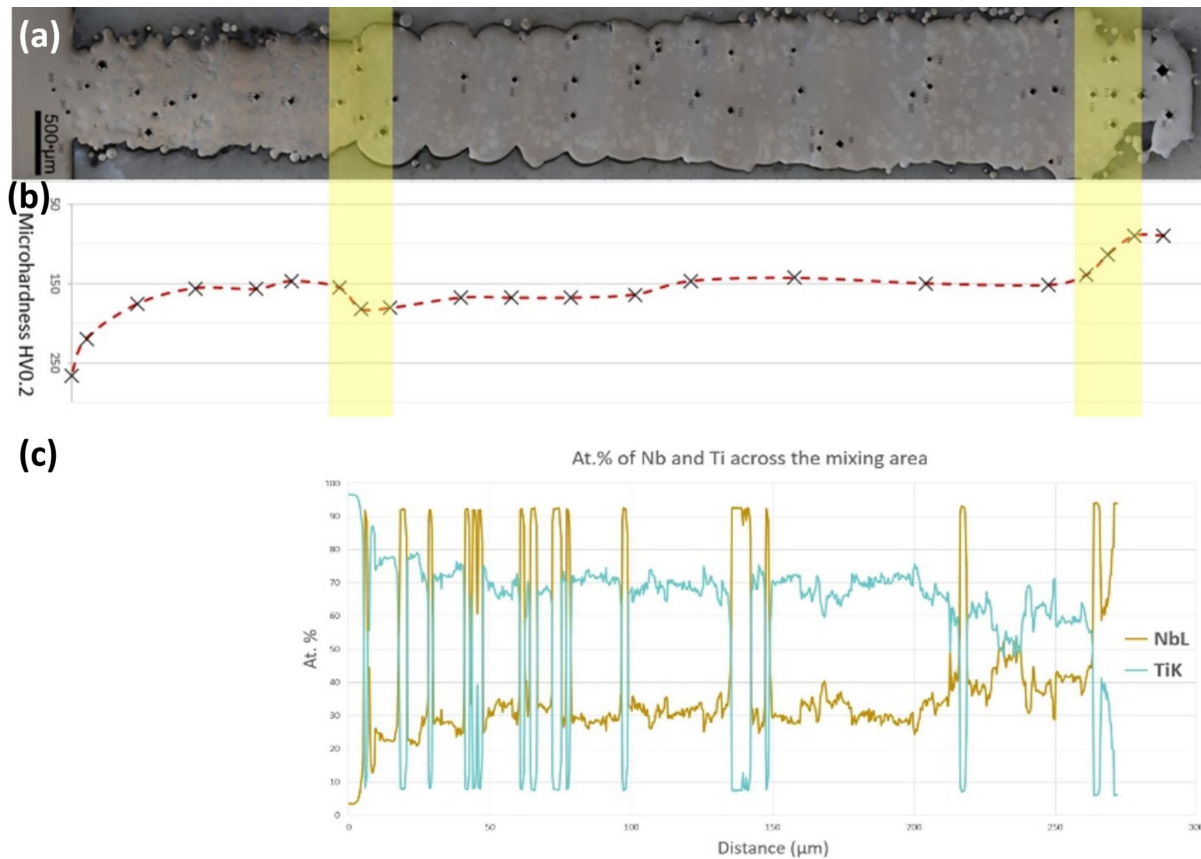


Fig. 13. (a) OM image of cross-section of G4_1. (b) Microhardness profile along the building direction from Ti through the Ti+Nb mixing zone to Nb. Yellow boxes show transitions between the pure metal and the mixing zone. (c) EDS line scan across the mixing area.

The pure Ti part has dimensions close to the programmed ones. The mixing area is longer and pure Nb part is shorter than programmed, which is a result of an unstable powder flow caused by absence of the 10 s waiting time. Many Nb particles were observed in the mixing area as seen by the sparks of Nb signal in the EDS mapping and in Figure 14, but neither crack nor porosity were present. Microhardness measurements in Fig. 13(b) and EDS line scan along the sample in Fig. 13(c) show results similar to those from G3_2: a $Ti_{90}Nb_{10}$ transition band follows immediately after the pure Ti, exhibiting an average microhardness of approximately 182 ± 1 HV. The primary part of the mixing area consists of a $Ti_{70}Nb_{30}$ solid solution as the matrix, with Nb particles embedded (the abrupt changes on the Nb curve in Fig. 13(c)). The average microhardness of the solid solution matrix and the embedded particles were measured to be 154 ± 10 HV and 85 ± 1 HV, respectively. The EDS map of Ti close to the Ti-to-Ti+Nb transition in Fig. 14 shows a slightly higher concentration of Ti between the first and second deposited mixing layers, which should be the same case for the layers above. Microhardness of these features ranged from 192 to 259 HV.

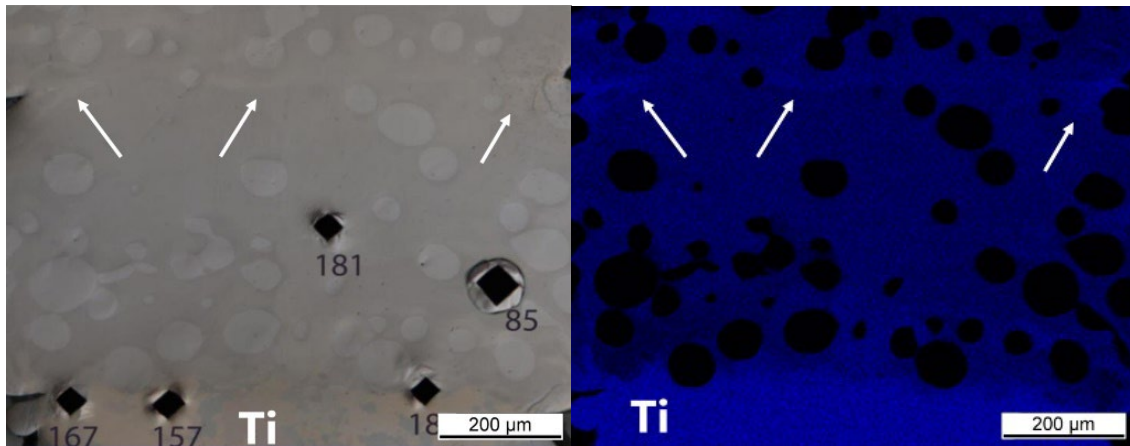


Fig. 14. OM image of the mixing area next to the pure Ti part (left) and EDS map of Ti of the same area (right). White arrows point to the features where Ti is slightly richer.

Unmelted or partially melted Nb particles. As for G2 (Nb on Ti bulk) and G3 (Nb on Ti wall) samples, Nb particles have been observed throughout the mixing area in G4_1 where Ti and Nb powders were fed together. Here also the overheating of the mixture Ti+Nb and the resulting heat dissipation could explain the presence of Nb particles that seem well distributed within one layer and not confined at the interface between two subsequent layers as reported by Schneider-Maunoury et al. [7]

From this study and the different configurations investigated, it appears that melting together materials with different melting points is challenging even for a simple material system leading to a solid solution. It would be interesting to measure then the temperature of the melting pool in this mixing zone depending on the Nb content. As proposed previously, a possibility to solve the issue of having unmelted particles would be to use finer particles for the higher melting point material, here Nb. However, working with fine powders induced flowability and safety issues. Preheating Niobium starting particles either in the container, the transporting line or in-flight after exiting the nozzle could be envisaged but would bring in potential fire hazard and add technical complexity to the system.

4. Conclusions

This preliminary study demonstrates the ability to deposit Titanium on Niobium and inversely Niobium on Titanium for building 3D structures using a direct energy deposition process. Additionally, a mixing zone obtained by the separate feeding of both powders could also be deposited with the additive manufacturing facility, offering new opportunities for building functionally graded materials.

The microscopic observations of the interfaces between these two metals as well as of the mixing zone reveal no cracks and a dense structure. The composition of the built walls varies from one pure metal to the other one through a solid solution that may present various compositions. The two metals grow with columnar grains whereas the solid solution shows an equiaxed structure. The hcp phase is only observed in pure Ti parts and as soon as Nb is present, the crystal structure becomes bcc. Fine grains due to the sharp transition between these two crystalline phases induces a high hardness.

Even if the energy input was always sufficient to melt completely the niobium particles, some unmelted Nb particles have been found at the interfaces with titanium in the mixing zone also far away from the bulk substrate. Further analyses are required to explain this phenomenon that could be induced by the evaporation of titanium that cools down the melt pool and absorbs the laser wavelength. These large particles could be an issue for the mechanical response of the material.

Future activities will then focus on the correlation between the process parameters and the Ti-Nb microstructures. This would be necessary for tailoring the performances such as tensile strength, fatigue strength, corrosion resistance and biocompatibility of the parts for industrial applications.

Acknowledgments

The authors are thankful to Bernhard von Gunten and Peter Ramseier (Laboratory for Advanced Materials Processing–EMPA Thun) for EBSD sample preparation EBSD. The authors would also like to thank Xavier Maeder (Laboratory for Mechanics of Materials & Nanostructures–EMPA Thun) for the assistance with EBSD analysis and Kai Zweiacker for assistance with X-CT analysis.

References

- [1] G.H. Loh, E. Pei, D. Harrison, M.D. Monzon: An overview of functionally graded additive manufacturing. *Additive Manufacturing* 23, 34–44 (2018).
- [2] L. Yan, X. Chen, W. Li, J. Newkirk, F. Liou: Direct laser deposition of Ti-6Al-4V from elemental powder blends. *Rapid Prototyping Journal* 22(5), 810–816 (2016).
- [3] B. Lanfant, F. Bär, A. Mohanta, M. Leparoux: Fabrication of Metal Matrix Composites by laser Metal Deposition-A New process Approach by Direct Dry Injection of Nanopowders. *Materials*, 12, 3584 (2019).
- [4] L. Yan, Y. Chen, F. Liou: Additive manufacturing of functionally graded metallic materials using laser metal deposition. *Additive Manufacturing* 31, 100901 (2020).
- [5] J. Feurst et al.: LASER Powder Deposition of Titanium-Tantalum Alloy Structured Interfaces for Use in Orthopedic Devices. In: *Medical Device Materials VI: Proceedings from the Materials and Processes for Medical Devices Conference 2011*, pp. 159–164. ASM International, Minneapolis (2013).
- [6] S. R. Pulugurtha: Functionally graded Ti6Al4V and Inconel 625 by laser metal deposition. PhD Dissertation. Missouri University of Science and Technology, Rolla (2014).
- [7] C. Schneider-Maunoury et al.: An application of differential injection to fabricate functionally graded Ti-Nb alloys using DED-CLAD® process. *Journal of Materials Processing Technology* 268, 171–180 (2019).
- [8] A. Mohanta et al.: Influence of temporal and spectral profiles of lasers on weld quality of titanium. *Optics and Lasers in Engineering* (2020).

DI CUI

Nationality: Chinese ◊ Current address: Thun, Switzerland
Mobile: +41 77 999 63 16 / +86 158 2704 8090 ◊ E-mail: di.cui@epfl.ch

EDUCATION

- École Polytechnique Fédérale de Lausanne (EPFL)** 9/2018 - 5/2023
Doctor of Philosophy PhD, in Materials Science & Engineering
- École Polytechnique Fédérale de Lausanne (EPFL)** 9/2015 - 4/2018
Master of Science MSc, in Materials Science & Engineering
Minor, in Management, Technology and Entrepreneurship
Overall GPA: 4.89/6
Core Courses: Metrology, Soft Matter, Fracture of Materials, Statistical Mechanics, Principles of Finance
- Zhejiang University (ZJU)** 9/2011 - 6/2015
Bachelor of Engineering BEng, in Materials Science & Engineering
Overall GPA: 3.53/4
Core Courses: Physical Chemistry, Basics of Materials Science, Modern Materials Analysis Technology

RESEARCH EXPERIENCE

- Interface control in Directed Energy Deposition (DED) of dissimilar metals.** 9/2018 - Present
PhD Thesis, Laboratory for Advanced Materials Processing, Swiss Federal Laboratories for Materials Science and Technology (EMPA) EMPA/EPFL
- Printed Ti directly on 316L by precise control of the interfacial brittle intermetallics and achieved Ti-316L interface with higher ultimate shear strength than Ti.
 - Collaboration with Medtronic: Printed Ti-Nb gradient material for potential medical application.
 - Presented the works on two international conferences.
 - Supervised master thesis students and international visiting students.
 - Formulated operation protocol and trained colleagues on the BeAM DED system.
- Characterization of Ti6Al4V powder recycled in additive manufacturing(AM)** 9/2017 - 3/2018
Master Thesis, Center of Rapid Forming of Tsinghua University (THU) THU/EPFL
- Studied changes in particle size distribution, thermal conductivity and other powder properties.
 - Simulated the AM process: powder bed spreading and subsequent single track forming.
 - Presented the work on an international conference.
- Powder jet focusing by electrostatic lenses for DED** 3/2017 - 8/2017
Industrial Internship, Laboratory for Advanced Materials Processing EMPA/EPFL
- Designed a powder focusing system using electrostatic field and simulated the system in COMSOL.
 - Demonstrated feasibility of the design by focusing stainless steel powder in experiments.
- Microstructure and mechanical properties of urchinteeth** 11/2014 - 6/2015
Bachelor Thesis, Institute of Metal Materials ZJU
- Described the features of urchin teeth's structural elements and characterized their micro-mechanical properties using SEM and micro-indentation.
 - Determined the organic contents in various zones of developing parts via thermogravimetric analysis.
 - Explained the self-sharpening mechanism of urchin teeth and discussed biomineralization in them.

Preparation of Silicon-based Nanostructured Anode for Li Batteries 6/2013 - 5/2014
Student Research Training Program, Institute of Metal Materials ZJU

- Explored the best proportions of silicon and carbon using variable-controlling method.
- Designed a sandwich structure to buffer the huge volume change of silicon particles during battery cycling and protect them from falling off the anode.

SOCIAL & STUDENT WORK

China National Knowledge Infrastructure (CNKI) 11/2017 - Present
External Translation Expert, International Publishing House (IPH) CNKI

- Translates research papers from Chinese to English.

Materials Science and Engineering Section (IMX) 11/2016 - 4/2018
Student Assistant EPFL

- Assisted Prof. émér. Wilfried Kurz in redrawing figures and obtaining copyright permissions for publishing a series of important review articles (over 80 pages, 100 figures, 1'500 references).

HONORS & AWARDS

- **Excellent Student** Awards of Zhejiang University (5%) 12/2012
- Scholarship for **Outstanding Students** of Zhejiang University (15%) 12/2012
- Scholarship for **Outstanding Merits** of Zhejiang University (15%) 12/2012
- 3rd Prize in the **Physics Contest** of Zhejiang Province (15%) 12/2012

RESEARCH SKILLS

Techniques Laser/e-beam AM, metallographic preparation, SEM, EDS, EBSD, mechanical tests
Softwares Simens NX, AutoDesk PowerShape & PowerMill, Photoshop, COMSOL, LabVIEW

LANGUAGES

- **Chinese** (native), **English** (fluent, TOEFL 100), **German** (basic, A1), **French** (basic, A1)

PUBLICATIONS

- Cui, D., Mohanta, A., Leparoux, M. **Interface Control in Additive Manufacturing of Dissimilar Metals Forming Intermetallic Compounds—Fe-Ti as a Model System**. *Materials* **2020**, 13, 4747.
- Cui, D., Lanfant, B., Leparoux, M., Favre, S. (2021). **Additive Manufacturing of Ti-Nb Dissimilar Metals by Laser Metal Deposition**. In: Meboldt, M., Klahn, C. (eds) *Industrializing Additive Manufacturing*. AMPA **2020**. Springer, Cham.
- Wasmer, K., Wüst, M., Cui, D., Masinelli, G., Pandiyan, V., Shevchik, S. (2023) **Monitoring of functionally graded material during laser directed energy deposition by acoustic emission and optical emission spectroscopy using artificial intelligence**. *Virtual and Physical Prototyping* **2023**, 18:1, e2189599.
- Pandiyan, V., Cui, D., Le-Quang, T., Deshpande, P., Wasmer, K., Shevchik, S. **In situ quality monitoring in direct energy deposition process using co-axial process zone imaging and deep contrastive learning**. *Journal of Manufacturing Processes* **2022**, 81, 1064.
- Pandiyan, V., Cui, D., Parrilli, A., Deshpande, P., Masinelli, G., Shevchik, S., Wasmer, K. **Monitoring of Direct Energy Deposition Process Using Manifold Learning and Co-Axial Melt Pool Imaging**. *Manufacturing Letters* **2022**, 33, 776.
- Nakajima, K., Leparoux, M., Kurita, H., Lanfant, B., Cui, D., Watanabe, M., Sato, T., Narita, F. **Additive Manufacturing of Magnetostrictive Fe–Co Alloys**. *Materials* **2022**, 15, 709.